High Fidelity, Multi-Disciplinary Analyses of Flow in Weapon Bays

by

Savio V. Babu (MEng.)

Thesis submitted in accordance with the
requirements of the University of Liverpool for
the degree of Doctor in Philosophy by
Savio V. Babu
August 2014

Abstract

Modern military aircraft employ weapon bays for carriage and release of stores. The clearance of these stores for release from aircraft may require several flight tests at a range of conditions where the trajectories of released stores are obtained through accelerometers located on the store. Although effective, this is expensive and time consuming and only limited flight tests can be accomplished at critical conditions. Predictions made using store release analysis through wind tunnels and Computational Fluid Dynamics (CFD) have the potential to reduce the number of flight tests required for store clearance. The motivation for the current work, stems from the need to investigate carriage and release of a store from a weapon bay, idealised as a rectangular cavity, through a unique blend of disciplines comprising Computational Fluid Dynamics, Computational Structural Dynamics (CSD), Computational Aero-Aeroacoustics (CAA) and High Performance Computing (HPC).

Detached-Eddy Simulations (DES) of flow in clean cavities were carried out to compare two cavities of different aspect ratios for configurations with doors-off and doors-on. Both cavities had similar acoustic signatures and the addition of doors channelled the flow causing acoustic waves to propagate further away from the cavity.

DES computations were carried out for a store at different positions relative to a cavity that showed that a store at carriage position pacified the cavity acoustics the most. Fin tip displacements were small for a store at carriage position and exhibited buzzing characteristics. This was similar to the case where a store was positioned at the shear layer of a cavity but with slightly larger displacements. While fin displacements were not large, the results highlighted concerns for fin fatigue life. Comparisons between rigid and elastic fins showed small differences in loads, however, aeroelastic simulations showed that where resonance of structural and cavity modes occurred, large amplitude fin oscillations were predicted.

Scale-Adaptive Simulations (SAS) were validated against experimental data for clean cavities and were found to be similar to DES results and could be run at a larger time-step. The cost savings and similarities of SAS to DES encouraged its use for store release computations. Store release computations from a cavity were conducted and the variability of a stores trajectory due to the unsteady cavity flow-field was investigated. Visualisations using Q-criteria highlighted instantaneous structures that were in contact with the store fins causing the trajectory to vary for different release times. Overall, the thesis suggests the use of SAS as an affordable method for analysing store release computations from a cavity and highlights the need for a stochastic evaluation of trajectories from transonic cavities.

A study comparing different signal lengths for post-processing unsteady pressure data revealed that, the minimum CFD signal length required to capture all dominant tones was around 0.05s. Different post-processing methods for spectral content were compared and the use of Maximum Entropy Methods (MEMs), based on Burgs Estimator, was suggested as it not only captured dominant tones but also predicted the highest Sound Pressure Levels (SPLs), that could be used to produce the maximum boundary of a given signal.

Declaration

I hereby declare that this dissertation is a record of work carried out in the School of Engineering at the University of Liverpool during the period from August 2010 to August 2014. The dissertation is original in content except where otherwise indicated.

August 2014

.....

(Savio V. Babu)

Acknowledgements

I would like to express my deepest appreciation to my supervisor Prof. George Barakos. It has been a long and difficult journey and I could ask for no one else but George to guide me. Without his dedication and persistent help, this thesis would not have been possible.

I would like to thank Prof. Ken Badcock, my second supervisor, Dr. Rene Steijl, for his support with the aeroelastic work and Dr. Mark Woodgate, for sharing his knowledge, critiquing my grids and always being there to restart my computer. I would also like to extend my gratitude to Dr. Nigel Taylor of MBDA UK for providing the data used in this work and his continued enthusiasm and support throughout the entire project. Special thanks to Steve Garton of MBDA UK for his contributions to the aeroelastic work. Other members of MBDA UK that I would like to extend my gratitude towards include Steve Lawson, Rodney Irvine and Ben Newby.

For the good part of four years, the CFD lab has been my home and the people I've worked with were like family and for that I would like to thank Marina, little George, Cathy, Mikolaj, Clement, Florent, Antonio, Matt, Massimo, Ghazal, Simone, Vladmir, Vincent, Jacob, and Jurr.

Most of all I would like to thank my family, for their unwavering love and support throughout this project.

The use of the POLARIS HPC cluster of N8 and the Chadwick HPC cluster of the University of Liverpool are also gratefully acknowledged. Finally, the financial support of the Engineering and Physical Sciences Research Council and MBDA through grant EP/C533380/1 is gratefully acknowledged.

Publications

Book Chapters

S.V. Babu, G. Zografakis and G.N. Barakos, Evaluation of Scale-Adaptive Simulations for Transonic Cavity Flows. *Notes on Numerical Fluid Mechanics and Multidisciplinary Design, S. Girimaji, W. Haase, S.H. Peng, D. Schwamborn (Eds.), Volume 130, pp 433-444, 2015, ISBN: 978-3-319-15140-3*.

Journal Papers

S.V. Babu, G. Zografakis and G.N. Barakos, Evaluation of Scale-Adaptive Simulations for Transonic Cavity Flows. *International Journal of Engineering Systems Modelling and Simulation. Accepted*, 2014.

S.V. Babu, F. Dehaeze and G.N. Barakos, Understanding Store Loads using DES and Strongly-Coupled Aeroelastic Simulations. *Under Review in Journal of Aircraft,2015*.

S.V. Babu and G.N. Barakos, Store Release Simulations using SAS and Overset Grids. *In Preparation*.

Papers in Conference Proceedings

S.V. Babu, F. Dehaeze and G.N. Barakos, Understanding Store Loads using DES and Strongly-Coupled Aeroelastic Simulations. *52nd AIAA SciTech Aerospace Sciences Meeting, Maryland, DC, USA, 13-17 January*, 2014.

S.V. Babu, G. Zografakis and G.N. Barakos, Evaluation of Scale-Adaptive Simulations for Transonic Cavity Flows. *5th HRLM Symposium, Texas A&M University, College Station, Texas, USA, 19-21 March*, 2014.

S.V. Babu and G.N. Barakos, Prediction of Acoustics of Transonic Cavities using DES and SAS. *49th International Symposium of Applied Aerodynamics: Aerodynamics and Environment, Lille, France, 24-26 March*, 2014.

S.V. Babu and G.N. Barakos, Store Release Simulations using DES, SAS and Overset Grids. *Royal Aeronautical Society Biennial Applied Aerodynamics Research Conference: Advanced Aero Concepts, Design and Operations, Bristol, UK, 22-24 July*, 2014.

Presentations without Proceedings

S.V. Babu and G.N. Barakos, Prediction of Acoustics of Transonic Cavities using DES and SAS. *3rd International Workshop: Computaional Experiment in AeroAcoustics, Svetlogorsk, Russia, 24-27 September*, 2014.

Internal Reports

S.V. Babu, *Unstructured Mesh Generation using ICEM CFD, TN10-023, October*, 2010

S.V. Babu and C.S. Johnson, *Proudmann's Method for Approximating Acoustic Levels, TN13-001, January*, 2013

S.V. Babu, *Flow-Field Reconstruction using POD in MATLAB, TN14-005, July*, 2014

Contents

List of Figures

List of Tables

Nomenclature

Acronyms	Definition
6DoF	Six Degrees of Freedom
AEDC	Arnold Engineering Development Center
AFSEO	Air Force SEEK EAGLE Office
AMRAAM	Advanced Medium-Range Air-to-Air Missile
BISPL	Band- Integrated Sound-Pressure Level
BLACS	Basic Linear Algebra Communication Subprograms
BLAS	Basic Linear Algebra Subprograms
CAA	Computational Aeroacoustics
CAN	Combined Asymptotic and Numerics
CCD	Charge-Coupled Device
CFD	Computational Fluid Dynamics
CFL	Courant-Friedrich-Levi condition number
CG	Centre of Gravity
CSD	Computational Structural Dynamics
CTS	Captive Trajectory System
CVT	Constant Volume Tetrahedron
dB	Decibels
DDES	Delayed Detached Eddy Simulation
DERA	Defence Evaluation and Research Agency
DES	Detached Eddy Simulation
DNS	Direct Numerical Simulation

EAL	Exact Arithmetic Library
FEM	Finite Element Model
FFT	Fast Fourier Transform
FSI	Fluid-Structure Interaction
GBU	Guided Bomb Unit
GPS	Global-Positioning-System
HMB2	Helicopter Multi-Block
HPC	High Performance Computing
IDAPS	Image Data Processing System
IHAAA	Institute of High Performance Computing Applications to Air Armament
JSF	Joint Strike Fighter
JTFA	Joint Time-Frequency Analysis
KLD	Karhunen-Loeve Decomposition
LAPACK	Linear Algebra PACKage
LES	Large Eddy Simulation
LIC	Line Integral Convolution
MDA	Missile Distributed Airloads
MDCFD	Minimum Domain CFD
MEM	Maximum Entropy Methods
MMTD	Miniature Munition Technology Demonstrator
MPI	Message Passing Interface
MUSCL	Monotone Upwind Schemes for Scalar Conservation Laws
MVBB	Minimum Volume Bounding Box
NAVAIR	Naval Air Systems Command
NAVSEP	Navy Generalized Separation Package
NCPA	National Center for Physical Acoustics
NED	North East Down

NICS	Navy Internal Carriage and Separation
OASPL	Overall Sound-Pressure Level
OMS	Overset Mesh Search
OVERFLOW	OVERset grid FLOW
PBLAS	Parallel Basic Linear Algebra Subprograms
PCA	Principal Component Analysis
PDE	Partial Differential Equation
PDGEMM	Parallel, Double precision, General Matrix Multiplication
PIV	Particle Image Velocimetry
POD	Proper Orthogonal Decomposition
PSD	Power Spectral Density
RANS	Reynolds-Averaged NavierStokes
RMS	Root-Mean-Square
S-A	Spalart-Allmaras
SAM	Spring Analogy Method
SAS	Scale-Adaptive Simulations
ScaLAPACK	Scalable Linear Algebra PACKage
SGS	Sub-Grid Scale
SPL	Sound-Pressure Level
SSB	Small Smart Bomb
SST	Shear Stress Transport
STFT	Short Time Fourier Transform
STOVL	Short Take-Off and Vertical Landing
SVD	Singular Value Decomposition
TetrUSS	Tetrahedral Unstructured Software System
TFI	Trans-Finite Interpolation
TWT	Trisonic Wind Tunnel
UCAV	Uninhabited Combat Air Vehicle

URANS	Unsteady RANS
WICS	Weapons Internal Carriage and Separation

Symbols	**Definition**
$\dot{p}, \dot{q}, \dot{r}$	Angular rate components in body axes
$\dot{u}, \dot{v}, \dot{w}$	Acceleration components in body axes
ℓ	Length scale
$\mathbf{F}$	Flux vector in the x-direction
$\mathbf{G}$	Flux vector in the y-direction
$\mathbf{H}$	Flux vector in the z-direction
$\mathbf{Q}$	Turbulent variables
$\mathbf{R}$	Flux residual
$\mathbf{u}^k$	Snapshots vector
$\mathbf{W}$	Vector of conserved variables
$\mathbf{W}_{i,j,k}$	Flux variables
Re_T	Turbulent Reynolds number
ω	Angular rate of the body
$\mathbf{x}_1$, $\mathbf{x}_2$, $\mathbf{x}_3$ and $\mathbf{x}_4$	Coordinates of the four face corners
A	Wall Area
a	Speed of sound
c	Reference length
C_F	Wall force coefficient
C_K	Kolmogorov constant
C_{DES}	Detached-Eddy Simulation constant
C_D	Drag coefficient
c_k	POD scalar coefficients vector
C_L	Lift coefficient
C_L	Roll moment coefficient, Root-bending moment coefficient
C_M	Pitch moment coefficient, Hinge moment coefficient

C_N	Yaw moment coefficient
C_P	Pressure coefficient
C_{SF}	Side-force coefficient
C_X	Axial force coefficient
C_Y	Side force coefficient
C_Z	Normal force coefficient, Panel-normal force coefficient
CG	Centre of gravity
D	Cavity depth
E	Total energy
e	Specific internal energy
$E(\kappa)$	Spectral distribution of energy
F	Fluid point
f	Frequency
f_i	Body forces vector
F_a	Aerodynamic force
f_m	Frequency of the m^{th} Rossiter mode
g	Acceleration due to gravity
H	Total enthalpy
I_{xx}	Roll inertia
I_{yy}	Pitch inertia
I_{zz}	Yaw inertia
J	Jacobian matrix
k	Coefficient of thermal conductivity, Specific turbulent kinetic energy
k_T	Coefficient of Thermal Conductivity
L	Cavity length
m	Mass of the store
m	Rossiter mode number

N	Number of samples/measurements
p	Pressure
p_{ref}	International standard for the minimum audible sound
Pr_T	Turbulent Prandtl number
Q	Dynamic pressure
q_i	(Favre-averaged) Heat flux vector
q_i	Heat flux vector
q_j^R	Turbulent contribution of the heat flux vector
q_∞	Free-stream dynamic pressure
R	Universal gas constant
Re_L	Reynolds number based on the cavity length, L
S	Reference area
S	Source Term for the Navier-Stokes Equations
S_1, S_2, S_3	Vertices of a triangular structural element
T	Temperature
t	Time
T_{ref}	Reference temperature
$T_{Rossiter1}$	Lowest Rossiter mode
T_S	Sutherland temperature
u, v, w	Velocity components
u_i	Velocity vector
U_{ij}	Input matrix for for ScaLAPACK routines
$u_i u_i$	Kinetic energy
V	Velocity of the store
V	Volume
$V_{i,j,k}$	Cell volume
W	Cavity width
x, y, z	Cartesian coordinates

x_i	Coordinates vector
a', b', c' and d'	Updated vectors a, b, c and d after structural deformation
a, b, c and d	Vectors used for the projection of a fluid node on a triangular structural element

Greek Symbols	**Definition**
α_i	Modal amplitude
α	Constant in Rossiter's formula representing a phase shift, Angle of attack
α, β, γ	Coefficients used to define the CVT association between fluid nodes and structural elements
β	Angle of sideslip
Φ	Spatial POD modes
δ_{ij}	Kronecker delta
$\dot{\phi}, \dot{\theta}, \dot{\psi}$	Euler angle rate components
η, τ, υ	Kolmogorov length, time and velocity Scales
γ	Ratio of specific heats
κ	Wavenumber
κ_v	Constant in Rossiter's formula representing convection speed of disturbances
λ	Eigenvalues vector from the POD
μ	Molecular viscosity
ν	Kinematic viscosity
$\overline{\phi}$	Mean part of a quantity
ϕ	Arbitrary flow quantity
ϕ'	Fluctuating part of a quantity
ϕ, θ, ψ	Euler angles
ρ	Density of air
ρ	Density
τ	Pseudo time-step

τ_{ij}	Viscous stress tensor
τ_{ij}^{R}	Reynolds stress tensor
ε	Dissipation rate of turbulent kinetic energy
ξ, η, ζ	Local coordinate system

Subscripts	**Definition**
∞	Free-stream value
i	Index i=1,2,3...
i	Inviscid component
j	Index j=1,2,3...
k	Index k=1,2,3...
v	Viscous component

Superscripts	**Definition**
$'$	Fluctuating part
b	Body axis
e	Earth axis
i	Inviscid component
n	Current time-step
$n+1$	Next time-step
v	Viscous component

Chapter 1

Introduction

1.1 Background and Motivation

The growing demand for stealth in modern manned and unmanned military air vehicles has pushed designers to move externally carried stores into internal weapons bays that have already found place in aircraft like the F-22 Raptor[1] (Figure 1.1(a)) and the modern F-35[2] (Figure 1.1(b)). This accelerated the research into transonic cavity flows in order to understand its complex nature and the acoustic footprint associated with it. After over seven decades of cavity flow research, studies into captive stores and store releases from cavities are now gaining popularity owing to the increasing sophistication of weapons bays.

The problem here is that high speed flow over an open weapons bay creates a harsh turbulent environment that can affect the store or the structure of the aircraft. This in turn affects the separation characteristics of a store as it passes through the unsteady turbulent layer of air established along the length of the open bay. The inclusion of weapons bays also bring about the need for fast and inexpensive design and analysis tools; expensive stores and release during manoeuvres further invokes this need.

Transonic weapons bay flow together with the carriage and release of stores present a challenging and complex problem where Computational Fluid Dynamics (CFD), Computational Structural Dynamics (CSD), Computational Aeroacoustics (CAA) and Body Dynamics come together in a unique way enabling the development of methods and tools for industry application; therein lies the motivation for the current and future work.

(a) F-22A Raptor (b) F-35 Lightning II

Figure 1.1: Exposed internal weapons bay of the (a) F-22A[1] showing a store being held by a rig and the complex design and packing of the (b) F-35[2] aircraft.

1.2 Literature Survey

The literature survey revealed the challenges in simulating the carriage and release of a store from a cavity, including its aeroelastic characteristics, and the lack of experimental data to validate trajectories of released stores. It also helped to establish the novelty of the research undertaken in this project.

The topics targeted for the survey included but were not limited to empty weapons bay flow, store release from weapon bays, aeroelastics of stores in weapons bays, simulation of store releases using overset grids and experimental data for store releases from weapons bays. The main search engines used for literature searches were Scopus[18], Web of Knowledge[19], the Defense Technical Information Center (DTIC)[20],the American Institute of Aeronautics and Astronautics (AIAA) library[21], and the NASA technical report server (NTRS)[22]. While a considerable number of papers were found on empty bay flow, usually referred to as clean cavity flow for idealised cavities, very few were found on store carriage and release from cavities, that are the primary subjects of this thesis. It must be noted that several studies[23–25] are available in literature relating to external store release from wings, which is a well studied problem that has even been extended to studying[26,27] the flutter of wings carrying stores.

A literature review on cavity flows was published by Lawson & Barakos[28] who summarised a large collection of works relating to weapon bays, idealised cavities and passive flow control devices.

1.2.1 Studies on Store Carriage and Separation from Cavities

Experimental Investigations

In the early 1980s, Stallings[29] conducted experiments to determine the aerodynamic characteristics of a wing-controlled store exiting a cavity at a supersonic Mach number of 2.36 and unit Reynolds number of $6.6 \times 10^6/m$, for a shallow cavity with L/D=11.36 and a deep cavity with L/D=4.44. The rig had an upstream splitter plate to establish a well defined flow-field approaching the cavity. The Langley Unitary Plan Wind Tunnel was used for the tests in which the aerodynamic loads acting on the store in carriage were measured through the use of a sting that allowed the model to be positioned relative to the cavity.

The aerodynamic data were then used to make simplified two-degrees-of-freedom calculations for a full-scale store, separating from a cavity, in an open and closed cavity flow-field, with an ejection velocity of 6.1m/s. From these calculations, the following conclusions were made: large interactions were seen to exist between the shallow cavity and the flat plate that resulted in unfavourable separation characteristics for the store, while for the deep cavity, the flow-field bridged the cavity length causing only minor interactions and hence favourable separation characteristics for the store.

As part of the Defence Evaluation and Research Agency (DERA) research programme on internal carriage of stores, Ross and Odedra[3], measured the component loads acting on a $1/10^{th}$ scale Advanced Medium-Range Air-to-Air Missile (AMRAAM) model located within cavities of different geometries. Cavities with L/D=10 (shallow) and 5 (deep), with and without doors, were used at test Mach numbers ranging from 0.6 to 1.35. Results for the shallow cavity (Figure 1.2) showed that high pitching moments were generated due to the interaction of the cavity outflow on the fins. It was suggested that the pitching moment could hence be reduced by removing the fins from the aft region of the cavity. Simulated store release trajectories (Figure 1.2(c)) using the computed loads showed that the store released from the shallow cavity had a large nose up pitching moment that recovered over time.

For both shallow and deep cavities, the store was subjected to high levels of unsteady pressure. Within the deep cavities, where the acoustic environment was harsh, most of the energy was found to be concentrated into a small number of discreet tones while for the shallow cavities, the store was subjected to a broadband frequency spectrum where the amplitude reduced with increase in frequency.

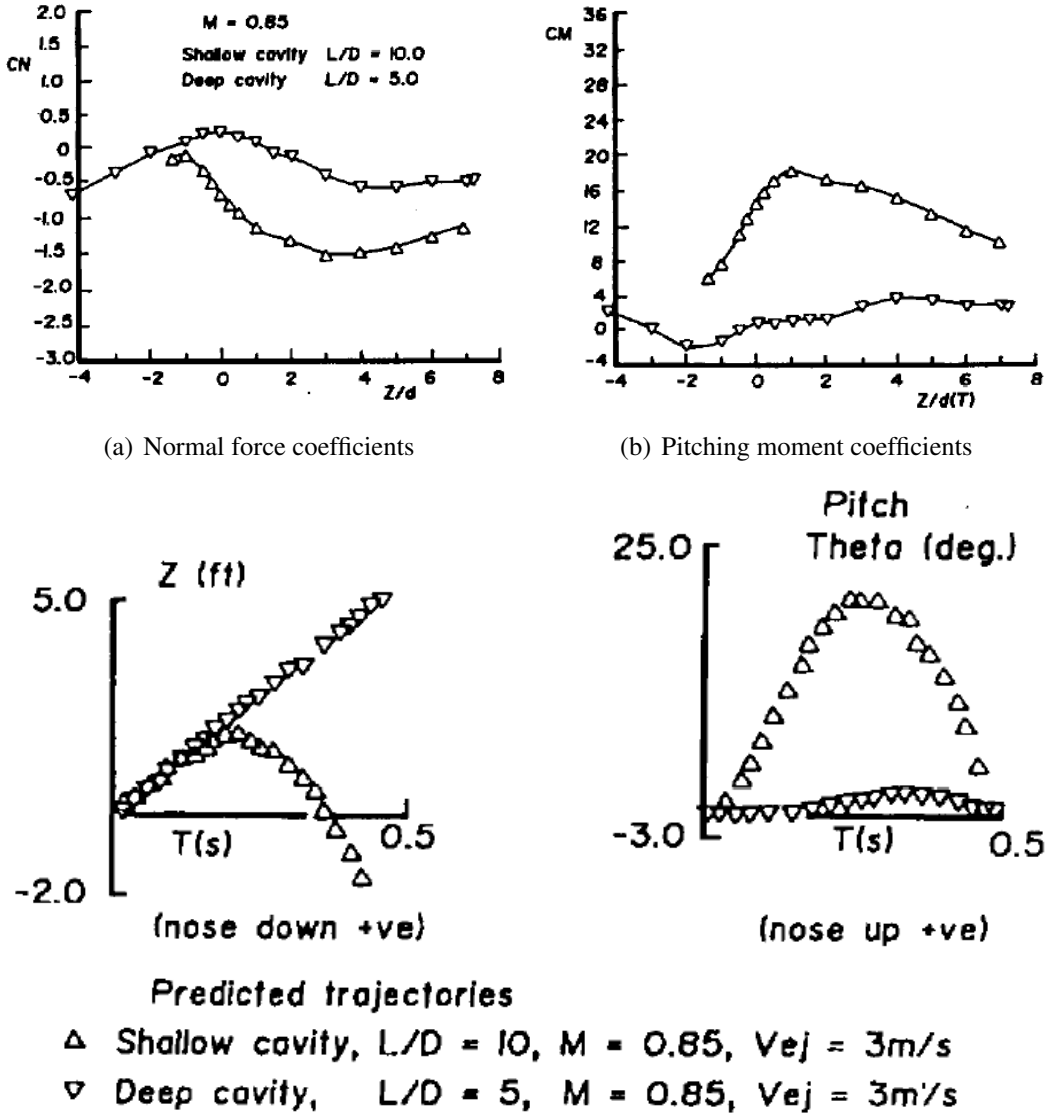

(a) Normal force coefficients

(b) Pitching moment coefficients

(c) Simulated trajectories

Figure 1.2: Comparison of normal force (a) and pitching moments (b) on an AMRAAM model used for simulated store release trajectories from shallow and deep cavities (c), showing normal displacement and pitching moment[3].

Murray *et al.* [4] studied the separation of a $1/15^{th}$ scale Guided Bomb Unit (GBU-38) from the Tri-Sonic wind tunnel at the National Center for Physical Acoustics (NCPA). Tests were conducted from an idealised rectangular cavity of L/D=6, at a Mach number of 1.5. The trajectory of the store was measured using a particle tracking method derived from Particle Image Velocimetry (PIV) which was applied to images acquired using a high-speed charge-coupled device (CCD) camera and strobe system.

Data were acquired by sampling the image acquisition trigger along with the pressure loads inside the bay so that the loads in the bay could be synchronised with the store's trajectory in order to observe the phase relationship. Figure 1.3 shows a frame from a schlieren video recorded during one of the store drops. Several test drops were performed at high and low ejection forces. Dynamic pressure transducers were installed to measure the cavity pressure fluctuations. The high ejection velocity resulted in a residence time for the store in the shear layer of approximately 2ms while the low ejection velocity resulted in a residence time of about 5ms. Large variations in pitch angle were found, and the phase relationship between the store release and the pressure oscillations in the cavity was also different for each test. The study suggested that this phase relationship was a key initial condition to determine the resulting trajectory and attitude of the store.

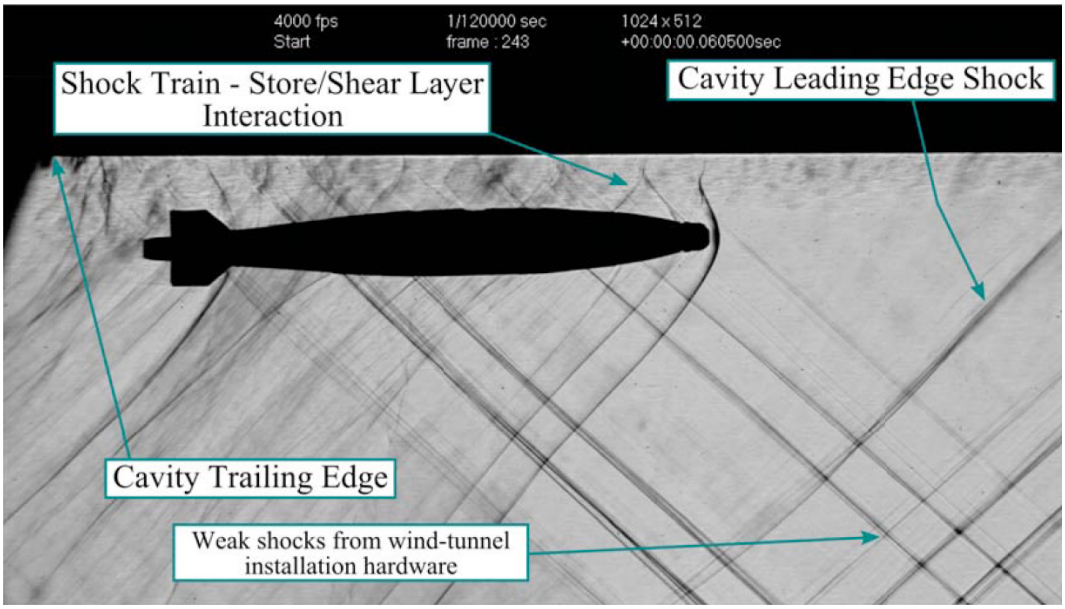

Figure 1.3: Schlieren image of the model store ejected from the L/D=6 cavity [4].

Numerical Investigations

A short account of attempts to use simple methods, to approximate the store release problem, is given to highlight the requirement for a high-fidelity simulation tool to approach the problem with. One such method, called combined asymptotic and numerical (CAN) method, was used by Shalaev *et al.* [30], who modelled the vertical motion and pitching moments of thin bodies of revolution separating from a rectangular cavity.

The study concluded that while some aspects of the body dynamics could be captured through approximate models, more complex flow phenomena, like the dynamics of the shear layer and the unsteadiness of the cavity flow-field, that affected the body separation, could not.

Sahoo *et al.* [31] used a low-order model to determine the trajectory of a store released from a supersonic cavity with and without microjets. The model, although validated against experimental data, was based on several major assumptions: the store had to be a slender axisymmetric body, the shear layer had to be thin in comparison to the cavity length, the external flow should be of high Reynolds number and the fluid inside the cavity should be quiescent.

Attempts at simplifying the problem have not just been made in terms of using methods like the ones mentioned earlier, but also through simplified CFD computations.

Kraft and Lofthouse[32] presented their attempt at studying the non-repeatability of store release from internal weapon bays through a 2D flow simulation. The OVERset grid FLOW (OVERFLOW) solver[33] was used in conjunction with overset grids to release a representation of a GBU-38 without an ejection velocity (gravity-released). The 2D configuration consisted of a cavity with L/D=4.5, obtained from the Weapons Internal Carriage and Separation (WICS) program wind-tunnel database, that had a leading and trailing flat plate. Computations were carried out using the Shear Stress Transport Delayed Detached Eddy Simulation (SST-DDES) turbulence model at a freestream Mach number of 0.95 and Reynolds number of approximately 5.2 million based on the store diameter of 10.75in. A 2D representation of the store was obtained by taking a cut along its centreline and leaving the fins out. The store was released from the bay at four starting points corresponding to four different time instances based on the loads acting on the store. While the release of the store was expected to give different trajectories for different instances it was released at, it was found that the 2D simulations were not able to show this due to the limitations and simplifications of the simulation.

Another example of simplified methods, applied to the store release problem, can be found in the study by Johnson *et al.* [34]. In order to reduce the large computational time generally associated with CFD computations, a low fidelity model was developed to obtain the force and moment loading on a store through the use of a Minimum Domain CFD (MDCFD) method.

MDCFD is a subset domain used to solve the flow-field of a minimum volume of interest. First the aircraft flow-field solution, without the store, was obtained. Then, a near-field domain was defined, containing the store and a portion of the aircraft close to the store, but large enough for the store to move away from the aircraft beyond any point of mutual interference. The store was allowed to move in the near-field domain, which was fixed relative to the aircraft. A far-field was defined to collect store data beyond the near-field domain. The flow-field around the aircraft was computed with the store at different positions in the near-field domain and a database of store force and moment data, as a function of store position, was built up to be used for a six-degrees-of-freedom simulation. In all domains, the steady flow was computed and at the boundaries of the near-field and far-field, the flow was interpolated. This technique was applied for the release of the Miniature Munition Technology Demonstrator (MMTD) store from the right main weapons bay of a $1/15^{th}$ scale F/A-22 aircraft wind-tunnel model. Computations performed at Mach numbers of 0.9 and 1.3 showed good comparison of average load data for the store. Store release computations however were not able to correctly predict the orientation of the store during release although the translations were captured well.

CFD computations of store carriage and separation are generally scarce in literature and mainly present simulations that are not time accurate, but instead based on a database of aerodynamic data obtained from isolated store computations.

Khanal *et al.* [5] compared DES computations to experimental data, for cavities of L/D=5.42 and L/D=6.25, at a Mach number of 0.8, with and without a generic ogive-cylinder body store, with a flat base, without fins and held to the floor of the cavity by a strut as seen in Figure 1.4. Negligible differences were seen in the C_P distribution along the front half of the cavity while a more pronounced effect was seen towards the rear of the cavity, possibly due to the reduced spanwise flow caused by the presence of the store. The blockage effect of store and strut on the spanwise flow was thought to be the reason limiting the spanwise and streamwise flow fluctuations.

A description of the weapon separation analysis process and the tools used by Arnold Engineering Development Center (AEDC) for the release of a Global-Positioning-System (GPS)-guided Small Smart Bombs (SSB) from a Boeing X-45A Unmanned Combat Air Vehicle (UCAV), was given by Smith and Schwimley[6].

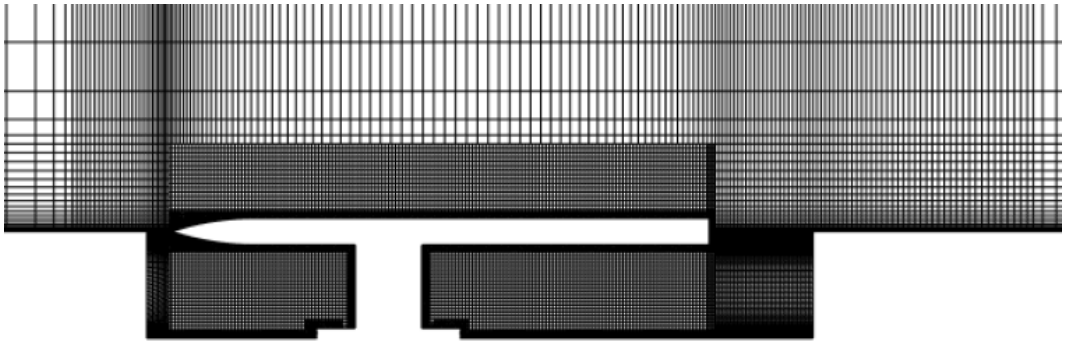

Figure 1.4: Mesh slice for cavity with a store grid [5].

CFD was used to obtain isolated aircraft flow-field data as well as to generate aerodynamic grid data for the store with folded and deployed wings at carriage, at the bay opening and at the bottom edge of the bay door.

Smith and Schwimley[6] used the Missile Distributed Airloads (MDA) code, which is an aerodynamics prediction method used by AEDC, to compute the effect of the aircraft flow field on the store aerodynamics. A combination of MDA data and freestream store aerodynamic data was used to predict the trajectory of a store released from the weapon bay of the X-45A; the trajectory was found to be benign.

While flight test data showed good comparison (Figure 1.5) with the predicted trajectory in terms of the translation of the store, the orientations did not compare as well. The authors noted that this was possibly due to the lack of incorporation of weapon bay flow phenomena that were missing from the simulation.

Lee *et al.* [35] presented CFD computations for the Marine Corps variant of the Joint Strike Fighter (JSF) for the analysis of stores separating from the internal weapons bays using the BEGGAR[36] solver. First, freestream validation of the stores was carried out following which the data were used with a couple of Short Take-Off and Vertical Landing (STOVL) conditions to generate CFD-based trajectory data. The study showed that STOVL ejections were safe and benign for the conditions that were investigated.

Coley[7] undertook a computational investigation to study the relationship between the acoustic modes of a cavity to the force and moment loading of a store located inside the cavity. Similar to the work by Kraft and Lofthouse[32], the WICS wind-tunnel data were used together with the OVERFLOW 2.1 solver[33]. A tenth-scale of a modified Mark-82 store was used along with a cavity of L/D=4.5 for simulations at a Mach number of 0.95 at a Reynolds number of $2.5 \times 10^6/ft$.

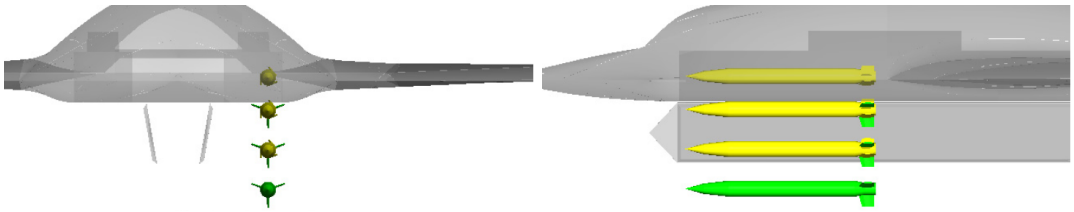

(a) SSB grid data positions

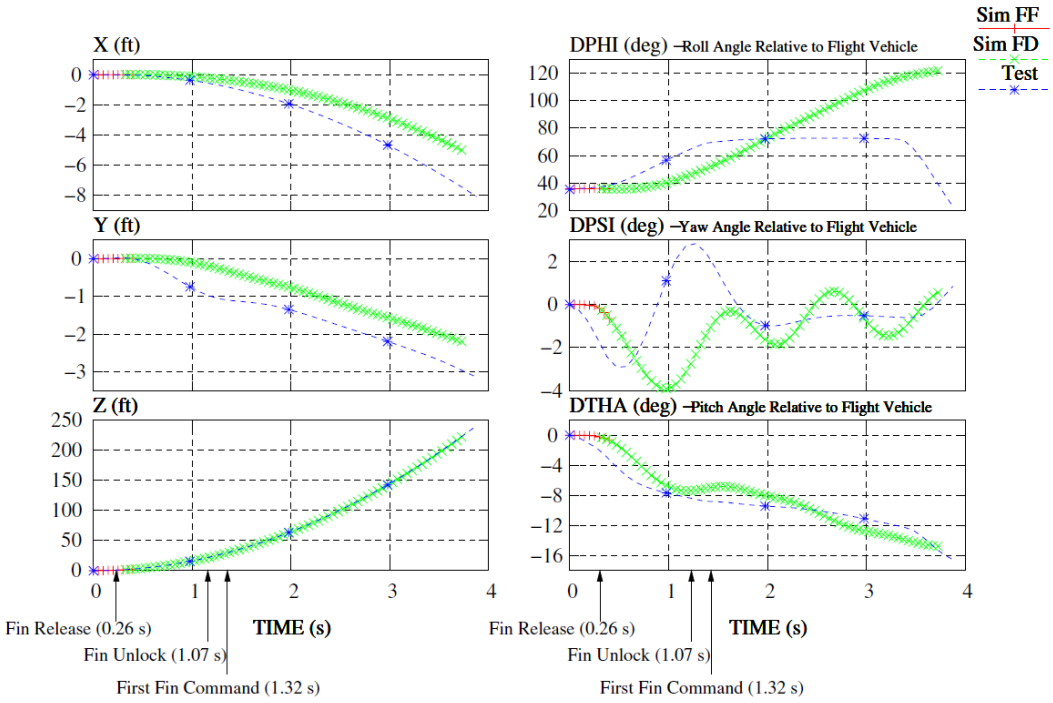

(b) X-45A flight data and simulation comparison

Figure 1.5: Grid data positions of the SSB (a) and comparisons of simulation and flight test data (b) for the store release[6] . FF: Fins folded, FD: Fins deployed, DPHI: Roll angle, DTHETA: Pitch angle, DPSI: Yaw angle.

Several configurations of the store at different positions relative to the store were studied using CFD and the following conclusions were drawn: the force and moment loading on the store correlated to the pressure fluctuations in the cavity, the presence of the store did not fundamentally alter the acoustics of the cavity, however it lowered the low-frequency response at the the aft-wall, the presence of the store at the shear layer did not suppress cavity vibrations and the stable configuration of the store in the cavity changed to an unstable one as it entered the shear layer.

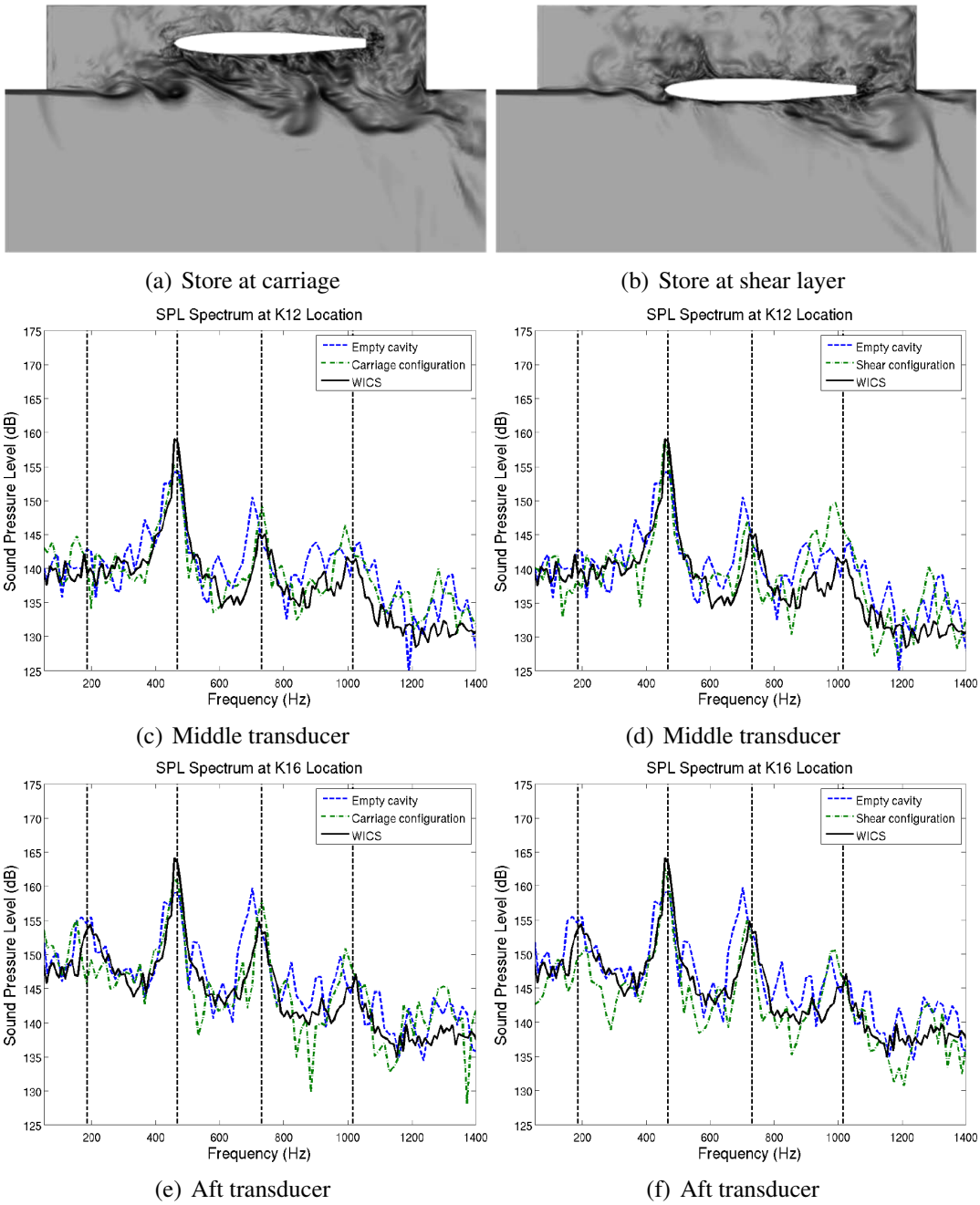

(a) Store at carriage (b) Store at shear layer

(c) Middle transducer (d) Middle transducer

(e) Aft transducer (f) Aft transducer

Figure 1.6: Numerical schlieren and SPL spectrum for the store at carriage (left column) and at the shear layer (right column) of the cavity[7]. Pressure transducers are for the middle and aft regions of the cavity.

Other works that have used DES for flow computations of weapon bays, include Berglind *et al.* [37] who performed computations for the the SAAB FS2020 concept aircraft, with a cavity of L/D=5.75, at a Mach number of 0.9, Reynolds number of $16 \times 10^6/ft$ and angle of attack, $\alpha = 9\,\text{deg}$. SPL levels on the cavity floor along the centreline ranged from 50dB to 150dB, for a range of frequencies less than 2000 Hz.

No tonal modes were observed in the spectra for which the authors speculated the cause to be the angle of attack. A store model of an AIM9L was later positioned inside and at the shear layer of the cavity. Computations for the store at the shear layer were carried out using a hybrid Reynolds-Averaged NavierStokes (RANS)- Large-Eddy Simulation (LES) HYB0 model, while for the store inside, a Spalart-Allmaras (S-A) RANS model was used. When the store was inside, the impact of the mixing layer was slightly altered, and the recirculating flow on the floor became more intensified. Moving the store to the opening of the bay largely altered its flow features, alleviating the impact on the cavity aft wall.

Finney[8] utilised the Navy Internal Carriage and Separation (NICS) experiments to compare with CFD results for a Mark 82 store at different cavity/store configurations for a cavity with L/D=4.5 at a freestream Mach number of 0.85. An unstructured CFD study was conducted modelling the aerodynamics of flow in the vicinity of the store along the traverse using a steady-state approach. CFD results indicated that the faired strut used to position the store inside the bay did not have a large influence on the loads acting on the store.

Forces and moments on the store were measured along a longitudinal traverse at the opening of the bay at different grid points that were used as input to Navy Generalized Separation Package (NAVSEP) along with ejector and inertial forces. This program was used to calculate the trajectory of a store released from a cavity.

Force measurements on the store using CFD were in qualitative agreement with the wind tunnel tests, both showing increasing pitching moments away from the opening of the bay as the store is positioned aft in the opening. CFD measurements under predicted the magnitude of the pitching moment by approximately 50% at each station. These differences were not as significant in the trajectory simulation however.

The trajectory predicted from the wind tunnel data fell within the standard deviation bounds for the CFD data in every parameter except for the y-axis displacement. Finney concluded from his study that CFD could be used as a rough estimate of the trajectory but was not accurate enough to be used to certify store releases or establish test sequences.

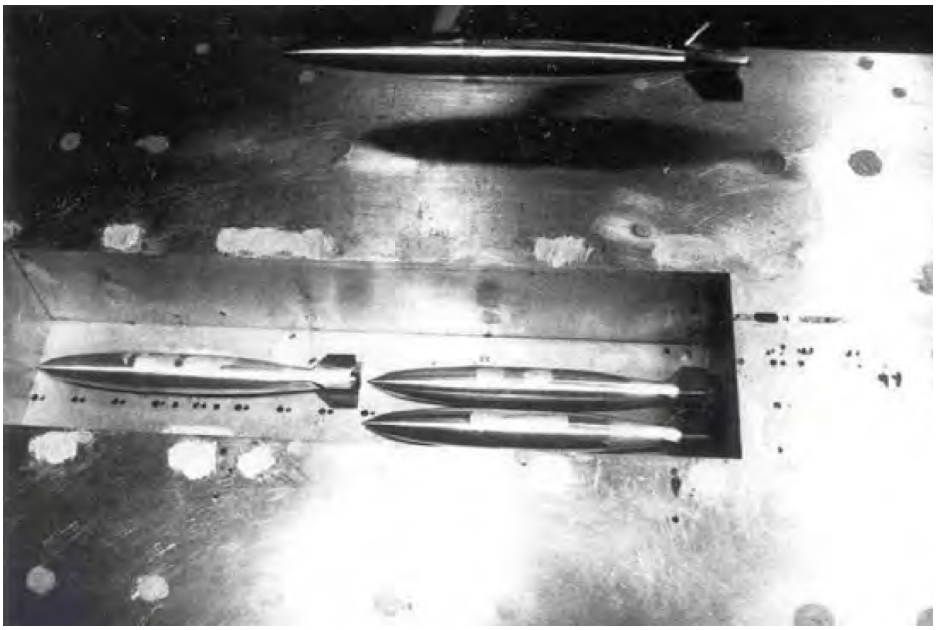

Figure 1.7: NICS cavity configuration[8] .

Efficient, time-accurate flow simulations around a weapons bay, still remains a challenging problem facing the applied aerodynamics and CFD communities[38–41,41]. With conventional engineering analysis methods not being able to capture the temporal effects of the unsteady flow-field inside a bay, and the need for validation of computational techniques for store release, the Institute of High Performance Computing Applications to Air Armament (IHAAA) sponsored a collaborative effort to address this problem. This included the Naval Air Systems Command (NAVAIR), the Air Force SEEK EAGLE Office (AFSEO), and the Air Force AEDC. The objectives of this collaboration included the demonstration and validation of a computational tool to simulate time-accurate store release trajectories from a weapons bay, the comparison of results with conventional analysis methods and the documentation of lessons learned.

Spinetti and Jolly[9] documented this study for the release of a GBU-38 from the bay of a B-1B aircraft. The flow-field around the B-1B aircraft, its internal bay, with an L/D=1.875, and the trajectory of the GBU-38 after ejection were simulated with DES using the S-A turbulence model. Overset structured grids were used for the composition of the grids for the aircraft and the store, that were made up of 21.9 and 2.5 million grid points respectively and shown in Figure 1.8. Computations were performed for a full and partially full rack of stores, at a Mach number of 0.88 and nominal altitude of 15,800 ft using the BEGGAR[36] solver. Details of the store and ejector properties can be found in Reference [9].

Comparisons of trajectories obtained through CFD were made against telemetry and Image Data Processing System (IDAPS) flight-test data. CFD results for the trajectory of the store showed divergence from telemetry and IDAPS data for both translations and displacements. Disparity between the telemetry and the IDAPS flight-test measurements were also observed suggesting that the IDAPS camera may not have been correctly calibrated.

A sensitivity analysis of the trajectory to the store moment of inertia showed that by increasing the axial moment of inertia, I_{xx}, by an order of magnitude, the roll attitude was affected significantly with minor changes in the other attitudes. The translations of the store however, remained similar. Different locations and durations of the forward and aft ejectors were also analysed to show similar divergence in the trajectories as before. The pitch attitude and the vertical translational displacement, however showed better agreement.

Results for the partially full rack showed yaw predictions that were in better agreement with flight-test data than results for the empty aft-rack case, indicating the dependence of the store trajectory on the load-out configuration and the ensuing flow field within the weapons bay. Overall the study highlighted that accurate trajectory simulations required accurate store properties but also demonstrated time-accurate release of a store from a bay.

Another set of time-accurate computations were conducted by Johnson and Cary[10] for the release of SSB's from the bay of an F-111 aircraft. All simulations were performed using second order spatial discretisation and first order time integration of the Euler equations on a system of overset computational grids using the BEGGAR[36] solver. Trajectories were computed at Mach numbers of 0.8 and 0.95 and compared well with wind tunnel and flight test data.

Aeroelastics of Stores in Cavities

To date, the only work available in literature regarding fluid-structure interactions of a store in a cavity is that by Arunajatesan *et al.* [11] that presents the use of a one-way coupled Fluid-Structure Interaction (FSI) framework for the simulation of a flexible store in a cavity.

The SIGMA CFD solver, was initially validated using data from the Weapons Internal Carriage and Separation (WICS) cavity database and in-house measurements[42] at Sandia National Laboratories using Sandias Trisonic Wind Tunnel (TWT) facility.

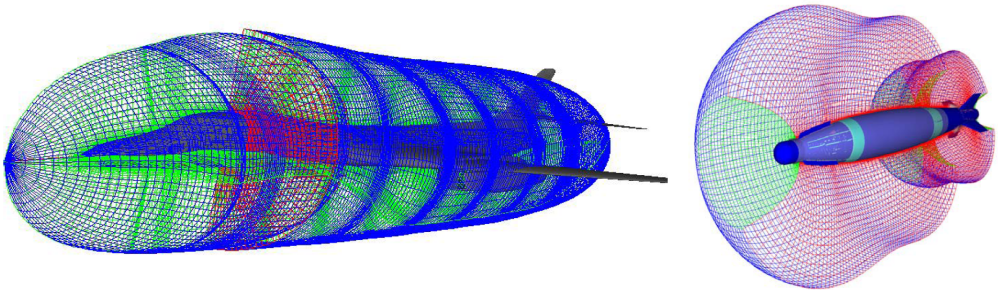

(a) Aircraft grid system (b) Store grid system

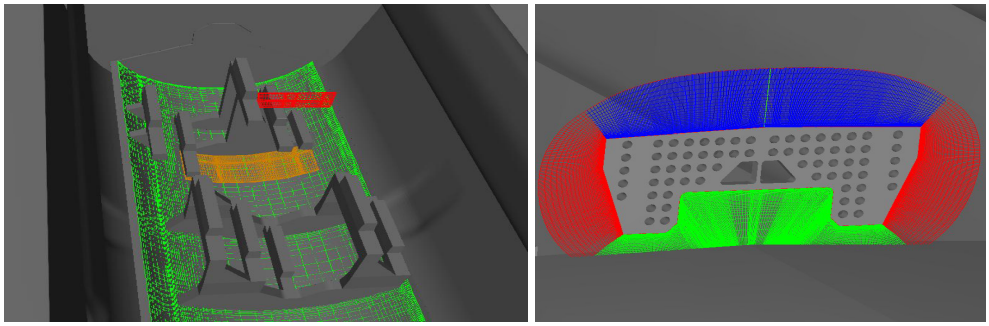

(c) Suspension equipment inside the cavity (d) Porous spoiler grid

Figure 1.8: Overset grid system used, for the aircraft (a), store (b), cavity and store suspension equipment (c) and a porous spoiler (d), by Spinetti and Jolly[9].

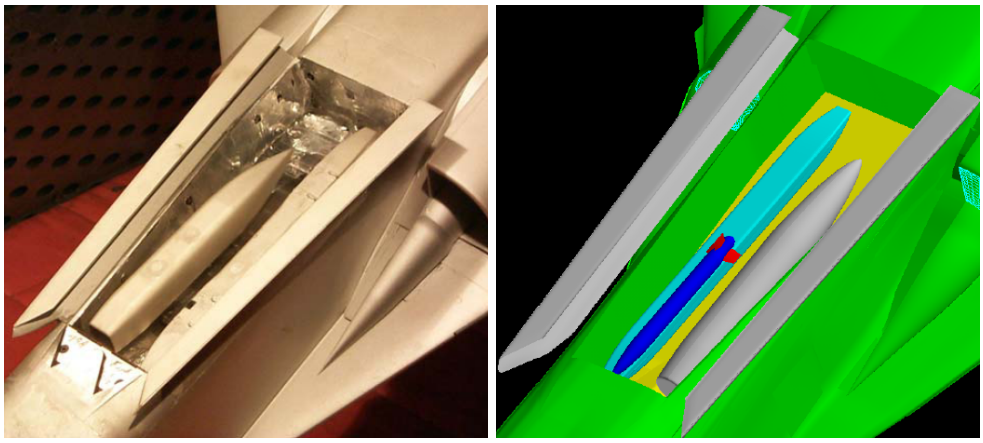

(a) Wind tunnel model (b) CFD model

Figure 1.9: Wind tunnel (a) and CFD (b) model of the F-111 weapons bay [10].

WICS data consisted of data for a cavity of L/D=4.5 at Mach numbers of 0.6 and 0.95 and Reynolds numbers of $2 \times 10^6/ft$ and $3 \times 10^6/ft$, respectively and Sandia TWT data featured a L/D=5 cavity at Mach numbers of 0.8 and 1.5. The Salinas CSD solver developed at Sandia National Laboratories was used for finite element analysis of the store structure. A one-way or loosely coupled method requires pressures obtained from the CFD code to compute deflections in the CSD code which are not transferred back to the CFD code.

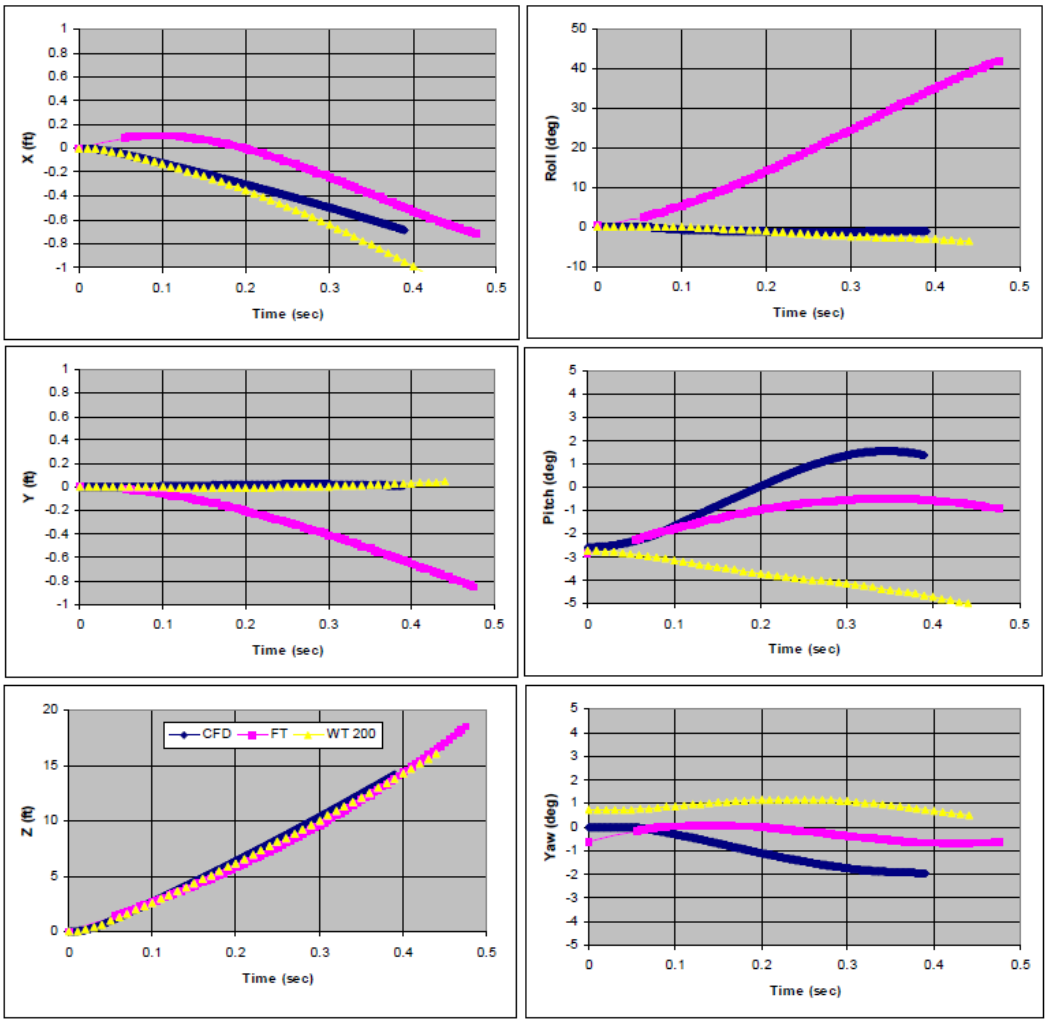

Figure 1.10: Trajectory comparison for the release of an SSB at Mach 0.8 from the bay of an F-111[10]. WT: Wind Tunnel, FT: Flight Test.

This method was applied to a generic finned store in a rectangular cavity held at two fixed nodes on the store using a CFD time step of $\times 10^{-6} s$. Maximum surface displacements of $1.016 \times 10^{-4} m$ were seen that were less than the thickness of the first CFD cell off the wetted surface.

1.2.2 Outcomes

The literature survey summarised the work carried out for stores in cavities and recent methods used to simulate the release of a store from a cavity. What is apparent is the shortage of experimental and numerical data for the release of a store from a cavity as well as the elastic effects of a store and its control surfaces in the presence of the unsteady cavity flow-field.

Table 1.1: Summary of experimental and numerical studies. Part 1.

Study	Store Carriage	Store Release from Cavity	Aeroelastics of a Store in Cavity
Experimental			
Stallings[29] (1983)	Wing controlled store, L/D=11.36 and L/D=4.44, M:2.36, R:$6.6 \times 10^6/m$, EV: $6.1m/s$	Two-degrees-of-freedom method	-
Ross and Odedra[3] (1998)	One-tenth scale AMRAAM, L/D=10 and L/D=5, M:0.6-1.35	Two-degrees-of-freedom method	-
Murray *et al.* [4] (2008)	One-fifteenth scale GBU-38, L/D=6, M:1.5	PIV, CCD	-
Numerical			
Shalaev *et al.* [30] (2002)	-	CAN, Two-degrees-of-freedom analysis	-
Johnson *et al.* [34] (2004)	-	SSB, MDCFD, M:0.9-1.3, decoupled six-degrees-of-freedom method	-
Johnson and Cary[10] (2004)	-	SSB, M:0.8, 0.95, BEGGAR[36] coupled six-degrees-of-freedom method	-
Smith and Schwimley[6] (2006)	-	SSB, grid based method and six-degrees-of-freedom method	-

M: Mach Number • R: Reynolds Number • EV: Ejection Velocity • PIV: Particle Image Velocimetry • CCD: Charge-Coupled-Device CAN: Combined Asymptotic Numerical Method • SSB: Small Smart Bombs • MDCFD: Minimum Domain CFD

Table 1.2: Summary of experimental and numerical studies. Part 2.

Study	Store Carriage	Store Release from Cavity	Aeroelastics of a Store in Cavity
Numerical			
Sahoo *et al.* [31] (2007)	-	Low-order model, slender body aerodynamics, Two-degree of freedom method	-
Spinetti and Jolly[9] (2007)	-	GBU-38, L/D=1.875, M:0.88, BEGGAR[36] coupled six-degrees-of-freedom method	-
Berglind *et al.* [37] (2009)	-	Wing controlled store, M:0.9, R:$16 \times 10^6/ft$, RANS-LES S-A	-
Lee *et al.* [35] (2010)	-	BEGGAR[36] coupled six-degrees-of-freedom method	-
Finney[8] (2010)	-	One-tenth scale Mk-82, NICS, L/D=4.5, M:0.85, TetrUSS, NAVSEP (decoupled six-degrees-of-freedom method)	-

M: Mach Number • R: Reynolds Number • EV: Ejection Velocity • S-A: Spalart-Allmaras • NICS: Navy Internal Carriage and Separation • TetrUSS: Tetrahedral Unstructured Software System • NAVSEP: Navy Generalized Separation Package

Table 1.3: Summary of experimental and numerical studies. Part 3.

Study	**Store Carriage**	**Store Release from Cavity**	**Aeroelastics of a Store in Cavity**
Numerical			
Khanal *et al.* [5] (2011)	DES, L/D=5.42 and L/D=6.25, M:0.8, FLUENT	-	-
Coley[7] (2011)	-	One-tenth scale Mk-82, WICS, L/D=4.5, M:0.95, R:2.5 $\times 10^6/ft$, OVERFLOW[33]	-
Kraft and Lofthouse[32] (2011)	-	GBU-38, 2D SST-DDES, M:0.95, R:5.2 $\times 10^6$ OVERFLOW[33], coupled six-degrees-of-freedom method	-
Arunajatesan *et al.* [11] (2013)	-	-	Generic store with fins, WICS, L/D=5, M:0.6, R:3 $\times 10^6$, M:0.95, R:3 $\times 10^6$, SIGMA CFD, Salinas CSD, loosely-coupled method

M: Mach Number • R: Reynolds Number • EV: Ejection Velocity • SST: Shear-Stress-Transport
DDES: Delayed Detached Eddy Simulation • S-A: Spalart-Allmaras • WICS: Weapons Internal Carriage Separation Program

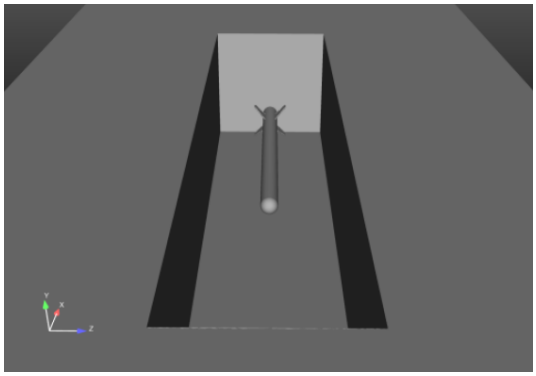

(a) Computational model of a store inside a cavity

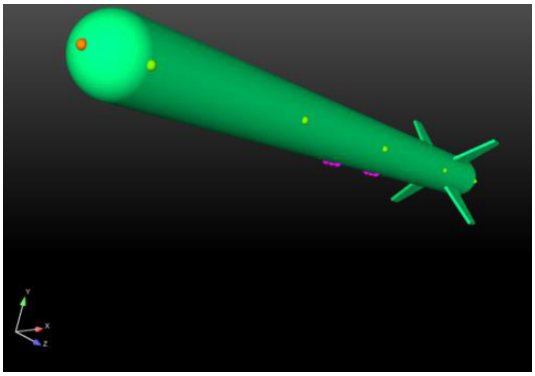

(b) Clamping of the store using two fixed nodes

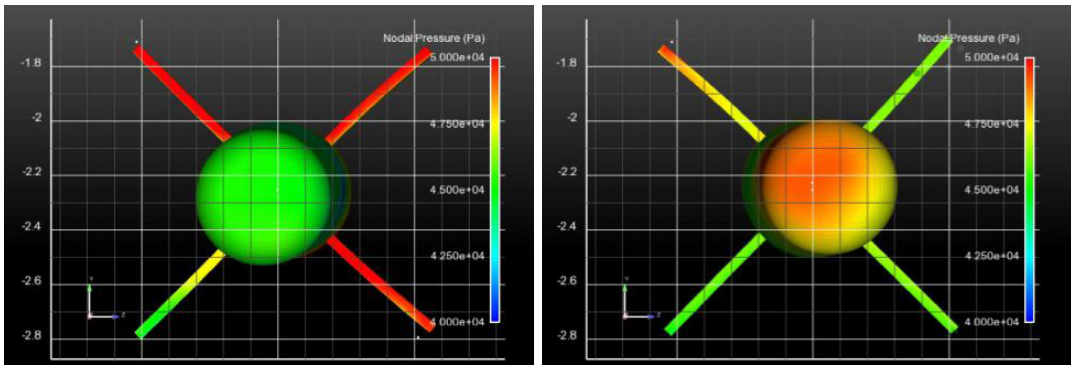

(c) Store displacements

Figure 1.11: Computational model (a,b) used by Arunajatesan *et al.* [11] and store displacements at different time instances in response to the computed flow fields (c).

1.3 Objectives

The main objectives of this research project are as follows:

- Simulation of flow in weapon bays idealised as rectangular cavities using Detached Eddy Simulation.
- Investigation of cavity acoustics and store loads for rigid and aeroelastic fin computations for a store at different positions relative to a cavity using DES.
- Evaluation of Scale Adaptive Simulations for transonic cavity flows.
- Store release simulations from a cavity including a study into the variability of store trajectory due to the cavity flow-field.

1.4 Thesis Outline

The thesis is organised as follows:

Chapter 1 gives the background of and motivation for the current work. A literature survey was conducted that categorised studies into relevant sections based on the content of the reviewed publications. Finally, the outcomes of the literature survey and the objectives of this research project are presented.

Chapter 2 presents descriptions for the governing equations of the flow, the employed turbulence models, the HMB2 CFD solver and other analysis methods developed for the study.

Chapter 3 compares the flow-fields for idealised clean cavity computations, for the M219 cavity and the cavity with L/D=7, where results for both doors-off and doors-on are presented.

Chapter 4 compares DES results for a clean cavity and a cavity with a store positioned at carriage, at the shear layer and outside.

Chapter 5 presents the aeroelastic analysis of store fins. Store and fin loads are presented and comparisons are made against rigid and elastic fins for two fin root configurations.

Chapter 6 validates numerical results obtained from SAS for the M219 cavity along with comparisons with DES.

Chapter 7 presents the validation of the six-degree-of-freedom method in HMB2 against experimental data for a generic store released from a wing.

Chapter 8 presents store release computations from a cavity using SAS, together with an investigation into the variability of the store trajectory.

The final chapter (Chapter 9) summarises the results of the study and draws conclusions from the work carried out in this project. Directions for future work are also given.

Appendix A discusses the effects of signal length and methods to post-process unsteady pressure data for cavity flows. Suggestions are made for minimum CFD signal length required for processing and a method for spectral analysis.

Appendix B presents the use of POD to enable reconstructions of velocity variables, implemented in MATLAB. An example test case for a clean cavity is provided.

Chapter 2

Mathematical Models and CFD Methods

This chapter presents the employed simulation tools is split into several sections. First, the Helicopter Multi-Block (HMB2) flow solver developed at University of Liverpool, is presented including the governing equations and descriptions of turbulence models. Next, the Proper Orthogonal Decomposition (POD) and method of snapshots for data reduction is discussed, followed by methods of data analysis and post-processing methods. The six-degree-of-freedom method and the chimera method for overset grids is then discussed and finally, the aeroelastic method for the deformation of store fins is presented.

2.1 Governing Equations

The Navier-Stokes equations consist of Partial Differential Equations (PDEs) describing the laws for the conservation of mass (continuity equation), momentum (Newton's 2^{nd} law) and energy (1^{st} law of thermodynamics). The continuity equation states that the mass must be conserved. In Cartesian coordinates, x_i, this is written as

$$\frac{\partial \rho}{\partial t} + \frac{\partial (\rho u_i)}{\partial x_i} = 0, \tag{2.1}$$

where ρ is the density of the fluid, t is the time and u_i is the velocity vector.

The second conservation principle states that momentum must be conserved. It is written in Cartesian coordinates as

$$\frac{\partial(\rho u_i)}{\partial t} + \frac{\partial(\rho u_i u_j)}{\partial x_j} = \rho f_i - \frac{\partial p}{\partial x_i} + \frac{\partial \tau_{ij}}{\partial x_j} \tag{2.2}$$

where f_i represents the body forces, p the pressure and τ_{ij} the viscous stress tensor, which is defined as

$$\tau_{ij} = \mu\left[\left(\frac{\partial u_i}{\partial x_j} + \frac{\partial u_j}{\partial x_i}\right) - \frac{2}{3}\delta_{ij}\frac{\partial u_k}{\partial x_k}\right] \tag{2.3}$$

μ is the molecular viscosity and δ_{ij} represents the Kronecker delta, which is defined as

$$\delta_{ij} = \begin{cases} 1 & \text{if} \quad \text{i=j} \\ 0 & \text{otherwise} \end{cases} \tag{2.4}$$

For the viscosity, Sutherland's law [43] is employed,

$$\mu = \mu_{ref}\left(\frac{T}{T_{ref}}\right)^{3/2}\frac{T_{ref}+T_S}{T+T_S}, \tag{2.5}$$

where T is the temperature of the fluid, T_{ref} is a reference temperature ($T_{ref} = 273.15K$), μ_{ref} is the viscosity at that reference temperature ($\mu_{ref} = 1.716\cdot 10^{-5} kg/ms$) and T_S is the Sutherland temperature ($T_S = 110.4K$).

The third principle of Energy conservation can be written in Cartesian coordinates as:

$$\frac{\partial \rho E}{\partial t} + \frac{\partial}{\partial x_j}\left[u_i(\rho E + p)\right] - \frac{\partial}{\partial x_j}\left(u_i\tau_{ij} - q_j\right) = 0. \tag{2.6}$$

where E is the total energy of the fluid, defined as:

$$E = \left[e + \frac{1}{2}u_i u_i\right] \tag{2.7}$$

and e is the specific internal energy with $u_i u_i$ representing the kinetic energy. The heat flux vector, q_i, is calculated using Fourier's Law:

$$q_i = -k\frac{\partial T}{\partial x_i} \tag{2.8}$$

where k is the thermal conductivity. An ideal gas approximation is used, with the adiabatic index set to $\gamma = 1.4$, and the pressure is related to density as:

$$p = \rho R T. \tag{2.9}$$

where R is the specific gas constant, $R = c_p - c_v = 287.058 Jkg^{-1}K^{-1}$.

2.1.1 Conservation Laws in Vector Form

These three laws of conservation can be combined and written in the equation shown below, which is referred to as the Navier-Stokes equation of viscous flow. For brevity, vector notation is used:

$$\frac{\partial \mathbf{W}}{\partial t} + \frac{\partial \left(\mathbf{F}^i + \mathbf{F}^v\right)}{\partial x} + \frac{\partial \left(\mathbf{G}^i + \mathbf{G}^v\right)}{\partial y} + \frac{\partial \left(\mathbf{H}^i + \mathbf{H}^v\right)}{\partial z} = \mathbf{S} \tag{2.10}$$

where $\mathbf{W}$ is the vector of conserved variables and is defined by

$$\mathbf{W} = (\rho, \rho u, \rho v, \rho w, \rho E)^T \tag{2.11}$$

with the variables ρ, u, v, w, p and E having their usual meaning of density, the three components of velocity, pressure and total energy, respectively. The superscripts i and v in Equation 2.10 denote the inviscid and viscid components of the flux vectors $\mathbf{F}$ (in the x-direction), $\mathbf{G}$ (in the y-direction) and $\mathbf{H}$ (in the z-direction). The inviscid flux vectors, $\mathbf{F}^i$, $\mathbf{G}^i$ and $\mathbf{H}^i$, are given by

$$\begin{aligned}
\mathbf{F}^i &= \left(\rho u, \rho u^2 + p, \rho uv, \rho uw, u(\rho E + p)\right)^T, \\
\mathbf{G}^i &= \left(\rho v, \rho uv, \rho v^2 + p, \rho vw, v(\rho E + p)\right)^T, \\
\mathbf{H}^i &= \left(\rho w, \rho uw, \rho vw, \rho w^2 + p, w(\rho E + p)\right)^T.
\end{aligned} \tag{2.12}$$

while the viscous flux vectors, $\mathbf{F}^v$, $\mathbf{G}^v$ and $\mathbf{H}^v$, contain terms for the heat flux and viscous forces exerted on the body and can be represented by

$$\begin{aligned}
\mathbf{F}^v &= \frac{1}{\mathrm{Re}} \left(0, \tau_{xx}, \tau_{xy}, \tau_{xz}, u\tau_{xx} + v\tau_{xy} + w\tau_{xz} + q_x\right)^T, \\
\mathbf{G}^v &= \frac{1}{\mathrm{Re}} \left(0, \tau_{xy}, \tau_{yy}, \tau_{yz}, u\tau_{xy} + v\tau_{yy} + w\tau_{yz} + q_y\right)^T, \\
\mathbf{H}^v &= \frac{1}{\mathrm{Re}} \left(0, \tau_{xz}, \tau_{yz}, \tau_{zz}, u\tau_{xz} + v\tau_{yz} + w\tau_{zz} + q_z\right)^T.
\end{aligned} \tag{2.13}$$

where the term τ_{ij} represents the viscous stress tensor and q_i the heat flux vector and S is the source term.

Although the Navier-Stokes equations completely describe turbulent flows, the large number of temporal and spatial turbulent scales associated with high Reynolds numbers make it difficult to resolve all the turbulent scales computationally. In such circumstances, the number of turbulent scales are reduced by time averaging the Navier-Stokes equations to give the RANS equations. This results in additional unknowns (called Reynolds stresses) which must be modelled. The viscous stress tensor mentioned in Equation 2.13 is then approximated using Boussinesq's hypothesis [44].

2.2 Turbulence Modelling

Work presented in this thesis, used Unsteady Reynolds-Averaged Navier-Stokes (URANS)[13], DES[45] and SAS computational methods. DES computations utilised the S-A turbulence model by Spalart and Allmaras[46] while URANS and SAS computations utilised the $k-\omega$ SST turbulence model, a hybridisation of the $k-\omega$ [47] and $k-\varepsilon$ model, by Menter[48].

2.2.1 Unsteady Reynolds-Averaged Navier-Stokes Simulation

The least expensive method in terms of computational cost is the RANS method. RANS splits the flow variables into a mean flow component with a fluctuating component superimposed on it. However, such an approach means that the mean terms are known but the fluctuating terms are not. Early studies of cavity flows using CFD focused on the use of Unsteady Reynolds-Averaged Navier-Stokes, which uses a time-varying mean component. To account for the effect of the fluctuating part of the flow, a turbulence closure is needed, which models all of the turbulent scales.

URANS models tend to predict well the larger scales associated with the lower frequency discrete acoustic tones but fail to provide the same accuracy in capturing the smaller, higher frequency and more intermittent time scales. The broadband noise is not captured by these models either. The presence of these multiple acoustic tones and of a large number of turbulent scales may mean that achieving a good level of accuracy and consistency with turbulence modelling is difficult for cavity flows. In order to attain reasonable behaviour from URANS, some studies modify the turbulence models or limit the level of eddy viscosity produced by the model. Therefore the shortfalls of URANS computations justify the use of more advanced methods.

2.2.2 Large Eddy Simulation

With Direct Numerical Simulation (DNS) being too expensive and URANS unable to predict the unsteadiness within the cavity correctly, studies using other methods also appeared in literature. The philosophy behind LES is to resolve the larger, energy-containing eddies on the grid, while a sub-grid scale (SGS) model is used to model the smaller, more isotropic scales. Since the smallest eddies are modelled, the grids can be less refined and the time-steps can be larger then those required for DNS.

Despite the potential of LES, there are problems in resolving the near-wall turbulent stresses since the required resources approach those of DNS. As a general rule of thumb, pure LES allows the use of 10 times higher Reynolds numbers than DNS for current computational resources. This means that it is of limited use for complex flows. One solution is to use wall functions at the solid boundaries and therefore very coarse grid spacings can be used. Another solution was to make a hybrid RANS-LES model.

2.2.3 Detached-Eddy Simulation

Even though studies using LES appear in literature, the computer resources required to accurately resolve all the flow features are still high. Therefore, for flows with a large range of turbulent scales (such as wall-bounded flows), proposals for hybrid RANS-LES models were put forward. The hybrid schemes use RANS for simulating near-wall areas and LES for the separated flow regions. The most popular was proposed by Spalart *et al.* [49] and is termed Detached-Eddy Simulation. Spalart argued that when computing solutions of 3D real-life geometries using 'Navier-Stokes and a Turbulence Model' equations (i.e. RANS or URANS), the accuracy of the converged solution can only be as good as that of the turbulence model. When applied to cavities, this new method was found to give good agreement with experimental data and at a reduced cost compared to LES simulations. Its underlying principle involved using RANS for the boundary layers and LES everywhere outside. Therefore the word 'detached' was used to imply that the 'attached' eddies internal to the boundary layer will be modelled and the detached ones resolved.

Spalart *et al.* [49] modified the one equation S-A turbulence model to achieve a DES equivalent. The destruction term for the eddy viscosity is proportional to $(\tilde{\nu}/d)^2$, where d is the distance to the nearest wall. In the Smagorinsky model,[50] the sub-grid scale (SGS) eddy viscosity is scaled with the grid spacing, Δ. Therefore for the DES formulation, the d is replaced by a length proportional to Δ. In practice, the modified distance is expressed as a comparison between the actual distance to the wall and that calculated by $C_{DES}\,\Delta$, where C_{DES} is a constant and Δ computes the size of the maximum cell length:

$$\tilde{d} = \min\left(d, C_{DES}\,\Delta\right) \tag{2.14}$$

$$\Delta = \max\left(\Delta_x, \Delta_y, \Delta_z\right) \qquad \forall \quad \text{cell.} \tag{2.15}$$

When $C_{DES}\ \Delta \ll d$, LES is triggered and the S-A model acts as an SGS model. RANS is activated when the converse occurs. The boundary between LES and RANS is therefore completely dependent on the geometry and on the density of the computational domain. In the CFD flow solver, C_{DES} has the value 0.65. Also note that other metric relations are possible for Δ.

A concern is the 'grey area' in which $C_{DES}\ \Delta$ is on the same order as d. In the separated regions, the detached boundary layer should grow 'free-shear-flow' eddies; however, it is not seeded with eddies from the boundary layer since they are suppressed by the RANS model.

2.2.4 Scale-Adaptive Simulation

While DES is capable of accurately predicting these flows, it still takes a considerable amount of time on a large number of processors. Since its introduction by Menter *et al.* [51–53] in 2003, the SAS approach gained popularity due to its LES-like behaviour in highly separated flow regions and found place in several studies. A detailed explanation of the theory and description of the model was given by Menter and Egorov [54] following which Egorov *et al.* [55] presented the application of the SAS model, implemented in ANSYS-FLUENT and ANSYS-CFX, for a range of complex flows.

The governing equations of the SST-SAS model differ from those of the SST-RANS model[48] by the additional SAS source term, Q_{SAS} in the transport equation for the turbulence eddy frequency, given by:

$$Q_{SAS} = max\left[\rho\zeta_2\kappa S^2\left(\frac{L}{L_{vK}}\right)^2 - C\frac{2\rho k}{\sigma_\Phi}max\left(\frac{1}{\omega}\frac{\partial\omega}{\partial x_j}\frac{\partial\omega}{\partial x_j}, \frac{1}{k}\frac{\partial k}{\partial x_j}\frac{\partial k}{\partial x_j}\right), 0\right] \quad (2.16)$$

where l is the length scale and L_{vK} is the von Karman length scale in classic boundary layer definition,

$$L = \frac{\sqrt{k}}{c_\mu^{1/4}\omega}, \quad L_{vK} = \kappa\frac{U'(y)}{U''(y)} \quad (2.17)$$

and the constants ζ_2 = 3.51, σ_Φ= 2/3 and C = 2.

SAS is an improved URANS model that can produce spectral content for unsteady flows by adjusting the turbulence length scale to the local flow inhomogeneities and balancing the contributions of modelled and resolved parts of the turbulent stresses.

For stationary flows, it acts like a RANS model and for flows with transient instabilities like those with large regions of separation, the model reduces its eddy viscosity according to the locally resolved vortex size represented by the von Karman length scale. The SAS model can resolve the turbulent spectrum down to the grid limit and avoids RANS-typical single-mode vortex structures.

2.3 Numerical Method

The Navier-Stokes equations are discretised using a cell-centred finite volume approach. The computational domain is divided into a finite number of non-overlapping control-volumes, and the governing equations are applied in integral-conservation form at each cell. The spatial discretisation of the NS equations leads to a set of ordinary differential equations in time,

$$\frac{d}{dt}(\mathbf{W}_{i,j,k}V_{i,j,k}) = -\mathbf{R}_{i,j,k}(\mathbf{W}) \tag{2.18}$$

where i, j, k represent spatial components. Note that no transformation into a Cartesian domain is done and the governing equations are solved in the i, j, k spatial domain. $\mathbf{W}$ and $\mathbf{R}$ are the vectors of the cell conserved variables and residuals, respectively. Osher's [56] upwind scheme is used to discretise the convective terms and Monotone Upwind Schemes for Scalar Conservation Laws (MUSCL) [57] variable interpolation is used to provide higher order accuracy. The Van Albada limiter [58] is used to prevent the oscillations near large changes of gradients, like shocks.

Using a fully implicit time discretisation and approximating the time derivative by a second order backward difference, Equation 2.18 becomes

$$\mathbf{R}^*_{i,j,k} = \frac{3V^{n+1}_{i,j,k}\mathbf{W}^{n+1}_{i,j,k} - 4V^{n}_{i,j,k}\mathbf{W}^{n}_{i,j,k} + V^{n-1}_{i,j,k}\mathbf{W}^{n-1}_{i,j,k}}{2\Delta t} + \mathbf{R}_{i,j,k}(\mathbf{W}^{n+1}) = 0 \tag{2.19}$$

Equation 2.19 is non-linear in $\mathbf{W}^{n+1}_{i,j,k}$ and cannot be solved analytically. This equation is defined to be the unsteady residual $\mathbf{R}^*_{i,j,k}$. Following the original implicit dual-time approach introduced by Jameson [59], Equation 2.19 is solved by iteration in pseudo-time t^*. This permits the acceleration techniques of steady state flow solvers to be used to obtain the updated solution and allows the real time step to be chosen based on accuracy requirements and without stability restrictions. Using an implicit time discretisation on the pseudo-time t^*,

$$\frac{\mathbf{W}^{m+1}_{i,j,k} - \mathbf{W}^{m}_{i,j,k}}{\Delta t^*} = -\frac{1}{V_{i,j,k}}\mathbf{R}^*_{i,j,k}(\mathbf{W}^{m+1}_{i,j,k}), \tag{2.20}$$

where the superscript $m+1$ denotes the time level $(m+1)\Delta t^*$ in pseudo-time. In Equation 2.20 the flux residual on the right hand side is evaluated at the new time level $m+1$ and is therefore expressed in terms of the unknown solution at this new time level.

The unsteady flux residual $\mathbf{R}_{i,j,k}(\mathbf{W}_{i,j,k}^{m+1})$ is linearised in the pseudo-time variable t^* as follows,

$$\begin{aligned}
\mathbf{R}^*{}_{i,j,k}\left(\mathbf{W}^{m+1}\right) &= \mathbf{R}^*{}_{i,j,k}(\mathbf{W}^m) + \frac{\partial \mathbf{R}^*{}_{i,j,k}}{\partial t^*}\Delta t^* + O(\Delta t^{*2}) \\
&\approx \mathbf{R}^*{}_{i,j,k}(\mathbf{W}^m) + \frac{\partial \mathbf{R}^*{}_{i,j,k}}{\partial \mathbf{W}_{i,j,k}}\frac{\partial \mathbf{W}_{i,j,k}}{\partial t^*}\Delta t^* \\
&\approx \mathbf{R}^*{}_{i,j,k}(\mathbf{W}^m) + \frac{\partial \mathbf{R}^*{}_{i,j,k}}{\partial \mathbf{W}_{i,j,k}}\Delta \mathbf{W}_{i,j,k}, \qquad (2.21)
\end{aligned}$$

where $\Delta \mathbf{W}_{i,j,k} = \mathbf{W}_{i,j,k}^{m+1} - \mathbf{W}_{i,j,k}^{m}$. Using the definition of the unsteady residual,

$$\frac{\partial \mathbf{R}^*{}_{i,j,k}}{\partial \mathbf{W}_{i,j,k}} = \frac{\partial \mathbf{R}_{i,j,k}}{\partial \mathbf{W}_{i,j,k}} + \frac{3V_{i,j,k}}{2\Delta t}\mathbf{I}, \qquad (2.22)$$

where $\mathbf{I}$ is the identity matrix. Substituting Equations 2.21 and 2.22 into 2.20, and rewriting it in terms of the primitive variables $\mathbf{P}$, the fully implicit system to be solved is as follows,

$$\left[\left(\frac{V_{i,j,k}}{\Delta t^*} + \frac{3V_{i,j,k}}{2\Delta t}\right)\frac{\partial \mathbf{W}_{i,j,k}}{\partial \mathbf{P}_{i,j,k}} + \frac{\partial \mathbf{R}_{i,j,k}}{\partial \mathbf{P}_{i,j,k}}\right]\Delta \mathbf{P}_{i,j,k} = -\mathbf{R}^*{}_{i,j,k}(\mathbf{W}^m). \qquad (2.23)$$

Note that the system is solved in the primitive variables formulation for simplicity and stability reasons.

Implicit schemes require careful treatment during the early stages of the solution. The conventional approach is to use a low initial value for the Courant-Friedrich-Levi condition (CFL) number and then increase it as the solution progresses. However, it was found that performing a number of explicit iterations to smooth out the initial flow before switching to the implicit algorithm was equally efficient. For unsteady simulations, the solution was progressed to a quasi-steady state before starting the unsteady steps, after which a specified number of unsteady steps were discarded before data were recorded.

Some of the computations for the cavity flow analysis were performed on the Beowulf 1200-processor cluster of the CFD Laboratory at the University of Liverpool.

However, most were conducted on High Performance Computing clusters in the UK such as Polaris of the N8 research partnership and the Chadwick cluster at the University of Liverpool. Polaris, located at Leeds University, consists of 5320 cores where each CPU is composed of 8 cores of the Intel@ Xenon E5-2670. Chadwick has a similar configuration to Polaris, but with a third of the number of cores.

2.4 Methods of Data Analysis

The solver produces flow-field output files, which are written at discrete time instances as specified by the user before starting the computation. It also produces specific 'probes' placed in the flow. The locations of the probes are defined at the beginning of the computation and are then written at every time step performed. For the cavity flow computations, these probes are usually defined in the same locations as the Kulite™ pressure transducers in experiments.

2.4.1 Rossiter's Semi-Empirical Formula

One of the first experimentalists to perform extensive tests on cavities was J.E. Rossiter[60–65]. Rossiter postulated that the frequencies at which periodic pressure fluctuations occurred were approximately proportional to the free-stream velocity and inversely proportional to the length of the cavity and so suggested that the Strouhal number (n), which is defined as:

$$n = \frac{fL}{U_\infty} \tag{2.24}$$

would be a significant parameter, where f is the frequency and U_∞ if the free-stream velocity. It was found that the results follow:

$$\frac{1}{n} = \frac{1}{m-\alpha}\left[\frac{1}{\kappa_v} + M_\infty\right] \tag{2.25}$$

where m is the mode number, is a constant representing a phase shift, κ_v is a constant dependent on the cavity geometry and test conditions and M_∞ is the free-stream Mach number. These constants were determined to be 0.25 and 0.57 respectively. Substituting the definition for the Strouhal number, this can be rearranged in terms of the periodic time of the pressure fluctuations:

$$T = \frac{1}{m-\alpha}\left[\frac{L}{\kappa_v U_\infty} + \frac{L}{a_\infty}\right] \tag{2.26}$$

where a_∞ is the speed of sound. Equation 2.26 shows that the period of the fluctuations is the same as the time it takes for a disturbance to travel the length of the cavity at roughly half of the free-stream velocity and then to traverse back up the cavity at sonic speed.

Rossiter also looked at the amplitude spectra of the pressure fluctuations at the rear of the cavities for varying L/D ratios. It was determined that as the L/D ratio of the cavity increased, the pressure fluctuations inside the cavity became more random and so the tones were replaced with a wider range of frequencies. In 1962, Rossiter modified Equation 2.25 to account for the frequencies of the narrow-band, high amplitude tones [62], where the frequency of the m^{th} mode was given by:

$$f_m = \frac{U_\infty}{L}\left[\frac{m-\alpha}{M_\infty + 1/\kappa_v}\right] \tag{2.27}$$

Rossiter based the formula on experimental results over a range of Mach numbers from 0.4 to 1.4 and on various cavity aspect ratios. However outside this range the accuracy of the predictions decreases and so Heller[66] modified the original et al.formula to compensate. The modified version is as follows:

$$f_m = \frac{U_\infty}{L}\left[\frac{m-\alpha}{M_\infty\left(1+\left[(\gamma-1)/2\right]M_\infty^2\right)^{-1/2}+1/\kappa_v}\right] \tag{2.28}$$

where f is the frequency, U_∞ is the free-stream velocity, m is the mode number, α is a constant representing a phase shift (0.25), κ_v is a constant dependent on the cavity geometry (0.57), M_∞ is the free-stream Mach number and γ is the ratio of specific heats. This version of Rossiter's formula is still used to predict the frequencies of acoustic tones in cavity flow.

2.4.2 Post-Processing Unsteady Pressure Data

The Power Spectral Density (PSD), Overall Sound-Pressure Level (OASPL) and Band-Integrated Sound-Pressure Level (BISPL) provide a means of comparing the numerical results to the experimental unsteady pressure data along the cavity floor. The PSD is used to study the frequency content of a signal at a given location and is based upon the unsteady pressure p', where $p' = p - \overline{p}$. The PSD was calculated using Burg's Estimator[67] (also known as Maximum Entropy Method or MEM) as it produces better resolved peaks for short signals than traditional Fast Fourier Transforms (FFT)[68].

For a description of the PSD in terms of decibels (dB), the natural definition is that of the Sound-Pressure spectrum Level[69] (SPL):

$$SPL(f) = 10\,\mathrm{LOG}_{10}\left[\frac{PSD(f)\,\Delta f_{ref}}{p_{ref}^2}\right] \tag{2.29}$$

where Δf_{ref} is a reference frequency, usually set to 1 Hz and p_{ref} is the international standard for the minimum audible sound, which has the value of 2×10^{-5} Pa[69].

The variation in pressure levels along the cavity floor was studied using the Root-Mean-Square (RMS) of the unsteady pressure, p'_{rms}, and can be obtained from the measurements using the following equation:

$$p'_{rms} = \sqrt{\frac{1}{N}\sum (p')^2} \tag{2.30}$$

Although p'_{rms} is measured in Pascals (or any other unit of pressure), it is customary in cavity flow studies to report it as the OASPL[69]:

$$OASPL = 20\,\mathrm{LOG}_{10}\left[\frac{p'_{rms}}{p_{ref}}\right] \tag{2.31}$$

which has the units of decibels.

BISPL plots show the energy content within a particular frequency range and is calculated using the following equation:

$$BISPL = 20\,\mathrm{LOG}_{10}\left[\left(\int_{f_1}^{f_2} PSD(f)\right)^{1/2} \cdot \frac{1}{p_{ref}}\right] \tag{2.32}$$

where f_1 and f_2 are the lower and upper limits of the desired frequency range. Although the magnitude of the BISPL aids in identifying which frequencies are significant, the shape of each banded mode is also important as it represents how each frequency band varies along the cavity length. For cavity flow studies, the BISPL plots are usually centred around the first four Rossiter Modes calculated using Rossiter's equation[64].

While it is common to visualise a signal in the time domain and the frequency domain, the representations do not show the evolution of frequency over time. Joint TimeFrequency Analysis (JTFA)[70] is used to identify the frequency content of a signal as well as show its evolution over time. JTFA consists of a set of transforms that maps a time domain signal into a two-dimensional representation of frequency versus time and space.

The Short Time Fourier Transform (STFT)[70] is the simplest JTFA transform that applies an FFT to short segments of a signal having a 90% overlap. A space-time map of the dominant modes is then used to show the change in frequency for a given dimension in space over the time signal.

Kegerise *et al.* [71] used JTFA to reveal the 'mode switching' phenomenon in open type cavity flow showing that energy was exchanged between the Rossiter modes so that the dominant Rossiter mode shifted in time. Examples of JTFA time-space maps that show mode-switching can be found in Chapters 3 and 6.

2.4.3 Flow-Field Analysis

Turbulent structures are inherently three-dimensional and so to better identify them within the flow, the Q-Criterion is used. Hunt *et al.* [72] proposed the Q-Criterion to identify vortex cores and reflects the amount of strain and vortical motions in a vector field. Let ∇u denote the gradient of the velocity field. The Q-Criterion is then defined as the positive second invariant of the velocity gradient tensor:

$$Q \equiv \frac{1}{2}\left(u_{i,i}^2 - u_{i,j}u_{j,i}\right) = -\frac{1}{2}\left(u_{i,j}u_{j,i}\right) = \frac{1}{2}\left(\| \Omega \|^2 - \| \mathbf{S} \|^2\right) \tag{2.33}$$

where $\mathbf{S}$ and Ω are the symmetric and anti-symmetric components of ∇u. The strain tensor is defined as the symmetric part and the antisymmetric part is closely related to the vorticity. Thus, the Q-Criterion represents the local balance between shear strain rate and vorticity magnitude [73] where $Q > 0$, vorticity dominates strain and so identifies a vortex region.

In order to visualise the unsteadiness in the flow-field, instantaneous numerical schlieren[74] is calculated and is defined as:

$$NS = c_1 \exp\left[\frac{-c_2(|\nabla\rho| - |\nabla\rho|_{min})}{(|\nabla\rho|_{max} - |\nabla\rho|_{min})}\right] \tag{2.34}$$

where c_1 and c_2 are constants with values of 0.8 and 10.0 respectively.

Imaging of vector fields was carried out through the use of Line Integral Convolution (LIC). LIC is an image processing technique first introduced by Cabral and Leedom [75] in 1993 and has been used by Khanal *et al.* [5,76,77] to study the flow behaviour in cavities with passive flow control devices and a cavity with a store. Some commonly used vortex visualisation techniques include velocity vectors, vorticity and streamlines. While each of these methods are well understood, they each have their own limitations. LIC is capable of providing the user with a high density streamline plot that illustrates all the in-plane features of the input vector field[76].

The algorithm applies a filter, based on an input vector field, to a noise texture to produce an output image with the apparent motion in the direction of the vector field as shown in Figure 2.1.

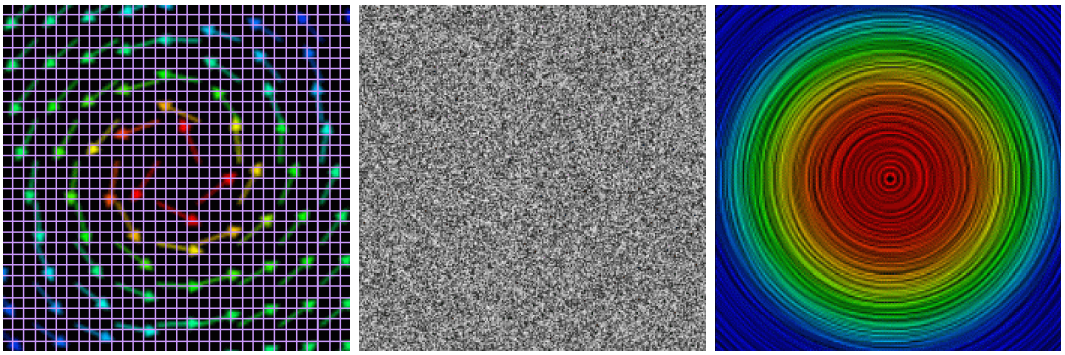

(a) Vector flow-field (b) White noise field (c) LIC image

Figure 2.1: Convolution of an input vector field (a) with a noise field (b) to produce an LIC image (c) [12].

2.4.4 The Proper Orthogonal Decomposition

The Proper Orthogonal Decomposition is a mathematical technique used in many applications, including image processing, signal analysis and data compression [78]. It aims to eliminate information which has little impact on the overall process. It was first introduced in the context of fluid mechanics and turbulence by Lumley [79] to decompose the flow into modes. These modes identify the large coherent structures which contribute to the flow. Many applications of POD use the 'method of snapshots', which was introduced by Sirovich [80] for high spatially resolved data. The 'snapshots' are taken at instances in time so that various states of the flow field are represented. The POD modes Φ can then be expressed in terms of a linear combination of the snapshots u^k:

$$\Phi = \sum_{k=1}^{N} c_k u^k \tag{2.35}$$

where c_k are scalar coefficients. The problem then involves finding the eigenvalues and eigenvectors of [81]:

$$Uc = \lambda c \tag{2.36}$$

where U is a symmetric $N \times N$ matrix and is defined as:

$$U_{ij} = \frac{1}{N} \left\langle u^j, u^i \right\rangle \tag{2.37}$$

where $\langle .,. \rangle$ is the inner product. The matrix c containing the eigenvectors are the temporal modes $a(t)$. The POD modes Φ can then be found using Equation 2.35. The eigenvalues from the decomposition (λ) are representative of the amount of energy stored in each mode of the flow. A nominal criterion, given by Sirovich [80], is that the number of modes retained (n) should be equivalent to 99% of the energy:

$$\sum_{i=1}^{n} \lambda_i \; / \sum_{i=1}^{N} \lambda_i > 0.99 \tag{2.38}$$

The original flow solution $u(x,t)$ can then be reconstructed in terms of the first n POD modes:

$$u(x,t) = \sum_{i=1}^{n} a_i(t)\Phi_i(x) \tag{2.39}$$

Applications of this method to cavity flow problems have shown that far fewer modes were needed in order to reconstruct the flow–field, with the resultant energy captured closer to 70% [82–84]. The snapshots are usually taken at key states of the flow. However, the flow over a cavity is extremely complex and contains frequencies over a broad range and so snapshots were taken at regular intervals in the flow over a time period equal to 10 periods of the lowest Rossiter mode ($T_{Rossiter1}$). The estimated value of $T_{Rossiter1}$ was provided by Equation 2.28 as previously discussed.

The scalar POD method is used [81] and so each flow variable has its own set of eigenvalues, spatial and temporal modes. Also, the POD is applied to the snapshots with the mean included. Although some applications remove the mean flow–field before performing the POD, a study by Gloerfelt [85] showed that better data compression can be achieved if the mean is retained as it enables a time variance in the mean flow–field. In this case, the first mode represents the mean flow–field and so would typically contain a large portion of the energy within the flow.

Three different methods fall under the generalised term of Proper Orthogonal Decomposition: Karhunen-Loeve Decomposition (KLD), Principal Component Analysis (PCA) and Singular Value Decomposition (SVD). However, in the context of turbulence and fluid mechanics, if the acronym POD is used, it generally refers to KLD.

Comparison of SVD and KLD

The energy fractions of the eigenvalues, for an example test case[13, 14] of a 2D flow over a cylinder, are plotted in Figure 2.2. For comparison, the SVD and the energy fractions for the singular values are also shown.

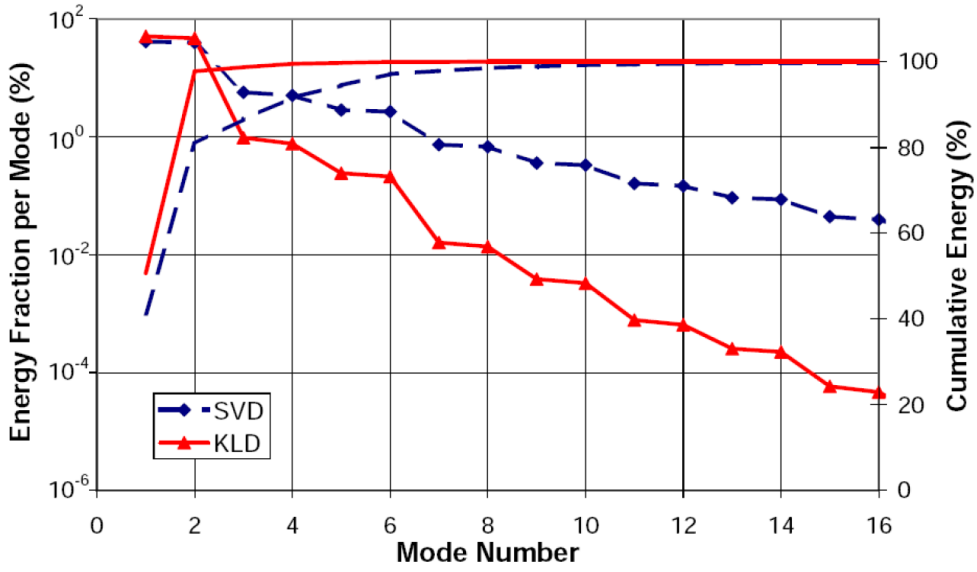

Figure 2.2: The energy fraction for each mode and the cumulative energy for the flow over a cylinder[13, 14]. Data for the SVD is also included in order to illustrate the differences between the methods.

For both methods, the eigenvalues (or singular values) came in pairs suggesting a symmetry in the flow. Also presented in Figure 2.2 is the cumulative energy for increasing numbers of modes, which shows that the lower modes for the KLD contain more energy than for the SVD. This suggests that the KLD is better at identifying coherent structures within the flow and would therefore be more efficient in terms of data compression.

2.4.5 Parallel Code Design

Routines from the ScaLAPACK (Scalable Linear Algebra PACKage) scientific library[86] were utilised to implement the POD method[84] since they are highly optimised. ScaLAPACK routines were used as they are parallel, portable, available within the public domain and are able to perform computations on dense matrices.

The input matrices are required to be distributed in a two-dimensional block-cyclic fashion over the processors. This makes the computations on dense matrices, such as Gaussian elimination, very efficient for distributed memory architectures. Also ScaLAPACK is written in Fortran 77 and so all variables have to be passed by reference when calling any of the routines. When the libraries are linked to a *C* program, passing single variables is a simple process. However, it means that extra care has be be taken when allocating multi-dimensional arrays that all the data are contiguous in memory.

The ScaLAPACK library is written on top of four other libraries: BLAS (Basic Linear Algebra Subprograms), BLACS (Basic Linear Algebra Communication Subprograms), LAPACK (Linear Algebra PACKage) and PBLAS (Parallel BLAS) and so any routines in these four libraries can also be used in conjunction with ScaLAPACK. The dimensions of the process grid are obtained using the Message Passing Interface (MPI) library, but it is then set up using the BLACS library. The call to the BLACS library produces a handle variable for the setup of the grid, which is then passed to any PBLAS or ScaLAPACK routines used in the code. The POD method involves a call to the PBLAS routine PDGEMM (Parallel, Double precision, General Matrix Multiplication) to calculate the input matrix U_{ij}. The driver routine PxSYEV computes the eigenvalues and the eigenvectors of the real symmetric $N \times N$ matrix in single or double precision by calling the recommended sequence of ScaLAPACK routines. The routine requires a distributed input matrix and outputs a distributed matrix containing the eigenvectors. The output array containing the eigenvalues is identical on all processors. An additional input array is needed for workspace.

2.5 Chimera Method

The chimera method [87] is based on composite grids, consisting of independently generated, overlapping non-matching sub-domains. Each of these sub-domains is referred to as a Level and are sorted hierarchically, with higher levels having priority. The exchange of information between sub-domains is achieved through interpolation and by following the level hierarchy.

An example is shown in Figure 2.4 that presents a composite two-level chimera grid for an isolated store in freestream. Level 0 is the background grid consisting of 96 blocks and 2 million cells and Level 1 is the store grid consisting of 304 blocks and 3.7 million cells.

In HMB2 the chimera method is described in Jarkowski *et al.* [87] In order to minimise the number of searches in the interpolation from one level to the other, a localisation procedure is carried out before the computation of the flow field starts. The localisation identifies the cells that require interpolated flow information from the grid they overlap with and provides interpolation weights for them. In order to do this, approximate Minimum Volume Bounding Boxes (MVBBs) are constructed around every solid in each level, based on the moment of area matrix.

An Overset Mesh Search (OMS) is then performed. By means of a range-tree algorithm, the points located inside the MVBB are identified and Exact Arithmetic Library (EAL) is used to guarantee that any point can only be located in one cell of a level it is localised against.

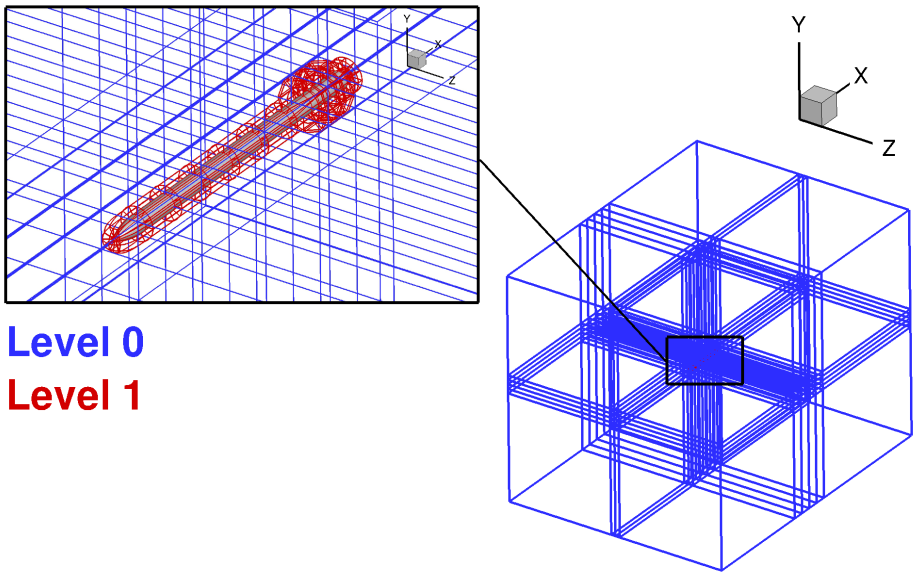

Figure 2.3: Chimera grid of an isolated store in freestream composed of two grids: the background grid, *Level 0* (96 blocks and 2 million cells) and the store grid, *Level 1* (304 blocks and 3.7 million cells).

Once 'localised' the cells are then classified into three groups, an example of which is shown in Figure 2.4 that shows the localisation of cells on the background grid, *Level 0*, and the store grid, *Level 1*. With reference to the localisation of cells on the background grid, *Level 0* (Figure 2.4(a)), the classification of cells are as follows: holes, that do not need interpolation as they overlap either with a hierarchically higher level cell (shown in light blue) or a solid (shown in dark blue), interpolation cells (shown in yellow), that require interpolated flow information from the grid they overlap, normal or computational cells (shown in green), that do not need any special treatment and represent the cells in which the flow is computed and fringe or boundary cells (shown in red), that represent the cells in the boundary of the higher level grid.

The interpolation cells are always flagged based on the viscous MUSCL stencil shape (13-point stencil in 3D), regardless of the CFD model employed (inviscid or viscous), hence, the two layers of interpolation cells. The dark blue cells in Figure 2.4(a) highlight the cells that intersect with the solid store body while the light blue cells represent the holes overlapping with the higher level store grid.

In a similar manner, the localisation was carried out for *Level 1*, see Figure 2.4(b). Here, only two types of cells are seen, fringe cells and computational cells, as this level is the highest level in the composite grid and therefore does not require information from another level.

Three interpolation methods are available in HMB2: zero order method, least squares method and inverse distance method. In the first method, the nearest neighbours are found and are copied to the interpolation cell. The second method uses a quadratic polynomial for the interpolation. The latter considers a cloud of nearest points and assigns larger weights to those closer to the interpolation cell. Further details of the method and its implementation in HMB2 are provided by Jarkowski *et al.* [87].

2.6 Six Degrees of Freedom Motion

In order to simulate store release, a mathematical model was used to describe a store's motion in six rigid-body degrees of freedom (three body position coordinates and three Euler-angle body attitudes). This was coupled with HMB2 to predict the motion during release. The method assumes that store release computations use the chimera method, such that a store has its own grid to which the computed position and orientation are applied at every instance in time.

The store axis system is a right-handed coordinate system, shown in Figure 2.5, where positive X_b coincides with the store's centreline (longitudinal axis), positive Y_b is starboard of the X-axis in the horizontal plane and positive Z_b, perpendicular to the horizontal plane, points down. X_b, Y_b and Z_b axes are respectively the roll, pitch and yaw axis of the store. The aerodynamic and gravitational forces acting on a store are resolved along the store's body axis that is fixed to its centre of gravity (CG). The earth axis system (Figure 2.5) uses the North East Down (NED) system where, X_e is positive in the direction of north, Y_e is positive in the direction of east and perpendicular to X_e axis and Z_e is positive towards the center of Earth (perpendicular to the $X_e - Y_e$ plane).

Force and moment coefficients acting on the store, obtained from HMB2 at every unsteady time step, are applied into the translational and rotational equations of motion[15] of a store in body axes that are summarised as:

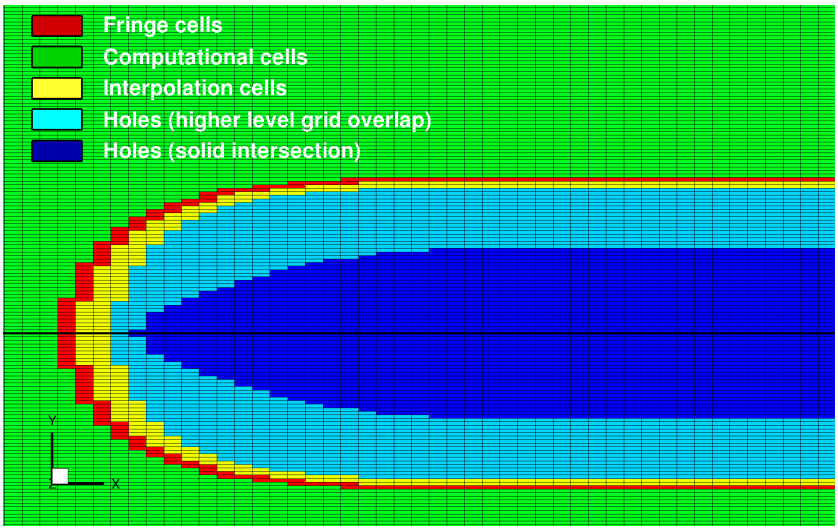

(a) *Level 0*: Background grid (96 blocks and 2 million cells)

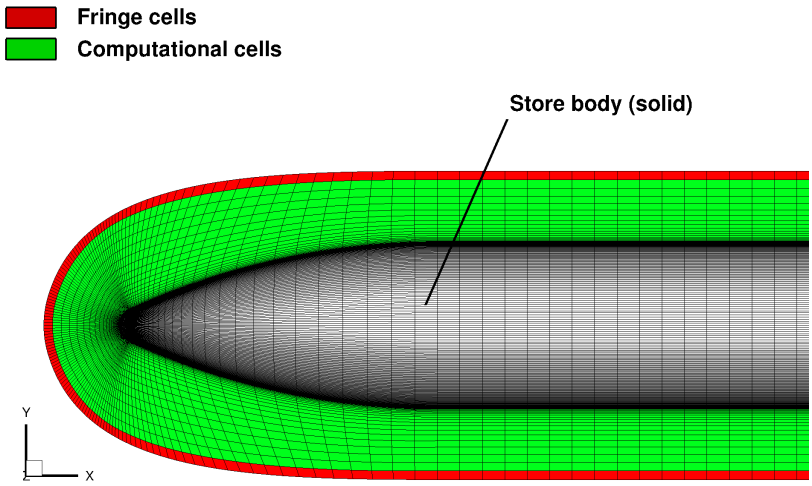

(b) *Level 1*: Store grid (304 blocks and 3.7 million cells)

Figure 2.4: Localisation of cells on the background grid, *Level 0* (a), and the store grid, *Level 1* (b), for the isolated store in freestream. The store grid is shown with the store body and surface mesh. Slices are shown through the centreline of the store.

Longitudinal Acceleration: $$\frac{du}{dt} = Rv - Qw - g\sin\theta(C_X qS)/m \tag{2.40}$$

Lateral Acceleration: $$\frac{dv}{dt} = Pw - Ru + g\cos\theta\sin\phi(C_Y qS)/m \tag{2.41}$$

Vertical Acceleration: $$\frac{dw}{dt} = Qu - Pv + g\cos\theta\cos\phi(C_Z qS)/m \tag{2.42}$$

Roll Acceleration: $$\frac{dP}{dt} = C_L(qSl_{ref}/I_x) + QR[(I_y I_z)/I_x] \tag{2.43}$$

Pitch Acceleration: $$\frac{dQ}{dt} = C_M(qSl_{ref}/I_y) + PR[(I_z I_x)/I_y] \tag{2.44}$$

Yaw Acceleration: $$\frac{dR}{dt} = C_N(qSl_{ref}/I_z) + PQ[(I_x I_y)/I_z] \tag{2.45}$$

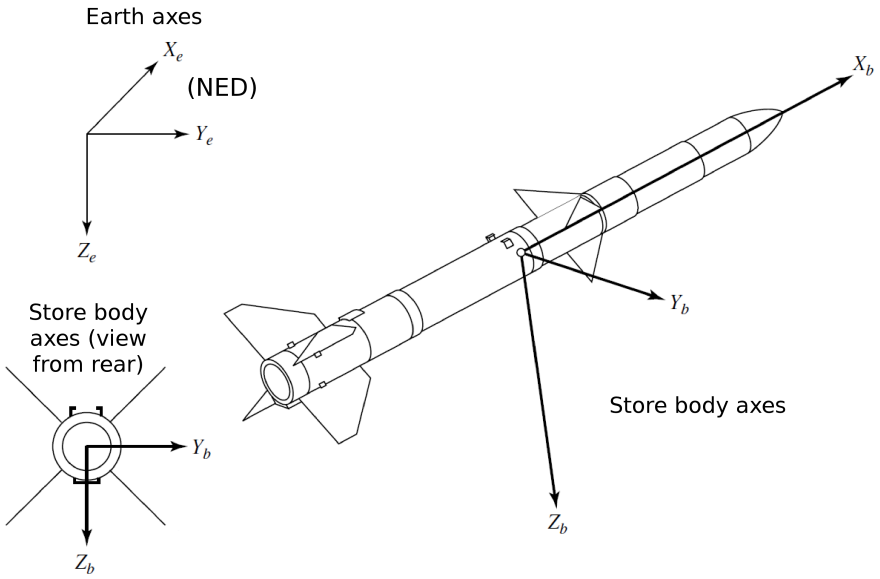

Figure 2.5: Orientation of store axes with respect to earth axes. Reproduced with modifications, originally from Siouris [15].

where, m is the mass of the store and q is the freestream dynamic pressure. u, v and w are the velocity components of the store. P, Q and R are the roll, pitch and yaw rates, respectively, of the store. C_X, C_Y and C_Z are the axial, side and normal force coefficients, respectively, and C_L, C_M and C_N are the rolling, pitching and yawing moment coefficients, respectively, acting on the store. l_{ref} is the diameter and S is the base area of the store. I_x, I_y, I_z are the moment of inertia of the store in the X, Y and Z axis respectively. As the stores used in this project are symmetric about the $X_b - Y_b$ plane, the off-diagonal product of inertia terms, are ignored.

The equations for the angular velocities[15] in terms of the Euler angles are as follows:

$$\frac{d\psi}{dt} = (Q\sin\phi + R\cos\phi)/\cos\theta \tag{2.46}$$

$$\frac{d\theta}{dt} = Q\cos\phi - R\sin\phi \tag{2.47}$$

$$\frac{d\phi}{dt} = P + (\frac{d\psi}{dt})\sin\theta \tag{2.48}$$

The equations of motion of a store are then integrated in time using an Euler method. It must be noted that, while the integrations take place in the earth axis, defined by the NED system, the flow, and hence the loads, computed by HMB2 are in a different axis system. So, once the loads are computed by HMB2, they are converted to the NED system and supplied to the six degrees of freedom method.

The computed position and orientation of a store is converted back to the HMB2 axis system and applied to the store grid which is then moved relative to the other grids in the composite grid. The localisation procedure is carried out and the weights of the cells are recomputed along with wall distances. This process is repeated until the end of the computation. The method was validated using wind tunnel data for the release of a generic store from under a wing [17] and is discussed in Chapter 7.

2.7 Fluid-Structure Interaction

In order to lower the cost of computing the deformation of store fins, a modal approach was chosen where a fin's deformation is expressed as a function of its eigenmodes. A Finite Element Model (FEM) of a fin was supplied through a datapack [88] and was used to obtain the eigenmode shapes and frequencies using Nastran [89] through a nonlinear mode analysis (SOL 106). The mode type and frequencies for the first four modes of a fin are shown in Table 2.1 together with the first four Rossiter modes of a clean cavity with L/D=7. The fin shape, ϕ, described as the sum of the undeformed eigenvector ϕ_0 and the sum of the eigenvectors, ϕ_i, that represent the displacement for each eigenmode multiplied by the corresponding modal amplitude, α_i, is give by:

$$\phi = \phi_0 + \sum_{i=0}^{n_m} \alpha_i \phi_i \tag{2.49}$$

where n_m is the number of eigenmodes. Knowing the eigenvectors, the modal amplitude, α_i, is obtained at every iteration by solving the differential equation:

$$\frac{\partial^2 \alpha_i}{\partial t^2} + 2\zeta_i \omega_i \frac{\partial \alpha_i}{\partial t} + {\omega_i}^2 \alpha_i = f\phi_i \tag{2.50}$$

where $\mathbf{f}$ is the aerodynamic load, ω_i is the eigenpulsation frequency and ζ_i is the damping coefficient.

The flow computation is initiated by keeping the fins rigid and allowing the solution to converge. Once converged, the aeroelastic simulation is initiated by applying the aerodynamic loads calculated from the fluid grid onto the surface of each fin, allowing them to oscillate freely. In order to create a stable transition from a rigid state to an oscillating state, the aeroelastic computation begins with a strong damping coefficient, $\zeta = 0.7$. This dampens the oscillations that arise from the sudden application of forcing introduced into the system.

Table 2.1: Mode type and frequencies for the first four modes of the fin. First four Rossiter modes are also shown for comparison. Rossiter modes are based on a Mach number of 0.85 and cavity length of 3.33m

Mode	Mode Type	Frequency (Hz)	Rossiter Mode (Hz)
1	Bending + Twisting	144.14	25.53
2	Bending	158.05	59.58
3	Twisting	232.02	93.63
4	Bending	923.55	127.68

As the flow continues to develop, the damping coefficient is gradually lowered to 0.3, allowing for larger deformations. At each pseudo-time step of every unsteady time step, the modal amplitudes are computed by solving the discretised Equation 2.50. The CFD grid is then deformed, using the methods described in the following sections, and the flow-field is updated by solving the N-S equations. At the end of each unsteady time step, the fins loads are extracted and reapplied to the system. This process is performed repeatedly until the end of the computation.

The tight coupling between the CFD and CSD domains requires the association of the nodes on the structural model to the nodes in the fluid mesh and vice-versa. The difference in resolution between the structural and fluid domain requires interpolation of the structural solution onto the surface of the fin in the fluid domains. This problem was addressed and documented by Dehaeze and Barakos [90] who amongst others used a hybrid technique for the deformation of the CFD mesh of a rotor blade, according to its structural model, while maintaining the mesh quality. The deformation technique is carried out in three stages through the use of a Constant Volume Tetrahedron (CVT) method, a Spring Analogy Method (SAM) and a Trans-Finite Interpolation (TFI). CVT is first used to interpolate the deformed shape of the fin surface, following which, the the vertices of the blocks are moved by the spring analogy method and finally the entire mesh is regenerated using TFI.

2.7.1 Constant Volume Tetrahedron

CVT is used for the exchange of information between the fluid and structural domains by projecting each fluid point to the nearest triangular structural element such that the fluid point moves linearly with the structural element while conserving the volume bound by the tetrahedron, formed by the coordinates of the triangular structural element and the fluid point.

First, the nearest triangular element, with coordinates (S_1, S_2, S_3) as shown in Figure 2.6, to each fluid point (F) is found. Then, the location of the fluid point can be expressed as follows:

$$c = \alpha a + \beta b + \gamma d \tag{2.51}$$

where $a = \overrightarrow{S_1 S_2}$, $b = \overrightarrow{S_1 S_3}$, $c = \overrightarrow{S_1 F}$ and $d = a \wedge b$. The coefficients α, β and γ can then be expressed as:

$$\alpha = \frac{(a \cdot c)\,\|b\|^2 - (a \cdot b)\,(b \cdot c)}{\|a\|^2 \|b\|^2 - (a \cdot b)^2} \tag{2.52}$$

$$\beta = \frac{(b \cdot c)\,\|a\|^2 - (a \cdot b)\,(a \cdot c)}{\|a\|^2 \|b\|^2 - (a \cdot b)^2} \tag{2.53}$$

$$\gamma = \frac{(c \cdot d)}{\|a\|^2 \|b\|^2 - (a \cdot b)^2}\,. \tag{2.54}$$

The initial position of the fluid point c is transformed into c' and is given by:

$$c' = \alpha a' + \beta b' + \gamma d'\,, \tag{2.55}$$

where a', b', c' and d' are the same vectors after the structural deformation.

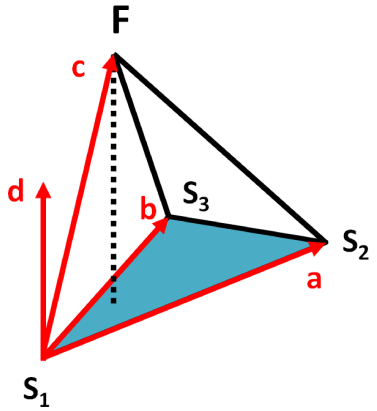

Figure 2.6: Notation for the projection of a point from the fluid grid (F) with a structural element (S_1, S_2, S_3).

2.7.2 Spring Analogy Method

Once the new positions of the fluid points are obtained, SAM is used to update the positions of the block vertices before the mesh is regenerated using TFI. Figure 2.7 shows the springs that are applied on each edge and diagonal of the first two layers of blocks around the fin i.e the first layer of blocks that are in direct contact with the fin and the immediate layer of blocks after. The springs on the edges of the block avoid large compression and expansion of the block faces while the springs on the block diagonals limit the skewness of the cells. Controlling the skewness of the cells is particularly important in areas close to solid surfaces where there is a refinement of cells with an exponential distribution. If the skewness is not controlled in these regions, even moderate deformations can lead to poor mesh quality or folding of cells giving rise to negative volumes in the block. In this way, SAM allows for large deformations while maintaining high mesh quality.

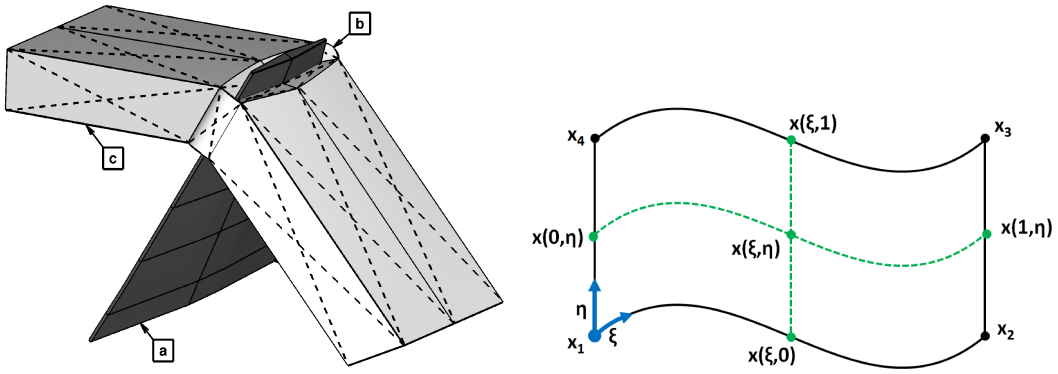

(a) Spring analogy method (b) Notation for the TFI application

Figure 2.7: Representation of the spring analogy method (a) and notation for the TFI application on a block face. Spring analogy method shows, a: solid fin surface, b: first layer of blocks around the fin and c: second layer of blocks around the fin.

2.7.3 Trans-Finite Interpolation

TFI is used, finally, to interpolate the block face deformation from the edge deformations and then the full block deformation from the deformation of the block faces. The mesh deformation uses a weighted approach to interpolate a face/block from the boundary vertices/surfaces respectively. The weight depends on the curvilinear coordinate divided by the length of the curve for which the notation is shown in Figure 2.7(b).

The generation of the mesh on a block face ($\mathbf{x}_1$, $\mathbf{x}_2$, $\mathbf{x}_3$ and $\mathbf{x}_4$) can be expressed as:

$$d\mathbf{x}(\xi,\eta) = \mathbf{f_1}(\xi,\eta) + \phi_1^0(\eta)[d\mathbf{x}_1(\xi) - \mathbf{f_1}(\xi,0)] + \phi_2^0(\eta)[d\mathbf{x}_3(\xi) - \mathbf{f_1}(\xi,1)], \quad (2.56)$$

where $\mathbf{f_1}$ is defined as:

$$\mathbf{f_1}(\xi,\eta) = \psi_1^0(\xi)d\mathbf{x}_4(\eta) + \psi_2^0(\xi)d\mathbf{x}_2(\eta), \quad (2.57)$$

with $d\mathbf{x}_1$, $d\mathbf{x}_2$, $d\mathbf{x}_3$ and $d\mathbf{x}_4$ representing the displacements of the four faces corners and ϕ and ψ representing the blending functions in the η and ξ directions. The blending functions are expressed as a function of the stretching functions s_1, s_2, s_3 and s_4:

$$\psi_1^0(\eta) = 1 - s_1(\xi) \quad (2.58)$$

$$\psi_2^0(\eta) = s_3(\xi) \quad (2.59)$$

$$\phi_1^0(\eta) = 1 - s_4(\eta) \quad (2.60)$$

$$\phi_2^0(\eta) = s_2(\eta). \quad (2.61)$$

The stretching function s_1 is defined by:

$$s_1(\xi) = \frac{\widehat{x_1 x(\xi,0)}}{\widehat{x_1 x_2}}, \quad (2.62)$$

where $\widehat{x_1 x_2}$ is the curvilinear length between $\mathbf{x}_1$ and $\mathbf{x}_2$. s_2, s_3 and s_4 are defined in a similar way for the curves x_2x_3, x_3x_4 and x_4x_1 respectively. The interpolation of the inside of the block from the shape of the block faces follows the same method.

Chapter 3

DES Computations for Clean Cavities

Past work[13,45,91,92] at the University of Liverpool used the M219 cavity of L/D=5, as a basis for cavity flow research, for different configurations, however, the current work uses a cavity of L/D=7. In view of this, results for both doors-off and doors-on computations for the M219 cavity and a cavity with L/D=7, are compared in this chapter. Simulations employed the DES S-A turbulence model[49] and were carried out to verify the common physics between the two cavities, at a Mach number of 0.85 and Re_L of 6.5 million. Averaged and instantaneous flow-fields were analysed. LIC was used to identify flow structures close to the cavity walls. The final sections present the POD modes of both cavities and analyse the reconstructed flow-fields.

3.1 Model Geometry and Computational Details

Previous cavity studies by Lawson[13] investigated the M219 cavity using DES at a freestream Mach number of 0.85 and Re_L of 1 million. The grids used were similar to the current study but the Re_L used for the L/D=7 cavity computations was 6.5 million. The computational model used by Lawson [13] (Figure 3.1(a)) was modified in cavity depth and width such that the resulting cavity had an L/D=7 and W/D=2, while keeping the cavity length at a non-dimensional value of 1. Therefore, in dimensionless form, the depth and width of the cavity were 0.14L and 0.28L respectively. DES data from Lawson [13] and experimental data from Nightingale *et al.* [16], for the M219 cavity, were used for comparisons with the L/D=7 simulations. Experimental data were obtained through 10 Kulite^{TM} pressure transducers (designated K20-K29) on the cavity floor, as shown in Figure 3.2. Computational and grid details are presented in Table 3.1.

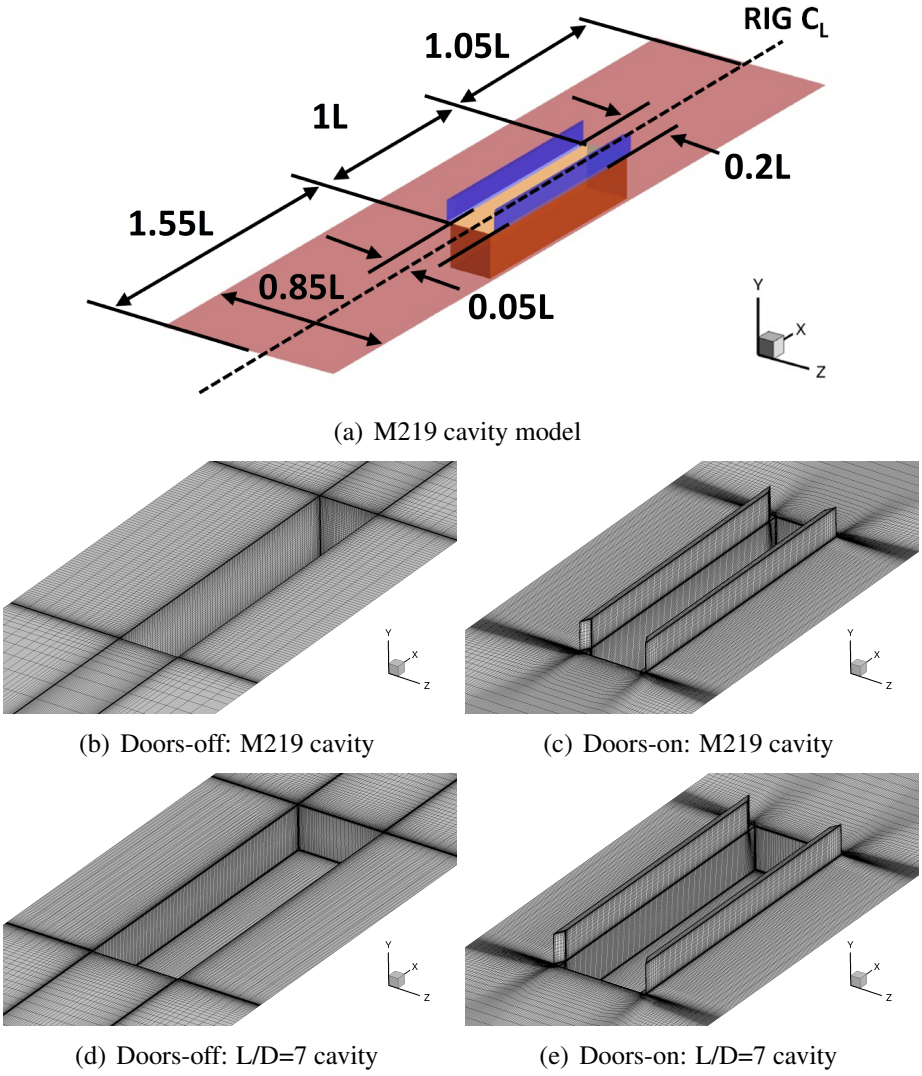

(a) M219 cavity model

(b) Doors-off: M219 cavity

(c) Doors-on: M219 cavity

(d) Doors-off: L/D=7 cavity

(e) Doors-on: L/D=7 cavity

Figure 3.1: Geometry of the computational model for the M219 cavity rig (a). Surface mesh of the M219 cavity with doors-off (b) and doors-on (c) and the L/D=7 cavity with doors-off (d) and doors-on (e).

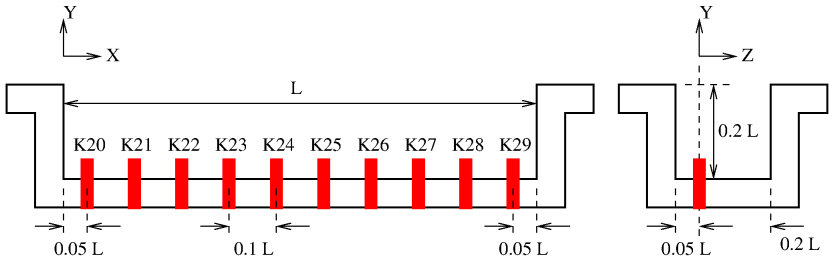

(a) Y-X view

(b) Y-Z view

Figure 3.2: Positions of the Kulite^{TM} pressure transducers used in combination with the M219 cavity[13, 16].

Table 3.1: Details of the computations and the associated grids. DES data for the M219 cavity were taken from Lawson[13].

Computation Details	**M219 Cavity**		**L/D=7 Cavity**	
Configuration	Doors-off	Doors-on	Doors-off	Doors-on
L/D	5	5	7	7
W/D	1	1	2	2
Grid size (10^6 cells)	5.0	5.92	5.0	5.92
Cells in cavity (10^6 cells)	1.02	1.20	1.02	1.20
Number of blocks	800	880	800	880
CFD time-step (10^{-6}s)	1.81	18.14	1.81	18.14
Number of time-steps	100,000	50,000	100,000	70,000
Signal duration (s)	0.18	0.09	0.18	0.12

3.2 Averaged Flow-Field

Time-averaged contours of Mach number for clean cavities with doors-off are shown in Figure 3.3 for the L/D=7 and the M219 cavities. Slices were taken along the rear end ($x/L = 0.85$) and centreline ($z/L = 0.0$). The structure of the mean flow-field was quite similar between the two cavities and showed the flow dip into the cavity just before 20% of the cavity length. Figures 3.3(a) and 3.3(c) show flow spillage over the sides walls of the cavities. Similarly, Figure 3.4 shows the doors-on configuration for both cavities. The presence of the doors channelled the flow and caused a reduction in flow spillage over the sides of the cavity. LIC was used to identify flow structures in the cavity and is shown with streamlines in Figure 3.5 for the time-averaged flow of the L/D=7 cavity with doors-off and doors-on. For the doors-off case, a large vortex (referred to as the primary vortex) existed close to the front wall of the cavity while a smaller vortex (referred to as the secondary vortex) was located at the lower aft corner. The addition of the doors was seen to give rise to a small vortex located at the lower front corner in addition to the primary and secondary vortices.

Time-averaged flow-field slices using LIC, similar to those presented by Khanal *et al.* [5,77], for the L/D=7 cavity with doors-off and doors-on are shown in Figures 3.6 and 3.7 respectively. Slices were extracted close to each wall and show the general flow structure inside the cavity. The side and aft walls clearly show the recirculation of the flow at the rear end of the cavity.

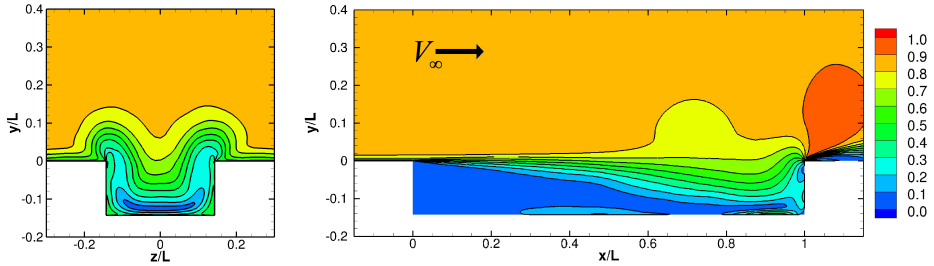

(a) $x/L = 0.85$ (b) $z/L = 0.0$

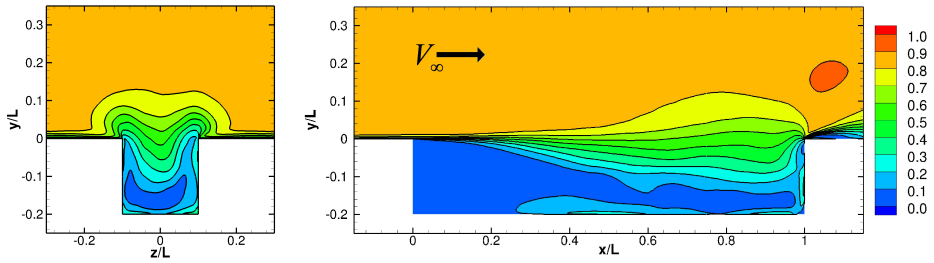

(c) $x/L = 0.85$ (d) $z/L = 0.0$

Figure 3.3: Time-averaged contours of Mach number for the L/D=7 cavity (a,b) and the M219 cavity (c,d) with doors-off. Planes are located at the rear end ($x/L = 0.85$) and centreline ($z/L = 0.0$) of the cavity.

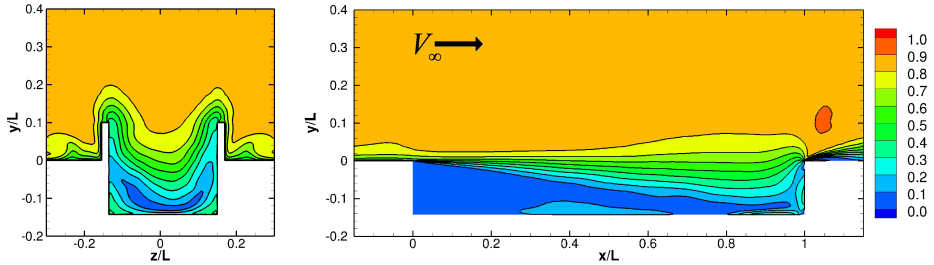

(a) $x/L = 0.85$ (b) $z/L = 0.0$

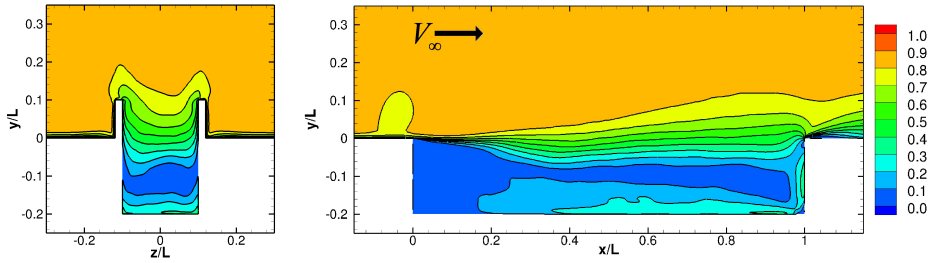

(c) $x/L = 0.85$ (d) $z/L = 0.0$

Figure 3.4: Time-averaged contours of Mach number for the L/D=7 cavity (a,b) and the M219 cavity (c,d) with doors-on. Planes are located at the rear end ($x/L = 0.85$) and centreline ($z/L = 0.0$) of the cavity.

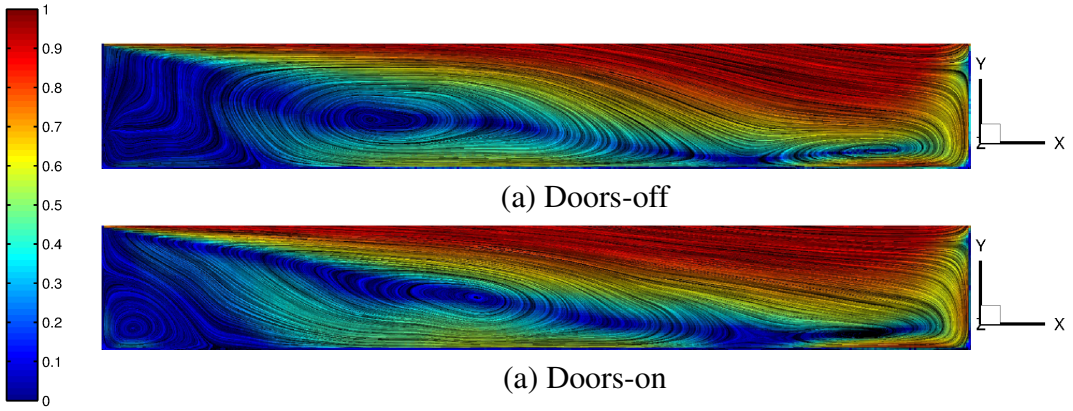

(a) Doors-off

(a) Doors-on

Figure 3.5: Time-averaged flow-field slices using LIC for the clean cavity, L/D=7, with doors-off (a) and doors-on (b). Planes are located at the cavity centreline ($z/L = 0.0$). Contours indicate velocity magnitude ranging from 0 (blue) to 1 (red).

3.3 Instantaneous Flow-Field

The shear layer is the driving force behind time-dependent features of a cavity. In order to visualise structures, iso-surfaces of Q-Criterion are presented in Figure 3.8 and show that the M219 cavity with doors-on had less structural content in the shear layer of the cavity than the doors-off case. Most of the structures for the M219 cavity with doors-off, were restricted to the shear layer in the aft-two thirds of the cavity. The doors-on case showed more structures at the front and rear of the cavity due to the flow interacting with the leading and trailing edge of the doors. The L/D=7 cavity showed similar structures to the M219 cavity with doors-off and doors-on. The doors-off case, however, showed more structures at the rear of the cavity due to more flow spillage for the L/D=7 cavity than the M219 cavity. Also, the doors-on case showed more structures inside the cavity and close to the floor, for the L/D=7 cavity, than the M219 cavity due to its depth being smaller.

3.4 Acoustic Propagation

To highlight the differences in acoustic wave propagation between the doors-off and doors-on configurations, Figure 3.9 shows instantaneous iso-surfaces of unsteady pressure and numerical schlieren. The pressure fluctuations at the shear layer travelled towards the aft wall, whilst outside the cavity, the pressure waves travelled out and towards the front wall, which made the trailing-edge of the cavity the source of the acoustic waves.

For the doors-on case, with the flow being more two-dimensional, the energy was directed back upstream rather than out of the cavity meaning that the acoustic waves were weaker and so propagated a smaller distance out of the cavity.

Iso-surfaces of unsteady pressure showed the structure of the waves propagating outside the cavity were similar for both cases. However, the doors helped to channel the flow and forced the shear layer to mainly oscillate at the second Rossiter mode. The mixed oscillations of second and third Rossiter modes in the doors-off configuration produced more frequent acoustic waves (Figure 3.9).

The OASPL distributions (Figure 3.10) showed that both cases generated very high OASPL (more than 170 dB) over the whole aft wall. As with the iso-surfaces of unsteady pressure, there were similarities between the two cases in how the waves propagated throughout the far-field domain; however, the levels in the doors-on cavity were generally lower.

While the density of the computational grid in the far-field is not adequately fine enough to preserve the acoustic waves reflected out of the cavity, comparisons were only possible since comparable grid densities were used for both cases.

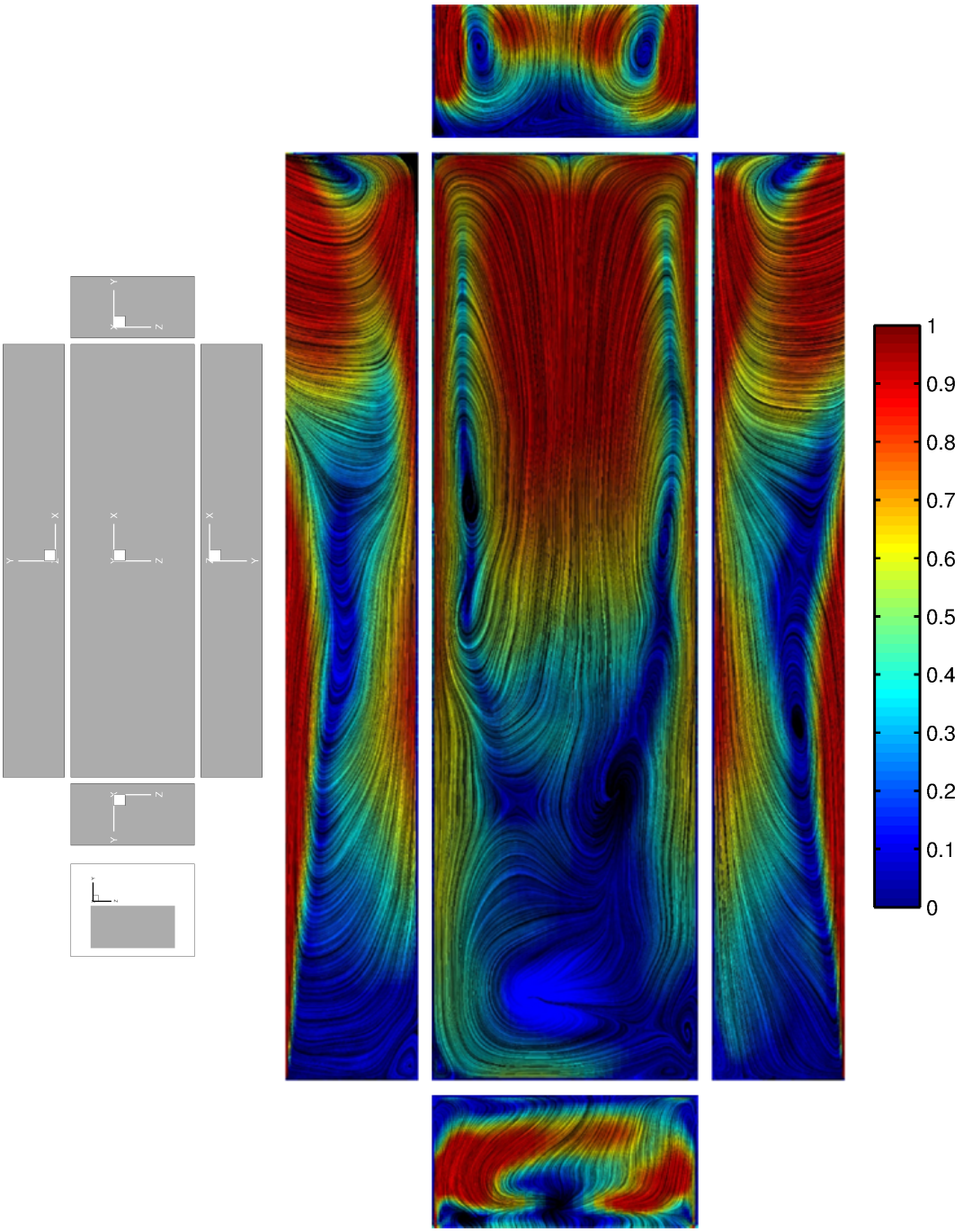

Figure 3.6: Time-averaged flow-field slices using LIC for the clean cavity, L/D=7, with doors-off. Planes are located close to each wall of the cavity. Contours indicate velocity magnitude ranging from 0 (blue) to 1 (red).

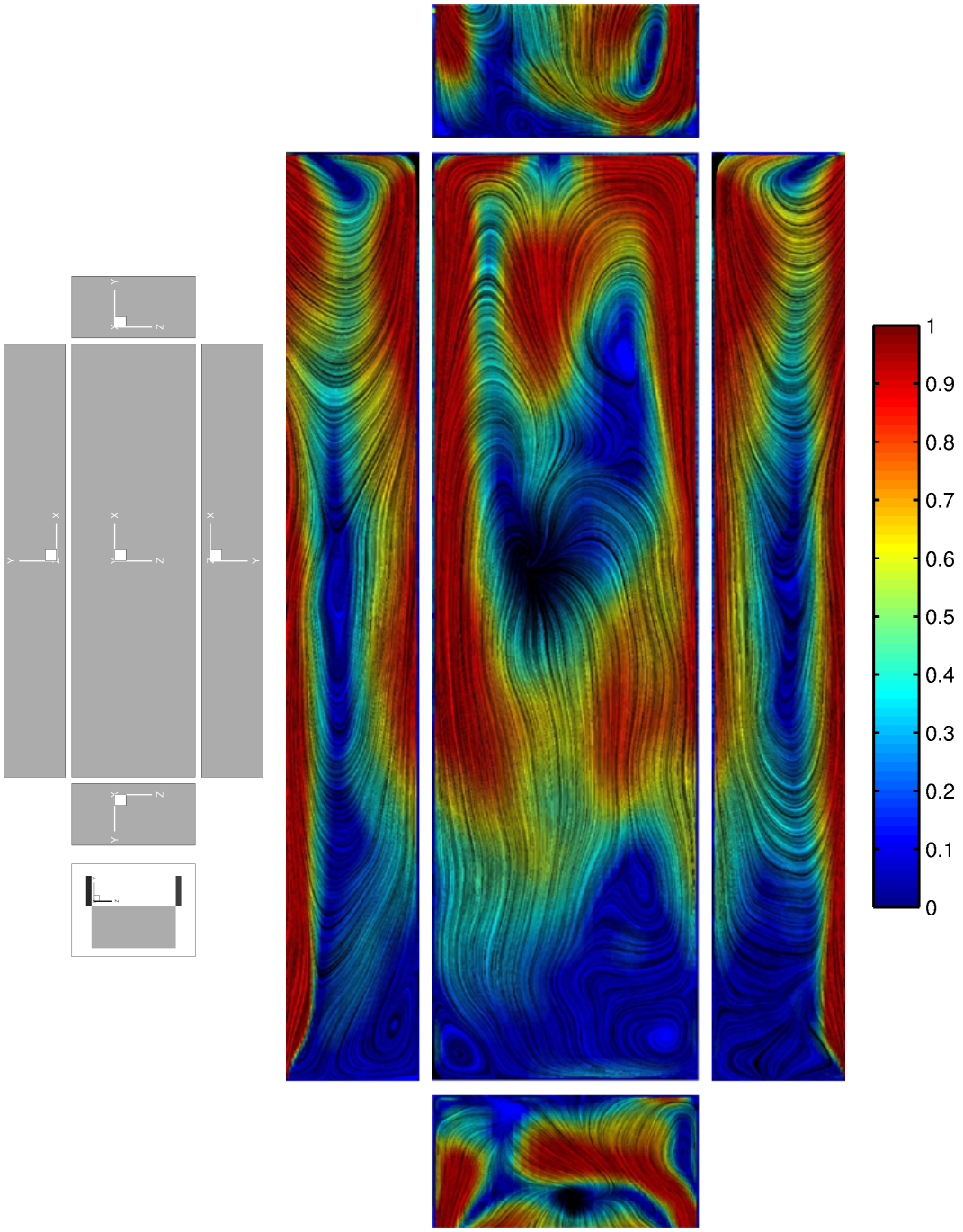

Figure 3.7: Time-averaged flow-field slices using LIC for the clean cavity, L/D=7, with doors-on. Planes are located close to each wall of the cavity. Contours indicate velocity magnitude ranging from 0 (blue) to 1 (red).

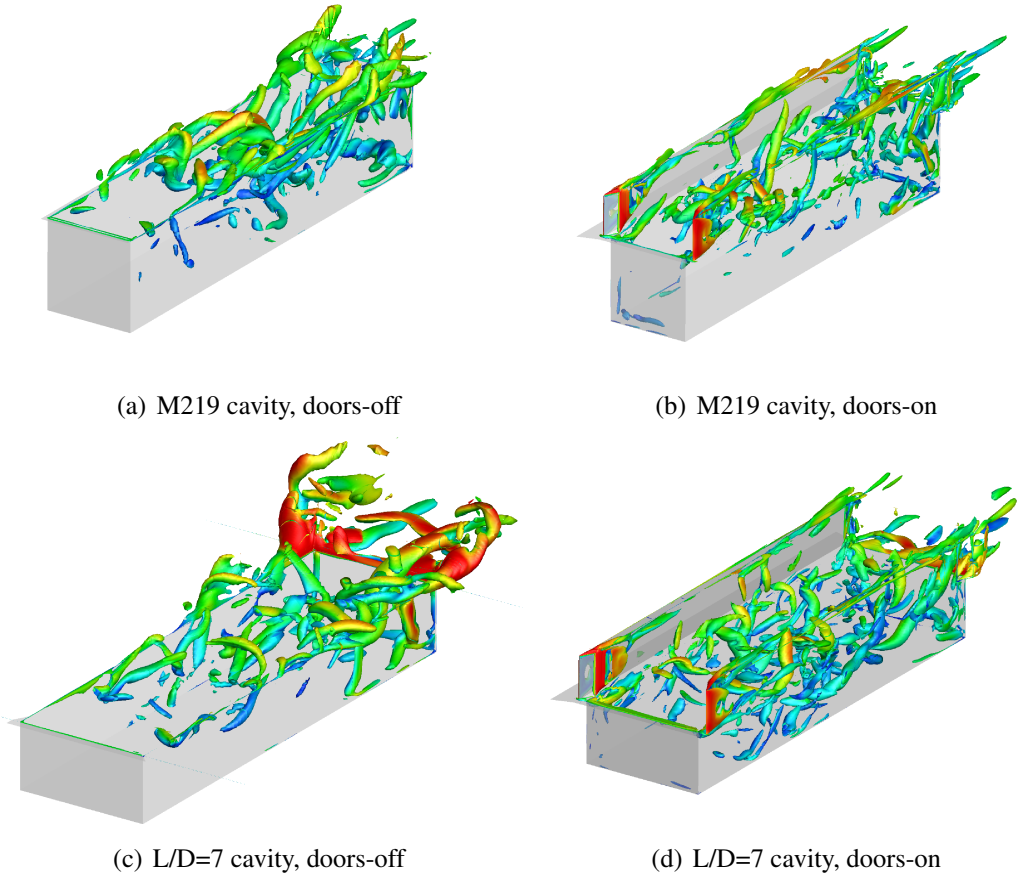

(a) M219 cavity, doors-off

(b) M219 cavity, doors-on

(c) L/D=7 cavity, doors-off

(d) L/D=7 cavity, doors-on

Figure 3.8: Instantaneous iso-surfaces of Q-Criterion for the M219 and L/D=7 cavity with doors-off and doors-on. Iso-surfaces at Q=2000 are shown and coloured with Mach number ranging between 0.0 (blue) and 1.0 (red).

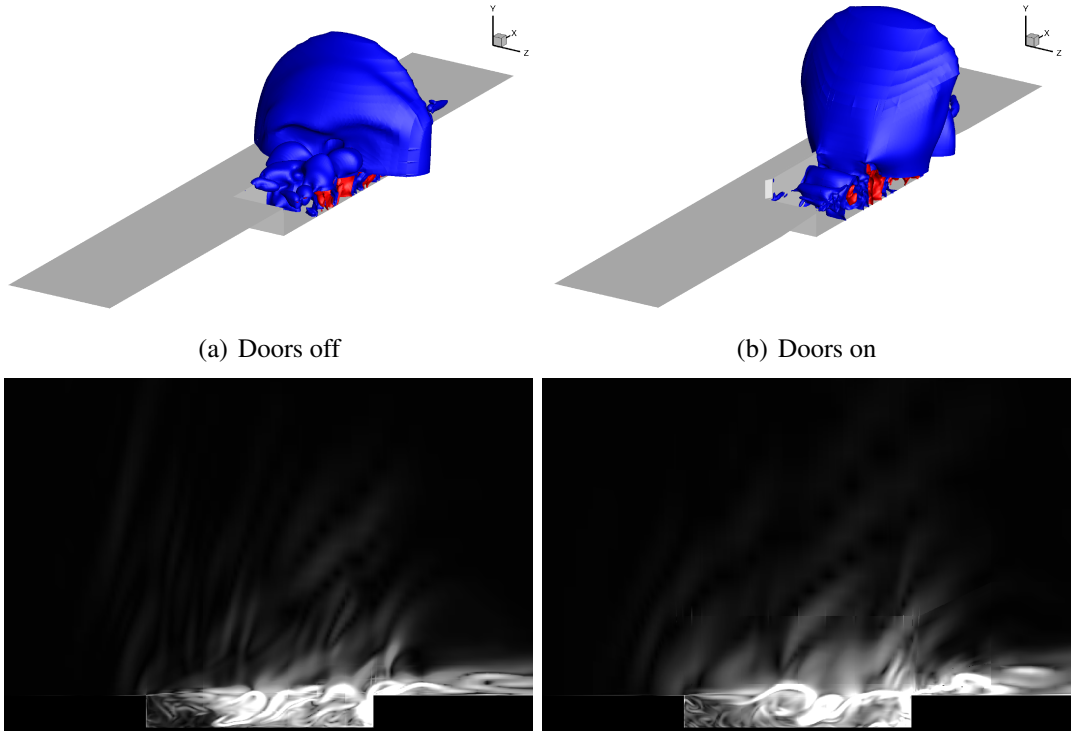

(a) Doors off (b) Doors on

(c) Doors off (d) Doors on

Figure 3.9: Instantaneous iso-surfaces of unsteady pressure (a,b) and numerical schlieren (c,d) for the L/D=7 cavity with doors-off (left column) and doors-on (right column). Iso-surface levels correspond to 160dB (blue) and 170dB (red). Planes for numerical schlieren are located at the cavity centreline ($z/L = 0.0$).

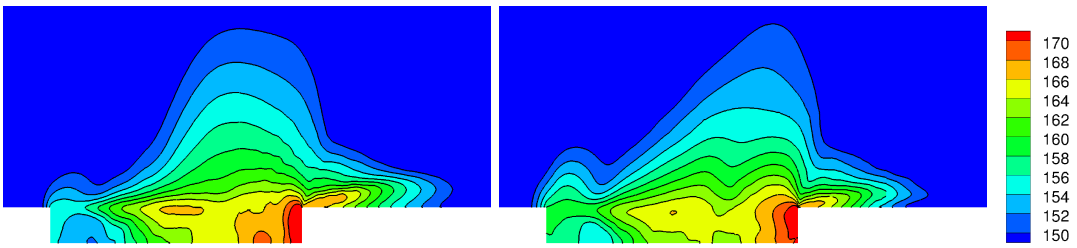

(a) Doors off (b) Doors on

Figure 3.10: Contours of OASPL along the cavity centreline ($z/L = 0.0$) for the L/D=7 cavity with doors-off (a) and doors-on (b).

3.5 Spectral Analyses

3.5.1 Doors-off

The PSD of pressure at the front, middle and rear of the cavity, along the cavity floor, is shown in Figure 3.11 comparing the M219 cavity and the L/D=7 cavities, for the doors-off configuration. Plots are compared with experimental data of the M219 cavity from Nightingale *et al.* [16]. Since the experimental signal had a longer duration, in order to compare with the DES results, it was cut down to the same length. PSD plots showed that the M219 cavity had peaks at the first four Rossiter modes at the front and rear of the cavity and peaks at second and fourth Rossiter modes in the middle of the cavity. At the front and rear, modes two and three had larger amplitudes than one and four and were seen to be dominant, while in the middle of the cavity, mode two was seen to be dominant. The L/D=7 cavity however, showed peaks at the first two Rossiter modes at the front and rear of the cavity and peaks at second and fourth Rossiter modes in the middle of the cavity. The behaviour at the middle of the cavity was quite similar for both cavities but the amplitude of the second mode was slightly lower for the L/D=7 cavity. Both cavities had clear tones as opposed to a single broadband spectrum.

OASPL and BISPL plots along the floor of the cavity (Figure 3.12) suggest similar trends between the two cavities varying only slightly in amplitude. DES results for the M219 cavity showed an almost constant overprediction of 5dB for the OASPL and between 1 and 5dB for the BISPL plots. This overprediction was shown in past work [13] to arise from the relative coarseness of the computational grid and that refining the grid or using LES reduced the overprediction. Both the M219 and L/D=7 cavity showed similar shapes for the OASPL and BISPL plots, both reached maximum values of 170dB by the aft wall of the cavity.

3.5.2 Doors-on

The PSD at the front, middle and rear of the cavity, along the cavity floor, is shown in Figure 3.13 comparing the M219 cavity and the L/D=7 cavity, for the doors-on configuration. Plots are compared with experimental data for the M219 cavity from Nightingale *et al.* [16]. Similar to the doors-off case, the experimental signal had to be shortened for comparison with the DES signals. The channelling effect of the doors affected the dominant modes in a similar manner for both cavities. All along the length of the cavity, mode two was dominant with similar amplitudes for both cavities.

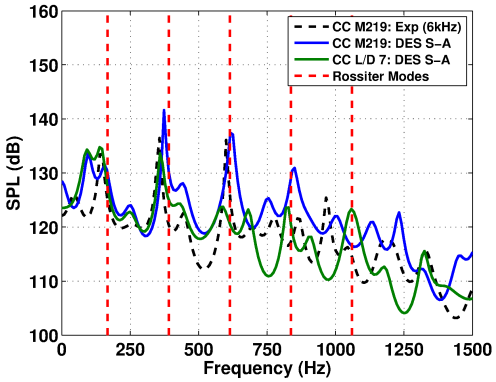

(a) $x/L = 0.05$

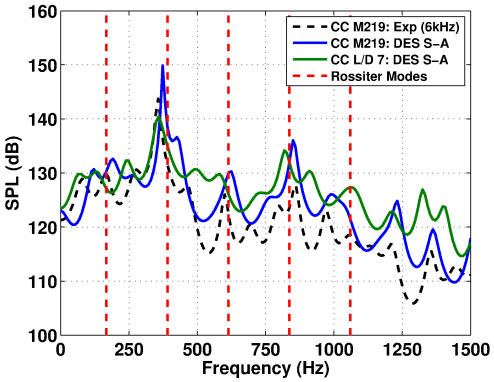

(b) $x/L = 0.50$

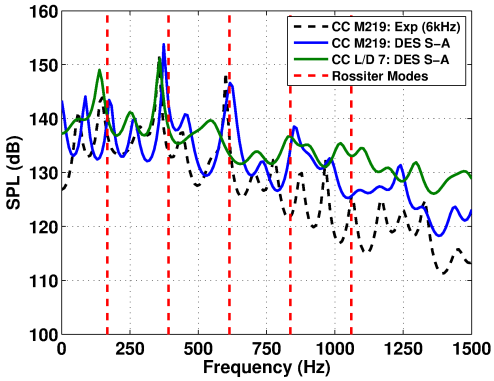

(c) $x/L = 0.95$

Figure 3.11: PSD plots along the cavity floor for the M219 cavity and L/D=7 cavity, with doors-off. Plots compare DES results for the M219 cavity from Lawson [13] to DES results for the L/D=7 cavity and experimental data for the M219 cavity from Nightingale *et al.* [16]. Plots are for the front (a) middle (b) and rear (c) transducers on the cavity floor and presented in terms of SPL. CC - Clean Cavity, S-A - Spalart Allmaras.

OASPL and BISPL plots along the floor of the cavity (Figure 3.14) had similar shapes but with variations in amplitude. Like for the doors-off case, an almost constant overprediction of 5dB was seen in the OASPL for the M219 cavity. BISPL plots around the first four Rossiter modes for the M219 cavity showed that most of the overprediction was in mode three. The OASPL curve for the L/D=7 cavity showed the same characteristic 'W' shape as the M219 cavity, although lower in amplitude.

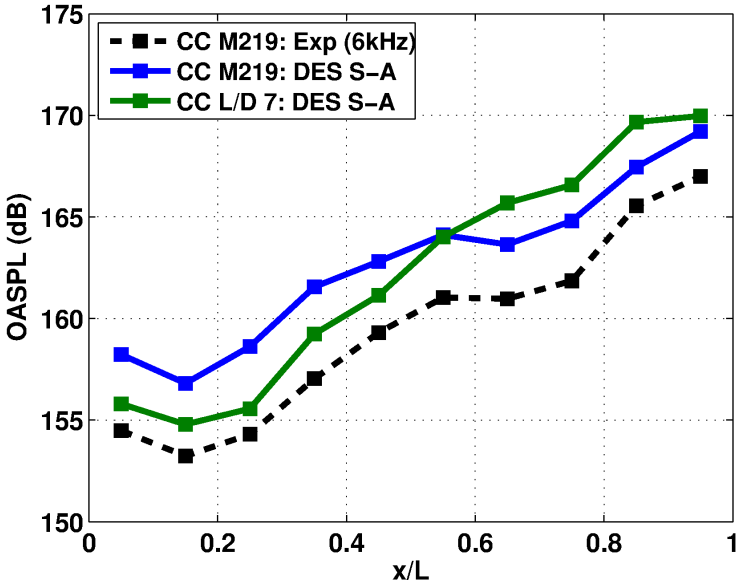

(a) OASPL

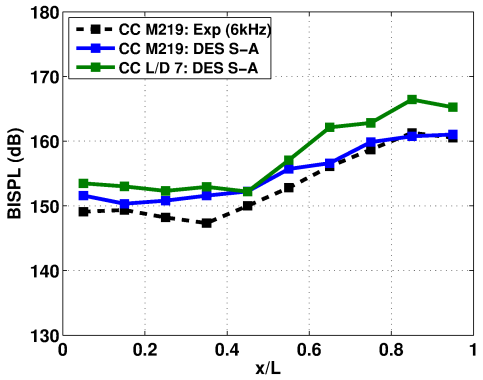

(b) Mode 1: $50 \leq f \leq 250$ Hz

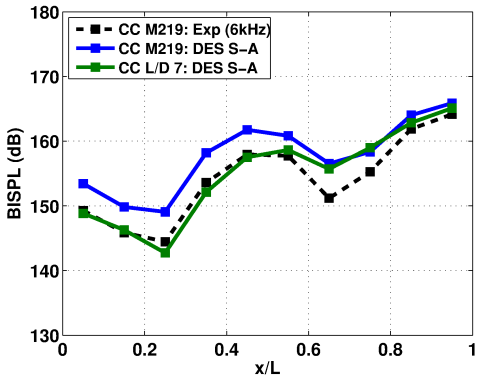

(c) Mode 2: $250 \leq f \leq 450$ Hz

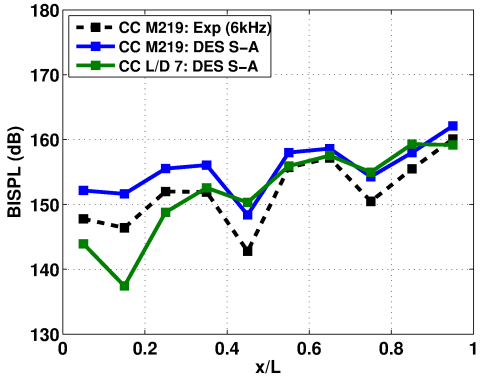

(d) Mode 3: $500 \leq f \leq 700$ Hz

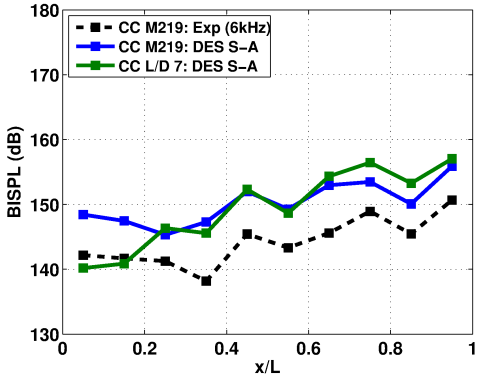

(e) Mode 4: $700 \leq f \leq 900$ Hz

Figure 3.12: OASPL (a) and BISPL plots (b-e) along the cavity floor for the M219 cavity and L/D=7 cavity, with doors-off. Plots compare DES results for the M219 cavity from Lawson [13] to DES results for the L/D=7 cavity and experimental data for the M219 cavity from Nightingale *et al.* [16]. CC - Clean Cavity, S-A - Spalart Allmaras.

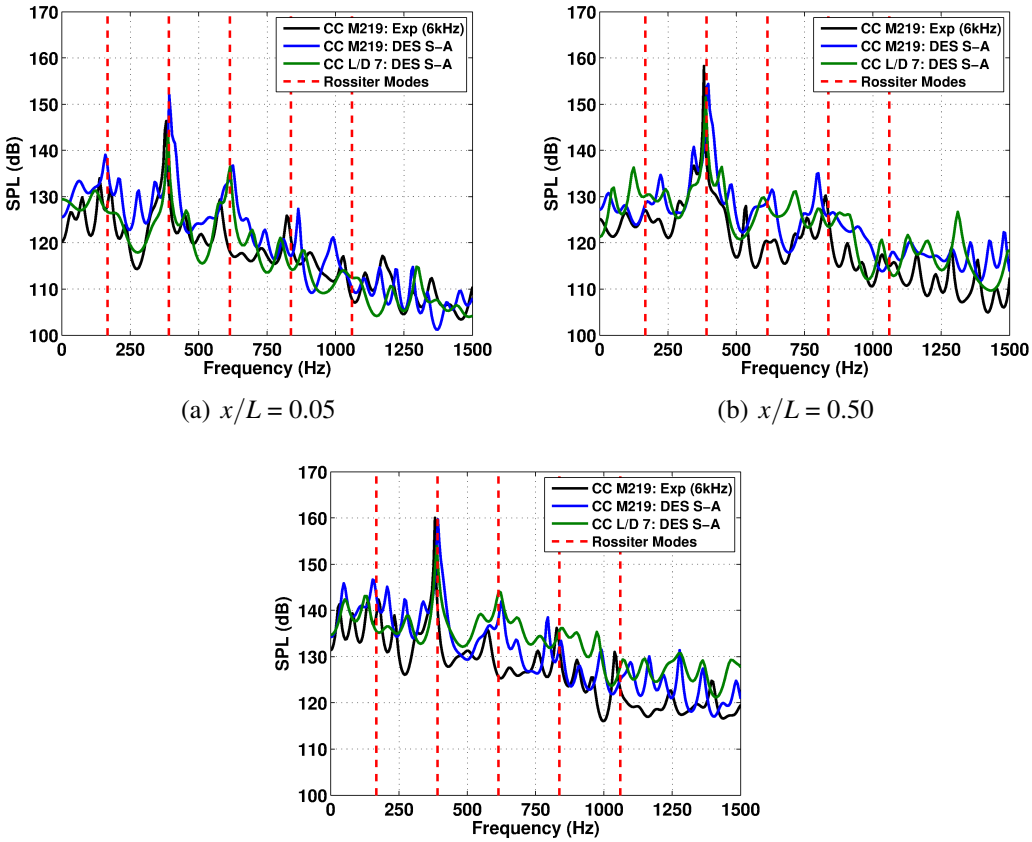

(a) $x/L = 0.05$ (b) $x/L = 0.50$

(c) $x/L = 0.95$

Figure 3.13: PSD plots along the cavity floor for the M219 cavity and L/D=7 cavity, with doors-on. Plots compare DES results for the M219 cavity from Lawson [13] to DES results for the L/D=7 cavity and experimental data for the M219 cavity from Nightingale *et al.* [16]. Plots are for the front (a) middle (b) and rear (c) transducers on the cavity floor and presented in terms of SPL. CC - Clean Cavity, S-A - Spalart Allmaras.

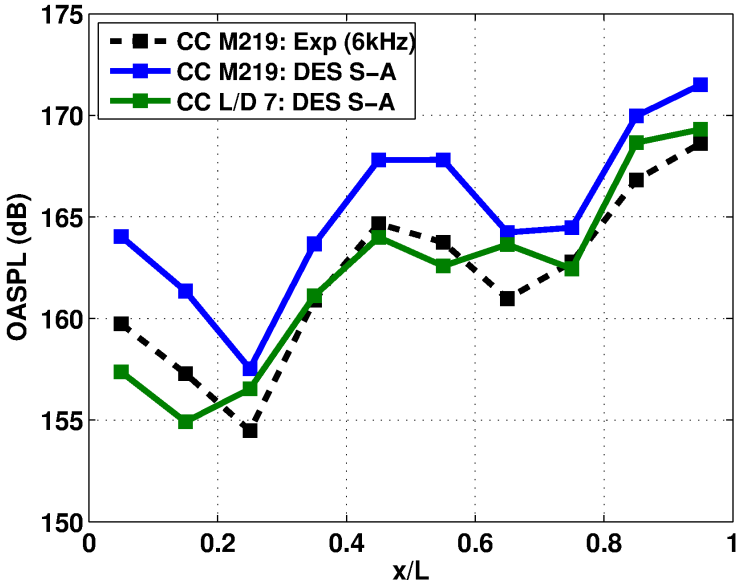

(a) OASPL

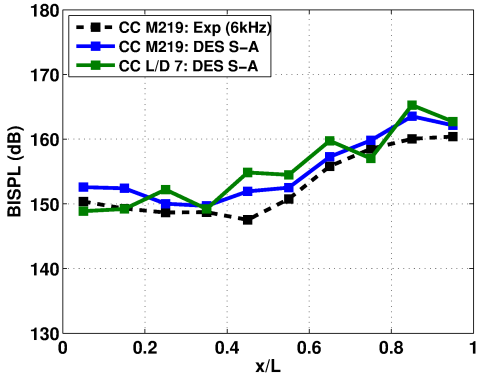

(b) Mode 1: $50 \leq f \leq 250$ Hz

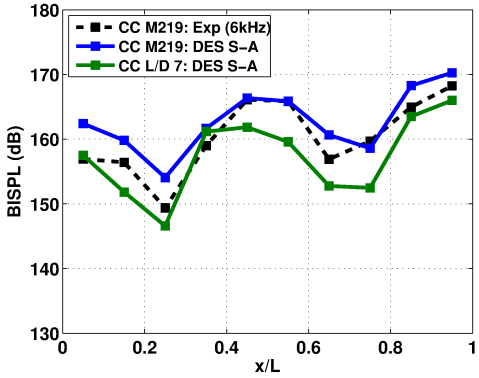

(c) Mode 2: $250 \leq f \leq 450$ Hz

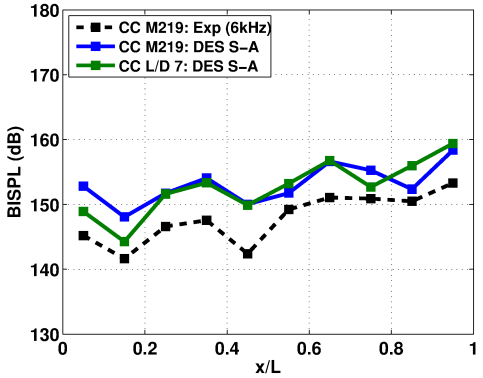

(d) Mode 3: $500 \leq f \leq 700$ Hz

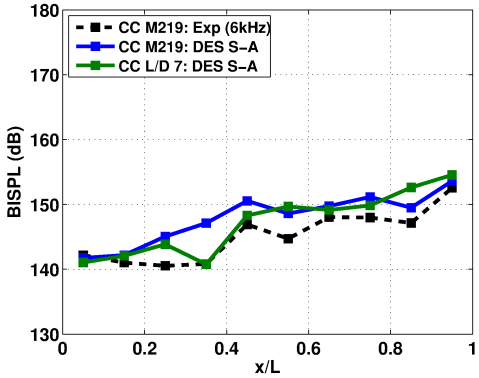

(e) Mode 4: $700 \leq f \leq 900$ Hz

Figure 3.14: OASPL (a) and BISPL plots (b-e) along the cavity floor for the M219 cavity and L/D=7 cavity, with doors-on. Plots compare DES results for the M219 cavity from Lawson [13] to DES results for the L/D=7 cavity and experimental data for the M219 cavity from Nightingale *et al.* [16]. CC - Clean Cavity, S-A - Spalart Allmaras.

3.6 Joint Time-Frequency Analysis

Joint time-frequency analysis along the cavity floor, as shown by the time-space map in Figure 3.15 for the doors-off configuration, provided evidence that the numerical solutions[13] for the M219 cavity, predicted similar instantaneous characteristics to the experiments. In the experimental data, for this period of time, the first three modes exchanged energy at different times. Overall, the third mode was dominant most of the time, with the first dominating in some instances. Both the experimental and numerical results displayed mode switching characteristics. The occasional appearance of the fourth mode was missing from the experimental results possibly due to the short computational signal to accurately resolve the mode.

The L/D=7 cavity showed that mode one was dominant at the front and rear of the cavity with mode switching seen between modes one and two towards the rear. Interestingly, both the M219 cavity and the L/D=7 cavity showed the dominance of mode two in the middle of the cavity, with occasional mode switching.

3.7 POD Analysis

To construct the POD modes, 201 snapshots were taken at regular intervals in the flow over a time period equal to 10 periods of the first Rossiter mode. This selection was limited by the available disk storage, for which the 201 snap-shots approached 120GB, for the L/D=7 cavity with doors-off and doors-on, each. The POD was performed on the five primitive variables: density, u, v and w velocities and pressure. With the mean mode ignored, the energy fraction per mode and the cumulative energy are shown in Figure 3.16, for the doors-off and doors-on configurations.

The pressure modes contained much more energy than the other variables, especially when compared to velocities. For example, Figure 3.16(b) shows that 80% of the energy in pressure can be gained from 40 modes, whereas approximately 80 modes would be needed to gain the same value for w velocity. This meant that the pressure field was more coherent and organised, and could be described using fewer modes, while the w velocity field contained smaller and possibly more turbulent structures, hence redistributing energy to the higher modes. For the doors-on case, shown in Figure 3.16(b), 80% of the energy in pressure can be gained from 20 modes, while the w velocity can be gained from 60 modes, further emphasising the channelling effect caused by the doors.

For both doors-on and doors-off configurations, the number of modes needed to fulfil the nominal criteria of capturing 90% of the energy was found to be just over 100. This equated to retaining about 67% of the total number of modes. The decomposition using the 201 snapshots and a reduced set of 51 snapshots were compared in Figure 3.17 for pressure, streamwise, normal and spanwise velocities. The ratios of the modes to the first mode were quite similar for both decompositions up to about mode number 20. Therefore, even the reduced set would give a good indication of the structure of the flow, although the modes would not be as well resolved.

Figure 3.18 shows the mode eigenvalues for the L/D=7 cavity with doors-off and doors-on. For the doors-on configuration, most of the energy was contained within the lower modes of the decomposition, especially for u and v velocities. The instantaneous flow in the cavity was highly three-dimensional; however, the averaged flow was less so. Therefore it makes sense that the eigenvalues of w velocity were similar for both cases, although for the doors-on case the flow was more restricted. The higher levels of energy contained in u and v velocity components suggested that the cavity with doors-on had a more coherent structure to the flow, which is explained by the dominance of the second Rossiter mode and the relatively small amount of mode switching that occurred.

3.7.1 Flow-Field Reconstructions

The L/D=7 cavity with doors-off was reconstructed using 2, 51 and 151 modes. The cavity flow-fields from the reconstructions are shown in Figures 3.19. Mach number contours along the cavity centreline showed that the full dynamics of the shear layer was only represented when more than 51 modes were used. Structures inside the cavity were seen when 151 modes were used. The areas of high difference between the original and the reconstruction with 51 modes, were generally restricted to the aft half of the cavity. The increase to 151 modes reduced the differences towards the aft half of the cavity. It should be noted that the time-varying mean flow-field (POD mode 1) was always included in the reconstructions. Therefore when the reconstructed data are averaged, the flow-field was unaffected by the number of modes used in the reconstruction.

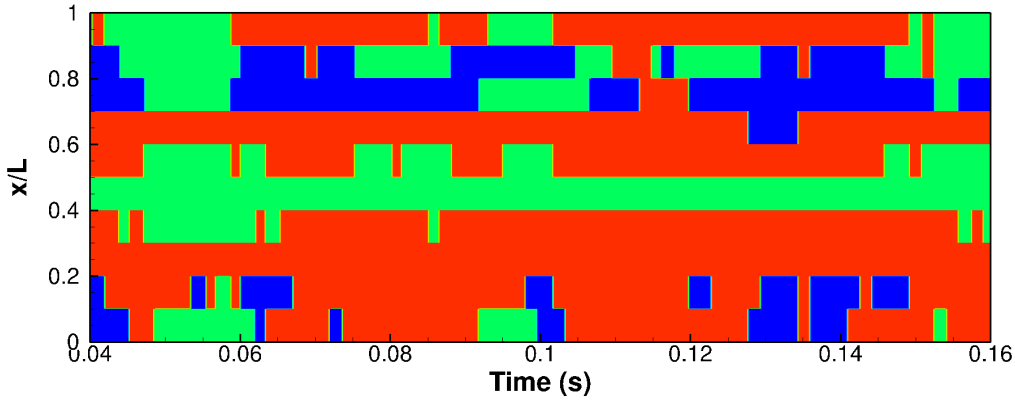

(a) Experiment: M219 cavity

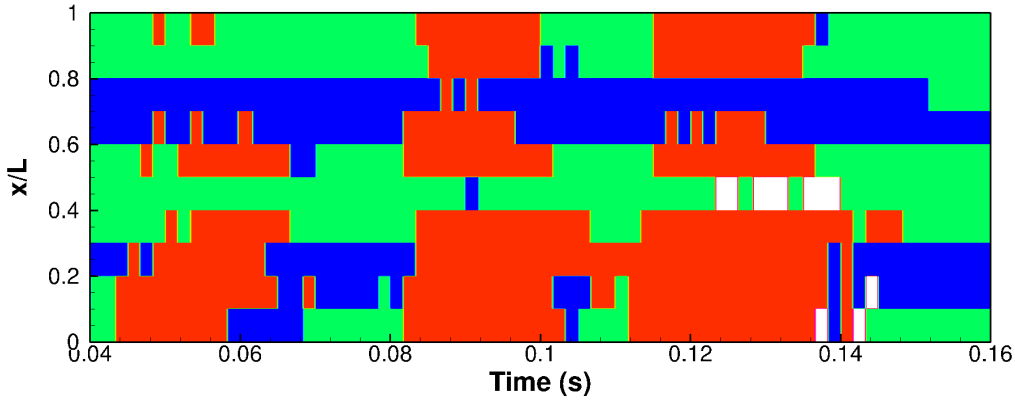

(b) DES: M219 cavity

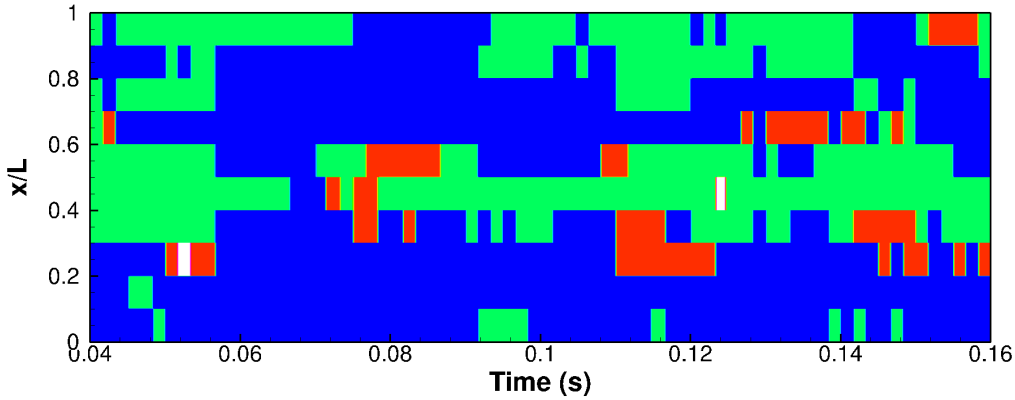

(c) DES: L/D=7 cavity

Figure 3.15: Time-space maps along the floor of the M219 cavity with doors-off comparing experimental (a) and numerical results for the M219 cavity (b) and numerical results for the L/D=7 cavity (c). Plots compare DES results for the M219 cavity from Lawson [13] to DES results for the L/D=7 cavity and experimental data for the M219 cavity from Nightingale *et al.* [16]. The different colours represent: blue - mode 1, green - mode 2, red - mode 3, white - mode 4.

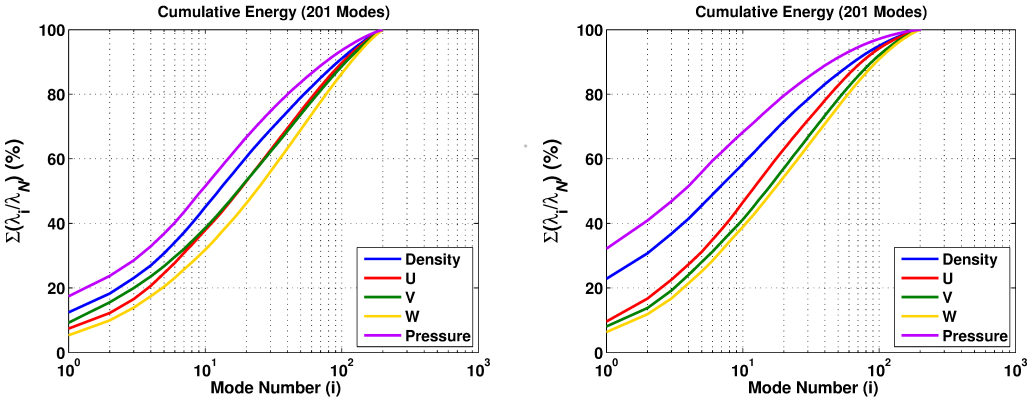

(a) Doors-off: Cumulative energy (b) Doors-on: Cumulative energy

Figure 3.16: Cumulative energy for increasing number of modes for the L/D=7 cavity, with doors-off (a) and doors-on (b).

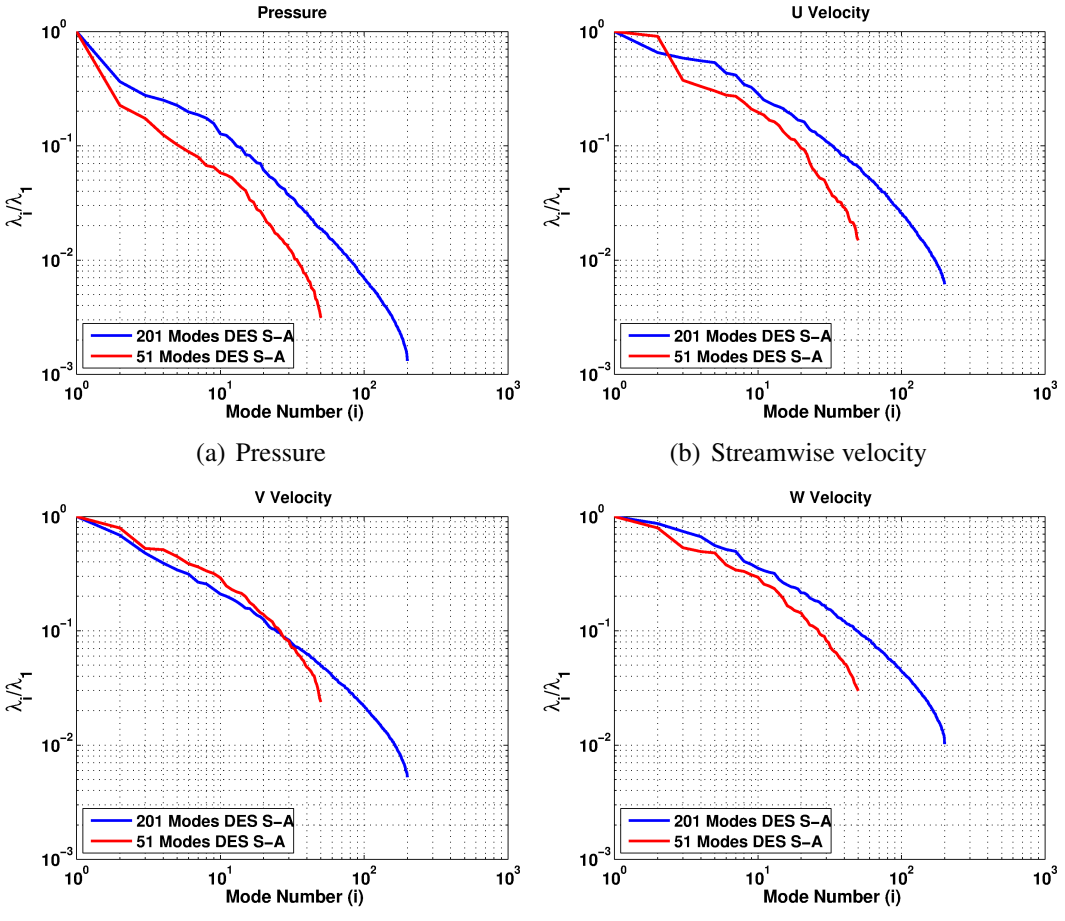

(a) Pressure (b) Streamwise velocity

(c) Normal velocity (d) Spanwise velocity

Figure 3.17: Mode eigenvalues normalised by the first mode eigenvalue comparing the POD using 201 and 51 snapshots for the L/D=7 cavity, with doors-off.

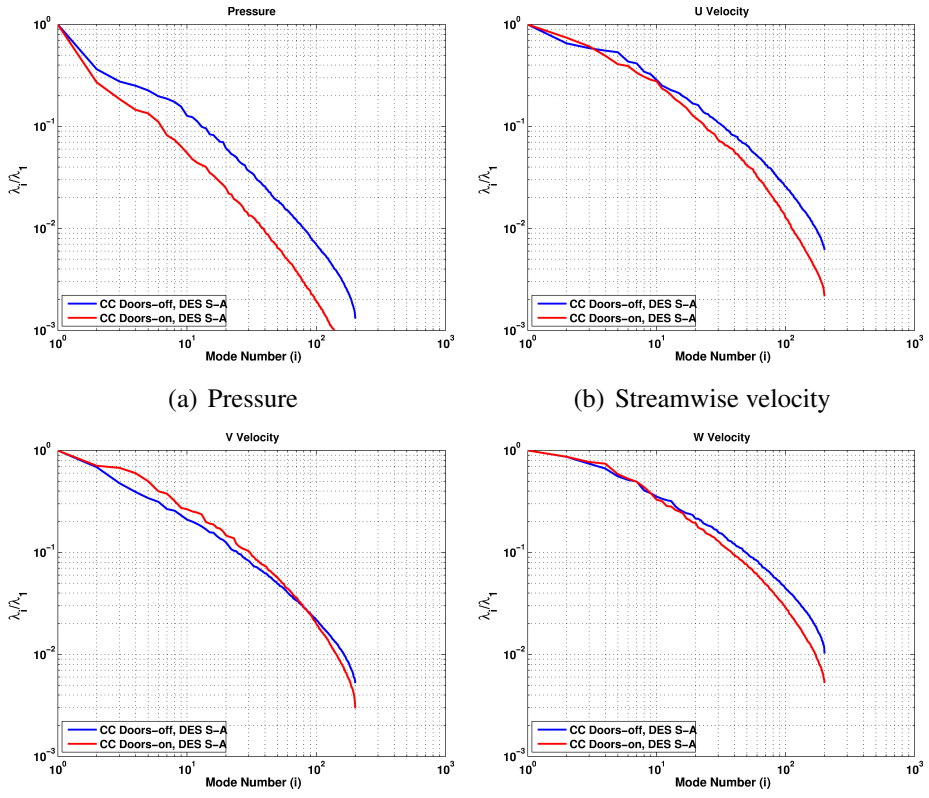

(a) Pressure (b) Streamwise velocity

(c) Normal velocity (d) Spanwise velocity

Figure 3.18: Mode eigenvalues normalised by the first mode eigenvalue comparing the decomposition using 201 for the L/D=7 cavity, with doors-off and doors-on.

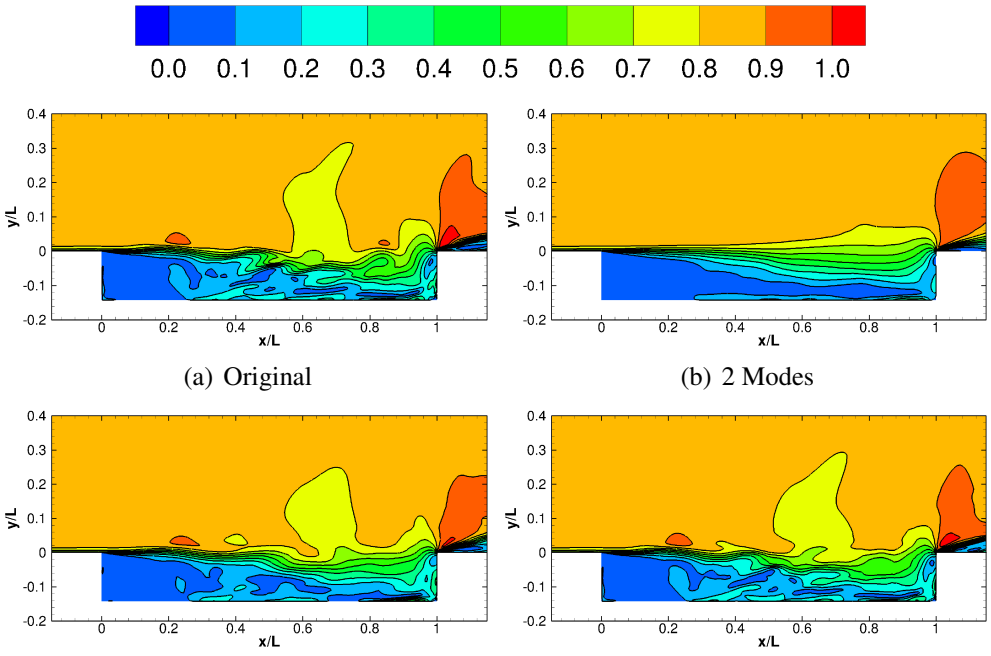

(a) Original (b) 2 Modes

(c) 51 Modes (d) 151 Modes

Figure 3.19: Reconstruction of the L/D=7 cavity flow-field, with doors-off, using increasing number of modes showing contours of Mach number.

Chapter 4

DES Computations for Cavity and Store Configurations

This chapter presents results for computations of a store located at different positions relative to an L/D=7 cavity. Simulations employed the DES S-A turbulence model [49] and were carried out at a Mach number of 0.85 and Re_L of 6.5 million. Results were compared to clean cavity computations to understand the influence of a store on the cavity flow-field. Averaged and instantaneous flow-fields are analysed along with flow angles inside the cavity and acoustic propagation.

4.1 Model Geometry and Mesh Generation

This section presents the geometry for all configurations and the fully-matched, structured multi-block meshes that were generated using ICEMCFD [93]. The geometry of the idealised L/D=7 cavity without doors, used in the previous Chapter, was combined with a generic store model, provided by MBDA[88]. The store had an ogive-cylinder body with four fins, where the roots of the fins were fixed into the body, and was 90% of the cavity length. All geometries were non-dimensionalised by the cavity length, $L = 3.33m$. Three positions of the store relative to the cavity were investigated: at carriage position, at the shear layer and outside the cavity as shown in Figure 4.1. For the first position of the store, at carriage, the store was placed inside the cavity with the centre of the store at half a cavity depth.

For the second position of the store, at the shear layer, the store was moved outwards from the carriage position by half a cavity depth such that half the store was outside the cavity and the other half was inside. For the third position of the store, outside the cavity, the store was moved outwards from the shear layer position by half a cavity depth. For all three cavity/store configurations, the store was oriented in a cross-configuration and placed in the middle of the cavity and along its centreline (Figure 4.1).

Grid slices along the centreline of the cavity ($z/L = 0.0$) and through the fins ($x/L = 0.85$) show that several cuts were made along the length of the fins. This was based on past experience[90] on deforming grids, and was done in order to better capture the aeroelastic deformations of the fins as the same meshes and flow solutions would be used to initiate aeroelastic computations, discussed in the following Chapter. All computations discussed in this Chapter relate to rigid stores and details of the associated grids and computations are summarised in Table 4.1.

Table 4.1: Details of the computations and associated grids.

Computation Details	**Store at Carriage**	**Store at Shear Layer**	**Store Outside Cavity**
Grid size (10^6 cells)	28.5	30.5	35.0
Number of blocks	3208	3678	4474
Processors	128	256	256
CFD time-step (10^{-6}s)	1.18	1.18	1.18
Unsteady tolerance	0.001	0.001	0.001
Number of time-steps	17000	21500	12700
Signal Duration (s)	0.20	0.25	0.15

4.2 Averaged Flow-Field

In order to study the effect of a store on the cavity flow-field, time-averaged contours of Mach number were visualised using slices along the centreline of the cavity and through the fins (Figure 4.2). The blockage introduced by the store at carriage made the shear layer more coherent and lowered the flow spillage over the sides of the cavity near the aft wall. In addition to this, the flow velocity at the aft wall of the cavity was also reduced (Figure 4.2(d)).

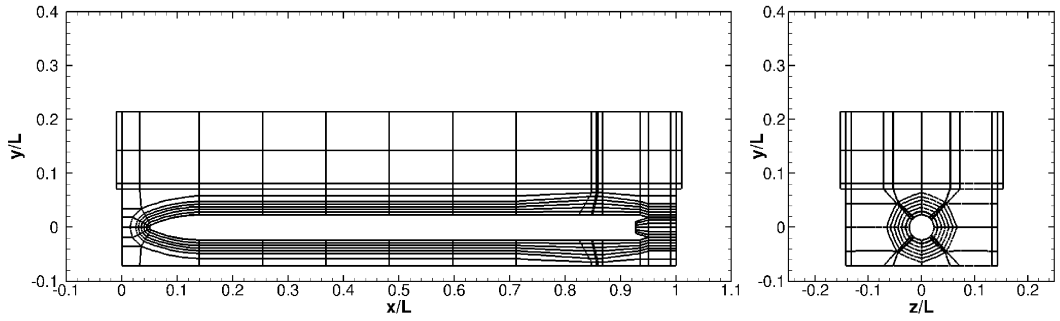

(a) Store at carriage position

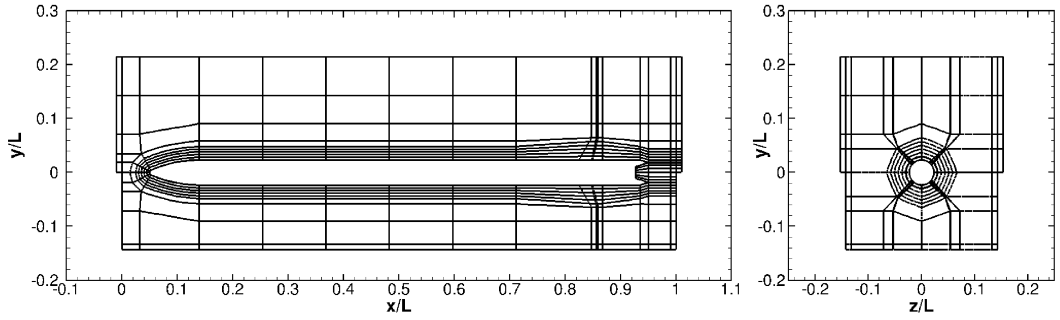

(b) Store at shear layer

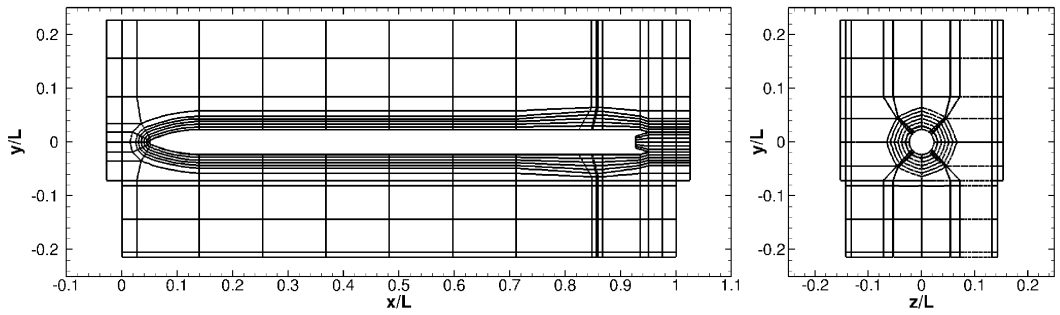

(c) Store outside cavity

Figure 4.1: Multi-block topology for the store at carriage (a) at the shear layer (b) and outside (c) the cavity. Planes are located at the rear end ($x/L = 0.85$) and centreline ($z/L = 0.0$) of the cavity.

When the store was placed at the shear layer, the blockage effect towards the aft of the cavity was reduced which increased the flow spillage over the sides of the cavity. The region of accelerated flow by the aft wall also increased compared to when the store was at carriage. Although the centreline of the cavity was directly affected by the presence of the store, the flow-field began to resemble the clean cavity flow-field in terms of the average Mach number field.

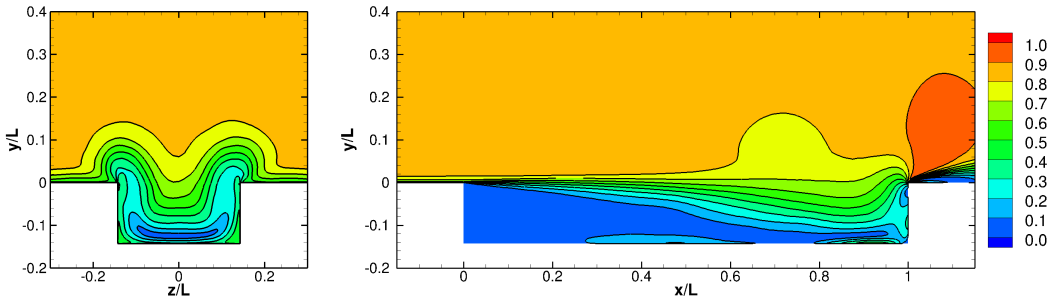

(a) $x/L = 0.85$ (b) $z/L = 0.0$

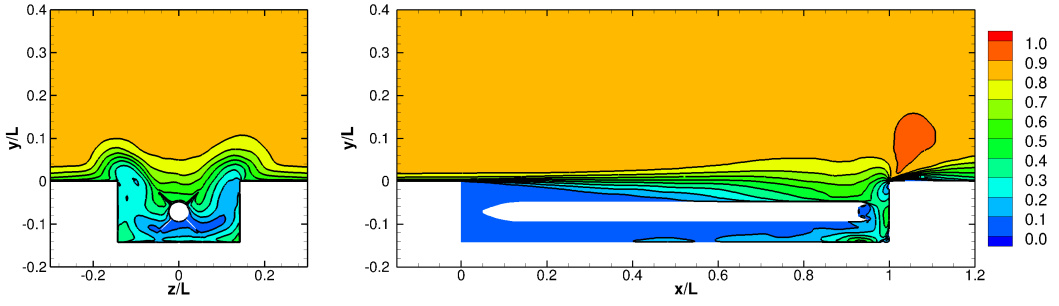

(c) $x/L = 0.85$ (d) $z/L = 0.0$

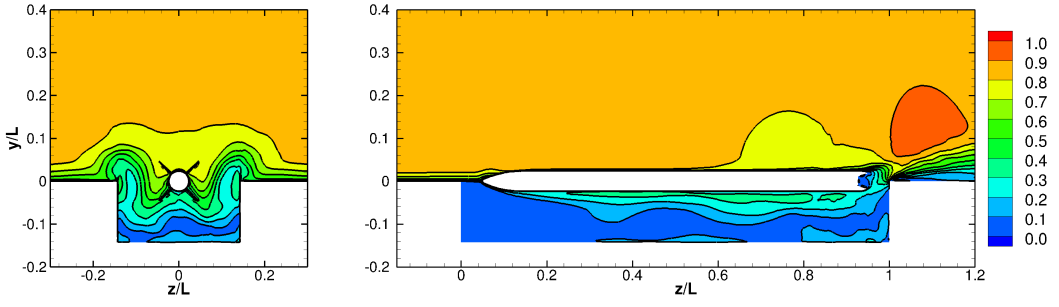

(e) $x/L = 0.85$ (f) $z/L = 0.0$

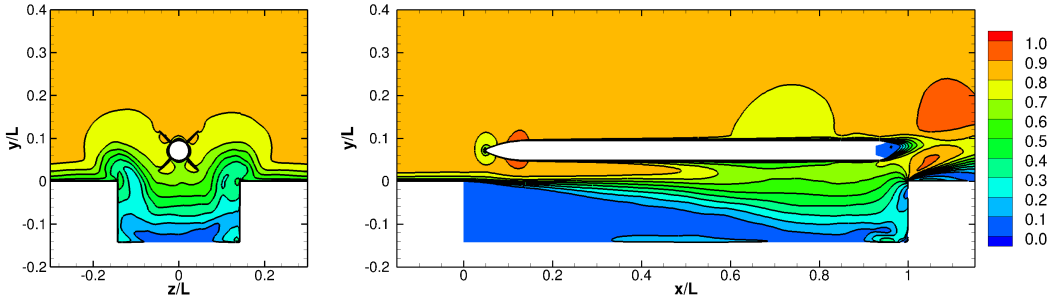

(g) $x/L = 0.85$ (h) $z/L = 0.0$

Figure 4.2: Time-averaged contours of Mach number for the clean L/D=7 cavity (a,b) and, with a store at carriage (c,d), at the shear layer (e,f) and outside (g,h). Planes are located at the rear end ($x/L = 0.85$) and centreline ($z/L = 0.0$) of the cavity.

Outside the cavity, the store had little to no influence on the flow-field inside the cavity evidenced by the similarities between Figures 4.2(a) and 4.2(g). The flow-field along the centreline resembles closely that of the clean cavity with some influence of the aft half of the store on the shear layer. Although the region past the aft wall is dissimilar to that of the clean cavity, due to the flow separating off the store, the overall flow-field is very similar to the clean cavity flow-field.

LIC was used to identify flow structures in the cavity in Figure 4.3 for the time-averaged flow of the clean L/D=7 cavity compared with the store at different positions relative to the cavity. The primary and secondary vortices identified in the previous Chapter, for the clean L/D=7 cavity without doors, are directly influenced by the presence of the store when at carriage. When the store was positioned at the shear layer, both vortices are seen to return although not as large as the ones in the clean cavity. When the store was outside, the primary and secondary vortices returned but additionally a small vortex was seen close to the primary vortex. This suggests that even though the store is outside, it may have some influence on the flow-field inside the cavity, although, it should be noted that the time-averaged flow-field for the clean cavity was obtained through a much longer computation of the flow. A longer computational signal contains more information about the flow and can provide better a frequency resolution that is generally more comparable to experimental data. More details about this can be found in Appendix A.

Time-averaged flow-field slices using LIC, similar to those presented by Khanal *et al.* [5,77], for the store at different positions relative to the cavity are shown in Figures 4.4, 4.5 and 4.6 respectively, for the store at carriage, at the shear layer and outside. Slices are shown close to each wall and show the general flow structure inside the cavity. While the side and aft walls of the cavity show a fair amount of symmetry, the slices close to the floor do not. This could be due to the disturbance in the flow, close to the floor, caused by the store when at carriage and at the shear layer. When the store was positioned outside, better symmetry was observed close to the floor of the cavity.

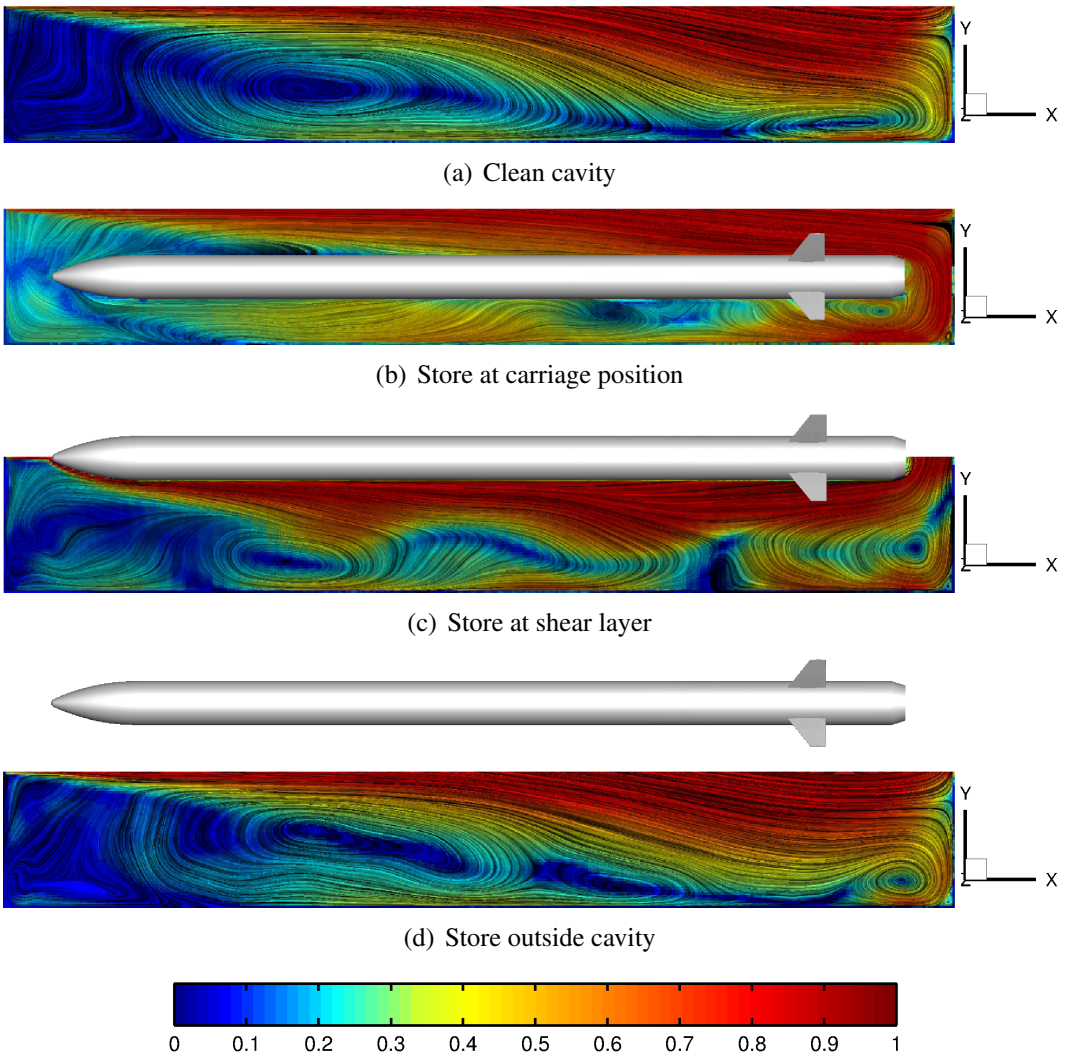

(a) Clean cavity

(b) Store at carriage position

(c) Store at shear layer

(d) Store outside cavity

Figure 4.3: Time-averaged flow-field slices using LIC for the clean L/D=7 cavity (a) and, with a store at carriage (b), at the shear layer (c) and outside (d). Planes are located at the cavity centreline ($z/L = 0.0$). Contours indicate velocity magnitude ranging from 0 (blue) to 1 (red).

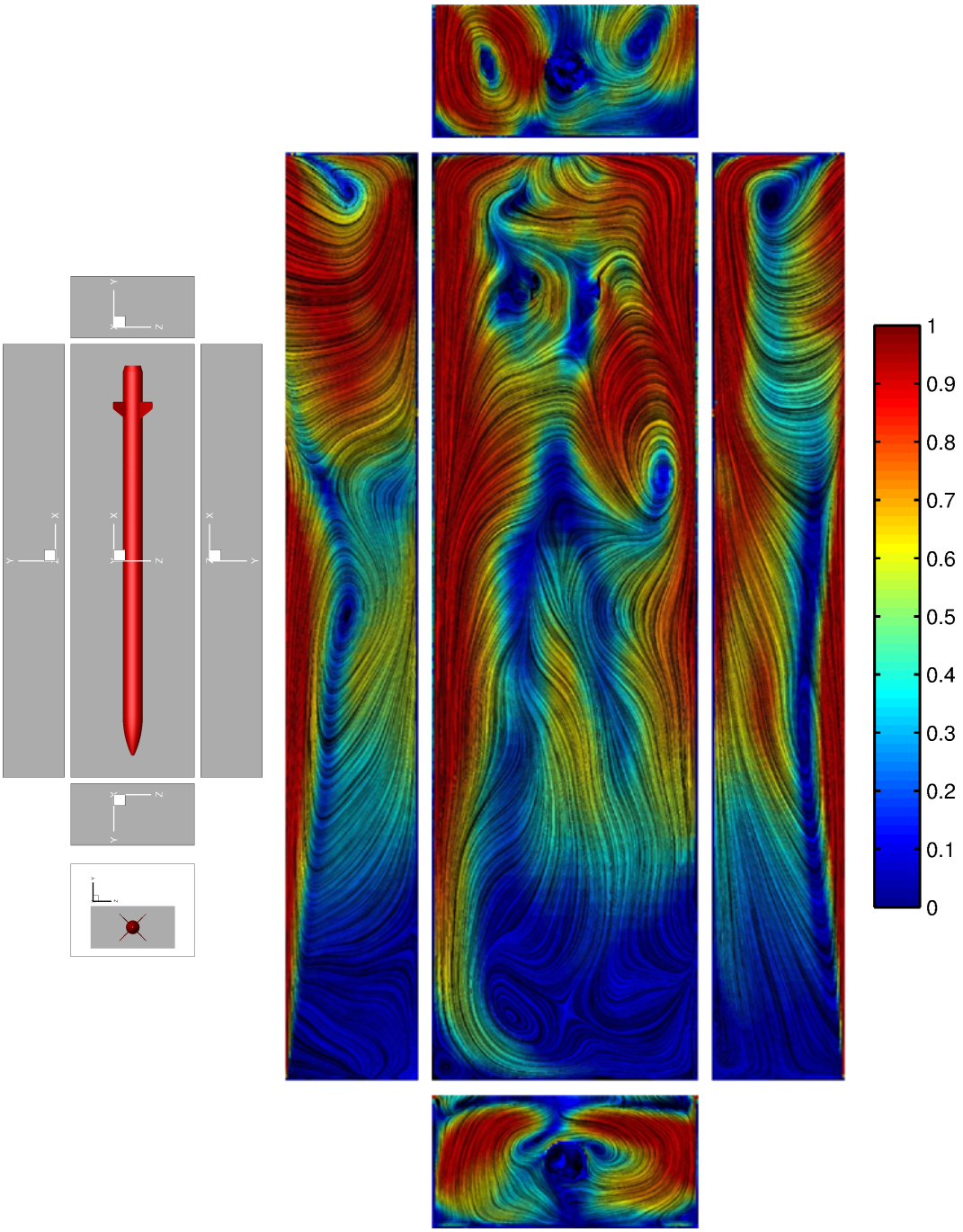

Figure 4.4: Time-averaged flow-field slices using LIC for the store at carriage. Planes are located close to each wall of the cavity. Contours indicate velocity magnitude ranging from 0 (blue) to 1 (red).

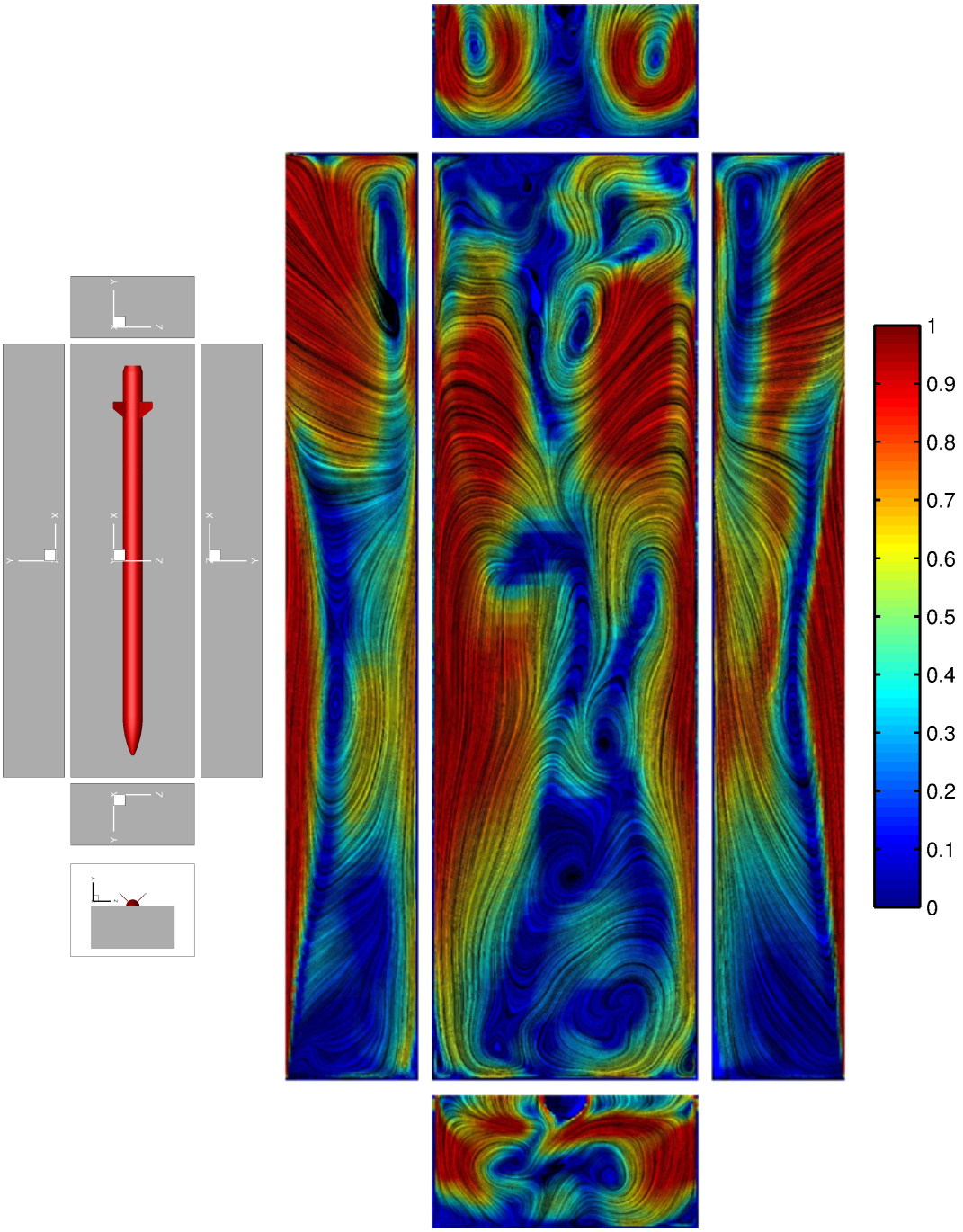

Figure 4.5: Time-averaged flow-field slices using LIC for the store at shear layer. Planes are located close to each wall of the cavity. Contours indicate velocity magnitude ranging from 0 (blue) to 1 (red).

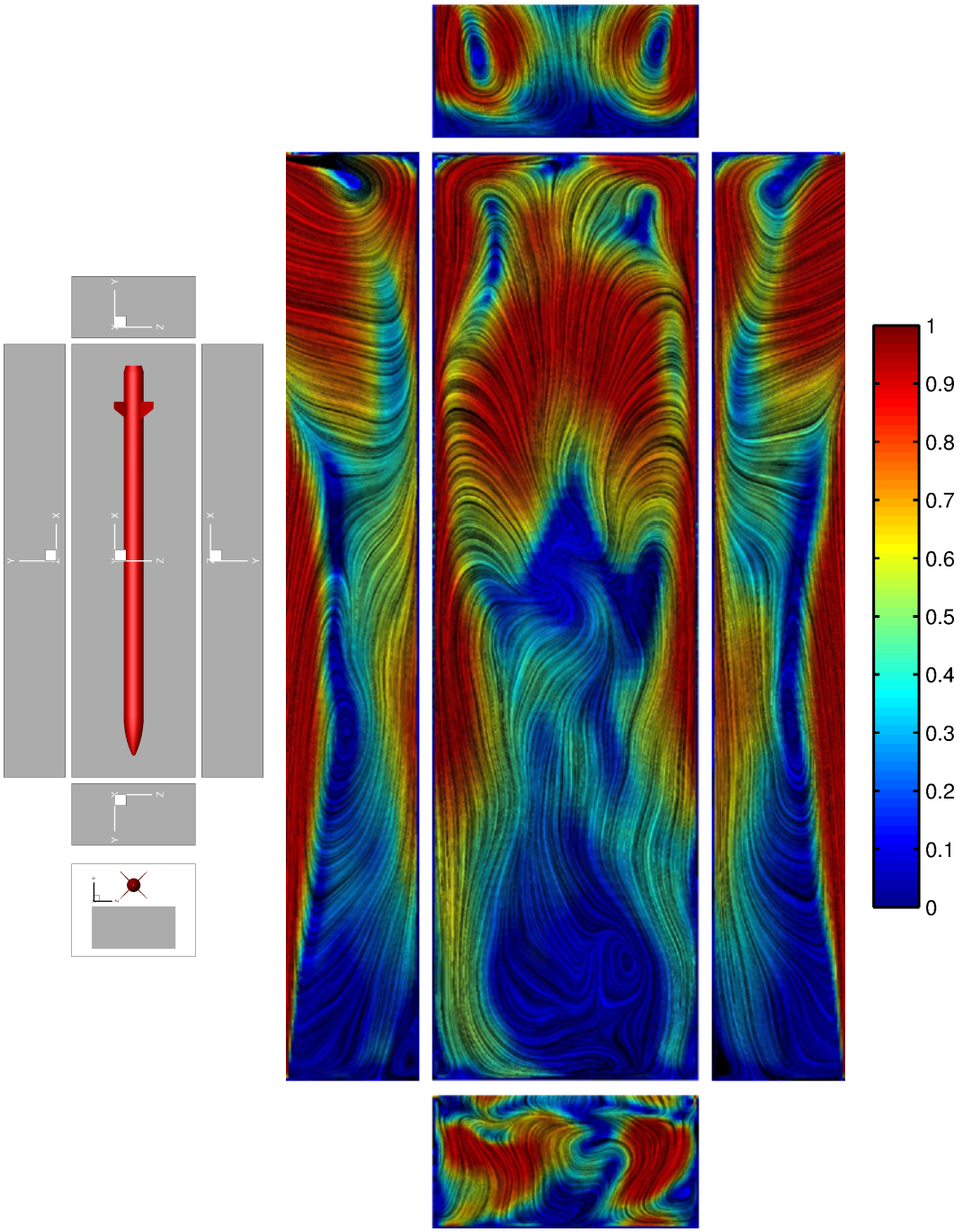

Figure 4.6: Time-averaged flow-field slices using LIC for the store outside cavity. Planes are located close to each wall of the cavity. Contours indicate velocity magnitude ranging from 0 (blue) to 1 (red).

4.3 Instantaneous Flow-Field

Peak-to-peak pitch and yaw flow angles, for the clean L/D=7 cavity and the store at different positions relative to the cavity, are shown in Figures 4.7 and 4.8. The peak-to-peak plots showed a clear reduction in the spillage of the flow over the sides of the cavity, when the store was at carriage position. At this position, there was little variation of the flow in pitch and yaw compared to the other positions of the store, where finer structures were seen in the contours. When at the shear layer, some interaction of the flow with the fins of the store was seen, especially for the fins that were inside the cavity. This suggests that if the store were released from the cavity at this point, its trajectory could be influenced by the cavity flow. As expected, when the store was outside the cavity, there was little to no interaction of the flow from the cavity with the store suggesting that once the store has cleared the shear layer, its trajectory may not be influenced by the cavity anymore.

In order to visualise structures, iso-surfaces of Q-Criterion are presented in Figure 4.9 that further evidenced the coherency of the shear layer when the store was at carriage position, due to the lack of structures at the shear layer. At carriage position, structures were only seen towards the rear end of the cavity where there was interaction with the store. When the store was positioned at the shear layer, some structures existed along the shear layer while the majority were confined to the rear end and just above the aft wall where the flow interacts with the rear end of the store. Outside the cavity, the store did not have much influence on the aft cavity region, creating less structural content in comparison to the other store positions but with more vortex shedding from the base of the store.

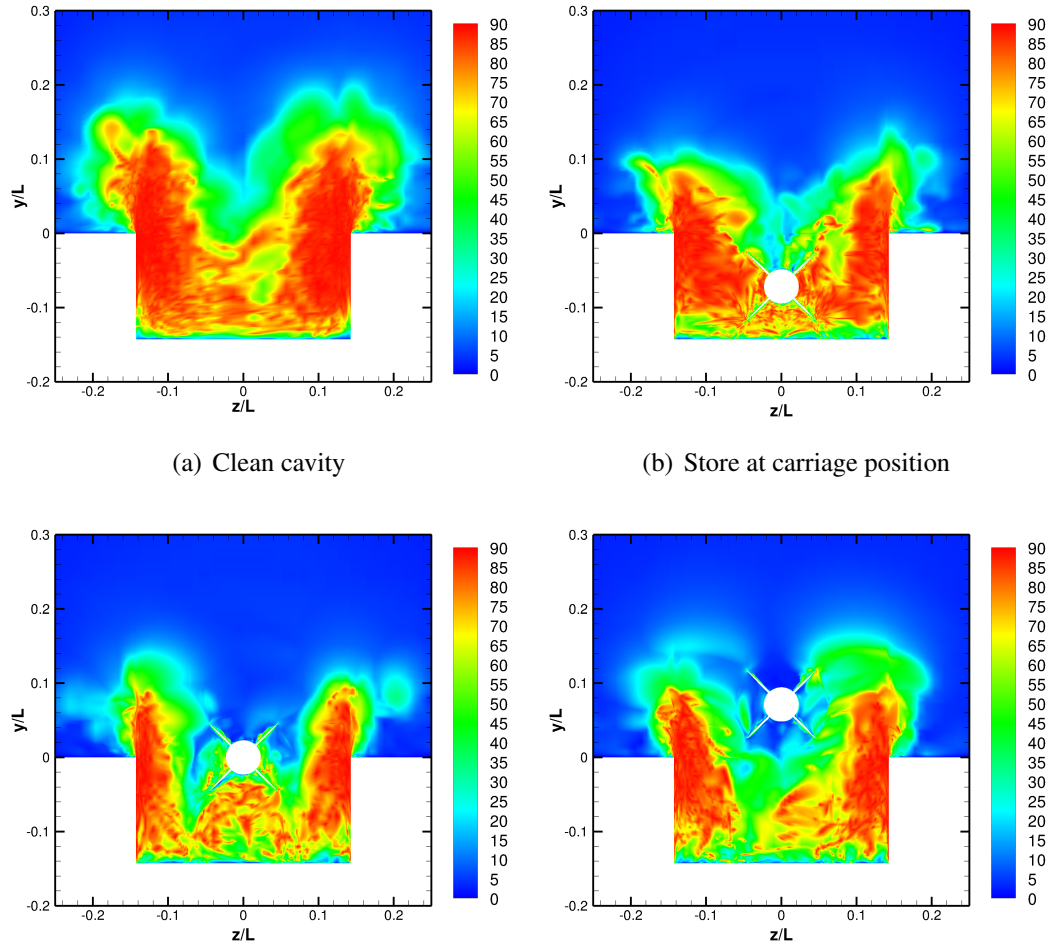

(a) Clean cavity

(b) Store at carriage position

(c) Store at shear layer

(d) Store outside cavity

Figure 4.7: Contours of peak-to-peak pitch flow angles, presented in degrees, for the clean L/D=7 cavity (a) and the store at different positions relative to the cavity (b-d). Planes are located at the rear end ($x/L = 0.85$) of the cavity, slicing through the fins.

4.4 Acoustic Propagation

Numerical schlieren contours are presented in Figure 4.10 to highlight the differences in acoustic wave propagation between the clean cavity and the cavity and store configurations. As discussed earlier, the shear layer appeared largely coherent when the store was at carriage position and the acoustic waves did not travel as far out as the clean cavity showing that the store pacified the cavity flow-field to some extent.

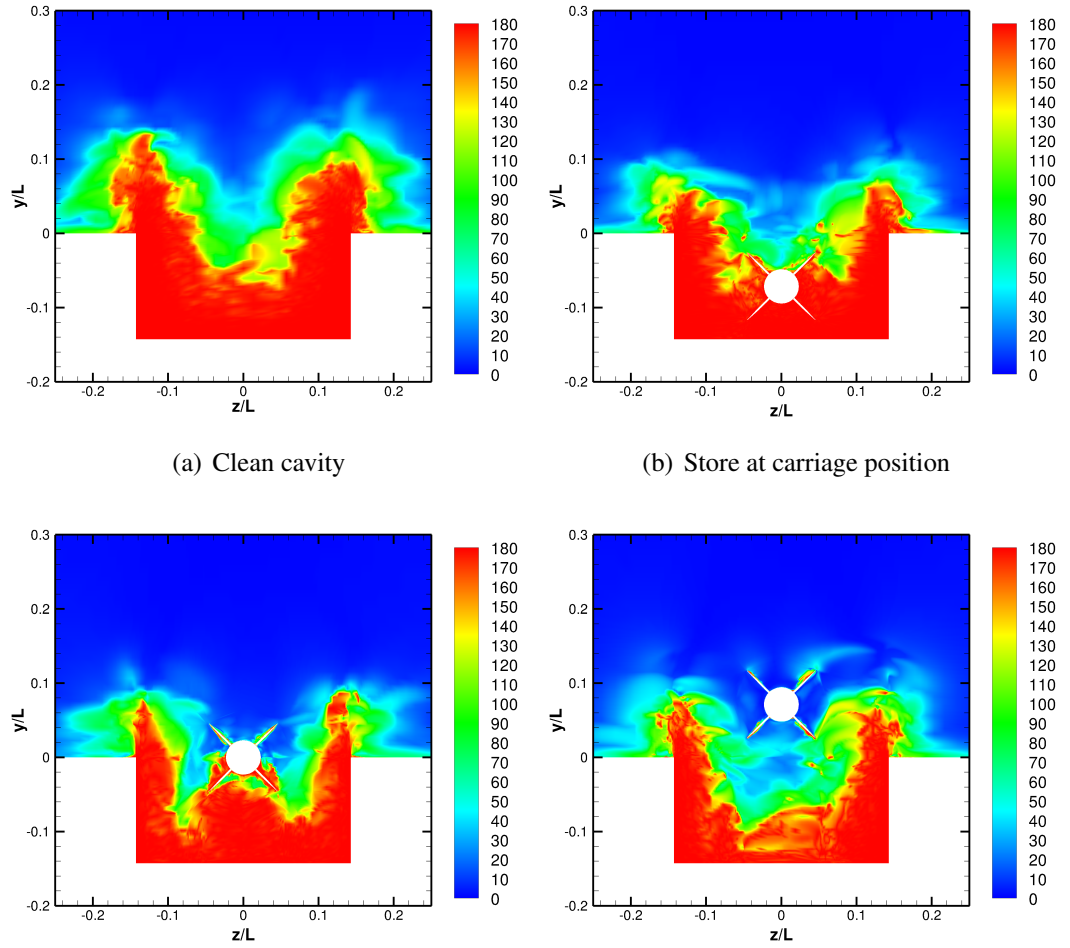

(a) Clean cavity

(b) Store at carriage position

(c) Store at shear layer

(d) Store outside cavity

Figure 4.8: Contours of peak-to-peak yaw flow angles, presented in degrees, for the clean L/D=7 cavity (a) and the store at different positions relative to the cavity (b-d). Planes are located at the rear end ($x/L = 0.85$) of the cavity, slicing through the fins.

When the store was positioned at the shear layer, strong acoustic waves interacted with the rear end of the store and some waves were seen to travel upstream. The centreline slices were fairly similar for the clean cavity and when the store was outside, showing strong fluctuations inside and outside the cavity with acoustic waves that travelled upstream and away from the cavity.

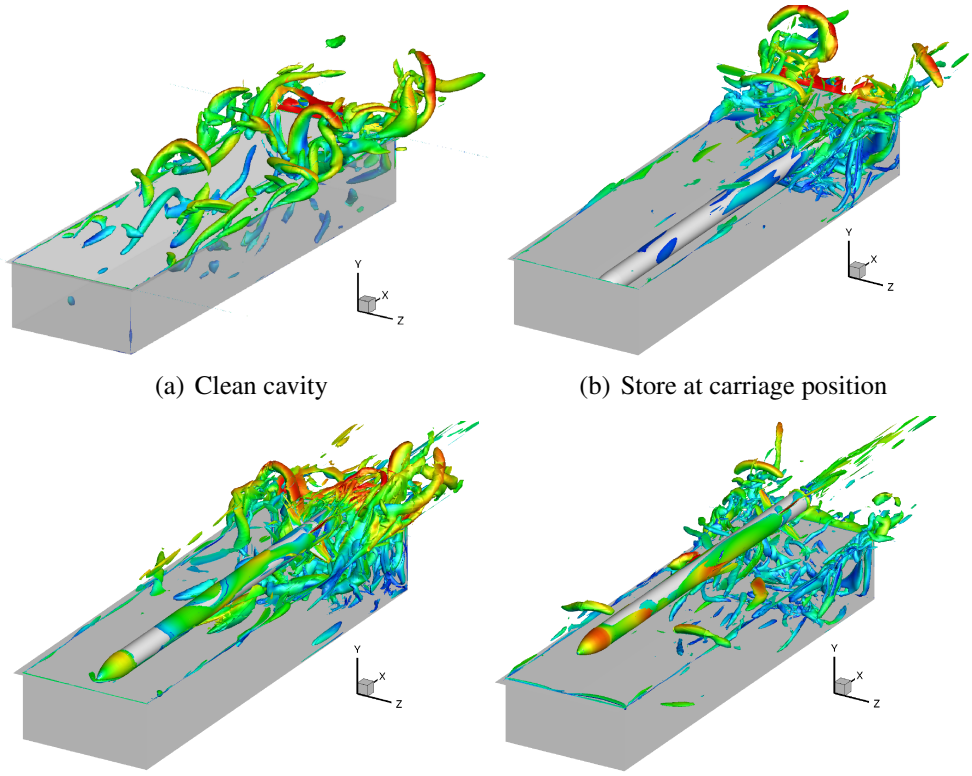

(a) Clean cavity (b) Store at carriage position

(c) Store at shear layer (d) Store outside cavity

Figure 4.9: Instantaneous iso-surfaces of Q-Criterion for the clean L/D=7 cavity and the store at different positions relative to the cavity. Iso-surfaces at Q=2000 are shown and coloured with Mach number ranging between 0.0 (blue) and 1.0 (red).

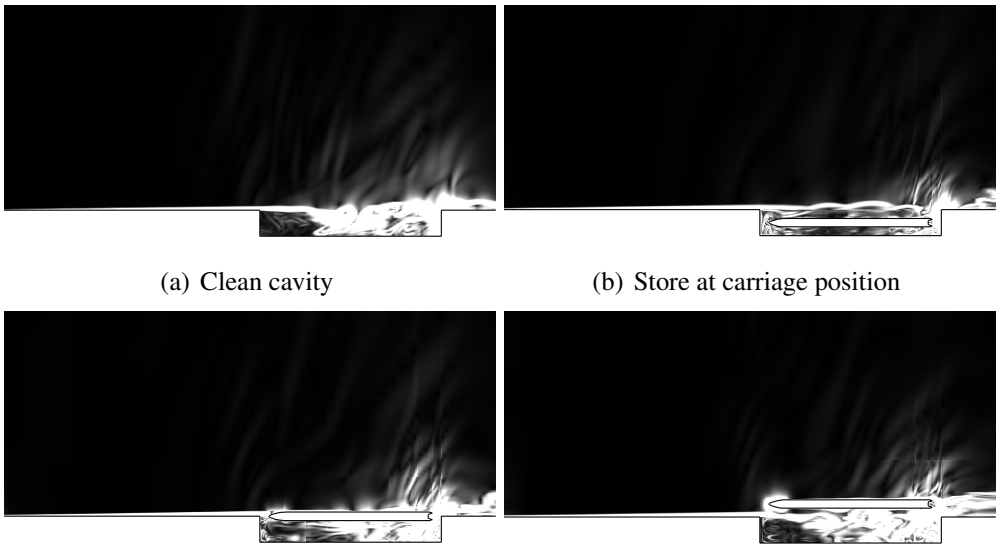

(a) Clean cavity (b) Store at carriage position

(c) Store at shear layer (d) Store outside cavity

Figure 4.10: Instantaneous contours of numerical schlieren for the clean L/D=7 cavity and the store at different positions relative to the cavity. Planes are located at the centreline ($z/L = 0.0$) of the cavity.

Chapter 5

Aeroelastic Analysis of Store Fins

Requirements for safe carriage and release of stores from a cavity include knowledge of time-accurate loads acting on the store and its control surfaces. During carriage the fins of a store may undergo deformations if the loads are large enough and forcing occurs at frequencies near their normal modes. With this in mind, aeroelastic computations of store fins were undertaken for a store at different positions relative to a cavity, to study the effects of unsteady loads on the structure of the fins. Two boundary conditions for the fin root were investigated to highlight any difference in loading. Simulations employed the DES S-A turbulence model [49] and were carried out at a Mach number of 0.85 and Re_L of 6.5 million. Comparisons are made between rigid and deforming fins for fin and store loads and tip displacements. Finally, acoustic spectra and sound pressure levels were compared.

5.1 Model Geometry and Mesh Generation

The computational models, meshes and flow solutions from rigid fin computations, discussed in the previous Chapter, were used to initiate aeroelastic computations for the store fins. The fully developed rigid fin computations, for a store at three positions relative to a cavity, was used together with input files to continue the flow simulation but allowing for the fins to deform. Forces computed from integrated pressure on fin surfaces were used to compute their deformation, and to avoid a sudden change in volume from the application of the force, a large damping coefficient of 0.7 was used to initiate the computations.

This was reduced to 0.5 after 5000 unsteady time steps and then to 0.3 after another 5000 unsteady time steps, where it was fixed at this value to allow for larger deformations of the fins while maintaining good cell quality in blocks close to the fins. Aeroelastic fin computations were performed for the store at carriage position, at the shear layer and outside the cavity, continuing from the developed flow solutions discussed in the previous Chapter.

In addition to the computational models discussed in the previous Chapter, modifications were made to allow for the free motion of the fin root, that was previously fixed into the body of the store. Figure 5.1 shows the modifications made to the root of the fins by introducing a 5*mm* gap, which was slightly larger than the typical gap found in realistic stores but was the minimum required to maintain good cell quality during deformations. In a similar manner, rigid fin computations were first performed, for the store at three positions, until the flow was developed, following which aeroelastic fin computations were initiated from the developed flow solutions.

The following must be noted: both fin configurations, for aeroelastic computations, used the same structural model that was provided by MBDA[88], the same fin structural mode shapes and frequencies, obtained from NASTRAN, were used for aeroelastic computations for both fin configurations, for the fixed fin root configuration, the first 5% of the fin height, measured from the root, was kept rigid as the fin root was fixed into the body of the store and deformations in this region would give rise to negative volumes, while for the free fin root configuration the entire fin was allowed to move and deform freely.

Computed loads are presented in the NED axis system, defined in Chapter 2, which is the customary axis system for the presentation of store loads and trajectories. The loads computed on the fins are presented in the fin local axis system shown for all four fins in Figures 5.2(b-e). The black circles indicate the location of probes placed in the flow domain to obtain unsteady pressure data and correspond to the same locations used in Chapter 3 for spectral analysis of clean cavities.

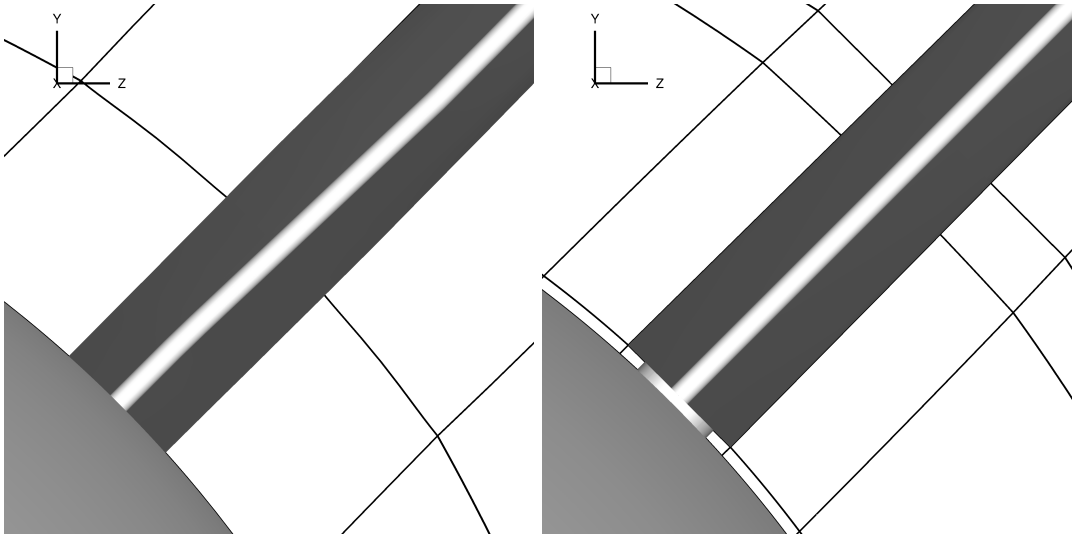

(a) Fixed fin root (b) Free fin root

Figure 5.1: Store model with fins fixed into the body of the store (a) and with a gap between the root of the fin and the body of the store (b). A slice showing the edges of the blocks around a fin, for both configurations, is shown.

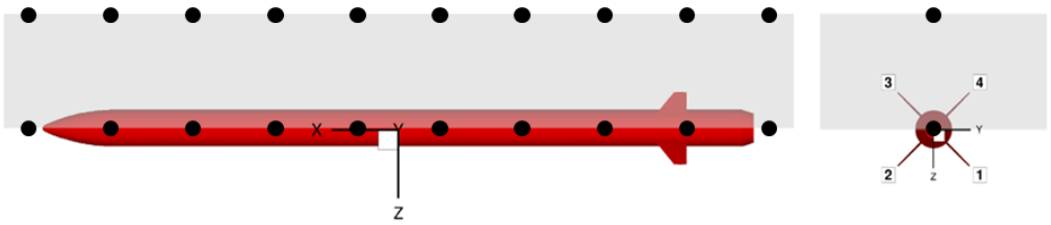

(a) Store axis system and fin numbering

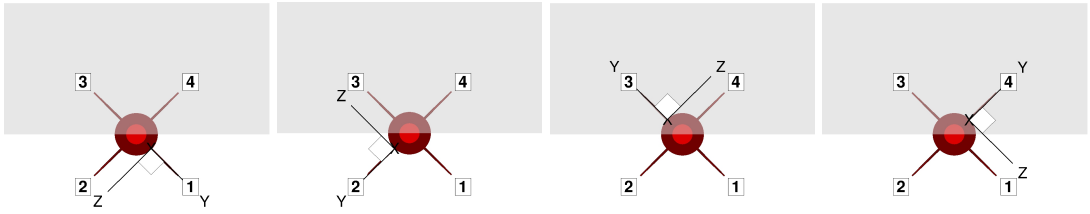

(b) Fin 1 axis (c) Fin 2 axis (d) Fin 3 axis (e) Fin 4 axis

Figure 5.2: Store (a) and fin (b-e) axis system for the presentation of loads. The grey area represent the cavity region and black circles represent locations of probes used in the flow solution. With respect to the fin axes, fin-normal force is defined as acting along the Z- axis and hinge moment is defined as acting about the Y-axis.

5.2 Time-Averaged Loads

Time-averaged store and fin forces and moments, for the store at three positions relative to a cavity, are shown in Figures 5.3 to 5.5. Computations where the fin root was fixed into the body of the store were referred to as 'Fixed Root', and those where the fin root was modified through the introduction of a gap were referred to as 'Free Root'. For both cases rigid and deforming fins were compared.

When the store was at carriage position, the overall loads acting on the store were small as seen in Figure 5.3. No differences were seen between rigid and deforming, and the fixed and free root configurations. Average fin-normal force and hinge moment coefficients were also found to be very small. This was expected as the store at carriage was shielded from most of the high velocity flow just outside the cavity. While the loads acting on the fins were not large enough to cause sudden failure, it could affect the fatigue life of the fins during carriage.

The store positioned at the shear layer experienced slightly higher loads in comparison to the store at carriage position. The loads contribution from the fins was seen to be a bit more significant however, no large differences were seen between rigid and deforming fins for either configuration. Interestingly, the loads acting on the fins show large fluctuations about the mean, despite the overall loads being small. This is an important position for a store as they are usually released from the cavity, close to the opening where large pressure fluctuations exist. At any instance in time the fin loads can lie anywhere within the region bounded by the peak values, and hence the trajectory of a released store could show variations in attitude due to these fluctuations if released at different time instances.

Outside the cavity, the flow-field around the store was almost steady with the axial force dominating [88]. Loads on the store fins were small and equal and opposite, and peak-to-peak values were low suggesting little to no influence of the cavity flow-field. Overall, no major differences were found between rigid and aeroelastic fins in terms of loads or due to the fin root gap.

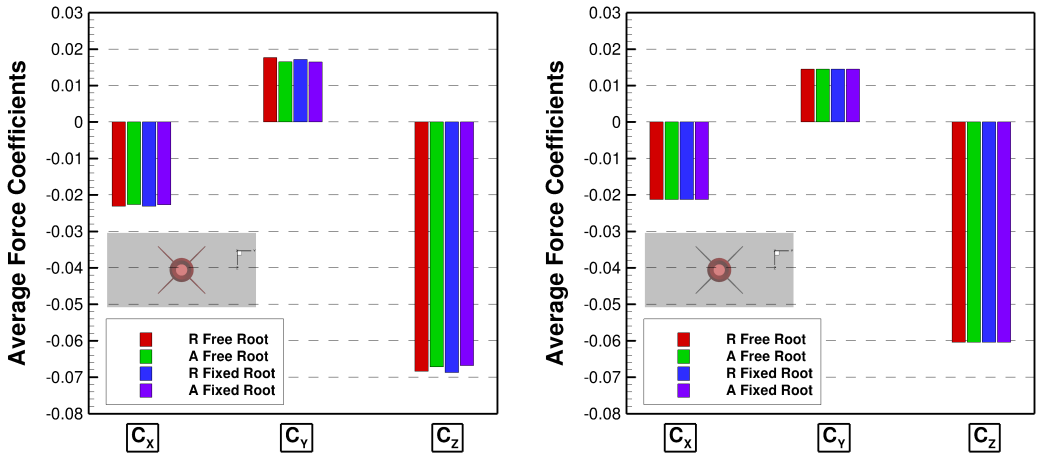

(a) Store with fins (b) Store body

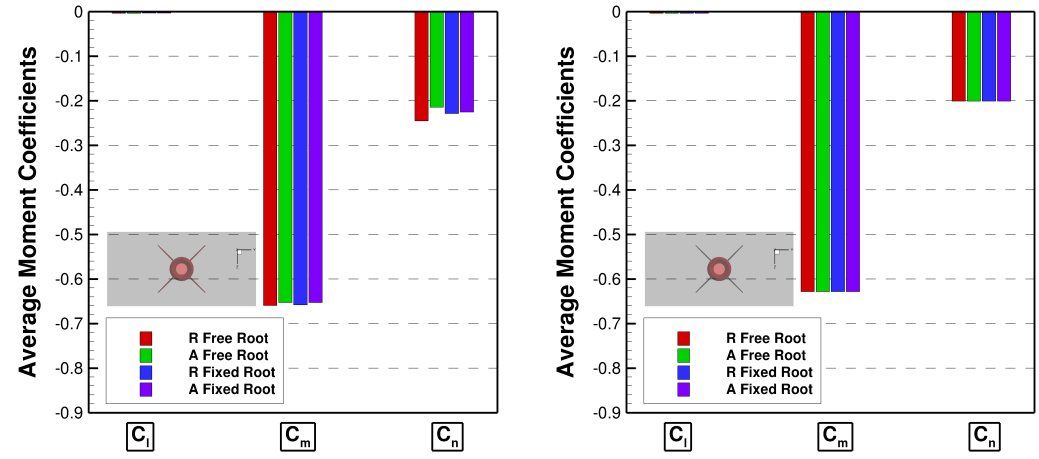

(c) Store with fins (d) Store body

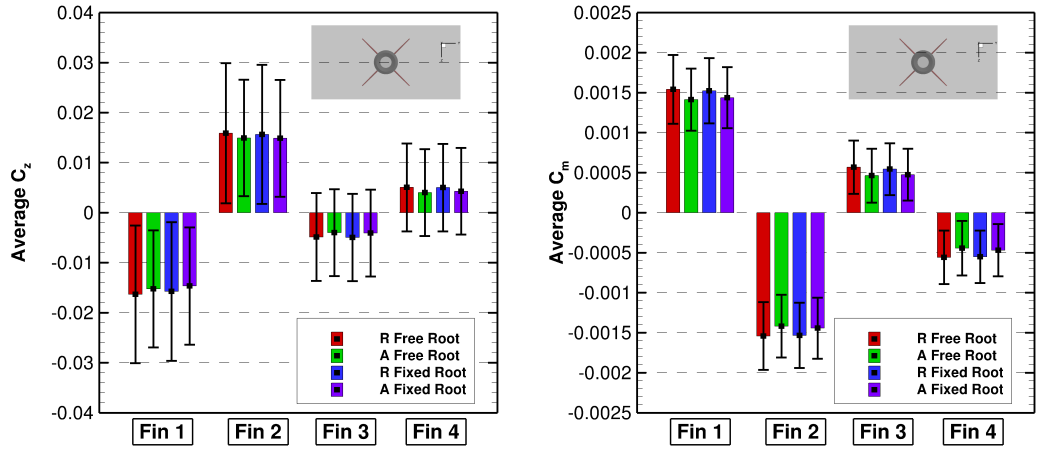

(e) Fin-normal force coefficients (f) Fin hinge moment coefficients

Figure 5.3: Comparison of time-averaged integrated force and moment coefficients acting on the store and fins (a,c) and store body (b,d) for a store at carriage position. Fin-normal force (e) and hinge moment (f) coefficients are also compared with bars showing peak-to-peak values. R: Rigid fin computation, A: Aeroelastic fin computation.

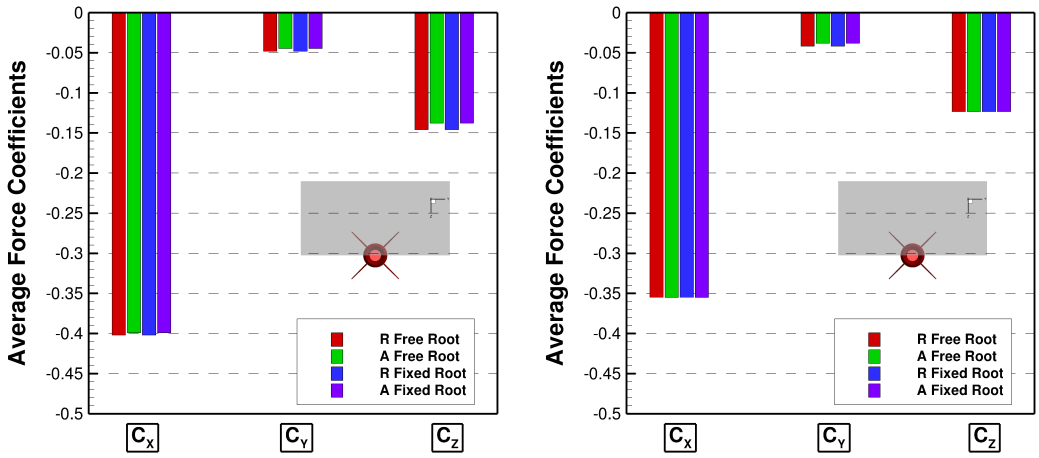

(a) Store with fins (b) Store body

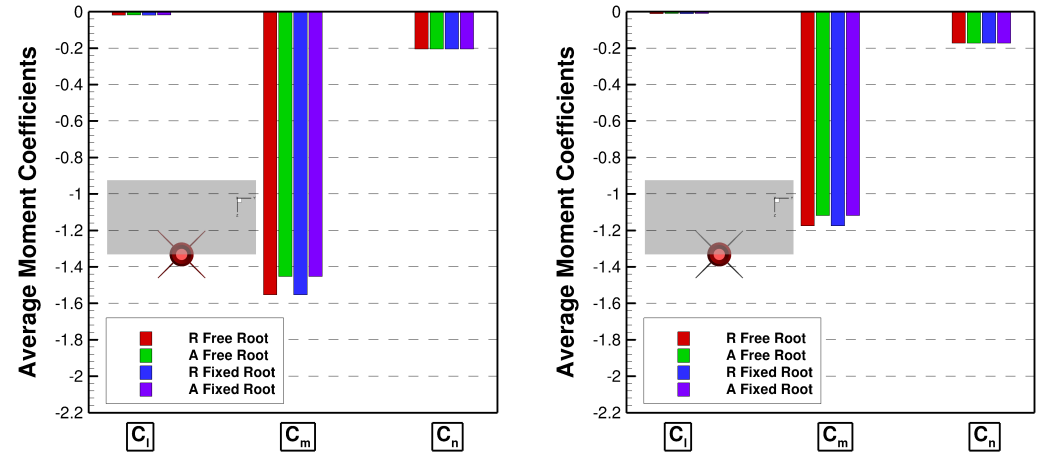

(c) Store with fins (d) Store body

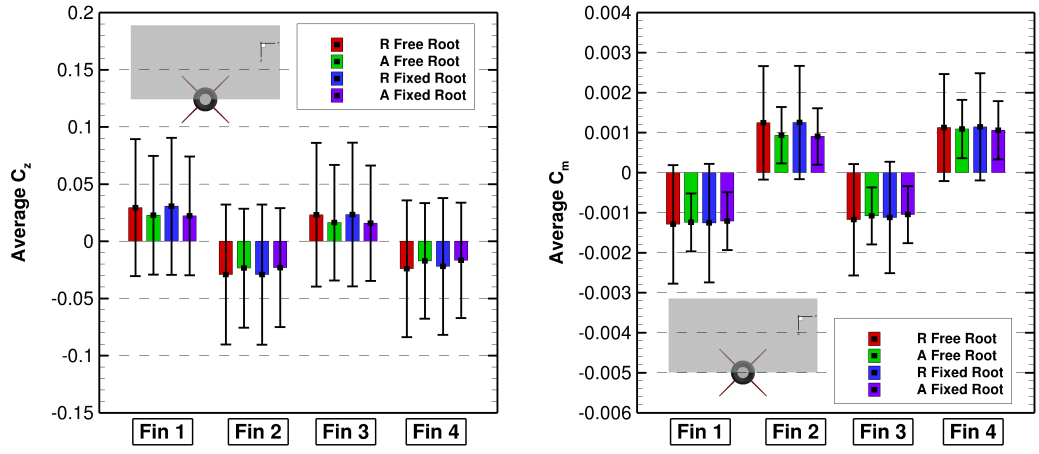

(e) Fin-normal force coefficients (f) Fin hinge moment coefficients

Figure 5.4: Comparison of time-averaged integrated force and moment coefficients acting on the store and fins (a,c) and store body (b,d) for a store at shear layer. Fin-normal force (e) and hinge moment (f) coefficients are also compared with bars showing peak-to-peak values. R: Rigid fin computation, A: Aeroelastic fin computation.

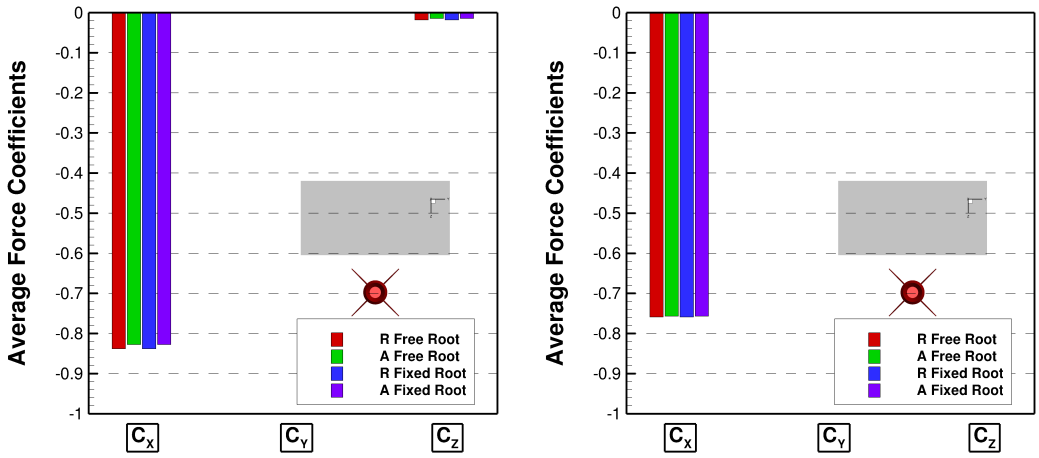

(a) Store with fins (b) Store body

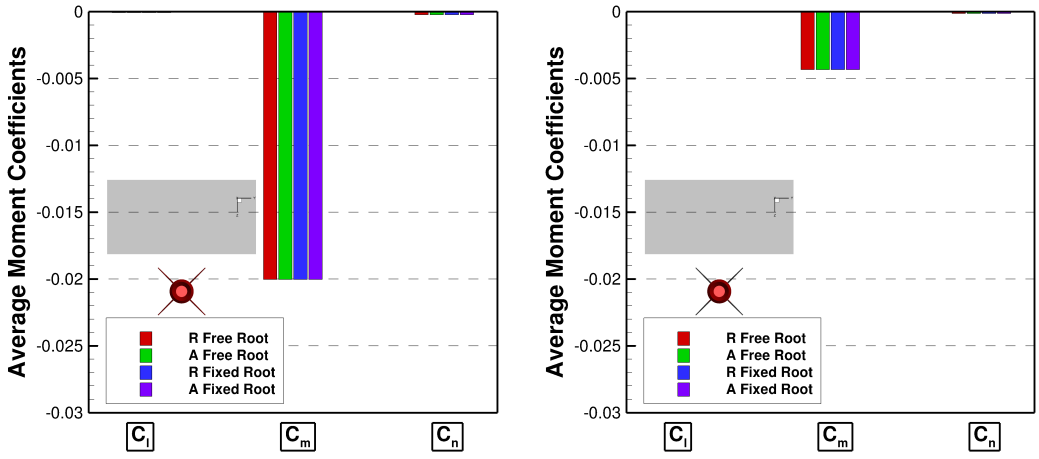

(c) Store with fins (d) Store body

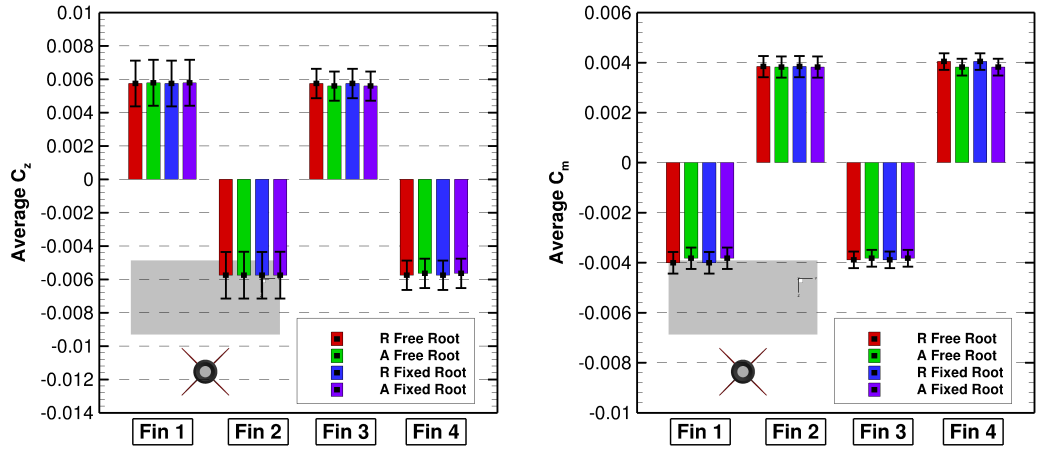

(e) Fin-normal force coefficients (f) Fin hinge moment coefficients

Figure 5.5: Comparison of time-averaged integrated force and moment coefficients acting on the store and fins (a,c) and store body (b,d) for a store outside cavity. Fin-normal force (e) and hinge moment (f) coefficients are also compared with bars showing peak-to-peak values. R: Rigid fin computation, A: Aeroelastic fin computation.

5.3 Fin Tip Displacements

A comparison of fin tip displacements, presented in Figure 5.6, was carried out in order to highlight the correlation between the fin structural modes and Rossiter modes of a cavity. The results presented hereafter are for fixed fin root configuration as the set of results for this configuration were run longer and hence longer time signals were available. Displacements of fin tip leading edges were tracked over time and their FFT were computed, for the store at carriage and at the shear layer. When the store was at carriage position, Fin 1 and Fin 2 were closer to the shear layer and slightly more active than Fin 3 and Fin 4, inferred from their tip displacements. The FFT showed low amplitude peaks close to the fin structural modes. For the signal length shown in Figure 5.6, the fins exhibited a buzzing characteristic with maximum tip displacements that were close to 0.3mm, comparable to the 0.1mm maximum deflections obtained by Arunajatesan *et al.* [11]. These displacements, although small may reduce the life of the store fins due to fatigue. It must be noted that for the fin structural model supplied by MBDA[88], the first three fin structural modes were very close to Rossiter modes of the cavity.

At the shear layer, the store fins were more active and the FFT showed peaks around the first and second fin structural modes and the fourth and fifth Rossiter modes. These modes fell in the frequency range of 125Hz and 175Hz. Fin 1 and Fin 2 that are just outside the cavity, and more in contact with the high dynamic head flow, had larger amplitudes than the fins inside the cavity. These plots highlight the frequencies excited by the store fins and the need to design them such that the structural modes are not coincident with the cavity modes.

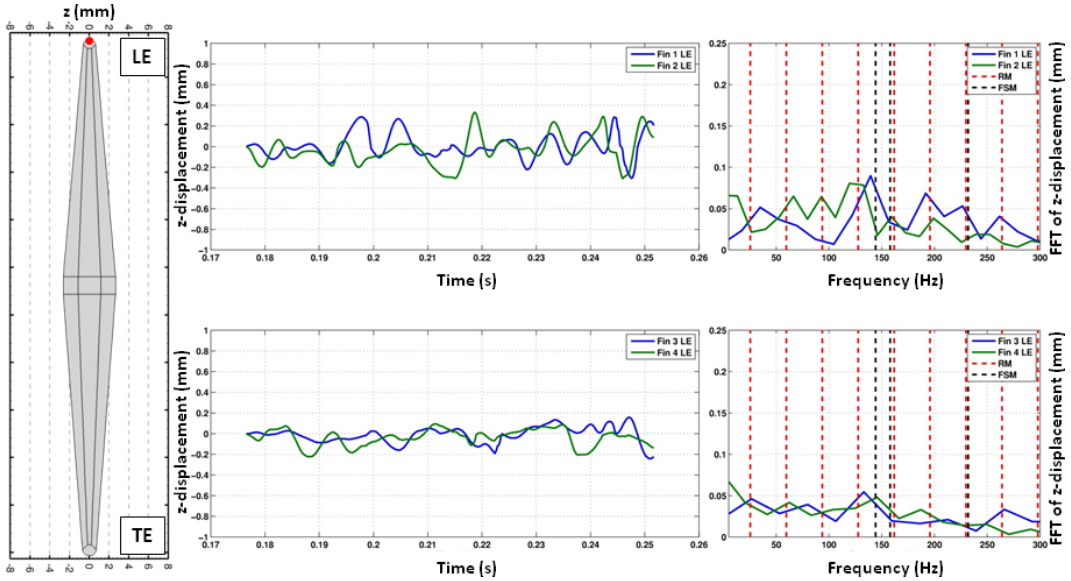

(a) Store at carriage position

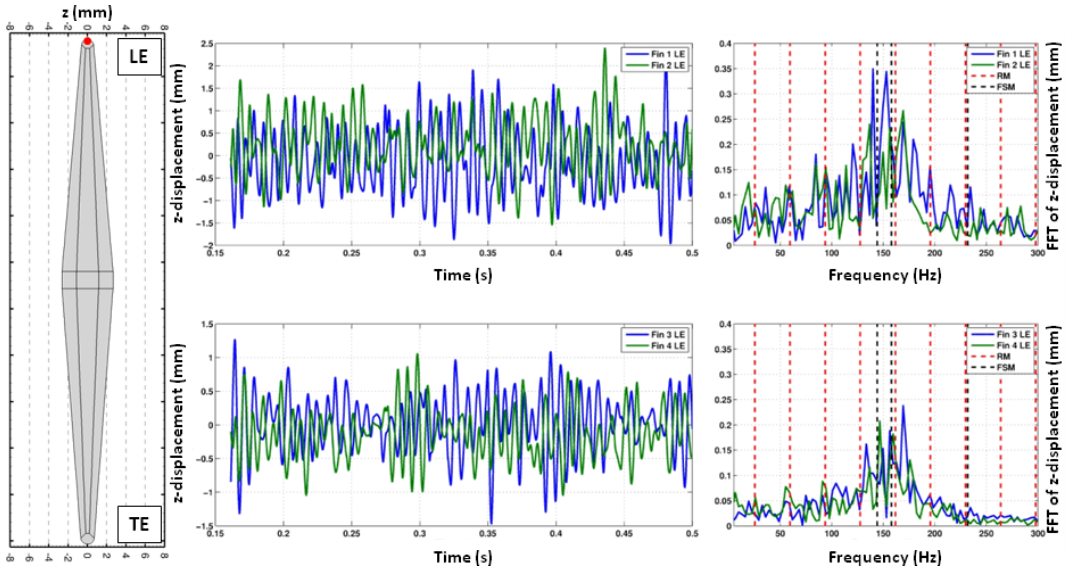

(b) Store at shear layer

Figure 5.6: Fin tip displacements in time and frequency domains for the store at carriage position (a) and at the shear layer (b) for the store model with fixed fin roots. FFT of fin tip displacements are shown on the right hand side, and compared against Rossiter mode frequencies (RM) and fin structural mode frequencies (FSM) shown in red and black dashed lines respectively. The red circle shows the point from where the displacements were tracked.

5.4 Spectral Analyses

OASPLs along the centreline of the ceiling of the cavity for a store at different positions are shown in Figures 5.7 to 5.9. With the store at carriage position, the OASPL along the ceiling was reduced by a maximum of 5dB between $x/L = 0.3$ to $x/L = 0.95$. Similar reductions were found along the shear layer but with a maximum reduction of 3dB between $x/L = 0.15$ to $x/L = 0.9$. The BISPL plots centred around the first four Rossiter mode frequencies, along the cavity ceiling, also showed a reduction of the SPL mainly in modes three and four.

When the store was at the shear layer, its influence on the flow close to the cavity ceiling was reduced showing maximum differences of 3dB. To the port and starboard of the centreline of the cavity, the presence of the store reduced the OASPL levels by a maximum of 3dB. BISPL plots showed similar shapes to the clean cavity with mode one and two having the largest maximum differences of 3dB.

Outside the cavity, the store did little to affect the OASPL along the ceiling and the shear layer and showed differences within 2dB of the clean cavity. BISPL plots, along the cavity ceiling, were almost unaffected suggesting that the store has little influence on the cavity flow-field. No significant differences in SPLs were found between the rigid and aeroelastic computations.

PSD plots are compared, in Figure 5.10, for the clean cavity and the store at different positions for rigid and aeroelastic computations. Plots were compared against the first five Rossiter mode frequencies and first three fin structural mode frequencies. The general trend in the spectra showed an increase in the SPL from the front wall to the aft wall and small reductions in higher frequency modes compared to those in the clean cavity. Large differences in SPL were found in Figure 5.10(b), when the store was at carriage position and directly affect the flow-field in the cavity. PSD plots for a store outside the cavity showed large similarities to the clean cavity, again suggesting the lack of influence of the store on the flow inside the cavity. The flow retained most of the dominant frequencies in the clean cavity.

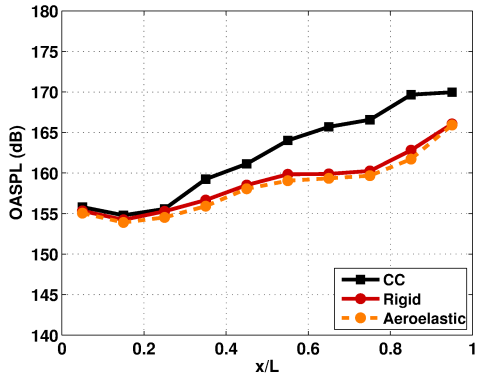

(a) OASPL, cavity ceiling

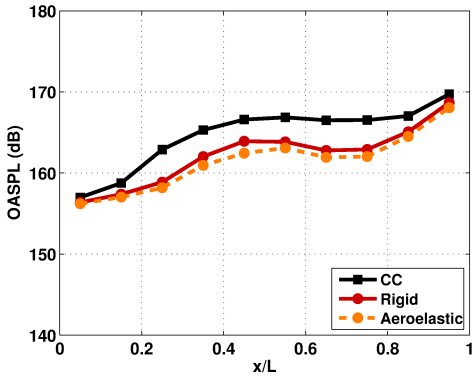

(b) OASPL, shear layer

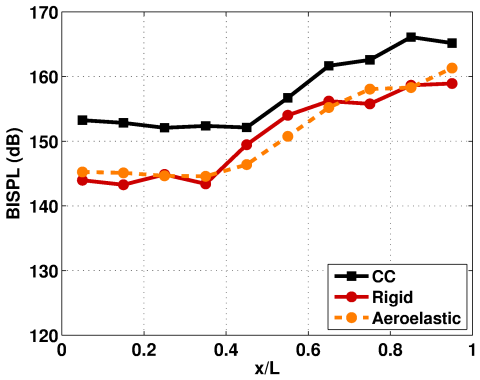

(c) Mode 1: $10 \leq f \leq 40$ Hz

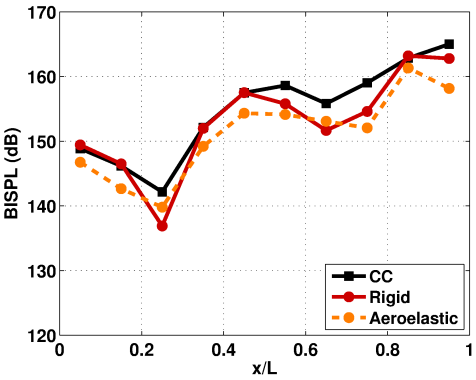

(d) Mode 2: $40 \leq f \leq 70$ Hz

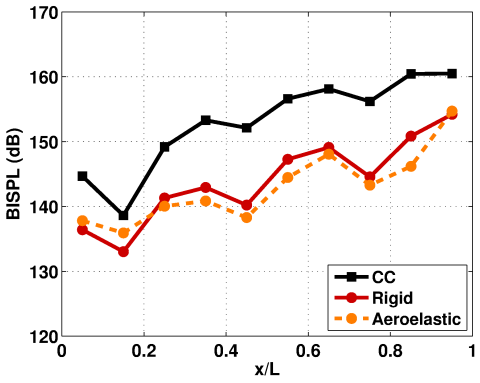

(e) Mode 3: $70 \leq f \leq 110$ Hz

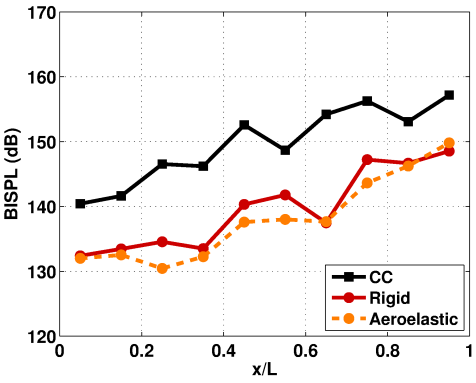

(f) Mode 4: $110 \leq f \leq 140$ Hz

Figure 5.7: OASPL along the centreline of the cavity ceiling (a) and shear layer (b) and BISPL (c-f) plots along the centreline of the cavity ceiling for the store at carriage position. Plots compare clean cavity (CC) results, with rigid and aeroelastic computations for the store model with fixed fin roots.

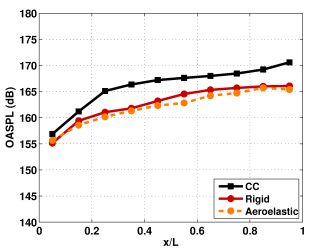

(a) OASPL, shear layer (port)

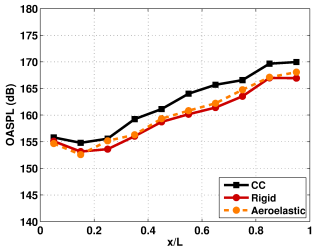

(b) OASPL, cavity ceiling

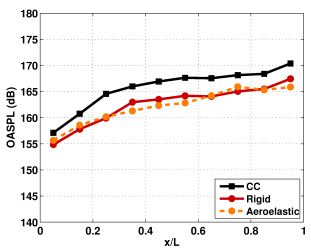

(c) OASPL, shear layer (starboard)

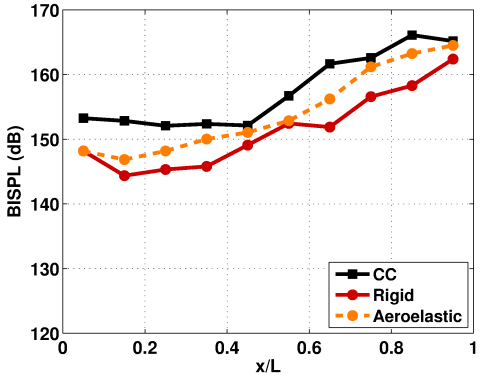

(d) Mode 1: $10 \leq f \leq 40$ Hz

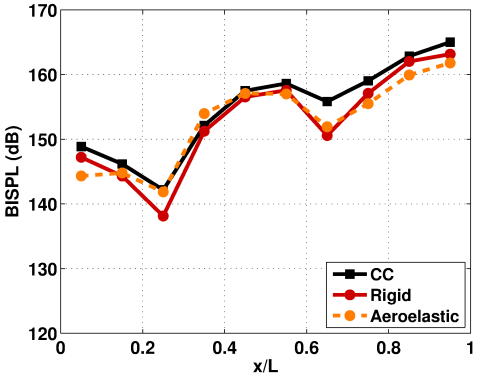

(e) Mode 2: $40 \leq f \leq 70$ Hz

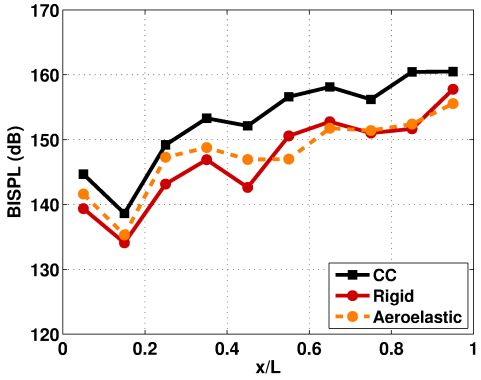

(f) Mode 3: $70 \leq f \leq 110$ Hz

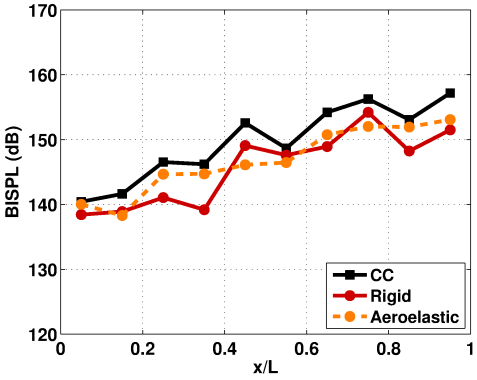

(g) Mode 4: $110 \leq f \leq 140$ Hz

Figure 5.8: OASPL along the shear layer of the cavity (a,c) and along the centreline of the cavity ceiling (b), and BISPL (d-g) plots along the centreline of the cavity ceiling for the store at shear layer. Plots compare clean cavity (CC) results, with rigid and aeroelastic computations for the store model with fixed fin roots.

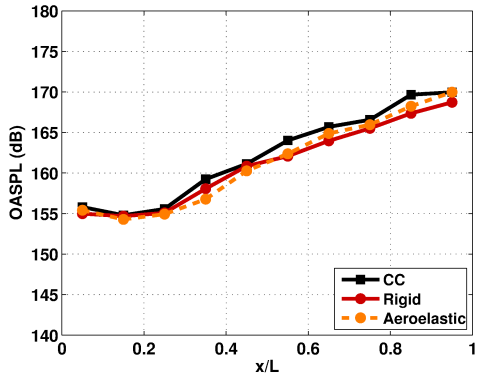

(a) OASPL, cavity ceiling

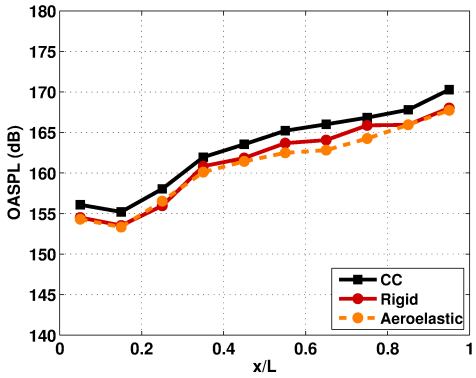

(b) OASPL, shear layer

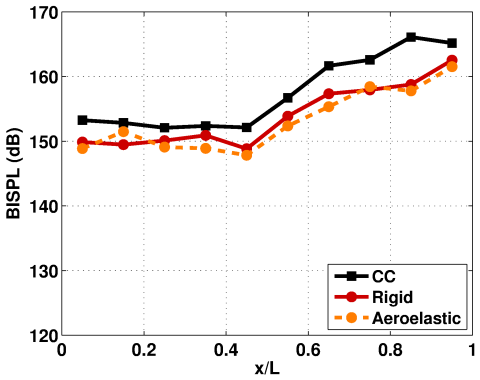

(c) Mode 1: $10 \leq f \leq 40$ Hz

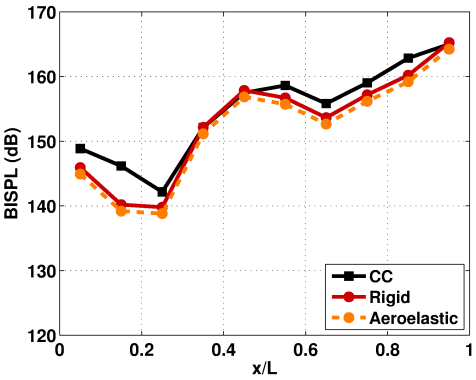

(d) Mode 2: $40 \leq f \leq 70$ Hz

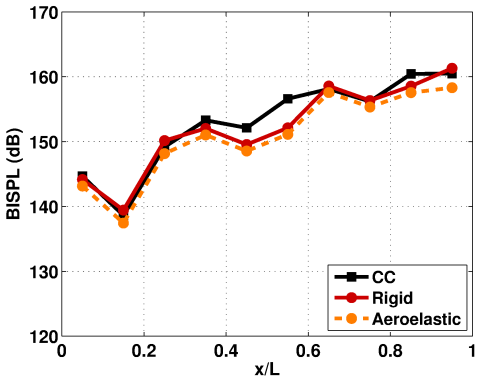

(e) Mode 3: $70 \leq f \leq 110$ Hz

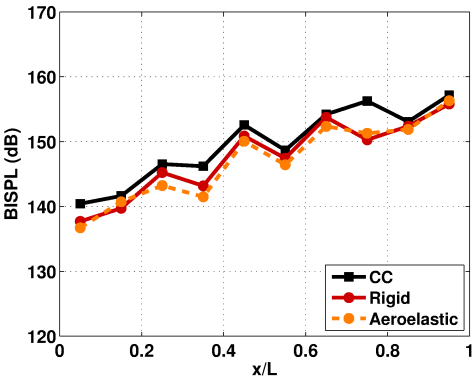

(f) Mode 4: $110 \leq f \leq 140$ Hz

Figure 5.9: OASPL along the centreline of the cavity ceiling (a) and shear layer (b) and BISPL (c-f) plots along the centreline of the cavity ceiling for the store outside. Plots compare clean cavity (CC) results, with rigid and aeroelastic computations for the store model with fixed fin roots.

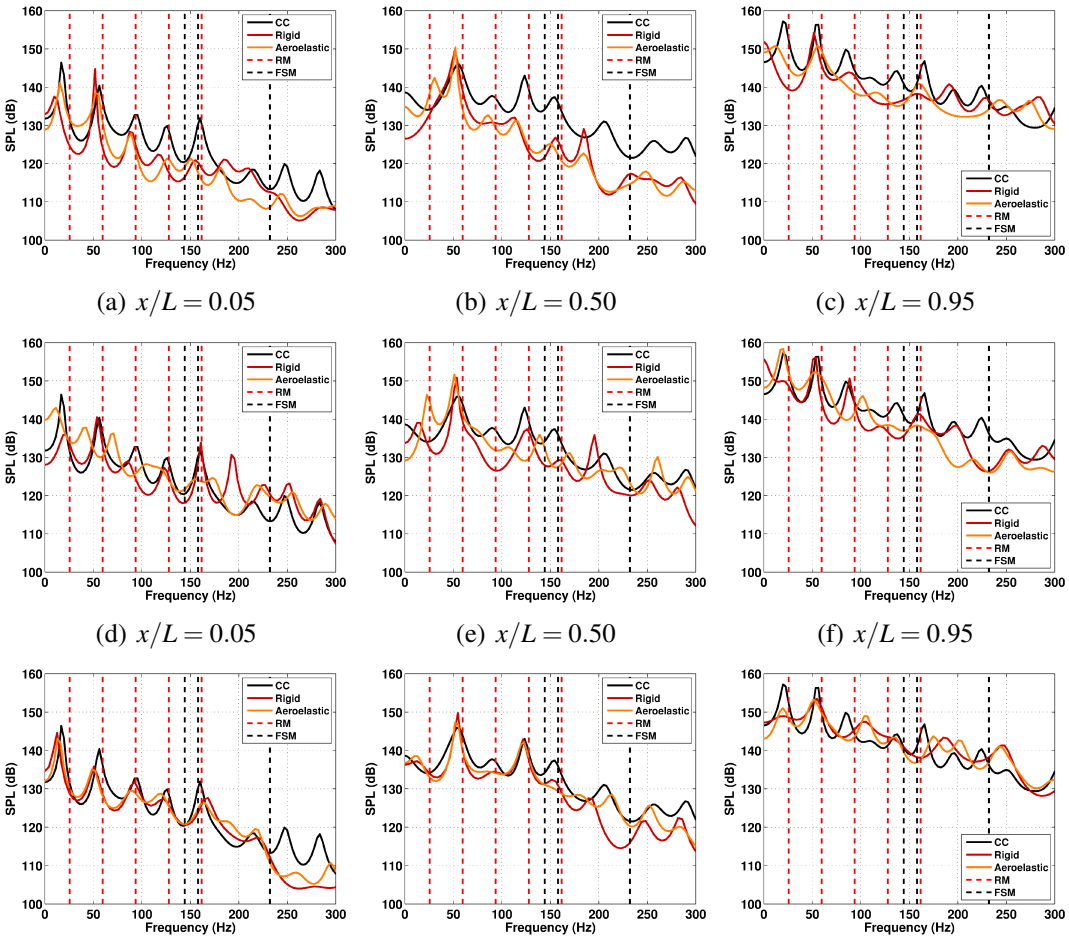

(a) $x/L = 0.05$ (b) $x/L = 0.50$ (c) $x/L = 0.95$

(d) $x/L = 0.05$ (e) $x/L = 0.50$ (f) $x/L = 0.95$

(g) $x/L = 0.05$ (h) $x/L = 0.50$ (i) $x/L = 0.95$

Figure 5.10: PSD plots for the clean cavity (CC), compared with results for rigid and aeroelastic computations of the store at carriage (a-c), at the shear layer (d-f) and outside (g-i), for the store model with fixed fin roots. Plots are for the front (left column), middle (middle column) and rear (right column) probes along the centreline on the cavity floor and presented in terms of SPL. PSD plots are compared against Rossiter mode frequencies (RM) and fin structural mode frequencies (FSM) shown in red and black dashed lines respectively.

Chapter 6

Evaluation of SAS for Transonic Cavity Flows

Validation of SAS results for the M219 cavity case as well as comparisons between SAS and DES results for the L/D=7 cavity are presented in this chapter. First, results of clean cavity computations, with doors-on and doors-off, using SAS are compared against DES and URANS to determine the suitability of SAS for transonic cavity flows. Simulations employed the SAS SST k-ω turbulence model [48] and were carried out at a Mach number of 0.85 and $Re_L$of 6.5 million. Spectra obtained from the computations are compared followed by instantaneous flow-fields to show similarities between the two methods. The final section presents a comparison of POD between DES and SAS.

6.1 Validation of SAS

DES data from Lawson [13] and experimental data from Nightingale [16], for the M219 cavity, were used for comparisons against SAS results. DES computations utilised the S-A turbulence model [46] while SAS and URANS computations utilised the SST k-ω turbulence model [48]. For all SAS and URANS computations, the free-stream Mach number was 0.85 and the Re_L was 6.5 million, which was close to the experimental Reynolds number, 6.78 million, of the M219 cavity . Computational details for the M219 grids are given in Table 6.2. The same grids used in Chapter 3 for the L/D=7 cavity were used for the SAS and URANS computations presented in this chapter.

Table 6.1: Computational details of the M219 cavity cases. DES data for the M219 cavity was taken from Lawson [13].

Computation Details	**Doors-Off**			**Doors-On**		
Method	DES	SAS	URANS	DES	SAS	URANS
Grid size (10^6 cells)	5.0	5.0	5.0	5.92	5.92	5.92
Cells in cavity (10^6)	1.02	1.02	1.02	1.20	1.20	1.20
Number of blocks	800	800	800	880	880	880
CFD time-step (10^{-6}s)	1.81	18.14	18.14	1.81	18.14	18.14
Number of time-steps	100,000	7500	5000	100,000	8000	5000
Signal duration (s)	0.18	0.13	0.09	0.18	0.14	0.09

$S-A$: Spalart Allmaras, SST: Shear Stress Transport.

6.2 Spectral Analyses

From past experience [13] with cavity flows, DES computations were run at a non-dimensional time-step of 0.001 for results presented in previous chapters, while SAS computations used a larger time-step of 0.01, similar to that used by Egorov *et al.* [55]. Figure 6.1 shows the comparison between DES and SAS computations run at the same non-dimensional time-step of 0.01 for the M219 cavity with doors-on. Evidently, the SAS model can be run at a larger time-step which was adopted for the rest of the work.

Doors-off

The PSD of pressure at the front, middle and rear of the M219 cavity with doors-off, is shown in Figure 6.2 for DES, SAS and URANS computations, compared against experimental data from Nightingale *et al.* [16] and modes obtained from the modified Rossiter equation [64]. The plots correspond to three pressure probe locations on the cavity floor at $x/L = 0.05$, $x/L = 0.50$ and $x/L = 0.90$ respectively that coincide with the locations of the Kulites^{TM} in the M219 cavity. Although the DES signal had a longer duration, in order to compare to the SAS and URANS, it was cut down to the shortest signal length. The same treatment was given to the experimental signal for the M219 cavity. DES and SAS predicted similar frequencies for the second and third Rossiter modes at the front and rear of the cavity and the second Rossiter mode in the middle of the cavity, but were overpredicted compared to the experiment. URANS, however, failed to predict the modes at the front and middle, and underpredicted the modes at the rear of the cavity. Predictions in past work[94] also reported to be very

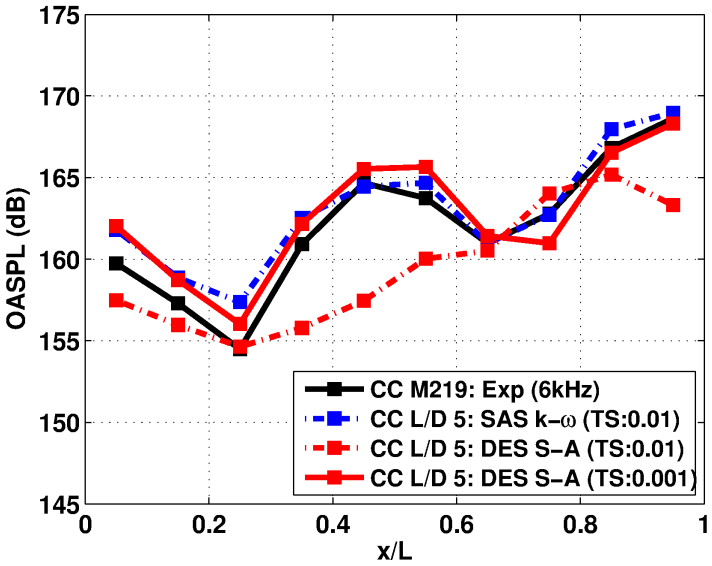

Figure 6.1: OASPL for the clean cavity with doors-on comparing DES and SAS results with experimental results from Nightingale *et al.* [16]. DES data for the M219 cavity were taken
from Lawson [13]. DES results are shown for two non-dimensional time-steps of 0.01 and 0.001, while SAS results are shown for a time-step of 0.01.

dependent on mesh density.

Similar PSD plots comparing DES, SAS and URANS for the L/D=7 cavity with doors-off, are presented in Figure 6.3. DES and SAS show similar predictions for the first and second Rossiter modes at the front and rear of the cavity and the second Rossiter mode in the middle of the cavity. URANS predicted several modes, that were not the dominant ones, along the front, middle and rear of the cavity.

The OASPL and BISPL for all three methods are presented in Figure 6.4 for the M219 cavity with doors-off. DES and SAS showed good comparison with the experimental data with an almost constant overprediction of 5dB along the length of the cavity while capturing the shape of the experimental data. URANS predicted a similar shape to the experimental data but underpredicted between 1 to 5dB along the length of the cavity. BISPL plots showed that the first three modes were predicted well by both DES and SAS. All three methods captured the overall shapes of the first four modes with the differences arising mainly in the magnitude being overpredicted by DES and SAS, or underpredicted by URANS. For all modes, DES and SAS had similar shapes and magnitudes and overpredicted the experimental data by about 4dB . URANS, on the other hand, predicted the shapes of the first three modes but failed with the higher frequency mode four.

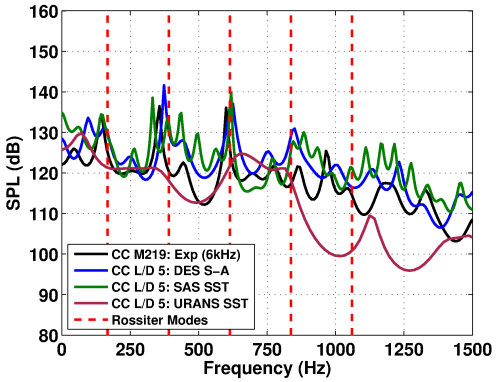

(a) $x/L = 0.05$

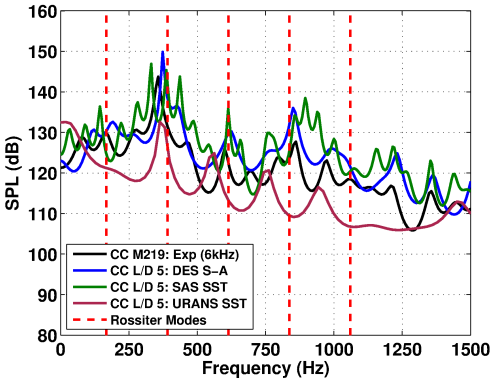

(b) $x/L = 0.50$

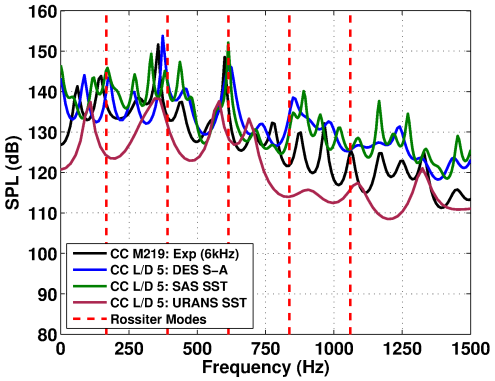

(c) $x/L = 0.95$

Figure 6.2: PSD plots for the front (a) middle (b) and rear (c) transducers along the cavity floor of the M219 cavity with doors-off, comparing results from DES, SAS and URANS methods to experimental data from Nightingale *et al.* [16]. DES data for the M219 cavity were taken from Lawson [13]. Plots are presented in terms of SPL. CC - Clean Cavity, S-A - Spalart Allmaras and SST - Shear Stress Transport.

Results for the L/D=7 cavity showed that DES, SAS and URANS had similar trends in terms of the shape of the curve and magnitude (Figure 6.5). Unlike the M219 cavity, URANS showed better comparisons with DES and SAS for the L/D=7 cavity. Not only did URANS capture the shapes of the modes quite well, it did so with similar magnitudes to that of DES and SAS, differing only from the middle to the rear of the cavity. DES and SAS showed very similar results to each other across the board.

Doors-on

The PSD of pressure at the front, middle and rear of the M219 cavity with doors-on, is shown in Figure 6.6 for DES, SAS and URANS computations, compared against experimental data from Nightingale *et al.* [16] and modes obtained from the modified Rossiter equation [64].

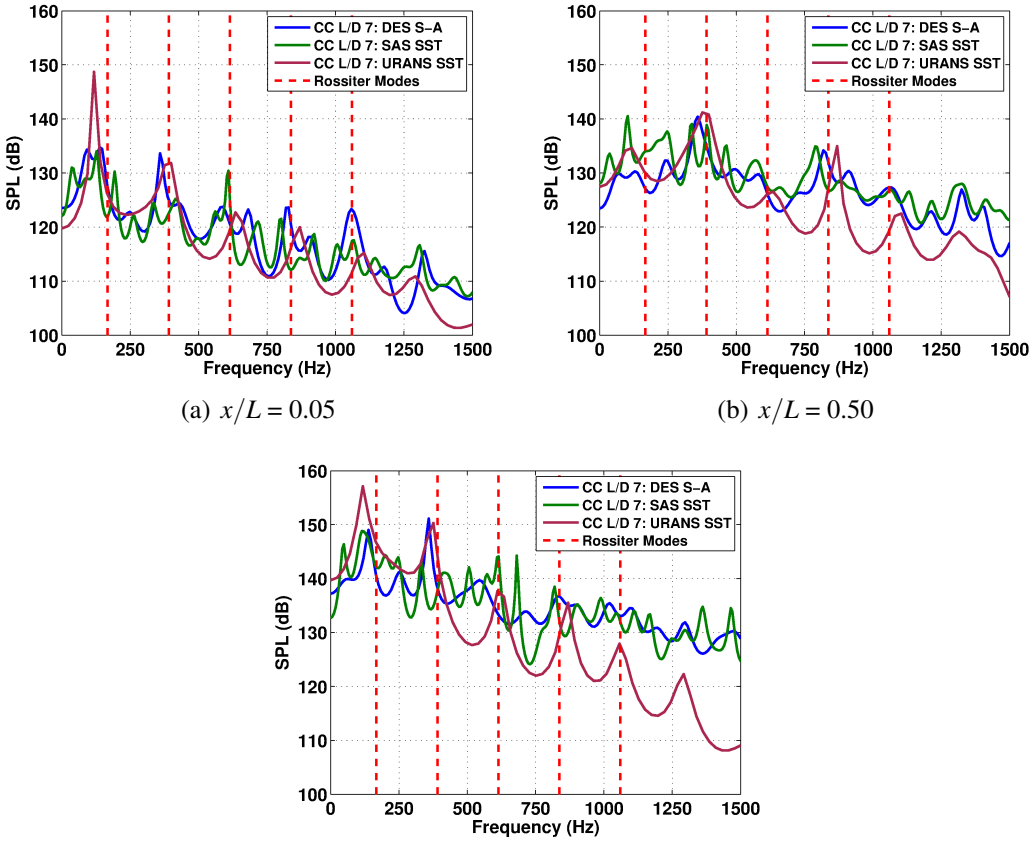

(a) $x/L = 0.05$

(b) $x/L = 0.50$

(c) $x/L = 0.95$

Figure 6.3: PSD plots for the front (a) middle (b) and rear (c), along the floor of the L/D=7 cavity with doors-off, comparing results from DES, SAS and URANS methods. Plots are presented in terms of SPL. CC - Clean Cavity, S-A - Spalart Allmaras and SST - Shear Stress Transport.

The addition of doors is known to make the second Rossiter mode dominant along the length of the cavity[13]. DES and SAS captured the dominant mode, along the length of the cavity, with SAS having slightly higher amplitude than DES. Much like in the previous configuration, URANS was not able to predict the dominant mode. DES and SAS showed similar results for the L/D=7 cavity with doors-on, as seen in Figure 6.6, however, a slight shift to the left of the second Rossiter mode was seen for SAS, possibly due to the signal length that was shorter for the doors-on case. In both cases, URANS gave a poor prediction compared to DES and SAS.

OASPL and BISPL plots for the M219 cavity with doors-on are presented in Figure 6.8 comparing all three methods to experimental data. Once again, DES and SAS show similar results for OASPL with an overprediction of around 5dB along the cavity length and reasonably capture the BISPLs around the first four Rossiter modes. In this case, URANS captures the 'W' shape of the OASPL curve, although with an overprediction.

URANS also roughly captured the shapes of BISPLs around the first four Rossiter modes, overpredicting mode one, and three and four for the first half of the cavity length. Although URANS showed fair comparison for the OASPL and BISPL, it must be noted that Figure 6.2 shows where it fails as a method for cavity flows.

The shapes of the curves were reasonably predicted given the relatively coarse mesh explored here. Based on experience with finer grids[91], the results are expected to improve with mesh refinement.

For the L/D=7 cavity, shown in Figure 6.9, URANS underpredicted the OASPL as a result of underpredicting the first, second and fourth modes in the BISPL plots. DES and SAS showed similar shapes and magnitudes for the OASPL as well as BISPL in modes one and two, with differences in modes three and four occurring around the middle of the cavity. A summary of the clock time for the different computations are given in Table 6.2, where the clock time shown in hours is based on the use of 32 cores for each computational case.

Table 6.2: Summary of clock time for DES and SAS computations.

Computation	**Method**	**Clock Time (hr)**
M219 Cavity, Doors-Off	DES S-A	3909
	SAS SST k-ω	312
M219 Cavity, Doors-On	DES S-A	4560
	SAS SST k-ω	364
L/D=7 Cavity, Doors-Off	DES S-A	4100
	SAS SST k-ω	400
L/D=7 Cavity, Doors-On	DES S-A	4850
	SAS SST k-ω	470

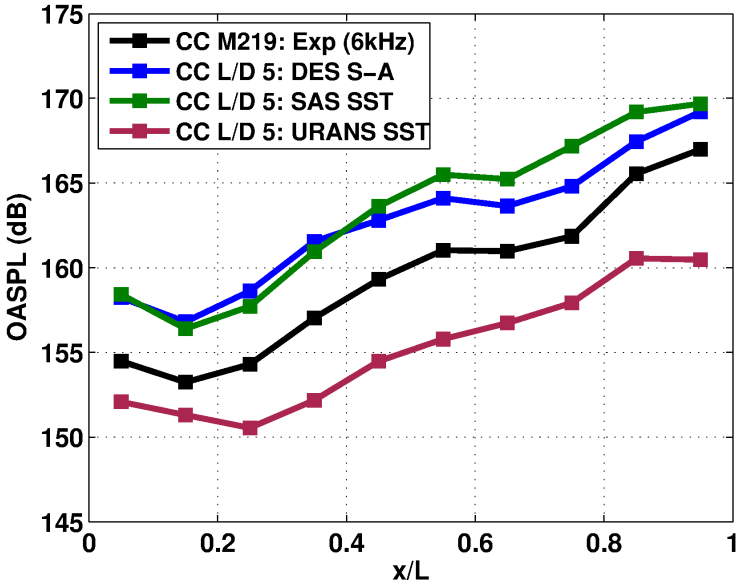

(a) OASPL

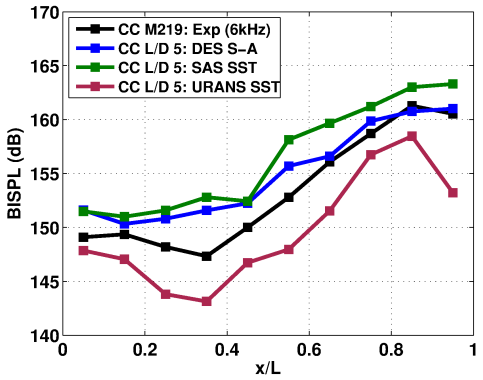

(b) Mode 1: $50 \leq f \leq 250$ Hz

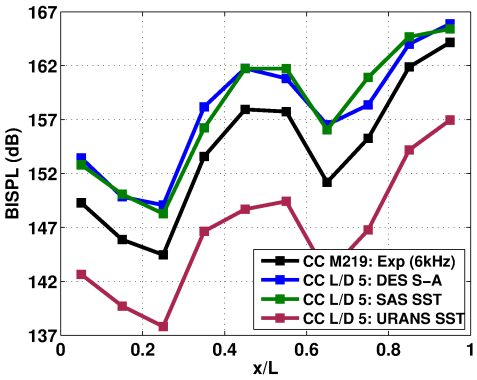

(c) Mode 2: $250 \leq f \leq 450$ Hz

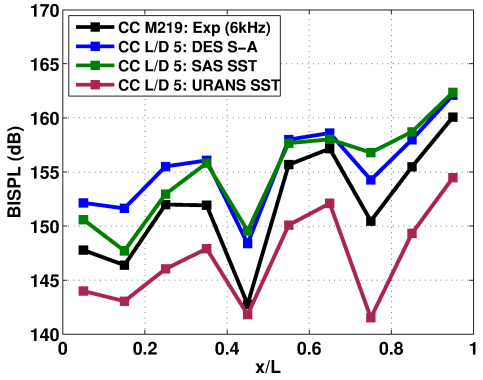

(d) Mode 3: $500 \leq f \leq 700$ Hz

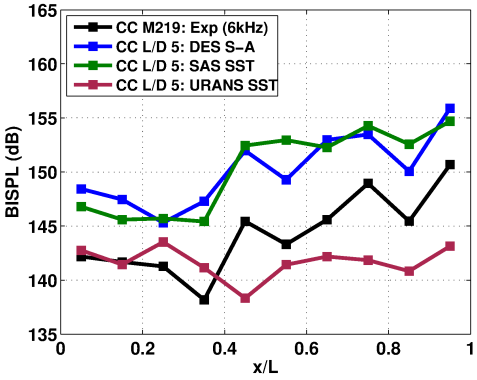

(e) Mode 4: $700 \leq f \leq 900$ Hz

Figure 6.4: OASPL (a) and BISPL plots (b-e) along the cavity floor of the M219 cavity with doors-off. Plots compare results from DES, SAS and URANS methods to experimental data from Nightingale *et al.* [16]. DES data for the M219 cavity were taken from Lawson [13]. CC - Clean Cavity, S-A - Spalart Allmaras and SST - Shear Stress Transport.

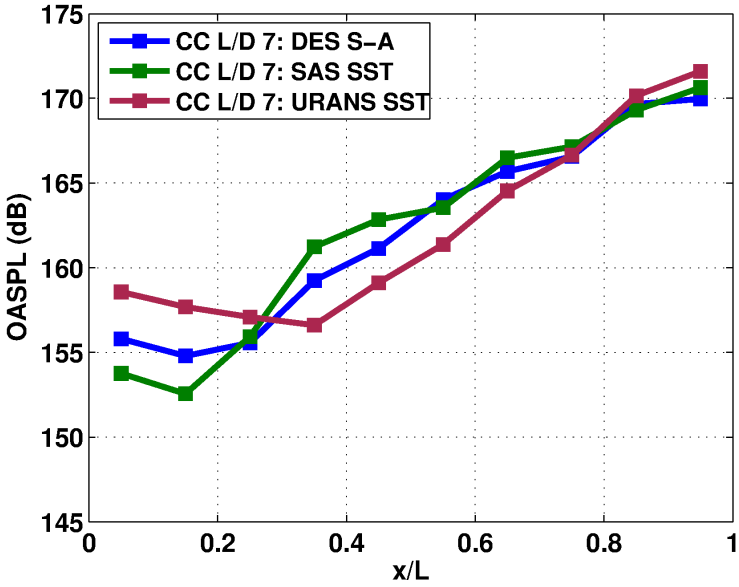

(a) OASPL

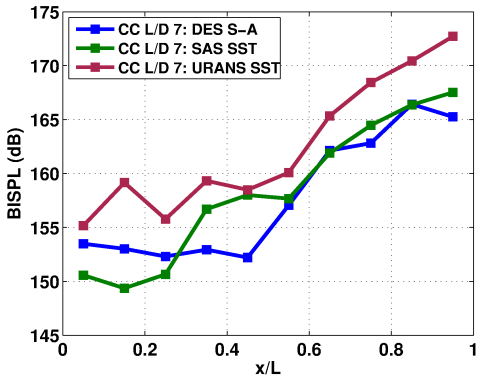

(b) Mode 1: $50 \leq f \leq 250$ Hz

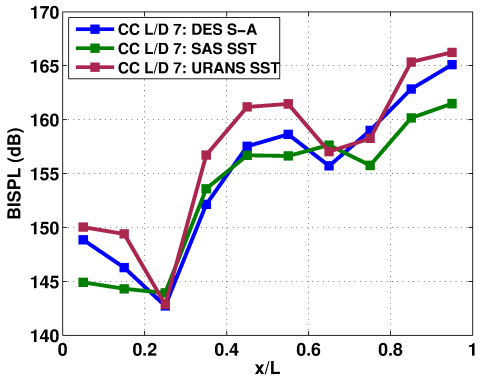

(c) Mode 2: $250 \leq f \leq 450$ Hz

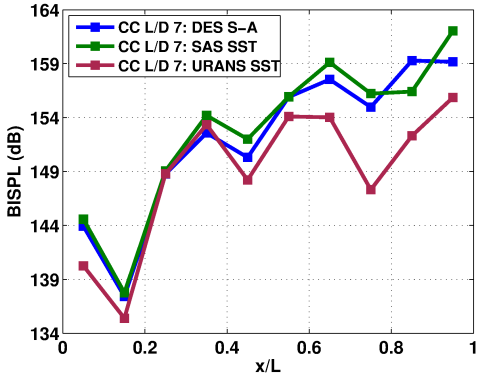

(d) Mode 3: $500 \leq f \leq 700$ Hz

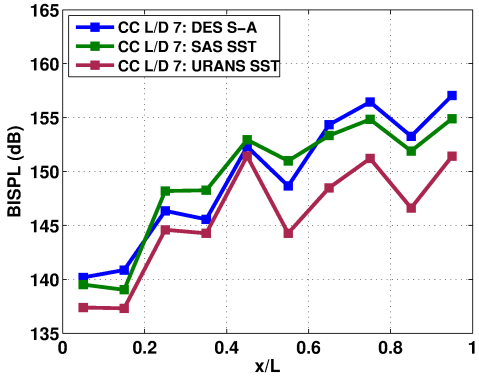

(e) Mode 4: $700 \leq f \leq 900$ Hz

Figure 6.5: OASPL (a) and BISPL plots (b-e) along the cavity floor of the L/D=7 cavity with doors-off, comparing results from DES, SAS and URANS methods. CC - Clean Cavity, S-A - Spalart Allmaras and SST - Shear Stress Transport.

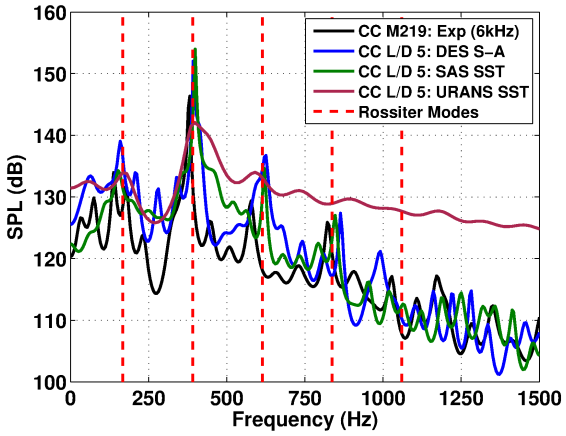

(a) $x/L = 0.05$

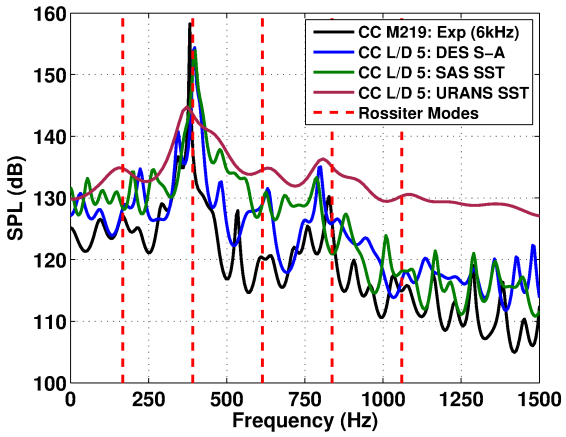

(b) $x/L = 0.50$

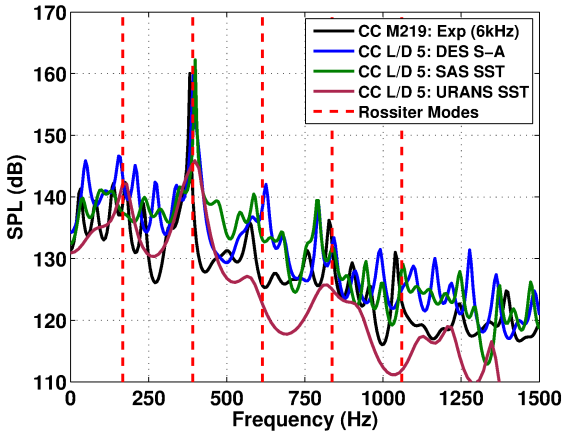

(c) $x/L = 0.95$

Figure 6.6: PSD plots for the front (a) middle (b) and rear (c) transducers along the cavity floor of the M219 cavity with doors-on, comparing results from DES, SAS and URANS methods to experimental data from Nightingale *et al.* [16]. DES data for the M219 cavity were taken from Lawson [13]. Plots are presented in terms of SPL. CC - Clean Cavity, S-A - Spalart Allmaras and SST - Shear Stress Transport.

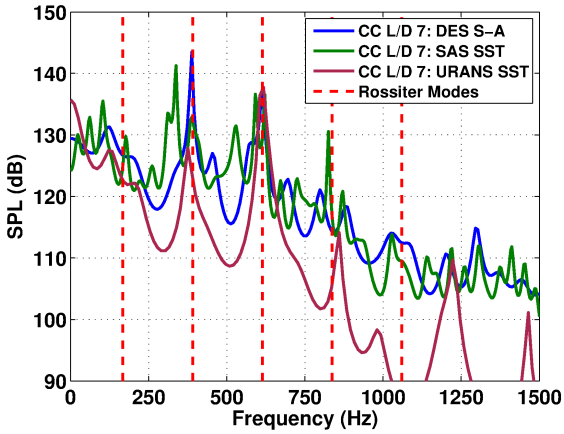

(a) $x/L = 0.05$

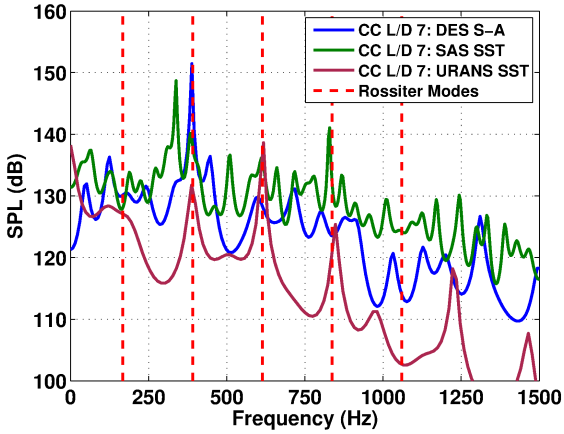

(b) $x/L = 0.50$

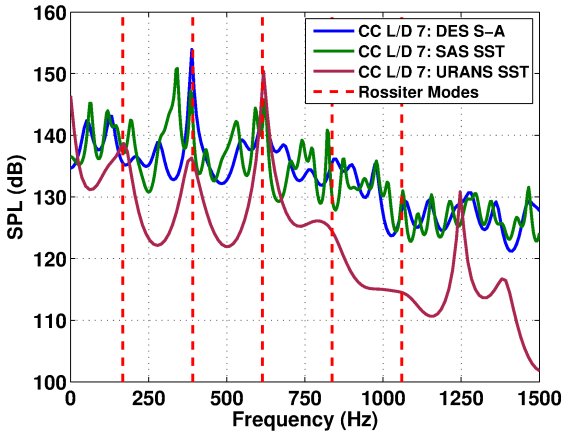

(c) $x/L = 0.95$

Figure 6.7: PSD plots for the front (a) middle (b) and rear (c), along the floor of the L/D=7 cavity with doors-on, comparing results from DES, SAS and URANS methods. Plots are presented in terms of SPL. CC - Clean Cavity, S-A - Spalart Allmaras and SST - Shear Stress Transport.

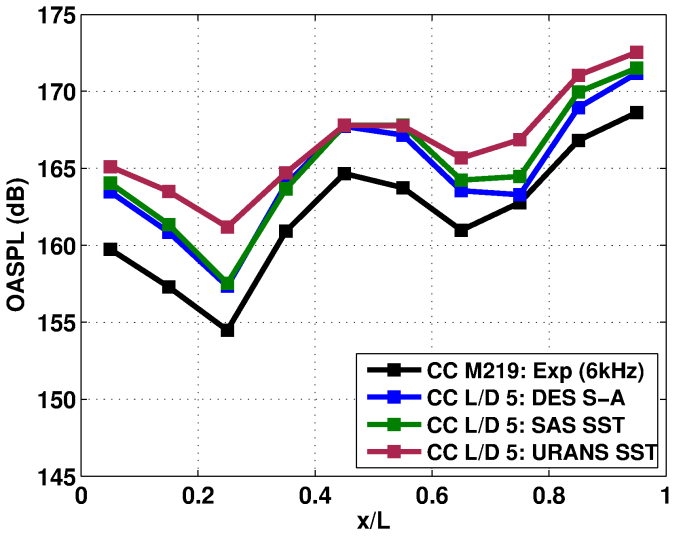

(a) OASPL

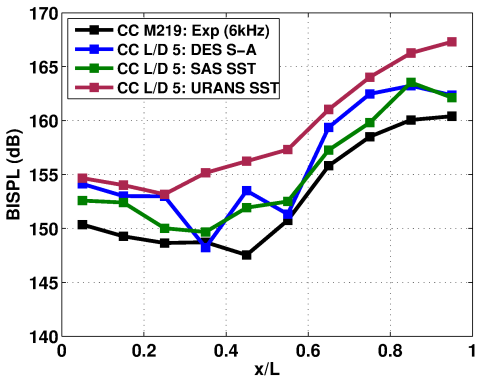

(b) Mode 1: $50 \leq f \leq 250$ Hz

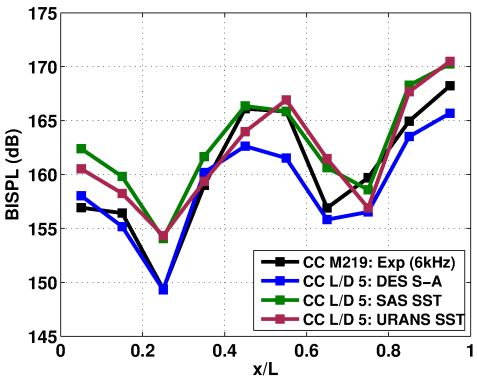

(c) Mode 2: $250 \leq f \leq 450$ Hz

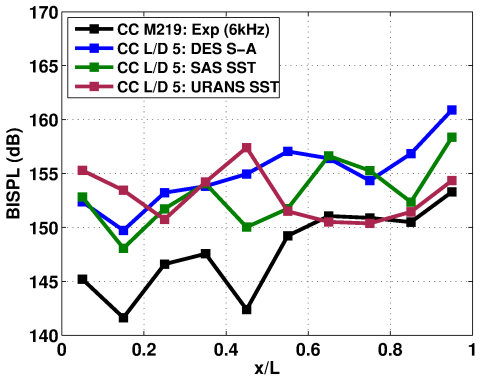

(d) Mode 3: $500 \leq f \leq 700$ Hz

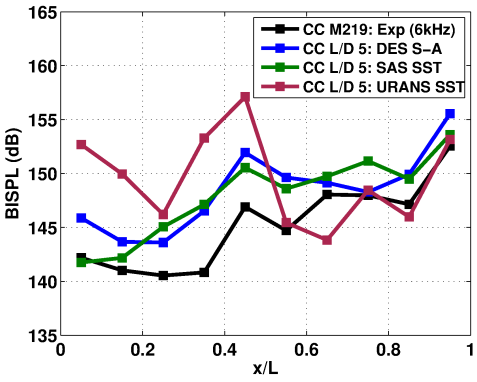

(e) Mode 4: $700 \leq f \leq 900$ Hz

Figure 6.8: OASPL (a) and BISPL plots (b-e) along the cavity floor of the M219 cavity with doors-on. Plots compare results from DES, SAS and URANS methods to experimental data from Nightingale *et al.* [16]. DES data for the M219 cavity were taken from Lawson [13]. CC - Clean Cavity, S-A - Spalart Allmaras and SST - Shear Stress Transport.

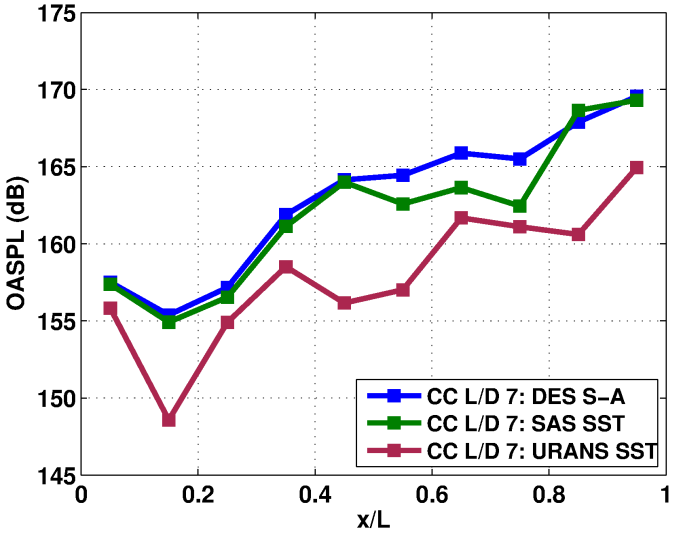

(a) OASPL

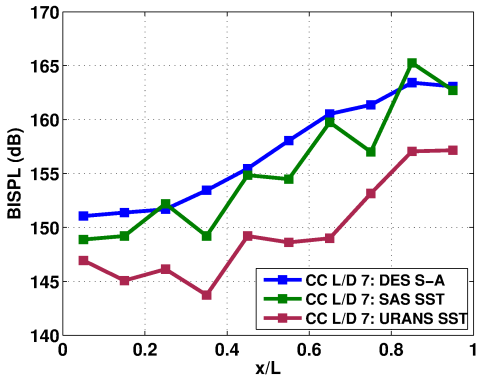

(b) Mode 1: $50 \leq f \leq 250$ Hz

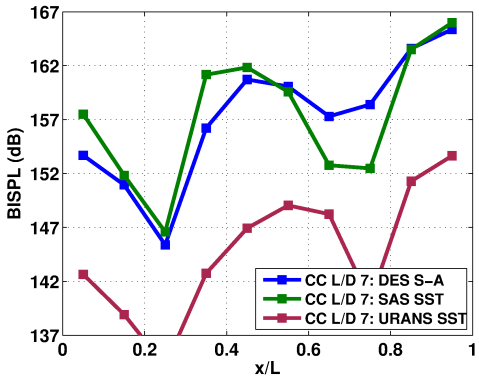

(c) Mode 2: $250 \leq f \leq 450$ Hz

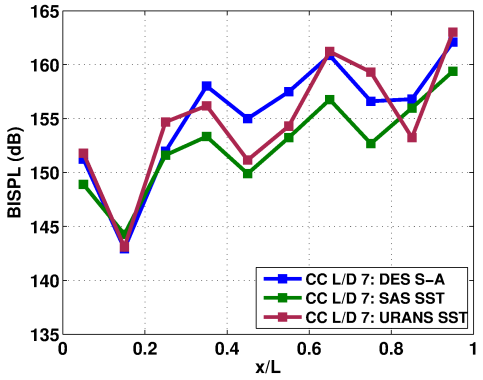

(d) Mode 3: $500 \leq f \leq 700$ Hz

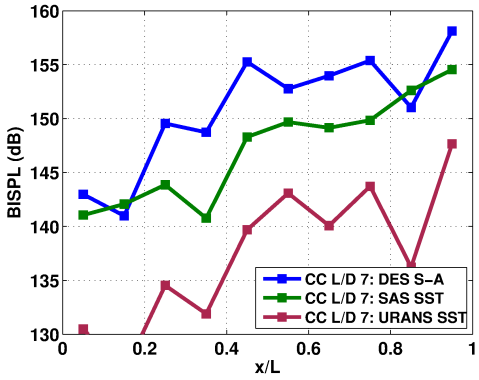

(e) Mode 4: $700 \leq f \leq 900$ Hz

Figure 6.9: OASPL (a) and BISPL plots (b-e) along the cavity floor of the L/D=7 cavity with doors-on, comparing results from DES, SAS and URANS methods. CC - Clean Cavity, S-A - Spalart Allmaras and SST - Shear Stress Transport.

6.3 Joint Time-Frequency Analysis

JTFA, presented as space-time maps, along the floor of the M219 cavity with doors-off and with doors-on are presented in Figure 6.10. DES and SAS results were compared with experimental data from Nightingale *et al.* [16]. DES results, as shown previously in chapter 3, showed good comparison to experimental data. SAS results showed that mode three was intermittent at the front and rear of the cavity, compared to the experiment. The relatively low mode three in SAS and the high mode one suggests a shift of energy to lower frequency modes. Mode two is still seen to dominate the middle of the cavity with infrequent occurrences of mode four as seen in DES. SAS captured the mode switching phenomenon, however DES showed a better comparison with the experimental data.

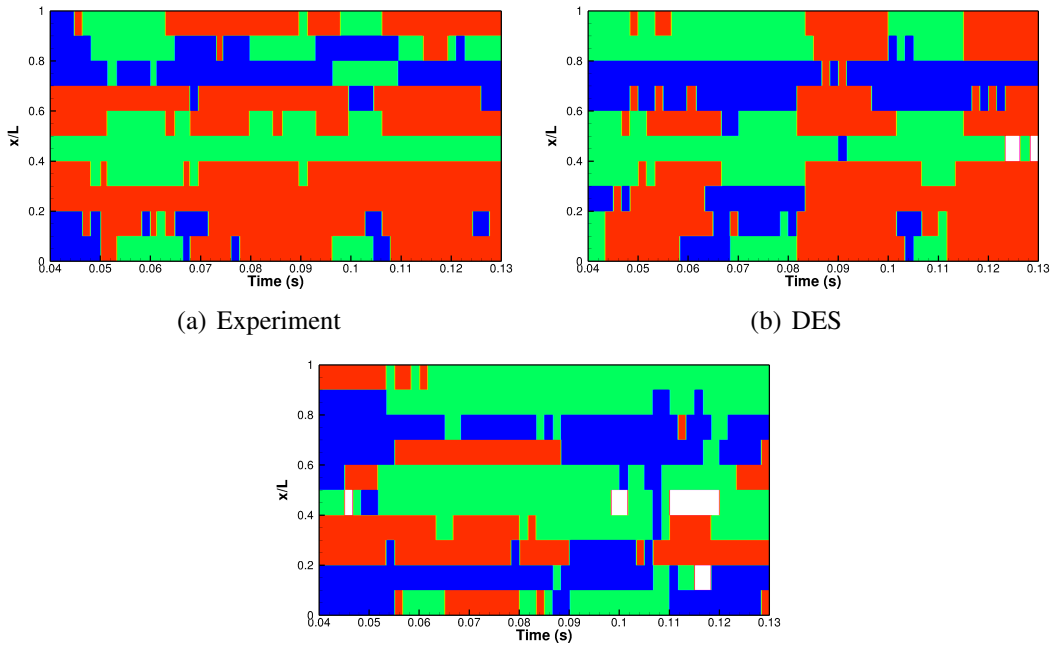

(a) Experiment

(b) DES

(c) SAS

Figure 6.10: Space-time evolution of the dominant Rossiter mode along the floor of the M219 cavity with doors-off comparing experimental data (a), DES (b) and SAS (c). Plots compare DES results from Lawson [13] to SAS results and experimental data for the M219 cavity from Nightingale *et al.* [16]. The different colours represent: blue - mode 1, green - mode 2, red - mode 3, white - mode 4.

Plots for the doors-on configuration are shown in Figure 6.11 where the effect of the doors was clearly seen by the dominance of the second mode along the length of the cavity with some mode one content towards the rear of the cavity. SAS produced similar frequency content as in the experiment but with more mode three at the front and less of mode one at the back.

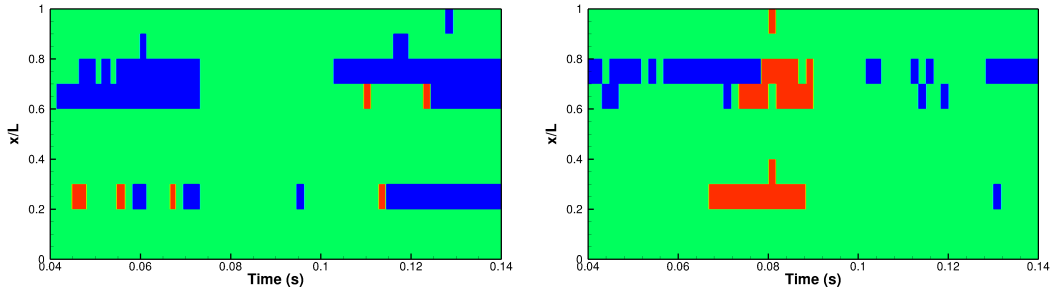

(a) Experiment (b) SAS

Figure 6.11: Space-time evolution of the dominant Rossiter mode along the floor of the M219 cavity with doors-on comparing experimental data (a) and SAS (b). Plots compare SAS results and experimental data for the M219 cavity from Nightingale *et al.* [16]. The different colours represent: blue - mode 1, green - mode 2, red - mode 3, white - mode 4.

6.4 Instantaneous Flow-Field

Instantaneous contours of Mach number, after ten travel times of the flow, for the M219 cavity with doors-on, as predicted using DES and SAS, are shown in Figures 6.12. Structures inside the cavity flow-field and along the doors are seen, and the restricted flow spillage along the side walls of the cavity. Moreover, the figure shows the similarities in the flowfield between the two methods.

6.5 POD Analysis

POD modes were constructed using 101 snapshots taken at regular intervals, for the SAS computation of the L/D=7 cavity with doors-off. The decompositions using 101 snapshots and a reduced set of 51 snapshots are compared in Figure 6.13 for DES and SAS computations. The ratios of the modes to the first mode were quite similar for both decompositions up to about mode number 20 for DES and SAS. The comparison of the decomposition between DES and SAS showed that most of the energy was contained within the lower modes. SAS shifted more of the energy into lower modes than DES.

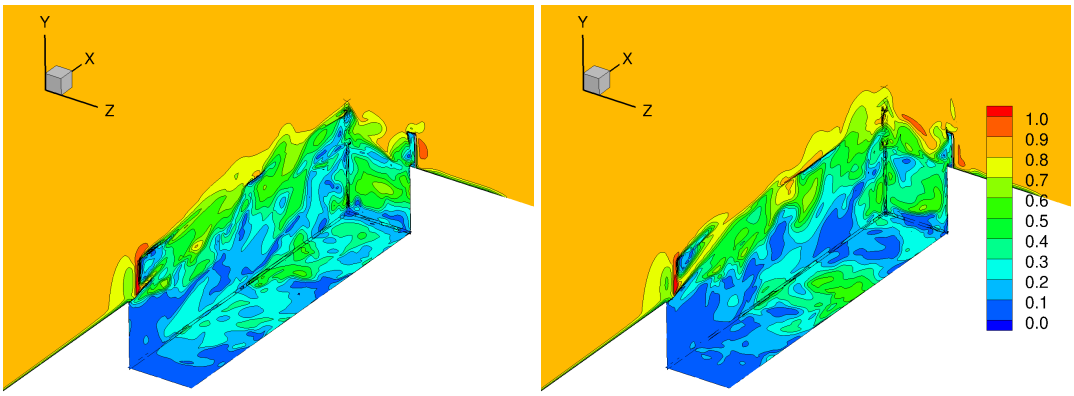

(a) DES: M219 cavity, doors-on (b) SAS: M219 cavity, doors-on

Figure 6.12: Instantaneous contours of Mach number for the M219 cavity with doors-on predicted using DES (a) and SAS (b). Planes are located at x/L=0.99, y/L=-0.19 and z/L=-0.04.

Pressure and normal velocity showed the biggest differences with curves for DES dropping faster after about 20 modes. This meant that more modes would be required by SAS than DES to capture the lower levels of energy in the flow.

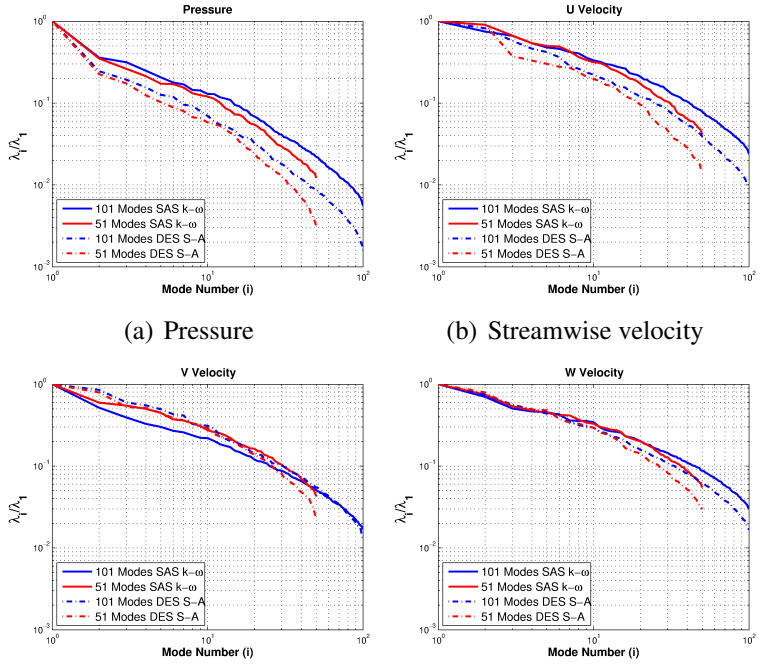

(a) Pressure (b) Streamwise velocity

(c) Normal velocity (d) Spanwise velocity

Figure 6.13: Mode eigenvalues normalised by the first mode eigenvalue comparing the POD using 201 and 51 snapshots, between DES and SAS, for the L/D=7 cavity, with doors-off.

Chapter 7

Six-Degree-of-Freedom Model Validation

This chapter presents the validation of the six degrees of freedom (6DoF) method coupled with HMB2. First, the 6DoF method was validated against wind tunnel experiments conducted at the AEDC[17] for the release of a generic store from a wing. Loads acting on the isolated store in free-stream, at different angles of attack, were validated against wind tunnel data following which, the trajectory of the store was validated using the 6DoF method in HMB2.

7.1 6DoF Validation Case

The following sections present the validation of the 6DoF method in HMB2 for the widely used wind tunnel test conducted at the AEDC[17]. Several studies[36, 95–112] have utilised this test case, using structured[36, 97, 104, 109], unstructured[96, 98–100, 110, 111] and meshless solvers[101], to validate the prediction of the store trajectory, making it a popular validation case in the absence of any open data for store release from a cavity.

The test provided pressure data for a geometrically simple wing and store under mutual interference as well as a realistic release trajectory. AEDC's 4-Foot Transonic Aerodynamic Wind Tunnel (4T) was used for the test together with its captive trajectory support system to simulate the motion of the store.

While data were available for two Mach numbers of 1.2 and 0.95, only the Mach number of 0.95 was used here as it was closer to the Mach number of 0.85 used for release computations from an idealised cavity.

7.2 Model Geometry and Mesh Generation

The computational model was based on the wind tunnel geometry as reported in the test [17]. While the wind tunnel test consisted of a wing, pylon and store configuration, the pylon was omitted from the computational model to simplify the overset mesh in the region where the pylon and the store are almost in contact. No large effects were seen due to the omission of the pylon which is evident in the store loads and computed release trajectory presented in the following section. The wind tunnel test model was 5% of a generic full-scale wing/pylon/store.

Figure 7.1 shows the models used for the experiment that include the store and the captive trajectory support system and the wing surface. The wing had a clipped delta wing planform with a 45 degree leading edge sweep and was made of a NACA 64A010 aerofoil section. The store had a tangent-ogive forebody and afterbody with a flat base and four fins, each at 90 degrees to its adjacent fin.

The composite grid used for the flow computation, composed using the chimera method [87], consisted of four individual grids, shown in Figure 7.2 for each level. *Level 0* consisted of the wing geometry and the far-field of the computational domain, *Level 1* was used to aid the localisation of cells between the wing and the store grids, *Level 2* was used to capture the release of the store, in *Level 3*. The axis system shown in Figure 7.2 was used for the generation of the grids, following which the composite grid was converted to the North-East-Down axis system (positive X, out through the nose of the store, positive Y, starboard and positive Z, down) in which the loads and trajectory were computed.

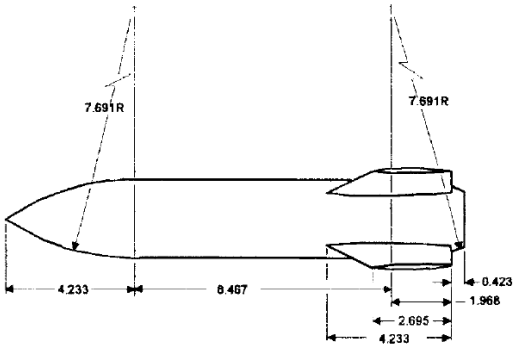

(a) Store model

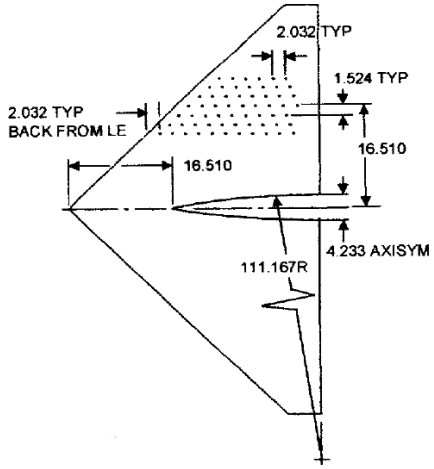

(b) Wing upper surface

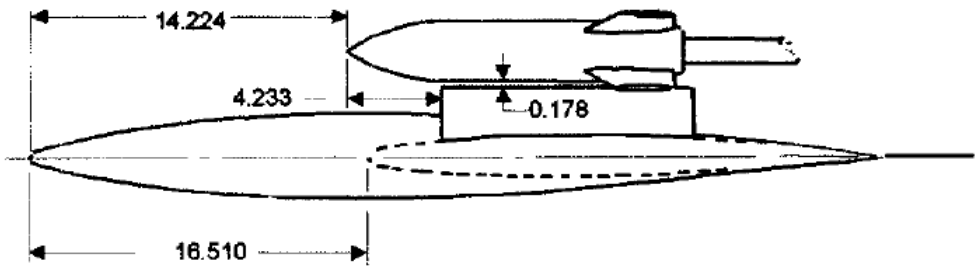

(c) Store at carriage

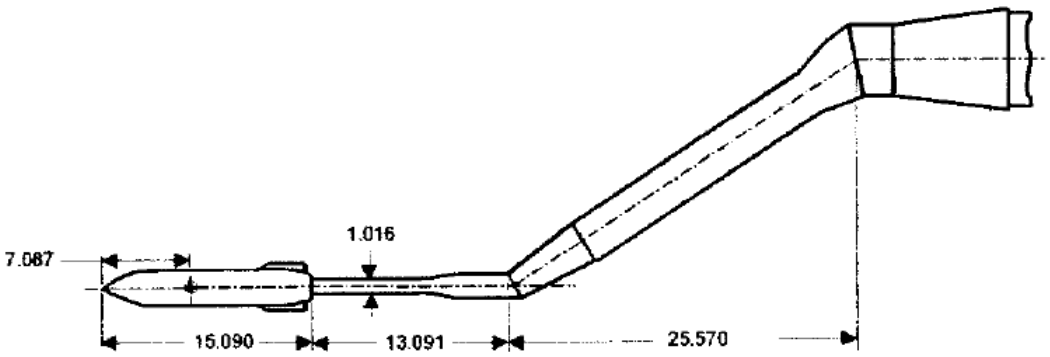

(d) Captive trajectory support system

Figure 7.1: Schematic of the experimental set up used by the AEDC [17].

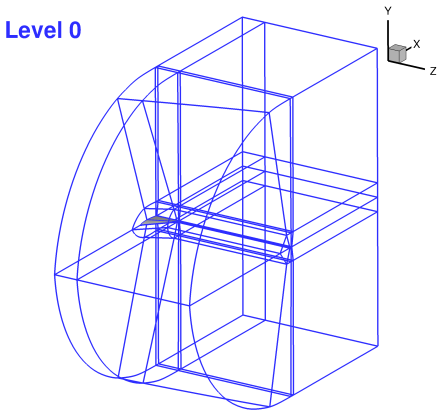

(a) Level 0 (40 blocks, 2.8M cells)

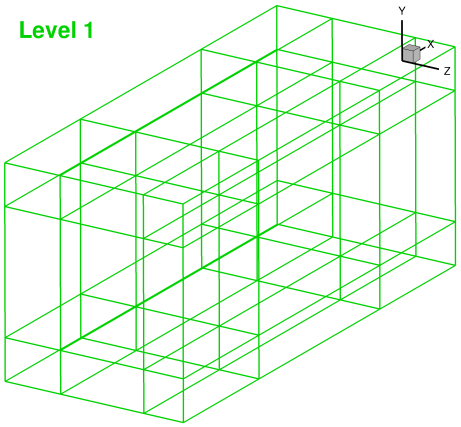

(b) Level 1 (27 blocks, 0.2M cells)

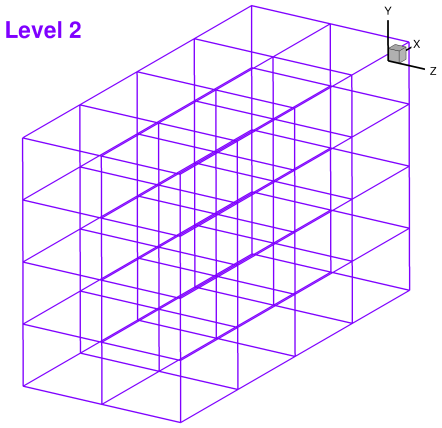

(c) Level 2 (32 blocks, 1.1M cells)

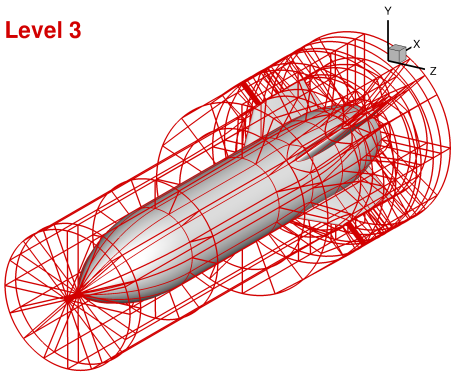

(d) Level 3 (392 blocks, 1.5M cells)

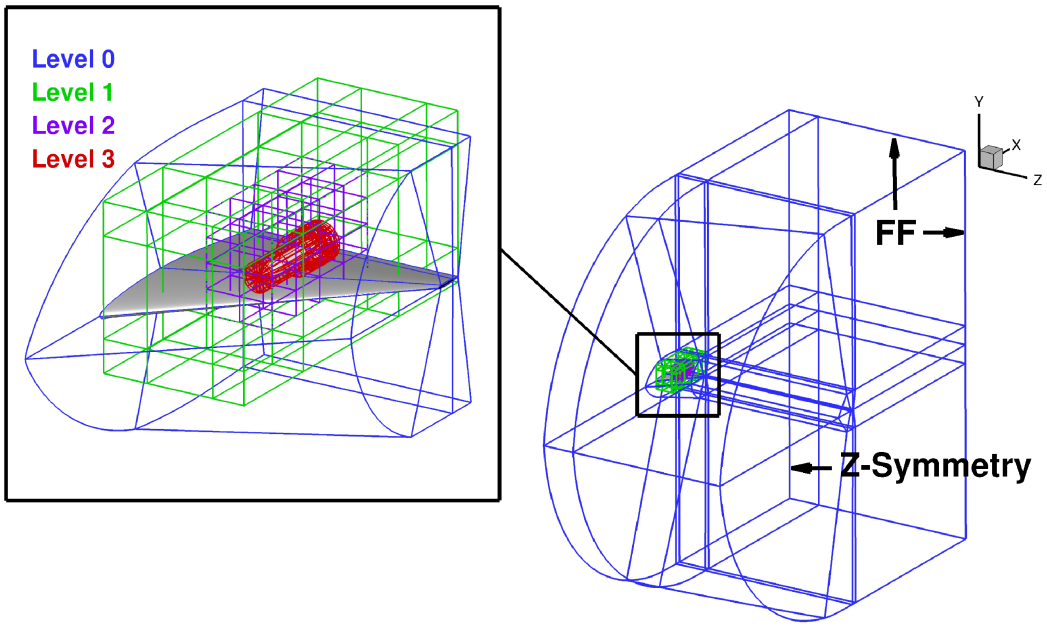

(e) Composite grid (491 blocks, 5.6M cells)

Figure 7.2: Individual grids (a-d) that are composed (e) for the wing-store computation.

Figure 7.3 presents the localisation of the cells on the *Level 1* grid. Here, red cells represent fringe or boundary cells of the *Level 1* grid, green cells represent computational cells, yellow cells represent interpolation cells that require interpolated information from the *Level 2* and *Level 3* grid, light blue cells represent holes that belong to the higher *Level 2* grid and dark blue cells represent holes that overlap with solid store surfaces.

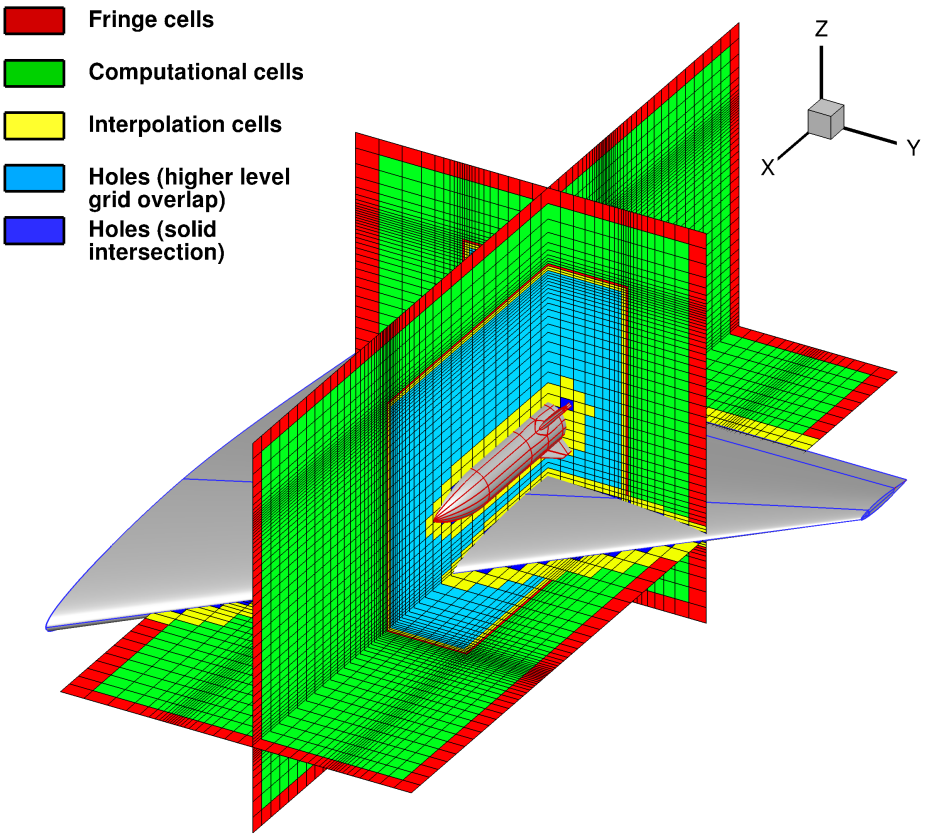

Figure 7.3: Localisation of cells of higher level grids on the *Level 1* grid.

7.3 Decoupled Analysis

Prior to running a fully coupled trajectory computation in HMB2, a decoupled approach was taken to compare the wind tunnel trajectory to that obtained from the 6DoF method in HMB2, by using force and moment coefficients from the wind tunnel data as input. In this way the 6DoF method could be tested without the expense of computing the flow at every instance in time and with the same aerodynamics as measured in the test. Therefore any discrepancies in the trajectory would be due to the 6DoF method.

Figure 7.4 shows a comparison of the wind tunnel trajectory to the trajectory computed by the 6DoF method in HMB2 with the decoupled approach, for the full available signal length of 0.92s. Velocity components and CG displacements agreed well with wind tunnel data, however, some divergence was seen in the pitch and yaw rates and hence the pitch and yaw angle. The initial part of the trajectory, controlled by the ejector forces compared closely to wind tunnel data, however, after about 0.3s the pitch and yaw rate started to drift away from wind tunnel data. This divergence over time, especially in pitch rate and attitude, was noticed in other studies[36, 99, 100] as well and could be due to the Captive Trajectory System (CTS).

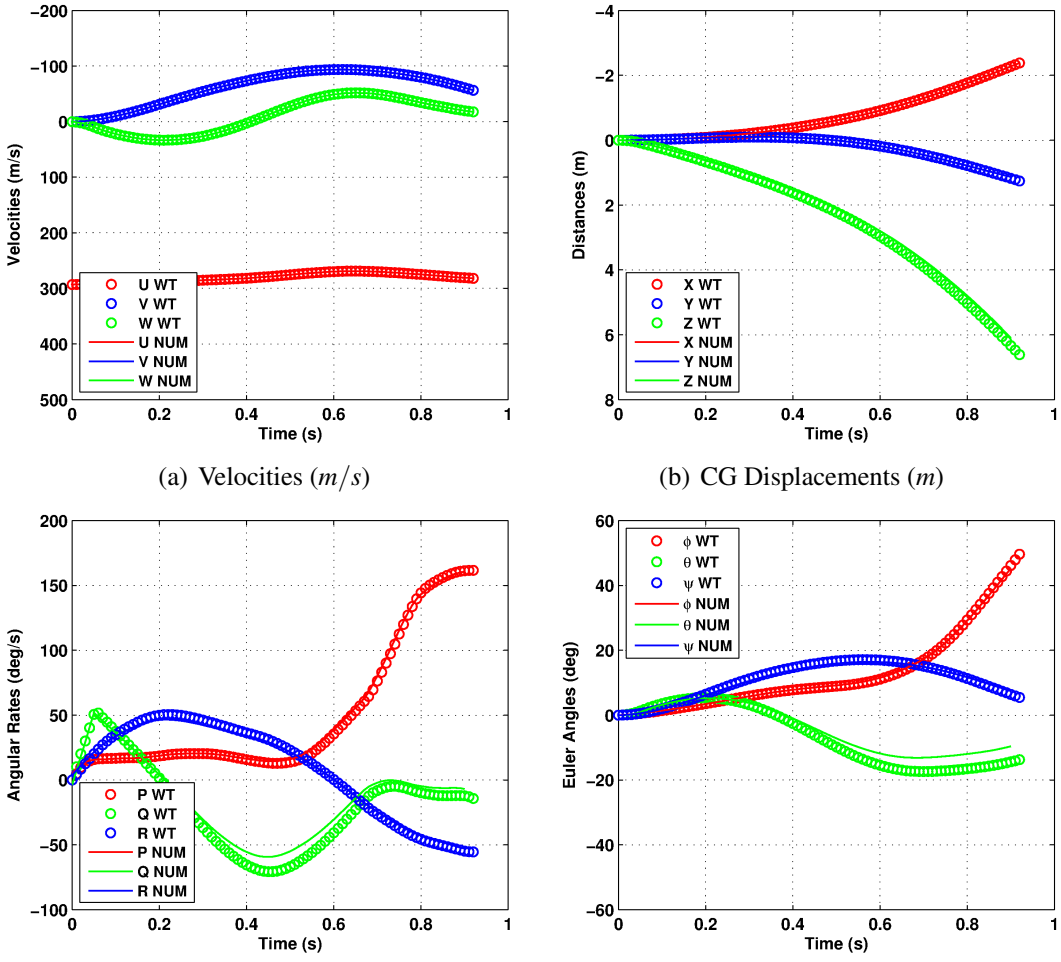

(a) Velocities (m/s)

(b) CG Displacements (m)

(c) Angular Rates (deg/s)

(d) Euler Angles (deg)

Figure 7.4: Comparison of trajectories computed using a decoupled approach in HMB2 and wind tunnel data[17]. WT: Wind tunnel, NUM: Decoupled results from HMB2.

The trajectory obtained from the decoupled approach was used to analyse windows of time-averaged trajectory parameters (Figure 7.5). 0.1 second long windows were averaged in time for pitching moment coefficient and the pitch rate. Nine windows were obtained as the total length of the signal was 0.9s. The pitching moment coefficient was scaled by a factor of 20 for comparison with the pitch rate. The effect of application of the ejectors was seen in the first two windows where a net positive pitch rate was produced. At these windows the pitching moment coefficient was seen to be negative and opposite to the pitch rate. Once the effect of the ejectors diminished, both quantities were in phase. The pitch rate reversed in sign and grew in magnitude and once the pitching moment coefficient reversed, the effect was seen in the pitch rate where it began to reduce in magnitude.

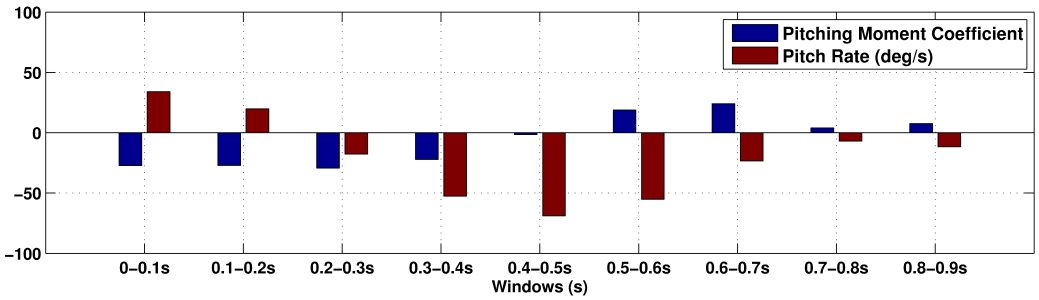

Figure 7.5: Time-window-averaged pitching moment coefficient and pitch rate obtained from the decoupled approach. The pitching moment coefficient was scaled by a factor of 20 for comparison with the pitch rate.

7.4 Store Loads and Trajectory

Euler computations were run to compare loads acting on the isolated store in freestream as well as during carriage, which is a common starting point for this case [17,95]. Computations were run at a Mach number of 0.95 and a Reynolds number of 1.0×10^6 (based on the root chord of the wing). Figure 7.6 presents the loads acting on the store when isolated in free-stream (Figure 7.6(a-c)) and during carriage under the wing (Figure 7.6(d)).

Isolated store computations were run at incidence angles of 0, 2 and -2 degrees. At 0 degrees, it was found that HMB2 underpredicted the axial force coefficient, C_X by 0.09 in the absence of viscous effects and base drag. Several studies[97,98,102,104,109,111] took this absence of viscous effects and base drag out of consideration by introducing a sting at the base of the store or by modifying the base to be more streamlined.

The base drag correction value was used for C_X at 0, 2 and -2 degrees, as well as for carriage, which then showed better agreement with wind tunnel data. All other force and moment coefficients also showed good agreement with wind tunnel data without any corrections. The characteristics of the store used in the 6DoF method, for the computation of its trajectory during release, are summarised in Table 7.1. Of interest are the ejector locations and forces shown in Figure 7.7(a), with the aft ejector having almost 4 times the force as the forward ejector, implying that the store will have an initial nose-up pitching moment about its centre of gravity.

Table 7.1: Full-scale store and ejector characteristics[17].

Characteristics	
Weight	8896.4 N
Centre of Gravity	1.41 m (aft of store nose)
Roll Inertia ($I_x x$)	27.12 $kg.m^2$
Pitch Inertia ($I_y y$)	488.1 $kg.m^2$
Yaw Inertia ($I_z z$)	488.1 $kg.m^2$
Forward Ejector Location	1.24 m (aft of store nose)
Forward Ejector Force	10675.7 N
Aft Ejector Location	1.75 m (aft of store nose)
Aft Ejector Force	42702.9 N
Ejector Stroke Length	0.1 m

The store release computation was initiated from a solution around the store at carriage position, after the flow was fully developed and the store loads obtained through HMB2 agreed with the wind tunnel data. Figure 7.7(b) shows the trajectory of the store starting from the carriage position at time $t = 0.0s$ in intervals of 0.1s. The trajectory visualised here shows the store having an initial nose-up pitching moment as expected from the difference in force between the forward and aft ejectors. The store recovers from the pitch, and is seen to have a growing negative yawing moment over time.

Figure 7.8 presents a comparison of the trajectory computed in HMB2 and the wind tunnel data. Six sets of trajectory parameters were compared for 0.4s of the simulation: force coefficients, velocity of the store centre of gravity (CG), displacement of the centre of gravity, moment coefficients, angular rates and Euler angles. It was apparent that the force coefficients, velocity and location of the CG closely matched the wind tunnel data. The store moved slightly rearward and inboard as it moved further away from the wing. Small discrepancies were seen in the moment coefficients that were carried into the angular rates and Euler angles. Initially, there was a slight underprediction of the rolling moment and overprediction of the pitching and yawing moment coefficients. The initial overprediction in the pitching moment coefficient did not affect the initial part of the trajectory in terms of CG location or pitch attitude as the ejector and gravity forces dominated the aerodynamic forces and moments in that direction.

The effect of the ejectors was seen clearly in the pitch rate that had a large gradient for the initial 0.5 seconds of the release. Once the ejector stroke length has been reached, the aerodynamic pitching moment on the store began to invert its pitching moment. The pitch and yaw curves showed a slight divergence from the wind tunnel data after about 0.3 seconds of the release. This divergence over time was not only observed in the original study by Fox[17], but also in other studies[36, 99, 100] as well, that have raised questions on the accuracy of the CTS data and its ability to accurately capture the motion of a released store.

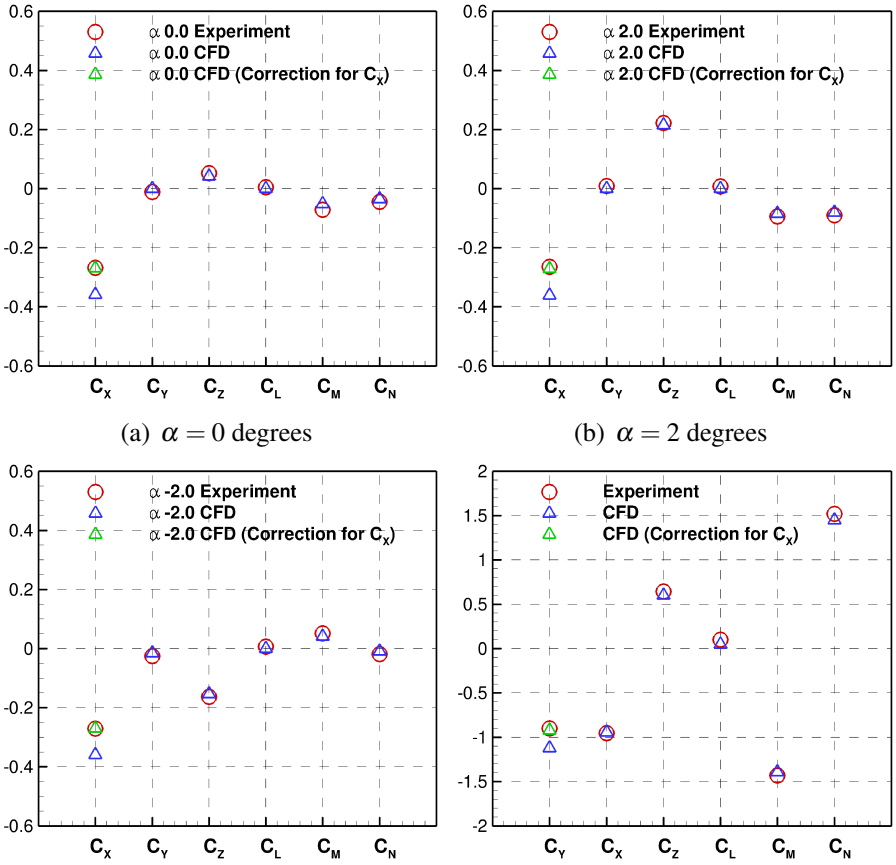

(a) $\alpha = 0$ degrees

(b) $\alpha = 2$ degrees

(c) $\alpha = -2$ degrees

(d) Carriage loads

Figure 7.6: Store free-stream (a-c) and carriage loads (d) compared with wind tunnel data[17].

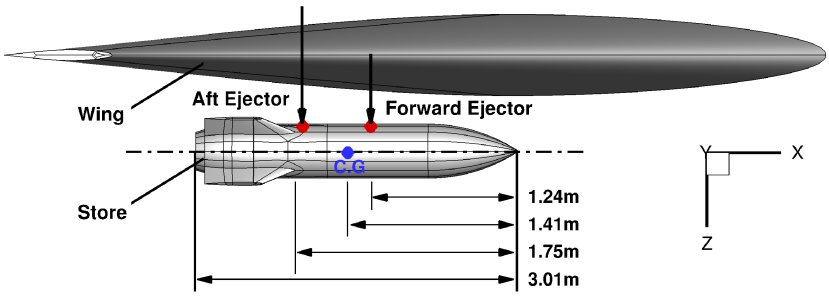

(a) Location of forward and aft ejectors on the full scale model

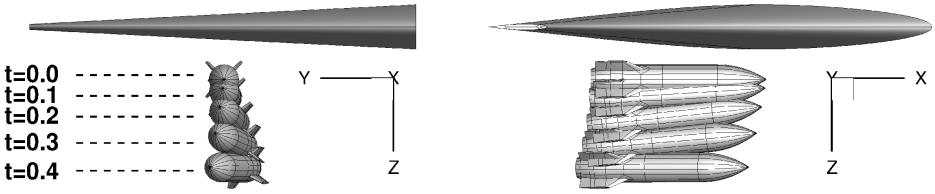

(b) Trajectory of store released from the wing

Figure 7.7: Ejector locations (a) and the trajectory of the store released from the wing at different instances in time (b).

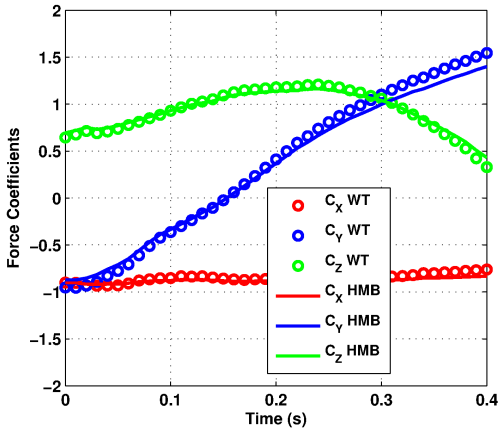

(a) Force Coefficients

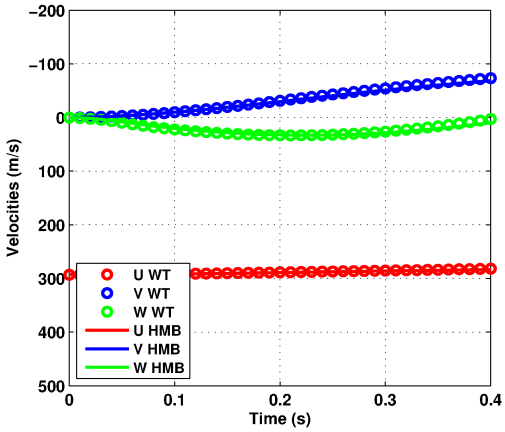

(b) Velocities (m/s)

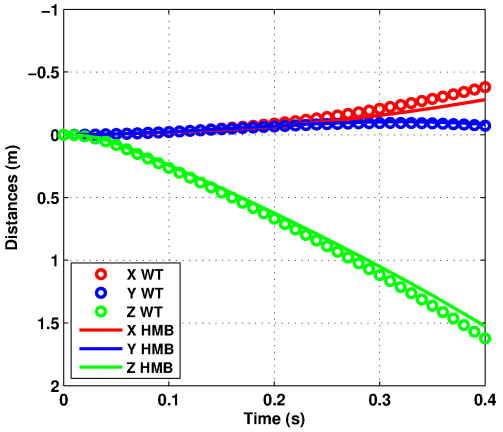

(c) CG Displacements (m)

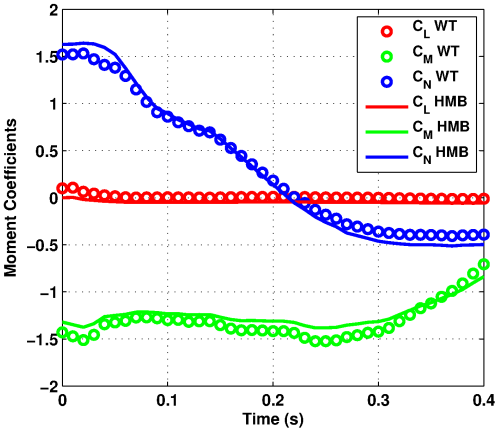

(d) Moment Coefficients

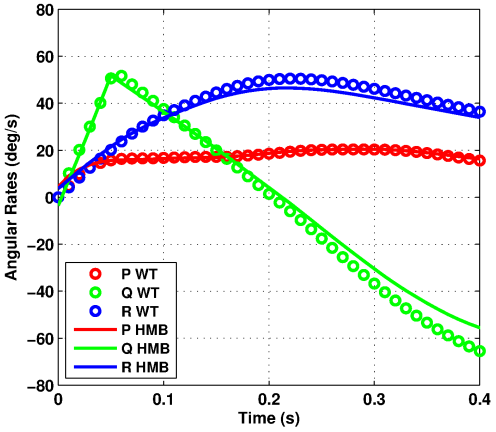

(e) Angular Rates (deg/s)

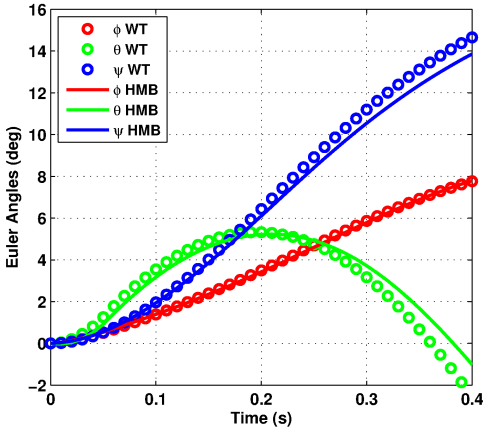

(f) Euler Angles (deg)

Figure 7.8: Comparison of trajectories computed using HMB2 and wind tunnel data[17]. WT: Wind tunnel.

Chapter 8

Computations of Store Release From a Cavity

This chapter presents SAS computations for the release of a generic store from an idealised cavity with L/D=7, at a Mach number of 0.85 and a Re_L of 6.5 million. First, the grids used for the release of a store from an idealised cavity are discussed. The variability of the store trajectory was studied through several computations performed starting from different release times from the fully developed cavity flow. The final section analyses flow visualisations, trajectories and fin loads for selected release times.

8.1 Model Geometry and Mesh Generation

The computational model consisted of two geometries: a rectangular L/D=7 cavity as used in Chapter 3 and a generic store model provided by MBDA[88], as used in Chapters 4 and 5. The composite grid used for the simulations was made up of two grids, one for each geometry: the cavity grid (*Level 0*) and the store grid (*Level 1*), details of which are shown in Figure 8.1. The cavity grid consisted of 800 blocks while the store grid, that had an O-grid around the body and an O-grid around each fin, consisted of 304 blocks. The composite grid therefore consisted of 1104 blocks and 21.4 million cells. The cells inside, and immediately outside the cavity were controlled so that the volume of the cells at the interface of the two grids were as close as possible to allow for better interpolation of the flow solution from one grid to another.

Mass and inertial properties of the store, supplied by MBDA[88], were used in the 6DoF method, for the computation of its trajectory during release. The store occupied 90% of the cavity length and was placed at the carriage position (half a cavity depth inside and along the centreline of the cavity).

The localisation of the cells on cavity grid (*Level 0*) is shown in Figure 8.2. The cavity and store geometries are shown along with the edges of the blocks of the corresponding grids in contact with the geometries, coloured in blue for the cavity grid and red for the store grid. As before, green cells are the computational cells, in which the flow is solved, red cells denote the boundary of the store grid, and light blue cells are holes that belong to the store grid. The store is initially localised at the carriage position following which the weights are recomputed and the localisation process is repeated for each step from the application of the stroke.

8.2 Store Loads and Release Trajectory

Computations of store release from a cavity were performed at a Mach number of 0.85 and Re_L of 6.5 million. The store was maintained at the carriage position while the flow was allowed to develop inside the cavity. Once the flow had developed, the store was moved downward till the length of the stroke, at an ejection velocity of $5m/s$, applied at the CG of the store. The full stroke length was equal to half cavity depth (0.237m) and the half stroke length was equal to a quarter cavity depth (0.118m).

Approximately 0.35s of real flow time was computed, to develop the flow inside the cavity, and the flow solution was then saved. It was then used for the ejection of the store and to continue developing the flow until the next release time. Eleven computations were performed in total, as summarised in Table 8.1, six applying a full stroke length and five applying a half stroke length at different instances in time. The acronyms FS and HS were used to identify the computation as a full stroke or half store respectively.

As in the previous chapter, six trajectory parameters are presented for each case. FS1 and HS1 were chosen as baseline computations for comparison with other cases. Figure 8.3 compares case FS1 and FS2 where the store was released after a time-signal of 0.35s and 0.42s respectively.

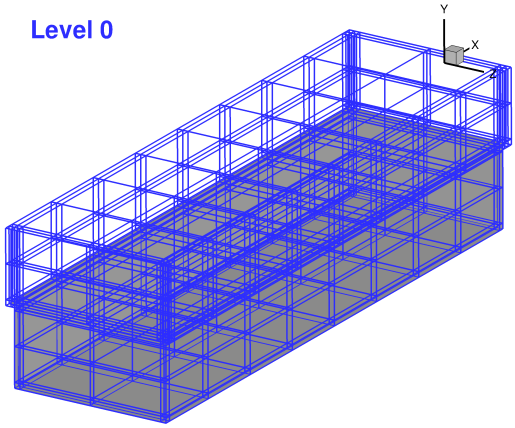

(a) Level 0 (800 blocks, 17.7M cells)

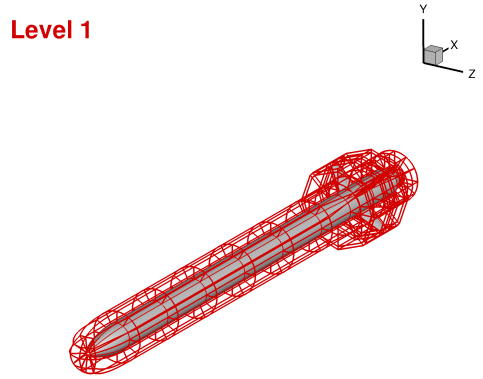

(b) Level 1 (304 blocks, 3.7M cells)

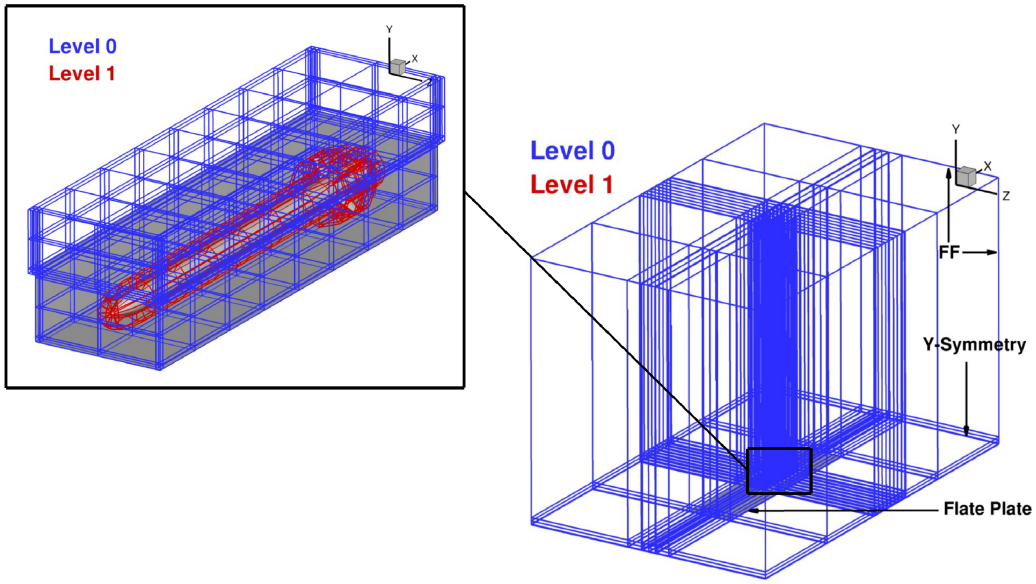

(c) Composite grid (1104 blocks, 21.4M cells)

Figure 8.1: Individual and composite grid used for store release from cavity simulations.

Displacements of the CG in the longitudinal and normal directions were very similar, however in the lateral directions they were almost equal and opposite. The 0.07s difference, in release time between the two cases, showed slight variations in the forces and moments acting on the body but mainly showed differences in the orientation of the store in the roll axis. Overall, case FS1 had a net positive roll attitude, that caused the store to roll to starboard, while FS2 had a negative roll attitude, that caused the store to roll to port.

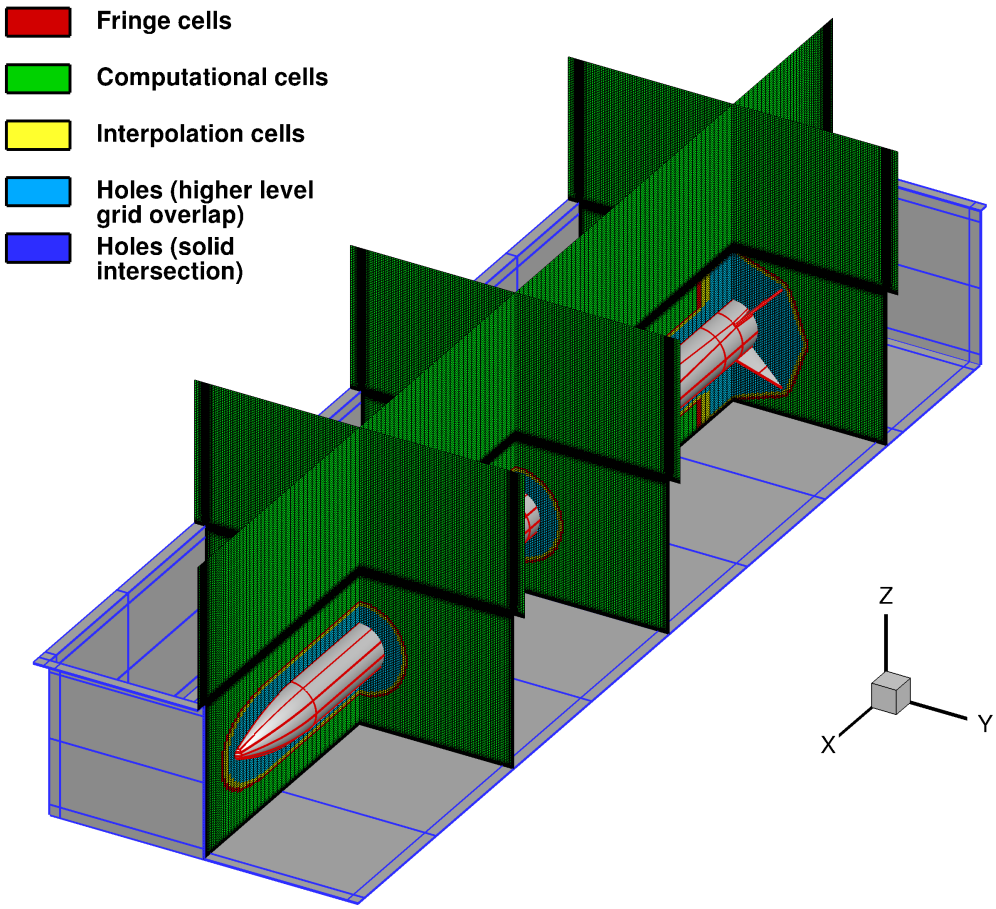

Figure 8.2: Localisation of cells of higher level grids on the background grid (*Level 0*).

Table 8.1: List of computations to demonstrate the variability in store trajectory for different release times and stroke lengths.

ID	Unsteady Steps Before Stroke Application	Time-Signal Length Before Stroke Application(s)	Stroke Length
FS1	3000	0.35	Full stroke
FS2	3680	0.42	Full stroke
FS3	3770	0.43	Full stroke
FS4	4200	0.48	Full stroke
FS5	4400	0.51	Full stroke
FS6	3500	0.40	Full stroke
HS1	3000	0.35	Half stroke
HS2	3680	0.42	Half stroke
HS3	3770	0.43	Half stroke
HS4	4200	0.48	Half stroke
HS5	4400	0.51	Half stroke

Full stroke: 0.5D (0.237m), Half stroke: 0.25D (0.118m). D: Cavity depth

A closer look at the time-history of fin forces and moments, given in Figure 8.4, shows how the fin loads vary during release and reveals the differences between loads acting on each fin between the two cases. Time windows of 0.01s each were taken and loads were averaged within these windows to highlight the change in magnitude and sign for different sections of the drop. Time-window-averaged loads are presented in Figure 8.5 for each fin where the windows correspond to 0s to 0.01s, 0.01s to 0.02s, 0.03s to 0.04s and 0.04s to 0.05s respectively, of the store trajectory. Differences are seen between the fins for FS1 and FS2 that give rise to the overall change in store attitude between the two cases. A closer look at the time-history of fin forces and moments shows how active the fins are during release and reveals the dissimilarities between loads acting on each fin between the two cases. Three instances in time, shown in Figure 7.11, that corresponded to peaks in the loads were chosen for an in-depth look at the flow-field and the surface CP on the fins during release. Cases FS1 and FS2 were compared (7.12) at these time instances and the figures highlighted the difference in pressure distribution over the fins. Relating to Figure 7.11, correlations could be seen between the peaks and the pressure distribution on the fins for the different times instances.

Slices were taken in the flow-field (Figure 8.6), through Fins 1 and 2, highlighting regions of low and high velocity flow around the fins at each instant in time. This further evidenced the reason for differences in the flow and hence the differences in loads between the two cases.

FS1 and FS3 (Figure 8.7) showed similar trajectories that caused both stores to roll to starboard. Loads acting on the store as well as the fins (8.8) showed very similar trends and several peaks in the fin loads were seen to be coincident. Instantaneous contours of surface C_P, at three different time instances were compared (Figure 8.9) and found to be similar between the two cases despite some differences seen along the cavity ceiling,

FS4 (Figure 8.10) was similar to FS2, in that, the net effect of the unsteady cavity flow-field caused the store to roll to port, however the flow-field in FS4 initially caused the store to roll to starboard. Comparisons of trajectories and store loads with FS5 (Figure 8.12), including fin loads (Figure 8.13), showed similarities to FS1 but had a slightly higher roll attitude. Overall, the full stroke cases had similar trajectories in terms of the translation of the store, however the roll attitudes varied, some more than others.

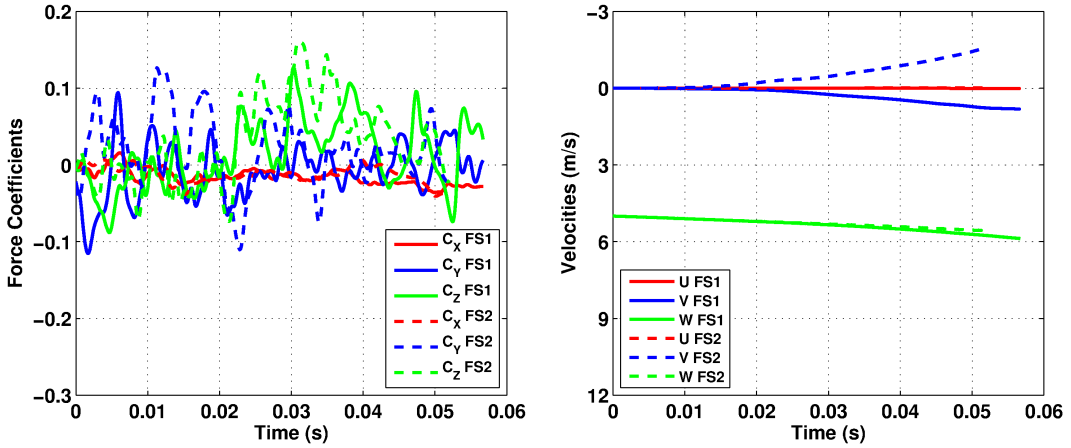

(a) Force Coefficients

(b) Velocities (m/s)

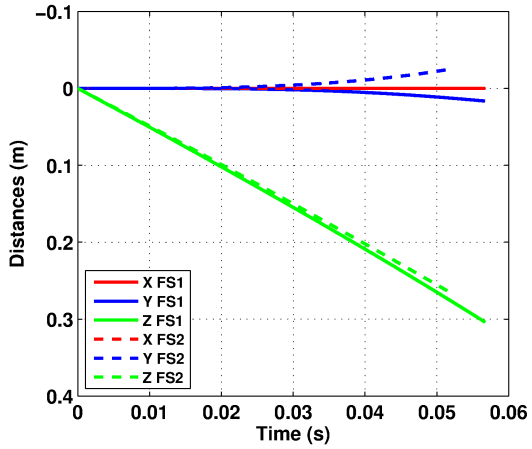

(c) CG Displacements (m)

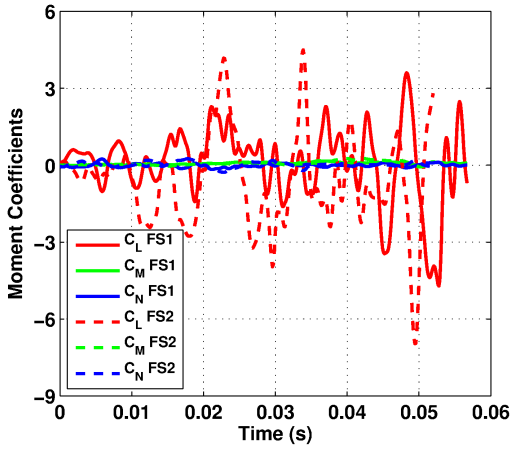

(d) Moment Coefficients

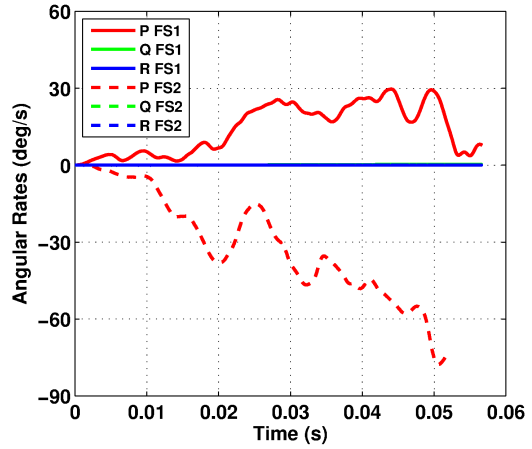

(e) Angular Rates (deg/s)

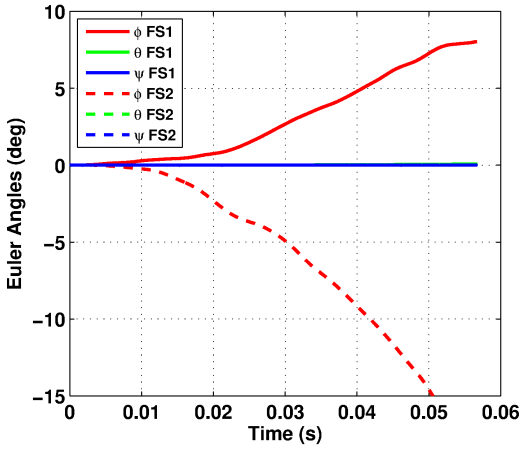

(f) Euler Angles (deg)

Figure 8.3: Comparison of trajectories for computations FS1 and FS2. FS: Full Stroke.

The effect of the stroke length was compared by first comparing cases FS1 and HS1. Comparisons are shown in Figure 8.14, and although similar in CG displacement,

the roll attitude oscillated more for HS1. The fin loads for HS1 (Figure 8.15) were slightly more active than FS1, possibly due to the increased residence time in the high pressure fluctuation region. Time-window-averaged fin loads comparing FS and HS1 are presented in Figure 8.16 for similar time windows are described earlier. The averaged values for HS1 have different magnitudes, and in some cases different signs, for each section and overall show a lot of difference to FS1.

Cases HS1, HS2, HS3 and HS5 showed the store to have a tendency to change the sign of roll attitude over time. Store fins were found to be more active in loads for half stroke computations especially in cases like HS4 where large fluctuations are seen to act on the fins over the duration of the drop. This suggested that in order to minimise variation in the release characteristics of the store, full stroke computations could be used.

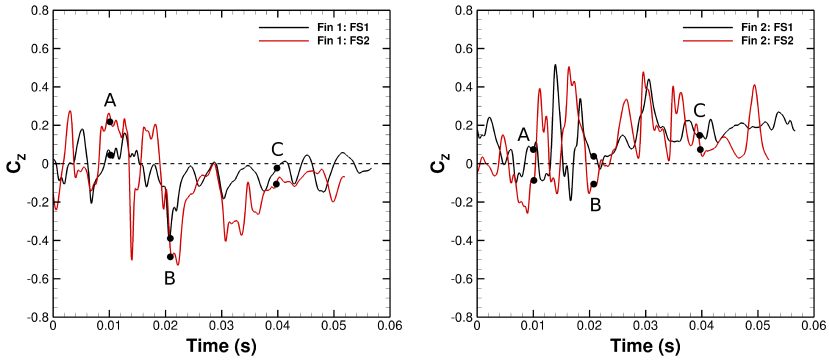

(a) Fin 1: Panel-Normal Force

(b) Fin 2: Panel-Normal Force

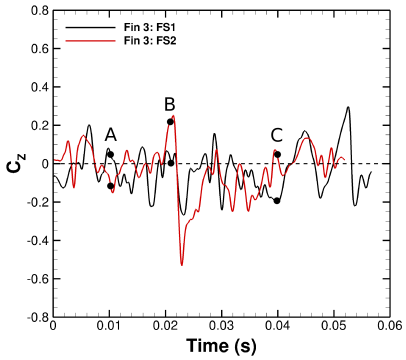

(c) Fin 3: Panel-Normal Force

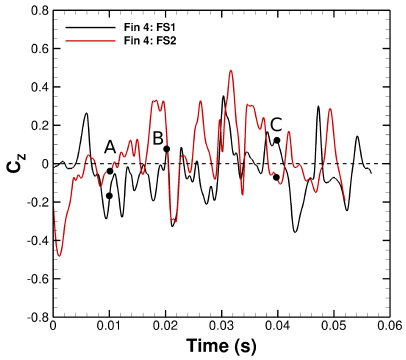

(d) Fin 4: Panel-Normal Force

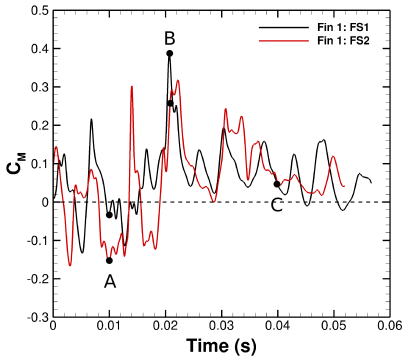

(e) Fin 1: Hinge Moment

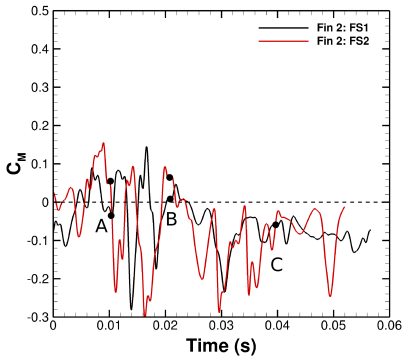

(f) Fin 2: Hinge Moment

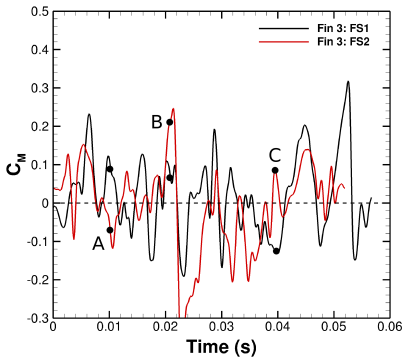

(g) Fin 3: Hinge Moment

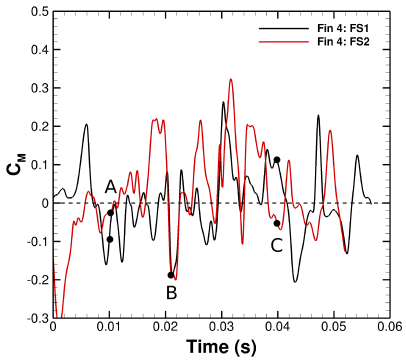

(h) Fin 4: Hinge Moment

Figure 8.4: Time-history of panel-normal-force (a-d) and hinge moment (e-h) coefficients acting on the fins comparing case FS1 and FS2. FS: Full Stroke.

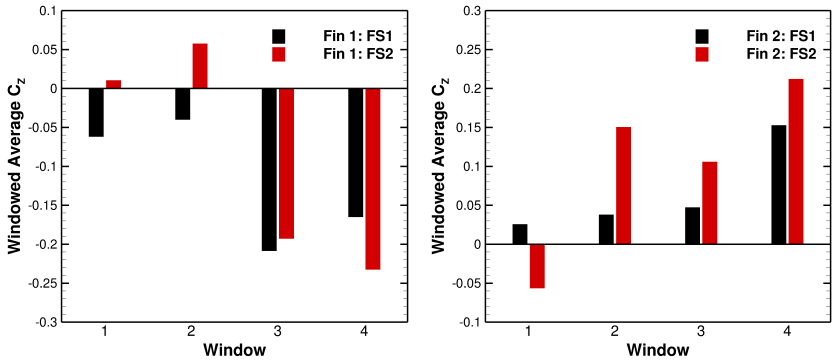

(a) Fin 1: Panel-Normal Force

(b) Fin 2: Panel-Normal Force

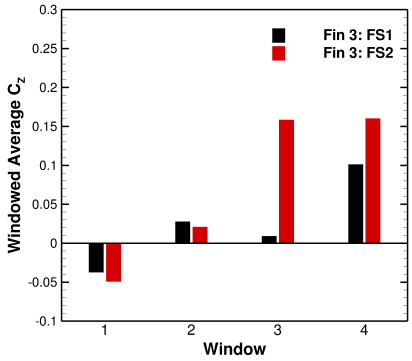

(c) Fin 3: Panel-Normal Force

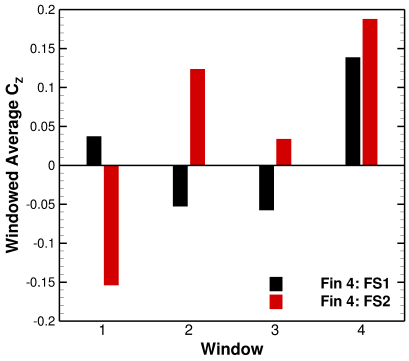

(d) Fin 4: Panel-Normal Force

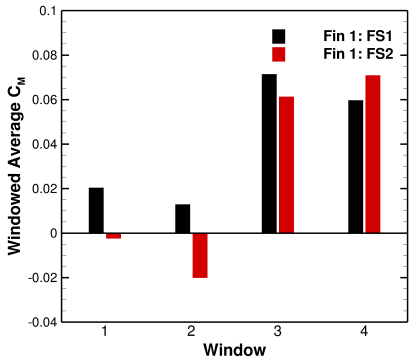

(e) Fin 1: Hinge Moment

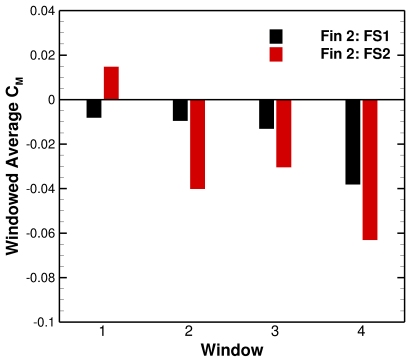

(f) Fin 2: Hinge Moment

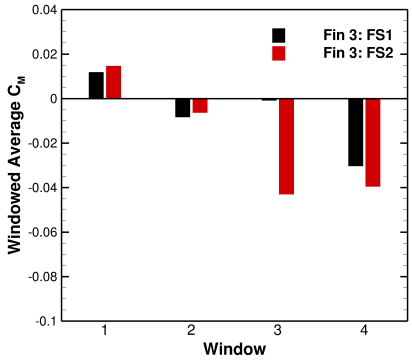

(g) Fin 3: Hinge Moment

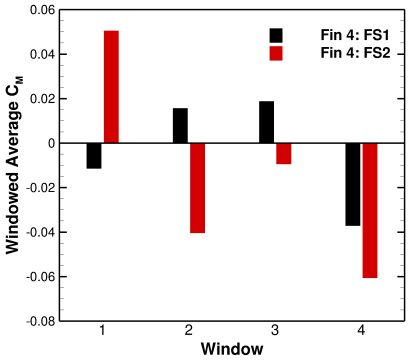

(h) Fin 4: Hinge Moment

Figure 8.5: Time-window-averaged panel-normal-force (a-d) and hinge moment (e-h) coefficients acting on the fins comparing case FS1 and FS2. FS: Full Stroke.

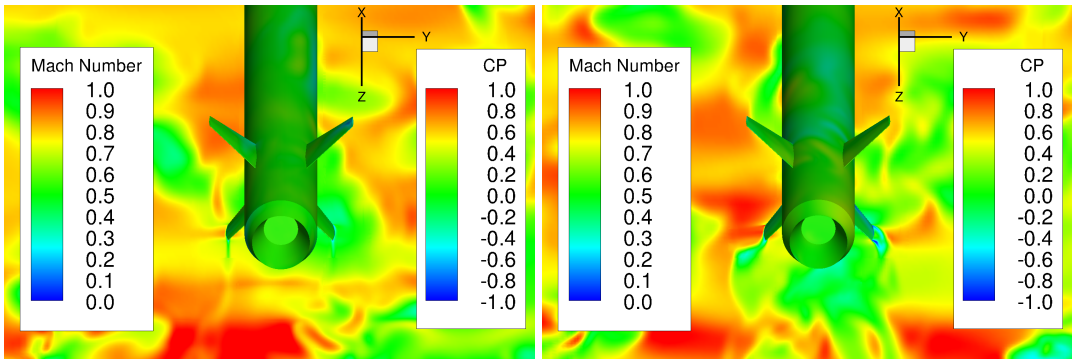

(a) Time A

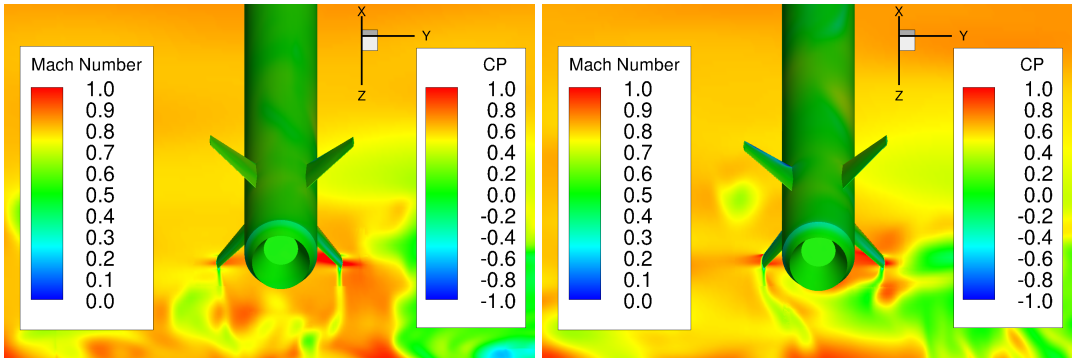

(b) Time B

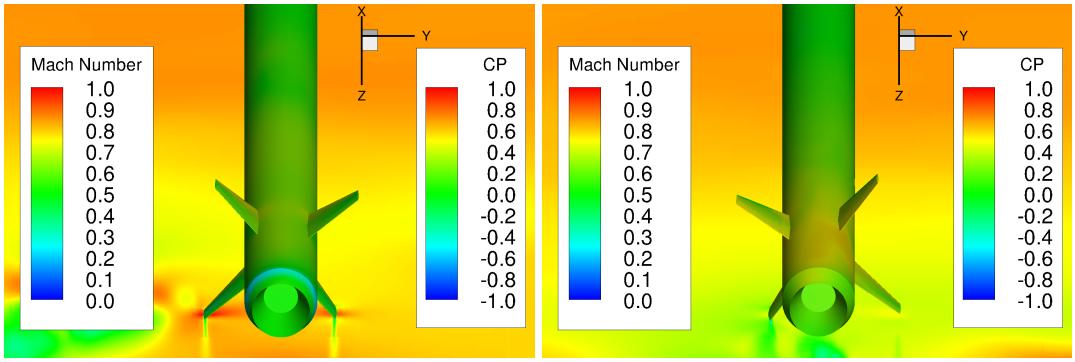

(c) Time C

Figure 8.6: Instantaneous contours of Mach number and surface C_P showing slices through Fins 1 and 2 for different time instances of the release. Cases FS1 (left column) and FS2 (right column) are compared to highlight differences in the flow-field during release.

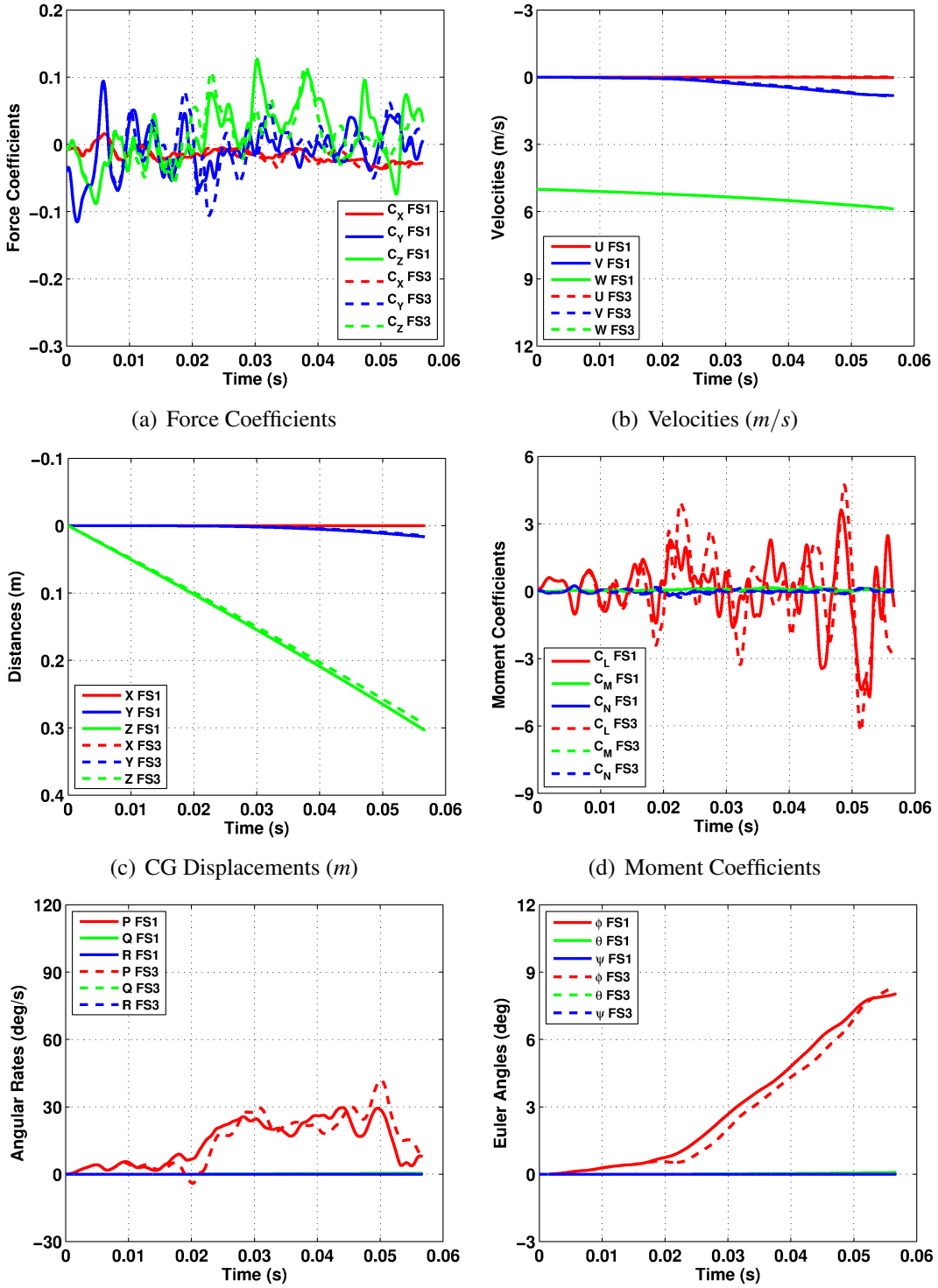

(a) Force Coefficients

(b) Velocities (m/s)

(c) CG Displacements (m)

(d) Moment Coefficients

(e) Angular Rates (deg/s)

(f) Euler Angles (deg)

Figure 8.7: Comparison of trajectories for computations FS1 and FS3. FS: Full Stroke.

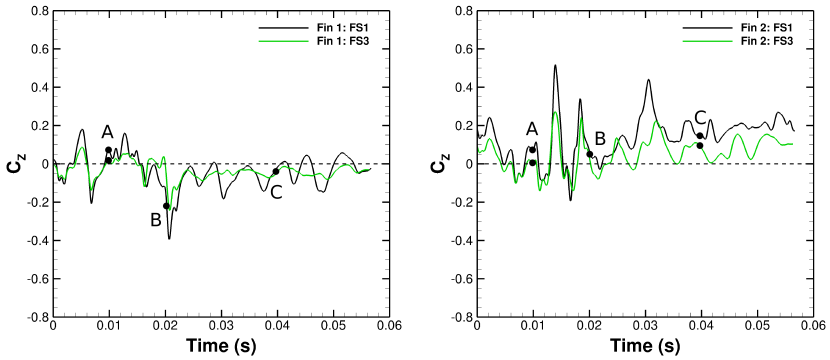

(a) Fin 1: Panel-Normal Force

(b) Fin 2: Panel-Normal Force

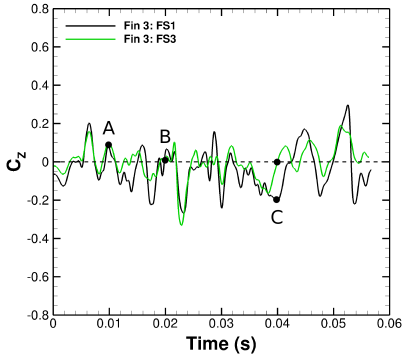

(c) Fin 3: Panel-Normal Force

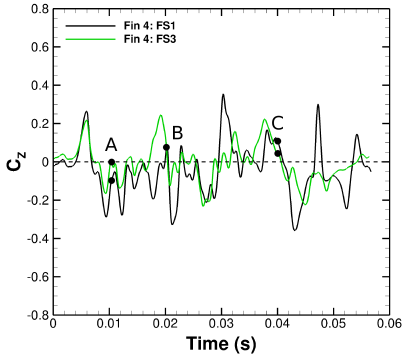

(d) Fin 4: Panel-Normal Force

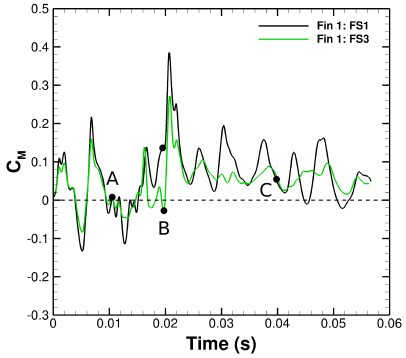

(e) Fin 1: Hinge Moment

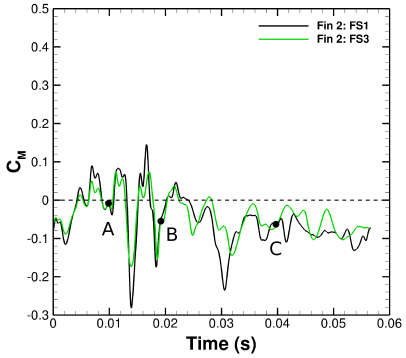

(f) Fin 2: Hinge Moment

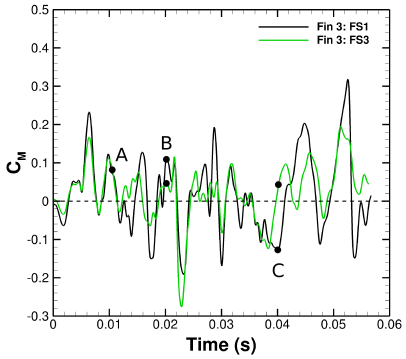

(g) Fin 3: Hinge Moment

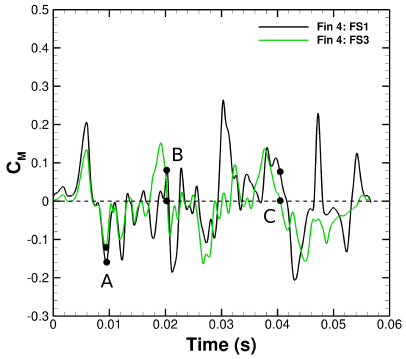

(h) Fin 4: Hinge Moment

Figure 8.8: Time-history of panel-normal-force (a-d) and hinge moment (e-h) coefficients acting on the fins comparing case FS1 and FS3. FS: Full Stroke.

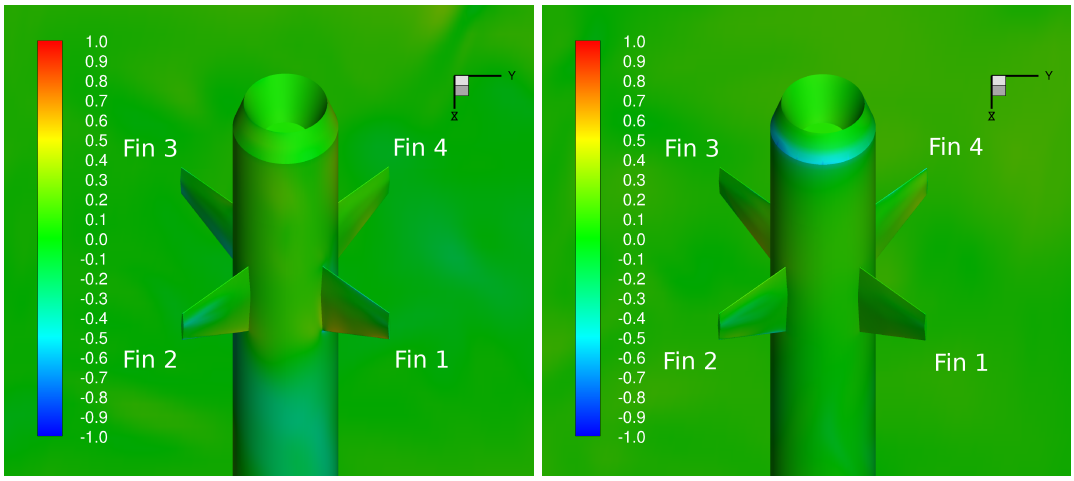

(a) Time A

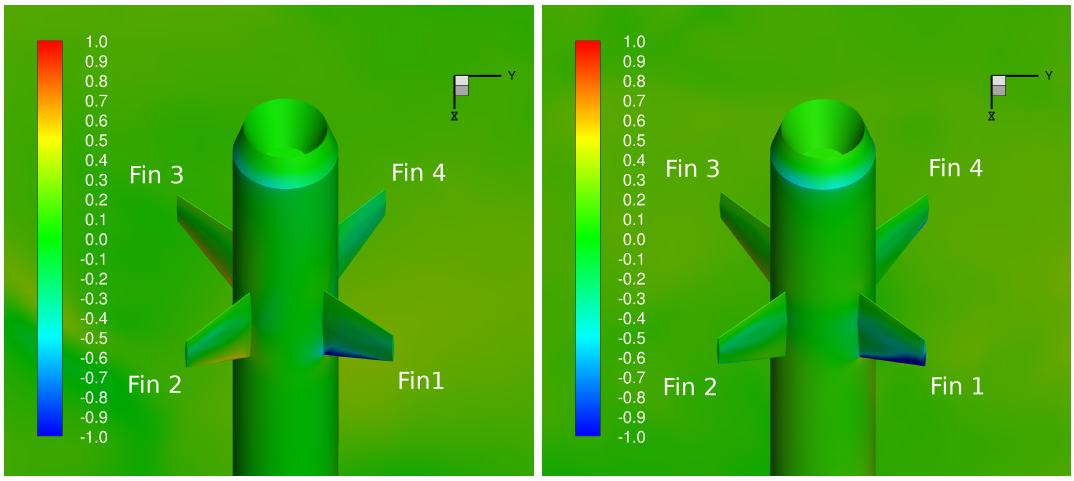

(b) Time B

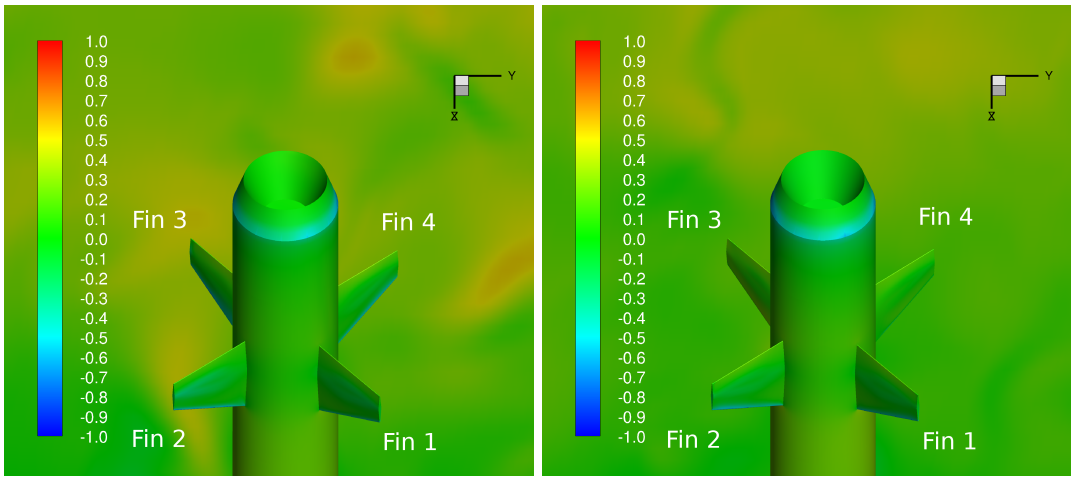

(c) Time C

Figure 8.9: Instantaneous contours of surface C_P comparing case FS1 (left column) and FS3 (right column) at different time instances (as denoted in the previous Figure 8.8). FS: Full Stroke.

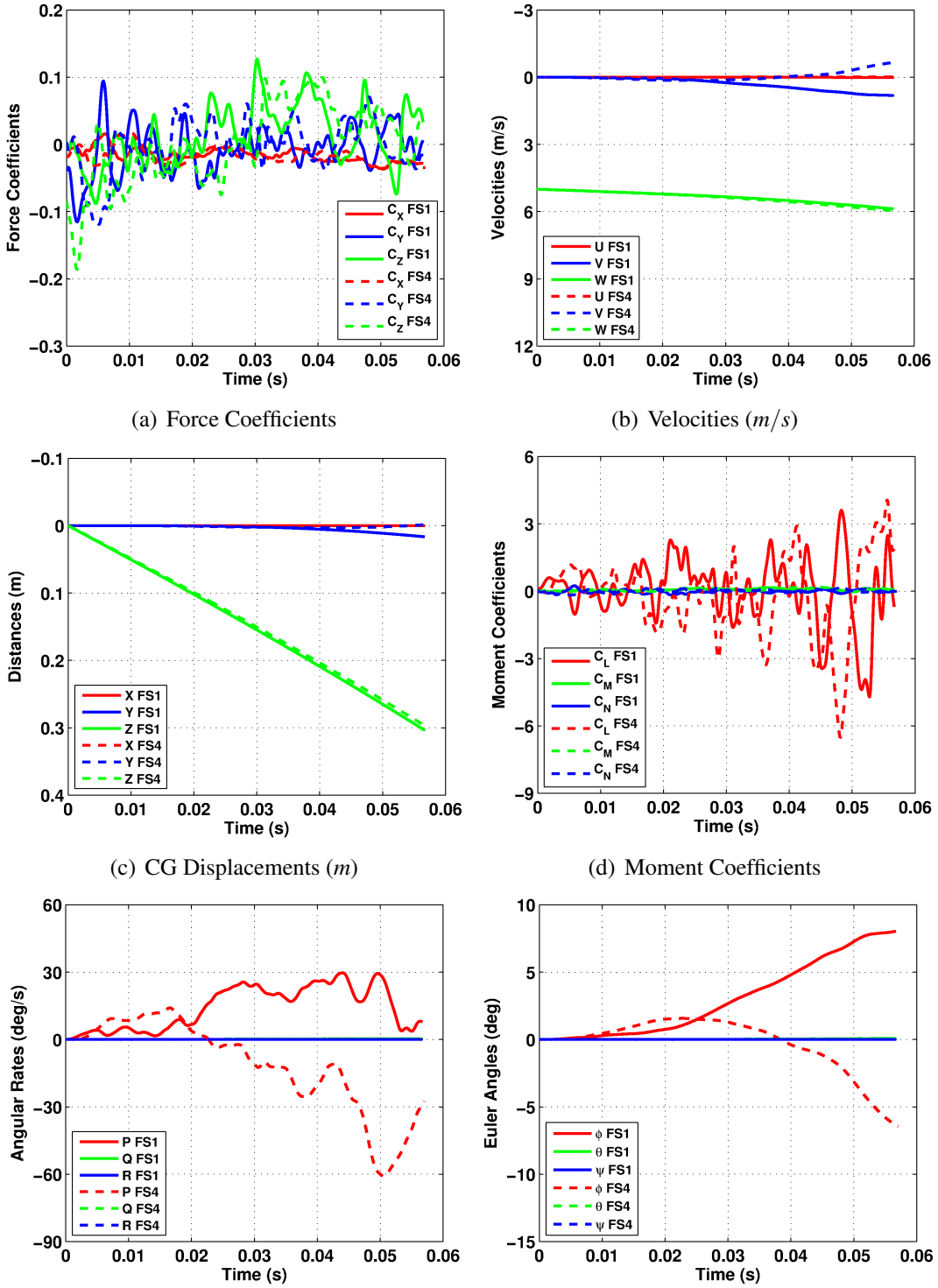

(a) Force Coefficients

(b) Velocities (m/s)

(c) CG Displacements (m)

(d) Moment Coefficients

(e) Angular Rates (deg/s)

(f) Euler Angles (deg)

Figure 8.10: Comparison of trajectories for computations FS1 and FS4. FS: Full Stroke.

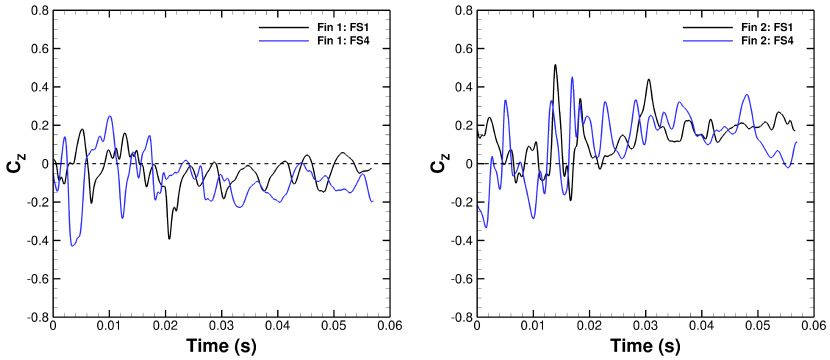

(a) Fin 1: Panel-Normal Force

(b) Fin 2: Panel-Normal Force

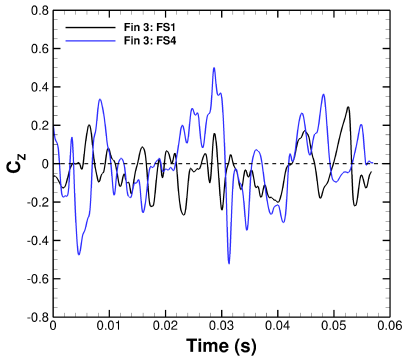

(c) Fin 3: Panel-Normal Force

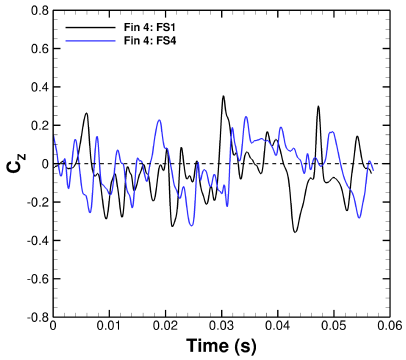

(d) Fin 4: Panel-Normal Force

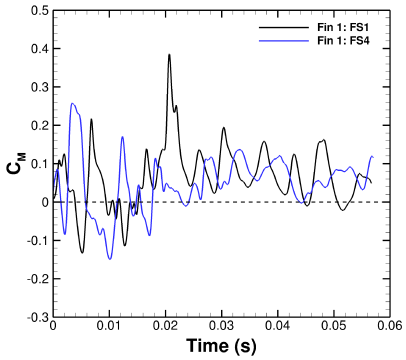

(e) Fin 1: Hinge Moment

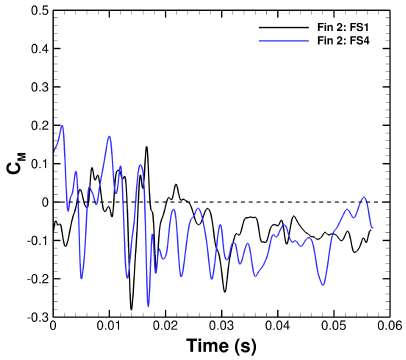

(f) Fin 2: Hinge Moment

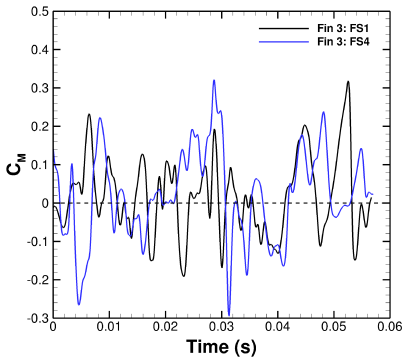

(g) Fin 3: Hinge Moment

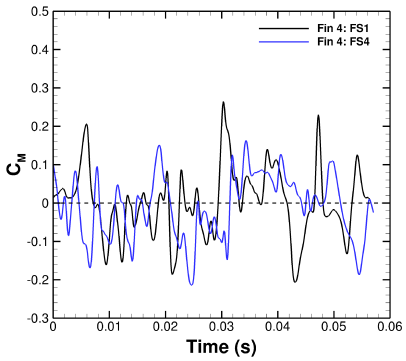

(h) Fin 4: Hinge Moment

Figure 8.11: Time-history of panel-normal-force (a-d) and hinge moment (e-h) coefficients acting on the fins comparing case FS1 and FS4. FS: Full Stroke.

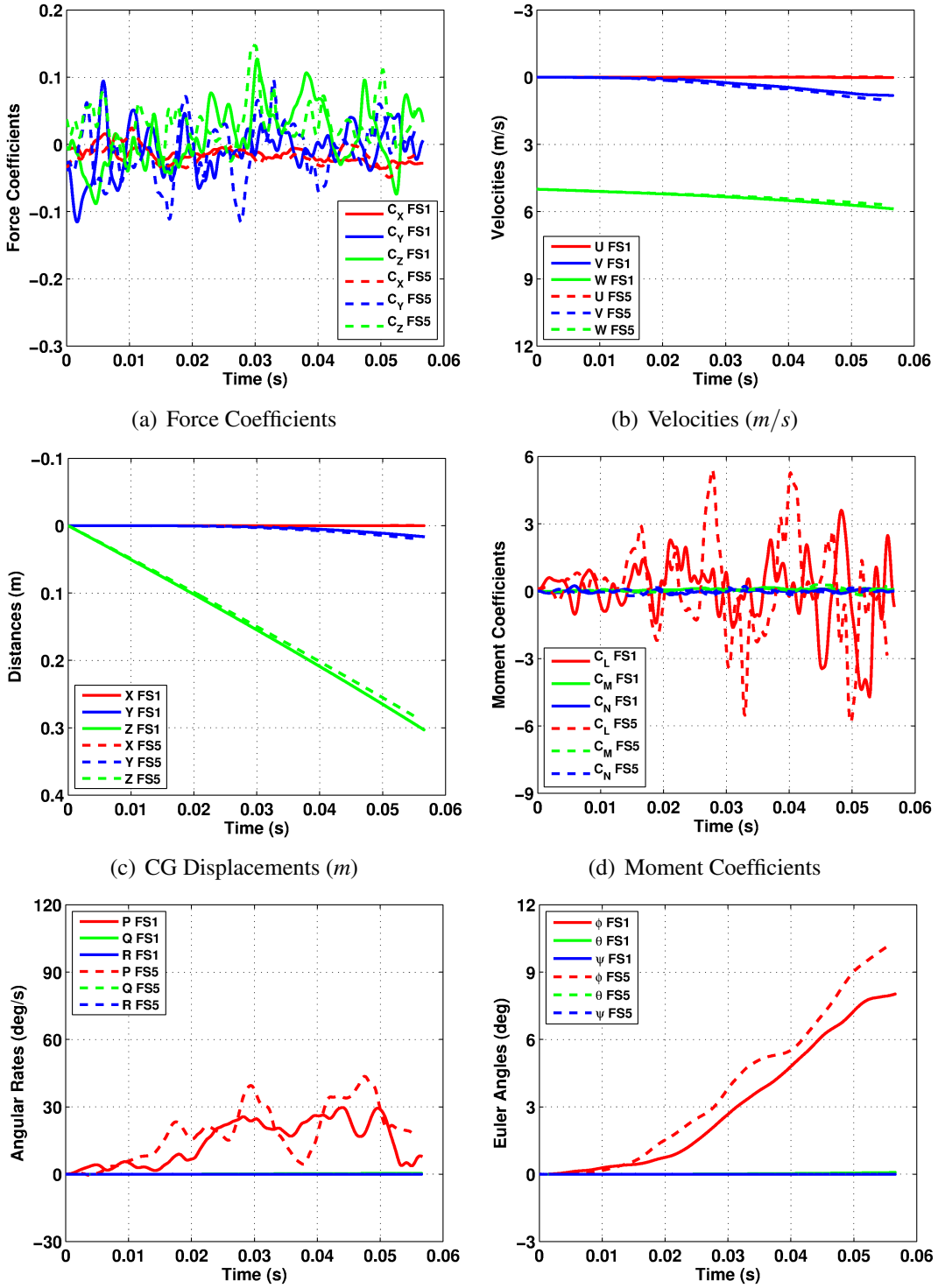

(a) Force Coefficients

(b) Velocities (m/s)

(c) CG Displacements (m)

(d) Moment Coefficients

(e) Angular Rates (deg/s)

(f) Euler Angles (deg)

Figure 8.12: Comparison of trajectories for computations FS1 and FS5. FS: Full Stroke.

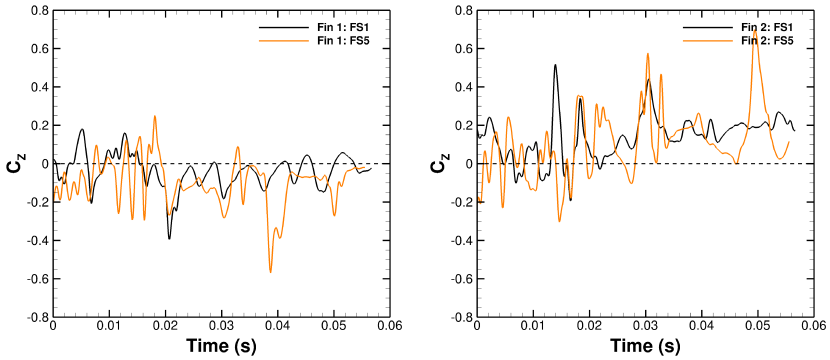

(a) Fin 1: Panel-Normal Force

(b) Fin 2: Panel-Normal Force

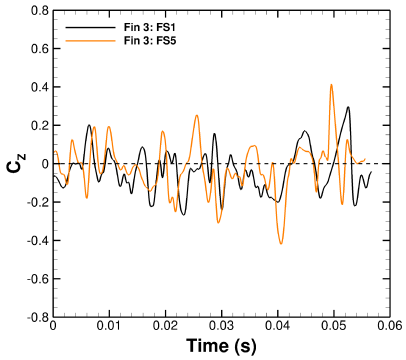

(c) Fin 3: Panel-Normal Force

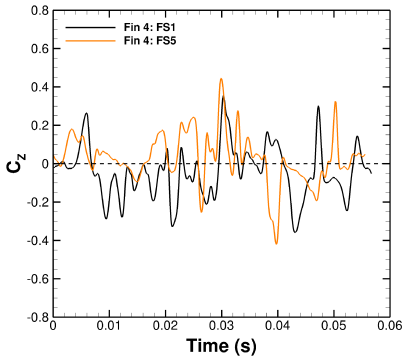

(d) Fin 4: Panel-Normal Force

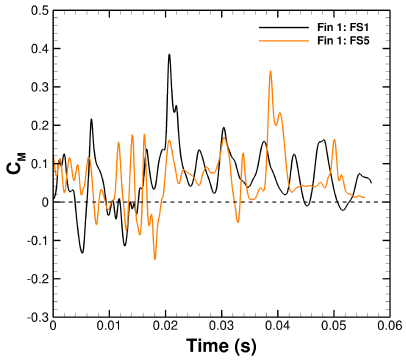

(e) Fin 1: Hinge Moment

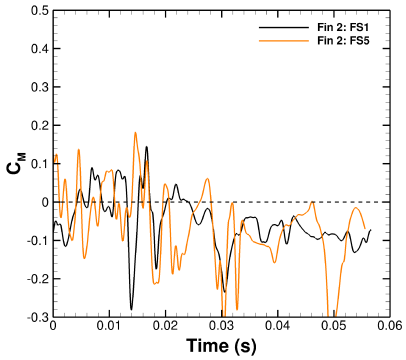

(f) Fin 2: Hinge Moment

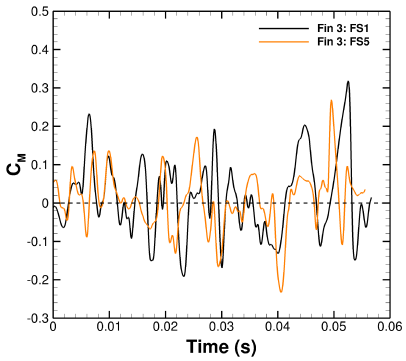

(g) Fin 3: Hinge Moment

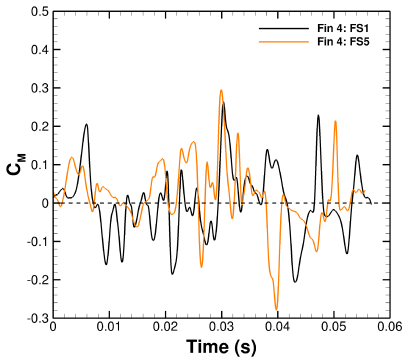

(h) Fin 4: Hinge Moment

Figure 8.13: Time-history of panel-normal-force (a-d) and hinge moment (e-h) coefficients acting on the fins comparing case FS1 and FS5. FS: Full Stroke.

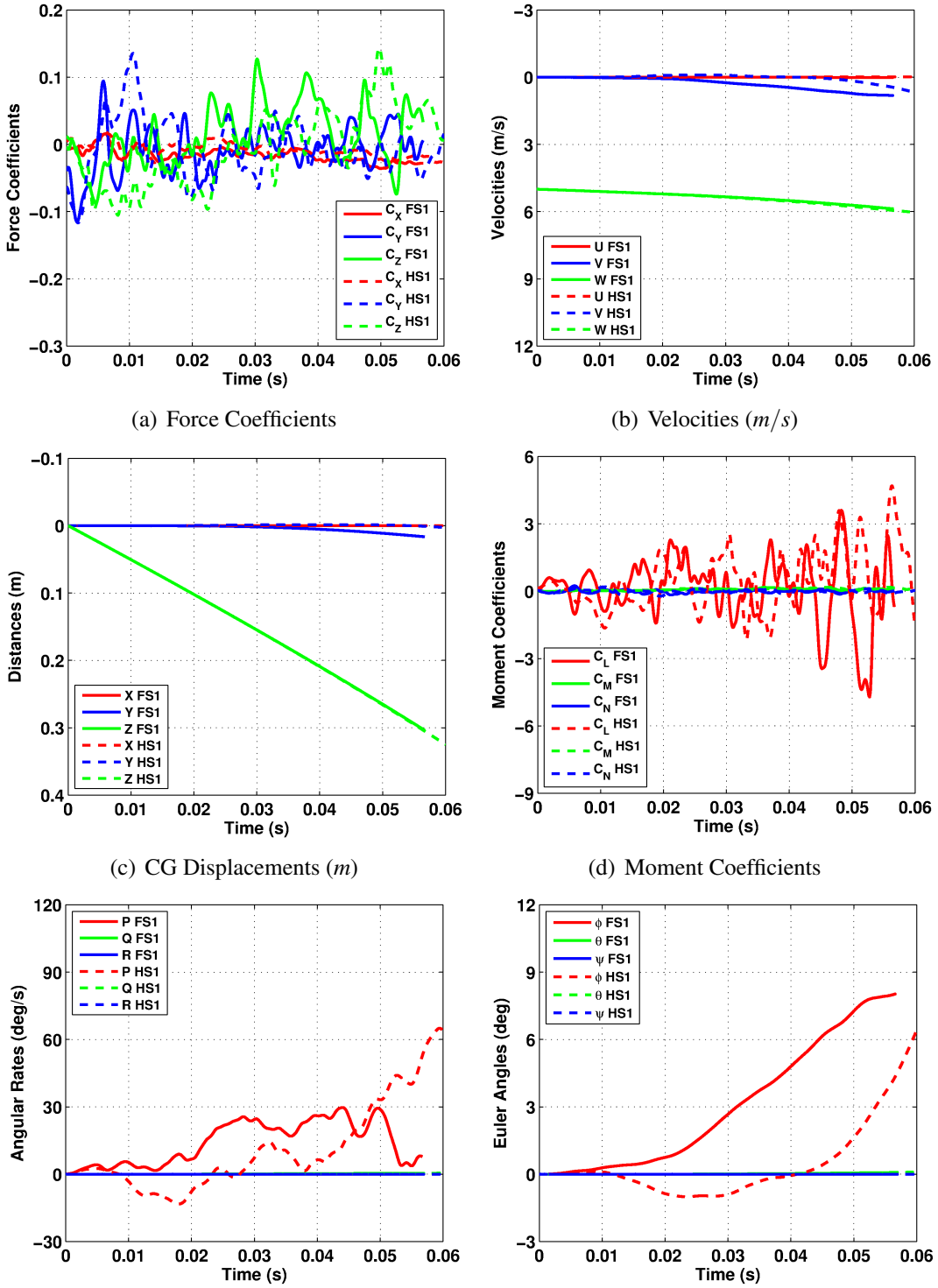

(a) Force Coefficients

(b) Velocities (m/s)

(c) CG Displacements (m)

(d) Moment Coefficients

(e) Angular Rates (deg/s)

(f) Euler Angles (deg)

Figure 8.14: Comparison of trajectories for computations FS1 and HS1. FS: Full Stroke, HS: Half Stroke.

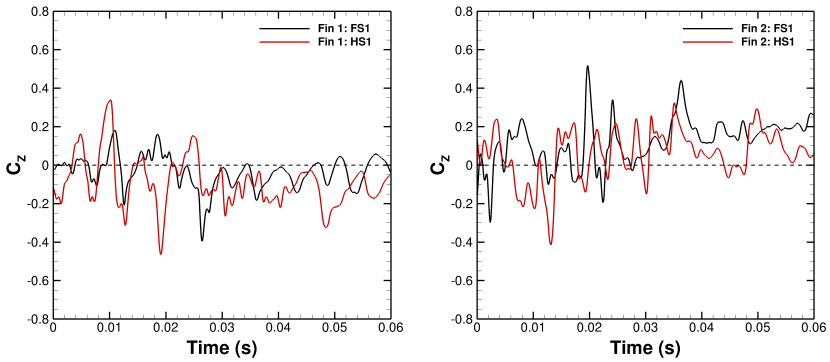

(a) Fin 1: Panel-Normal Force

(b) Fin 2: Panel-Normal Force

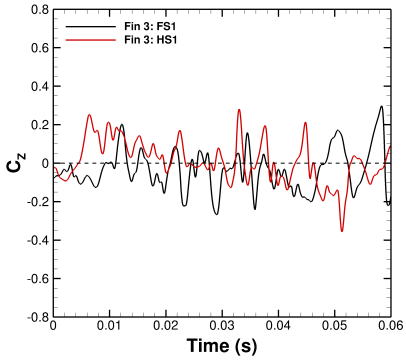

(c) Fin 3: Panel-Normal Force

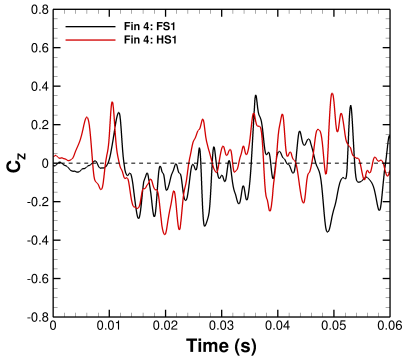

(d) Fin 4: Panel-Normal Force

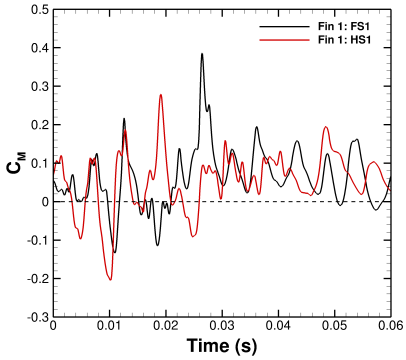

(e) Fin 1: Hinge Moment

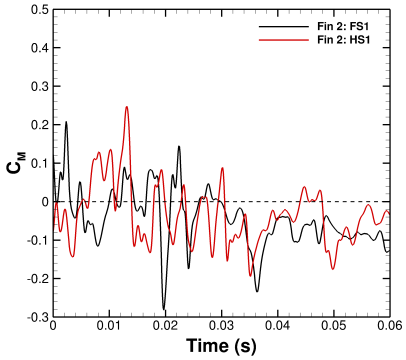

(f) Fin 2: Hinge Moment

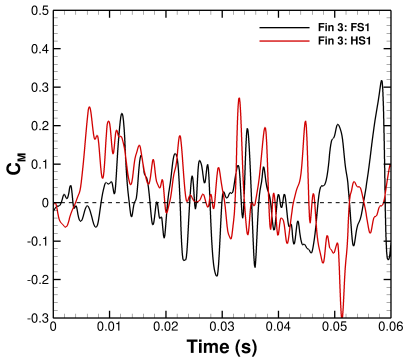

(g) Fin 3: Hinge Moment

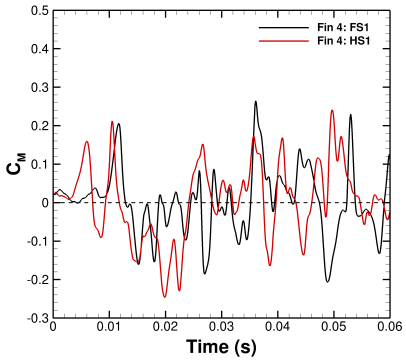

(h) Fin 4: Hinge Moment

Figure 8.15: Time-history of panel-normal-force (a-d) and hinge moment (e-h) coefficients acting on the fins comparing case FS1 and HS1. FS: Full Stroke, HS: Half Stroke.

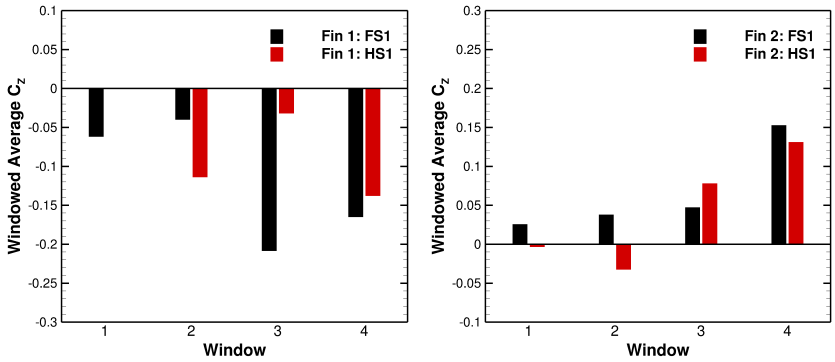

(a) Fin 1: Panel-Normal Force

(b) Fin 2: Panel-Normal Force

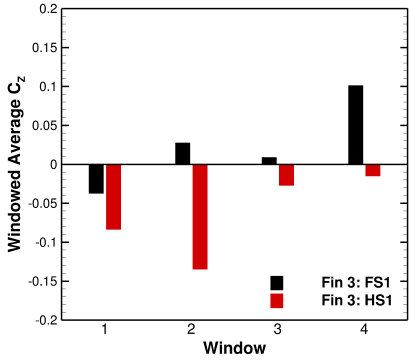

(c) Fin 3: Panel-Normal Force

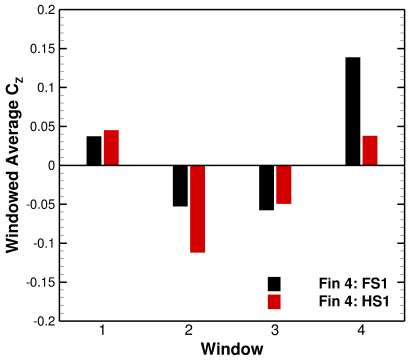

(d) Fin 4: Panel-Normal Force

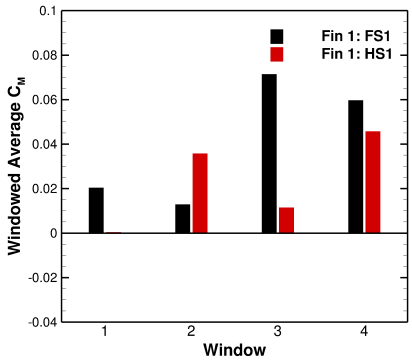

(e) Fin 1: Hinge Moment

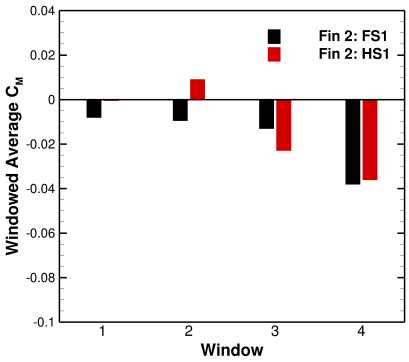

(f) Fin 2: Hinge Moment

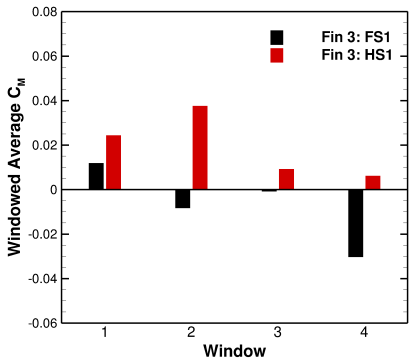

(g) Fin 3: Hinge Moment

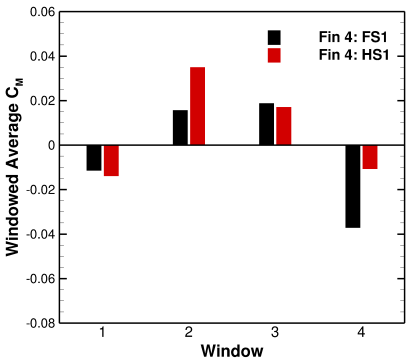

(h) Fin 4: Hinge Moment

Figure 8.16: Time-window-averaged panel-normal-force (a-d) and hinge moment (e-h) coefficients acting on the fins comparing case FS1 and HS1. FS: Full Stroke, HS: Half Stroke.

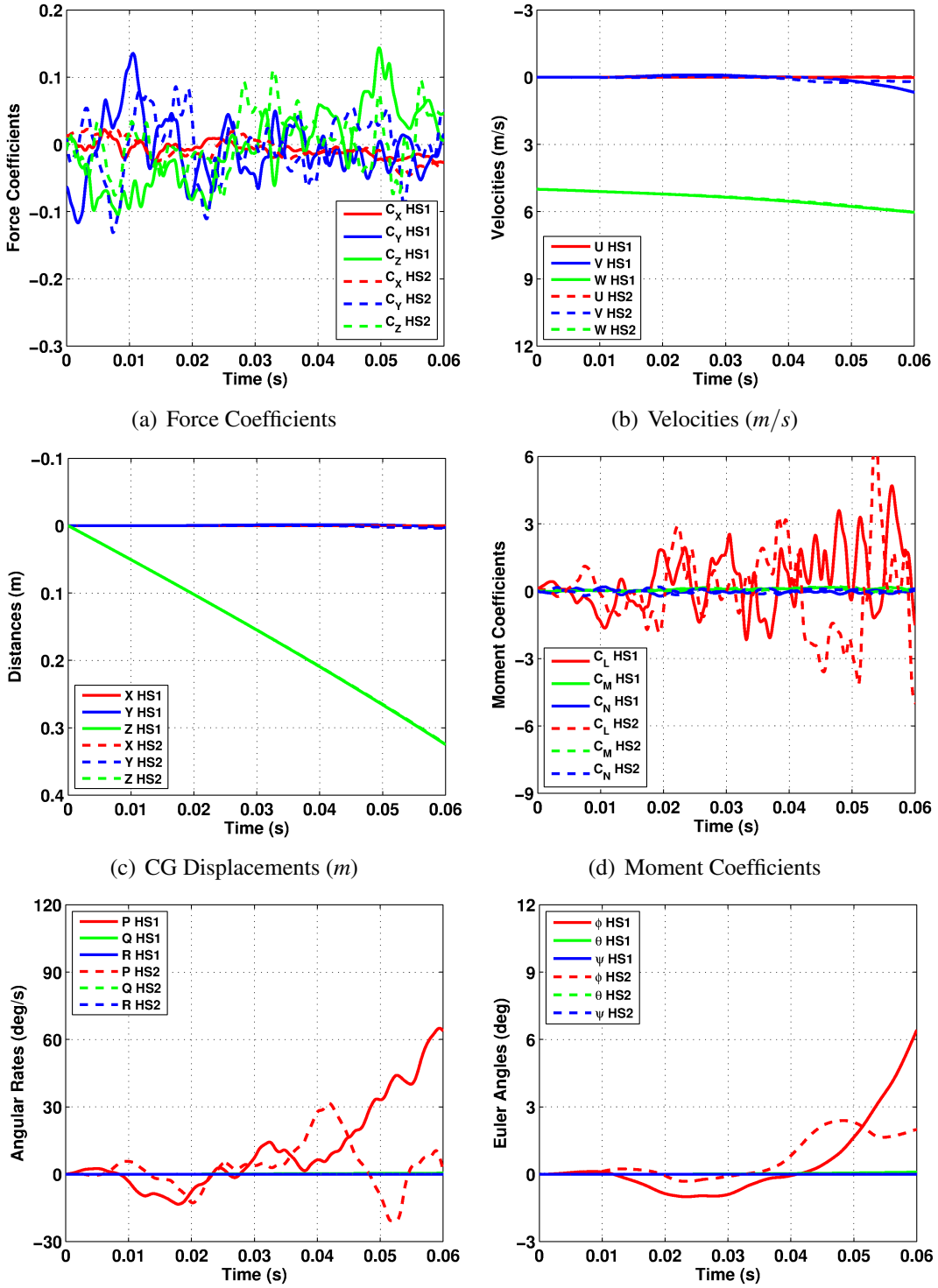

(a) Force Coefficients

(b) Velocities (m/s)

(c) CG Displacements (m)

(d) Moment Coefficients

(e) Angular Rates (deg/s)

(f) Euler Angles (deg)

Figure 8.17: Comparison of trajectories for computations HS1 and HS2. HS: Half Stroke.

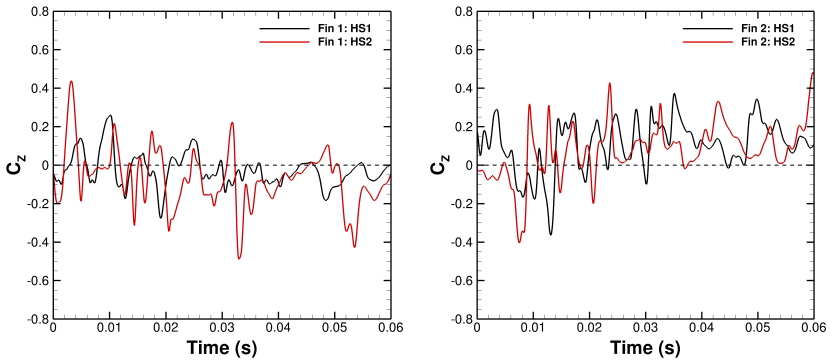

(a) Fin 1: Panel-Normal Force

(b) Fin 2: Panel-Normal Force

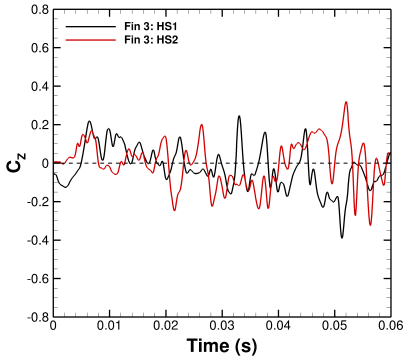

(c) Fin 3: Panel-Normal Force

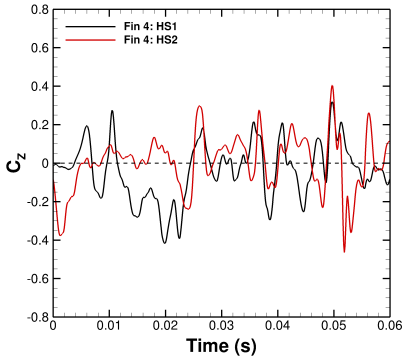

(d) Fin 4: Panel-Normal Force

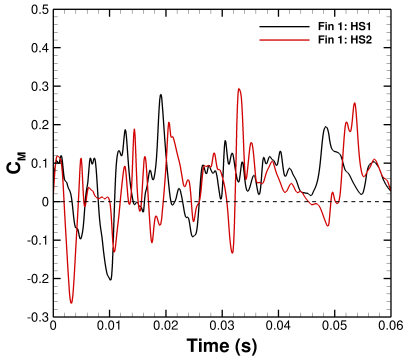

(e) Fin 1: Hinge Moment

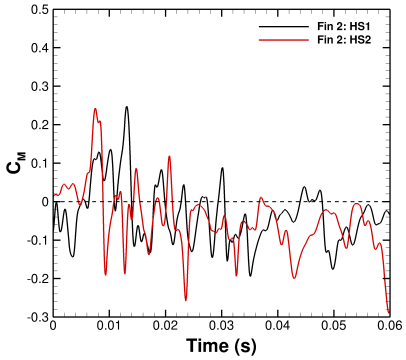

(f) Fin 2: Hinge Moment

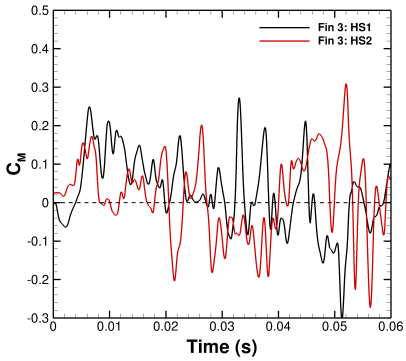

(g) Fin 3: Hinge Moment

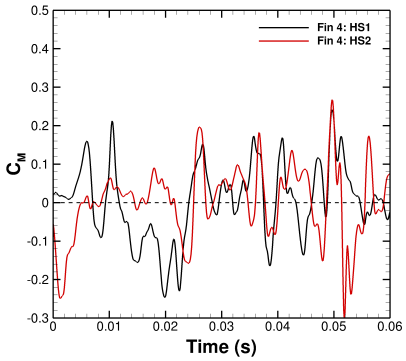

(h) Fin 4: Hinge Moment

Figure 8.18: Time-history of panel-normal-force (a-d) and hinge moment (e-h) coefficients acting on the fins comparing case HS1 and HS2. HS: Half Stroke.

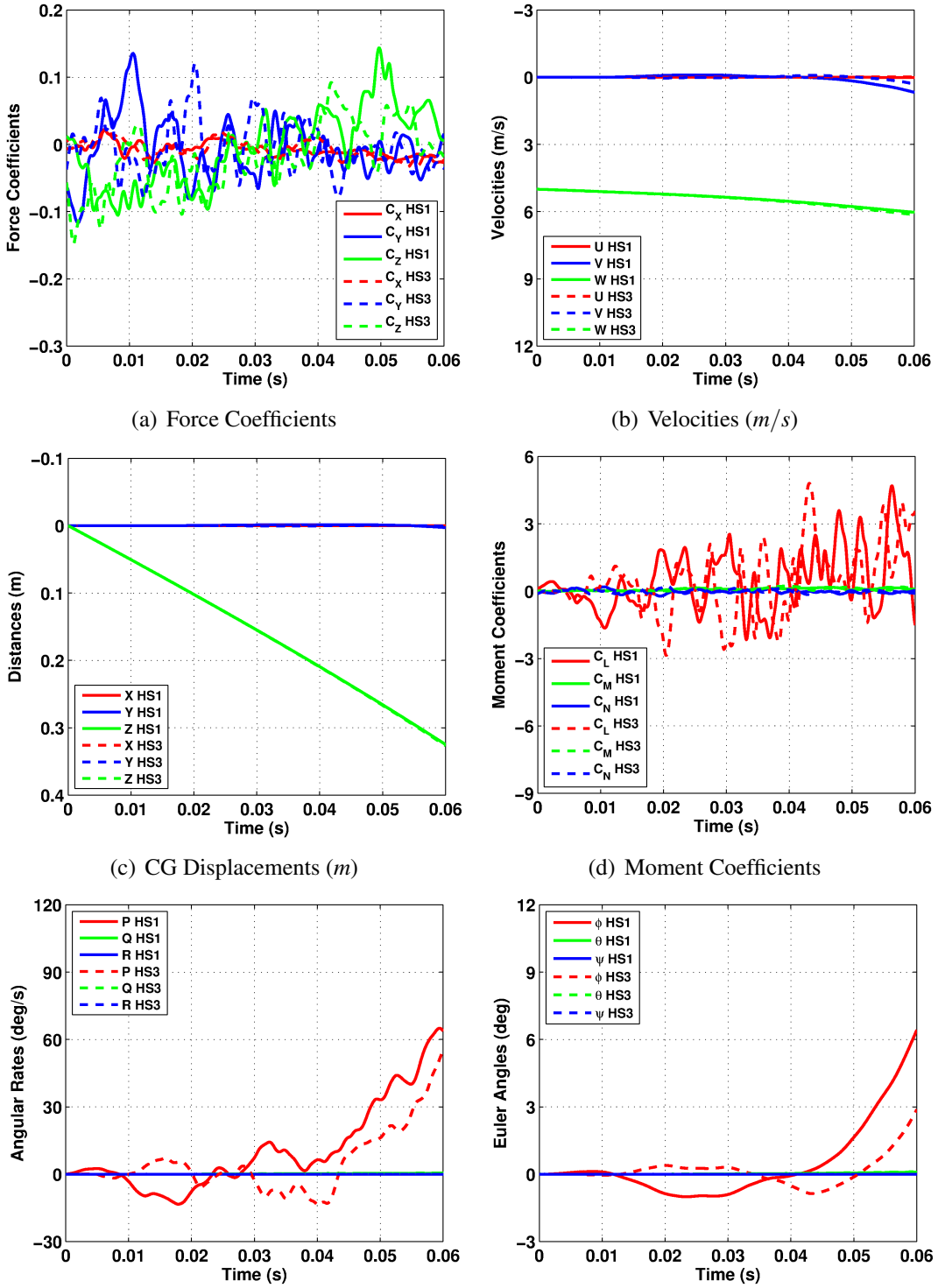

(a) Force Coefficients

(b) Velocities (m/s)

(c) CG Displacements (m)

(d) Moment Coefficients

(e) Angular Rates (deg/s)

(f) Euler Angles (deg)

Figure 8.19: Comparison of trajectories for computations HS1 and HS3. HS: Half Stroke.

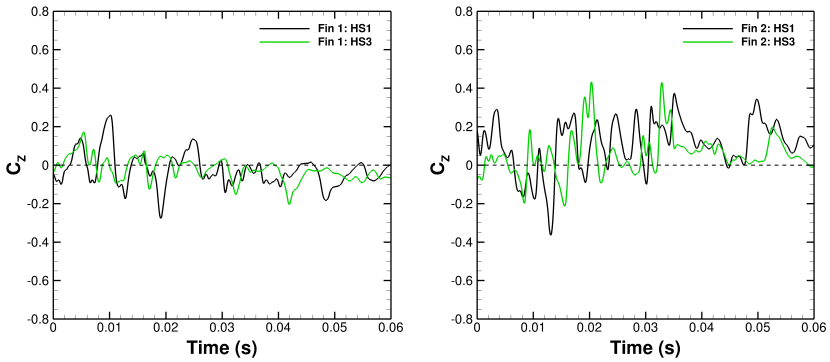

(a) Fin 1: Panel-Normal Force

(b) Fin 2: Panel-Normal Force

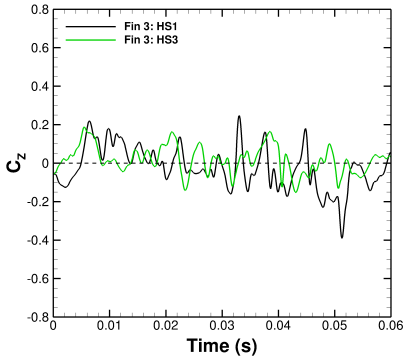

(c) Fin 3: Panel-Normal Force

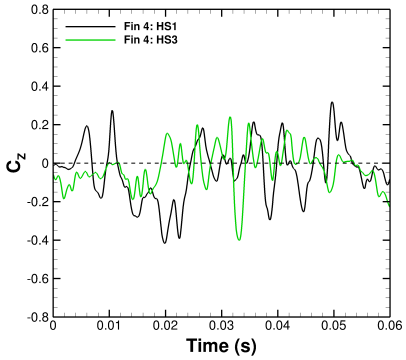

(d) Fin 4: Panel-Normal Force

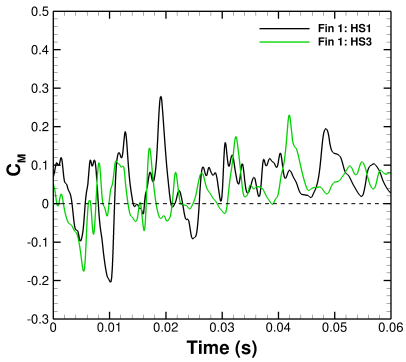

(e) Fin 1: Hinge Moment

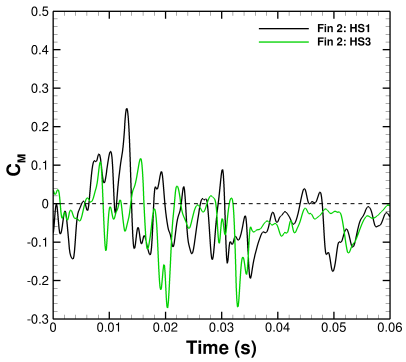

(f) Fin 2: Hinge Moment

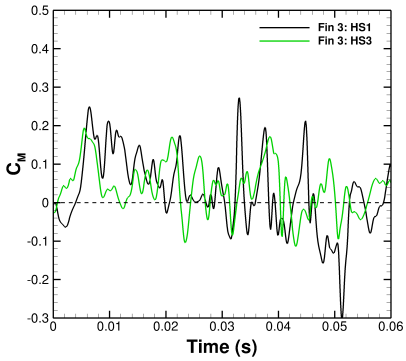

(g) Fin 3: Hinge Moment

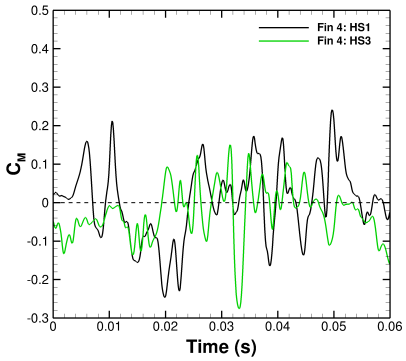

(h) Fin 4: Hinge Moment

Figure 8.20: Time-history of panel-normal-force (a-d) and hinge moment (e-h) coefficients acting on the fins comparing case HS1 and HS3. .HS: Half Stroke

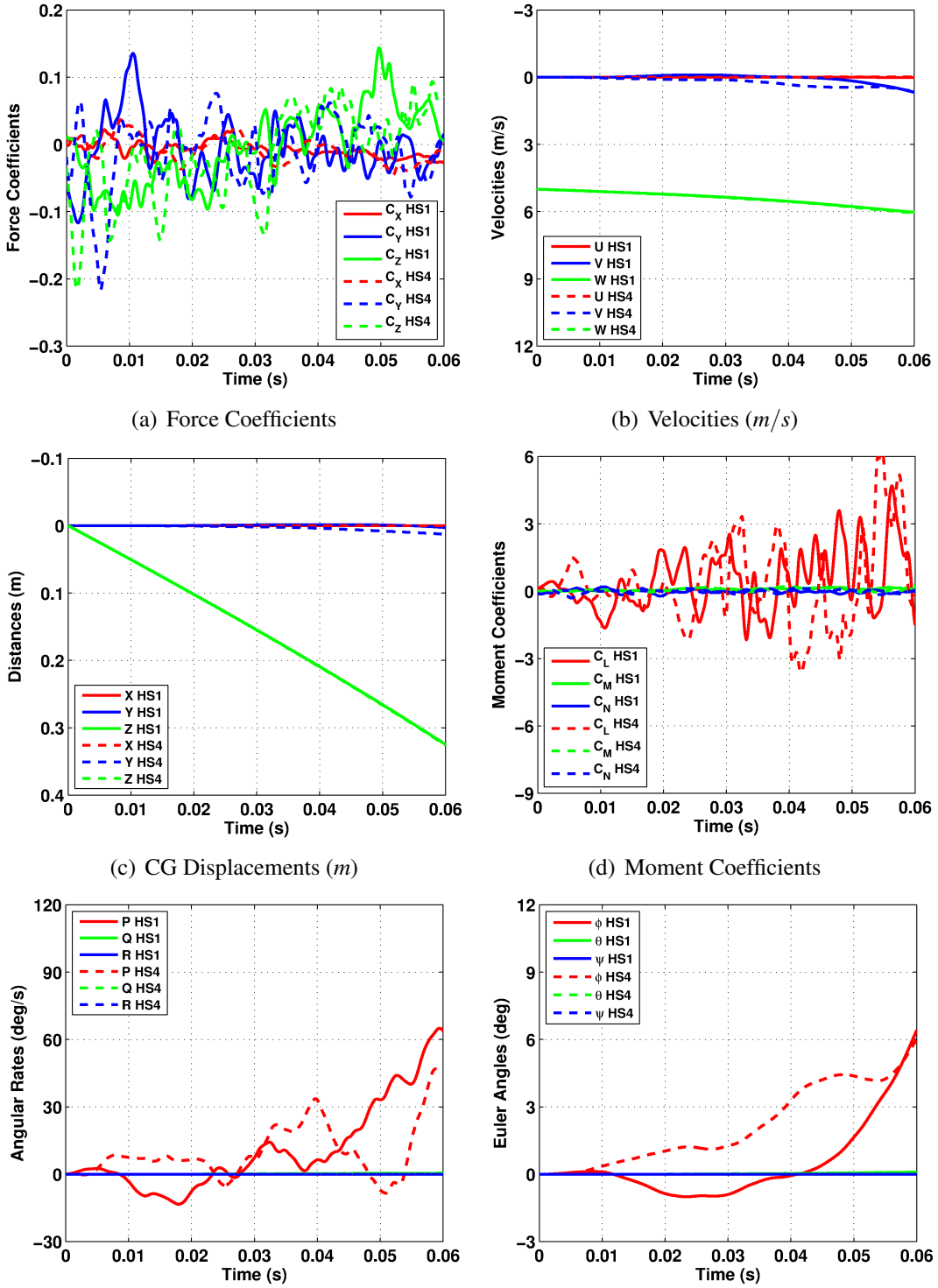

(a) Force Coefficients

(b) Velocities (m/s)

(c) CG Displacements (m)

(d) Moment Coefficients

(e) Angular Rates (deg/s)

(f) Euler Angles (deg)

Figure 8.21: Comparison of trajectories for computations HS1 and HS4. HS: Half Stroke.

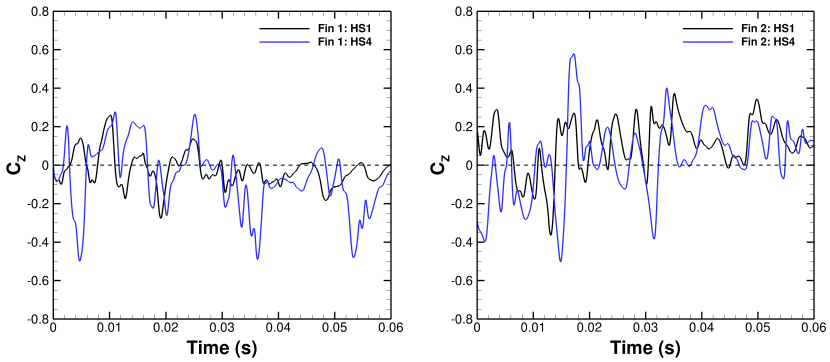

(a) Fin 1: Panel-Normal Force (b) Fin 2: Panel-Normal Force

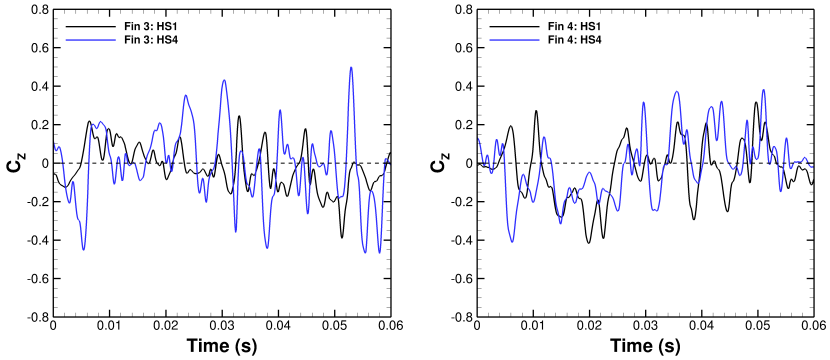

(c) Fin 3: Panel-Normal Force (d) Fin 4: Panel-Normal Force

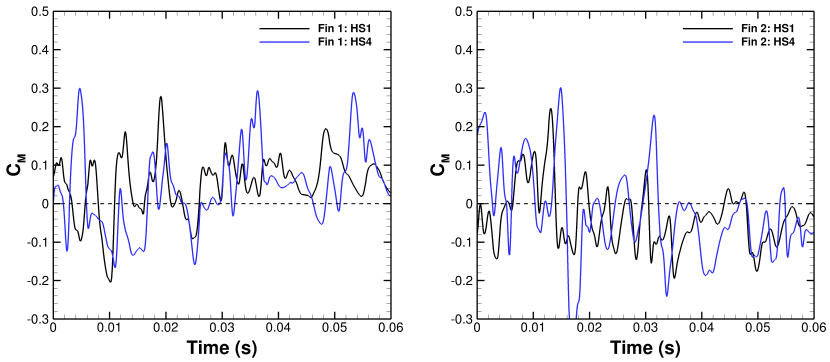

(e) Fin 1: Hinge Moment (f) Fin 2: Hinge Moment

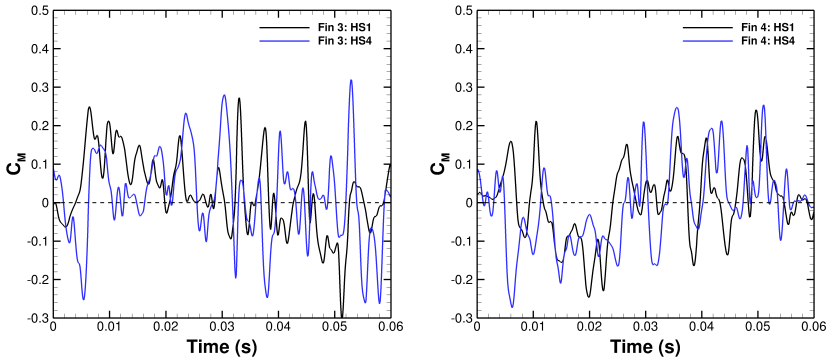

(g) Fin 3: Hinge Moment (h) Fin 4: Hinge Moment

Figure 8.22: Time-history of panel-normal-force (a-d) and hinge moment (e-h) coefficients acting on the fins comparing case HS1 and HS4. HS: Half Stroke.

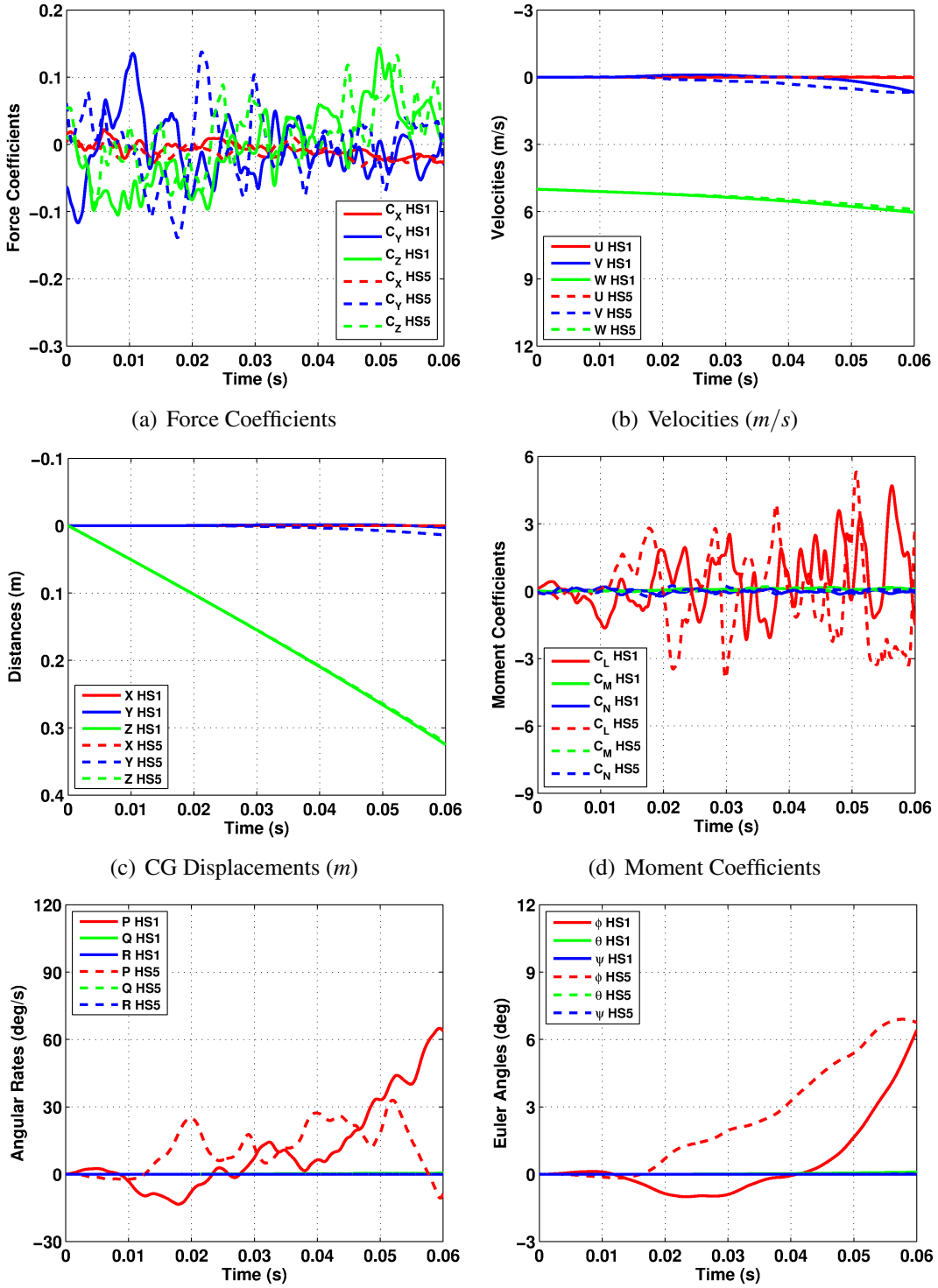

(a) Force Coefficients

(b) Velocities (m/s)

(c) CG Displacements (m)

(d) Moment Coefficients

(e) Angular Rates (deg/s)

(f) Euler Angles (deg)

Figure 8.23: Comparison of trajectories for computations HS1 and HS5. HS: Half Stroke.

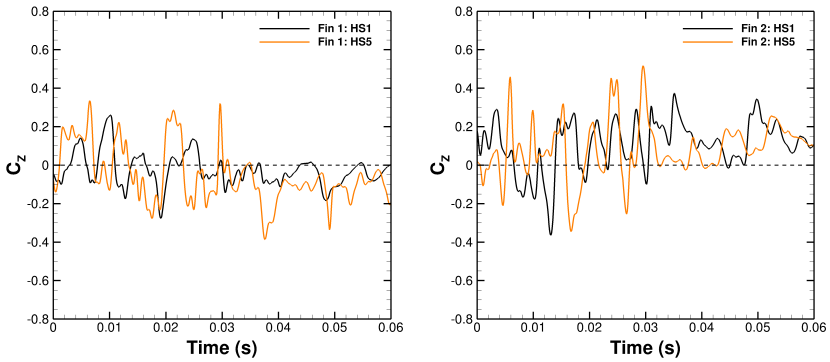

(a) Fin 1: Panel-Normal Force (b) Fin 2: Panel-Normal Force

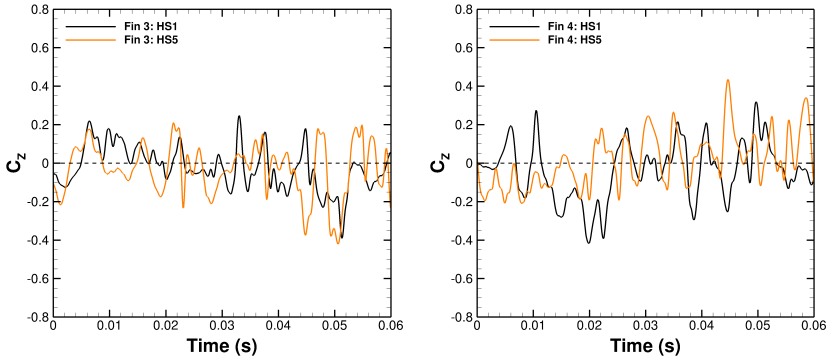

(c) Fin 3: Panel-Normal Force (d) Fin 4: Panel-Normal Force

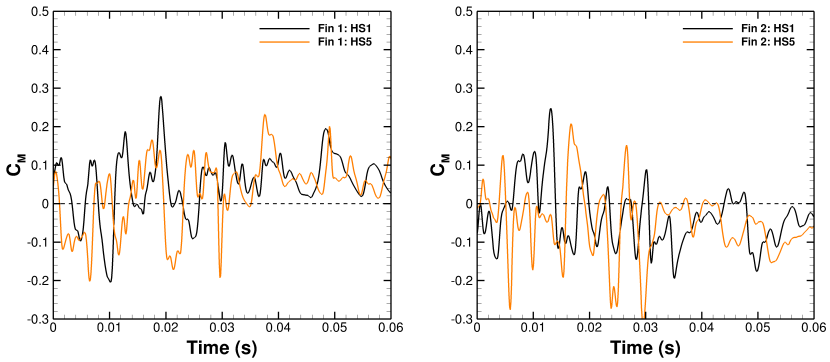

(e) Fin 1: Hinge Moment (f) Fin 2: Hinge Moment

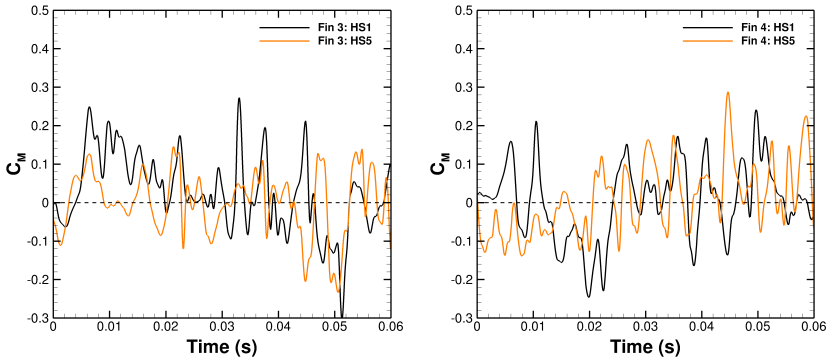

(g) Fin 3: Hinge Moment (h) Fin 4: Hinge Moment

Figure 8.24: Time-history of panel-normal-force (a-d) and hinge moment (e-h) coefficients acting on the fins comparing case HS1 and HS5. HS: Half Stroke.

While most cases showed similar store translations but with variations in roll attitude, one case was observed to have a different trajectory. This particular case labelled FS6 was compared with FS1 in Figure 8.25 for the store loads and trajectory. In FS6 the store was released after 0.4s and for the initial 0.02s showed similar CG displacements and variations in roll attitude. After this it developed a negative nose-down pitch attitude in addition to a growing roll attitude. The pitch attitude increased the axial force and also reduced the normal velocity until the velocity began to increase negatively. This affected the displacement of the CG such that the it moved back into the cavity. Figure 8.25(c) was marked at different time instances to present the corresponding flow visualisations.

Figure 8.27 presents the time history of the fin loads for FS6 compared with FS1 where several peak could be seen in the loads during the release. Time-window-averaged loads (Figure 8.28) showed variations in magnitude of the loads and in some instances the sign was seen to be reversed.

Figure 8.26 presents surface C_P contours and iso-surfaces of Q-Criteria to highlight the asymmetry of the flow. The figures correspond to case HS4, used as an example, at an instant in time corresponding to 0.015s after release and show how at that instant in time, Fin 2 was in contact with a vortical structure creating a region of low pressure. Fin 1, which is part of a fin pair of fins 1 and 2, is not in contact with a similar structure, in addition to which, differences in structural content can be seen on either side of the cavity. This asymmetry of the flow could suggest the differences in the roll attitudes between the different cases, as the flow at any two instances in time does not have to be the same. This is further highlighted in the time-accurate fin load histories showing panel-normal force and hinge moment coefficients in Figure 8.27 that compares cases FS1 and FS6. Each peak corresponds to a structure that comes into contact with a fin.

Flow visualisations of instantaneous Mach number and surface C_P, shown in Figures 8.29 and 8.29 respectively for case FS1 and FS6, show how the trajectory of the store and the flow-field in and around the cavity change over time. Interestingly, at Time D for FS6, high velocity flow dipped into the cavity along its centreline and came into contact with fins 1 and 2. Of the eleven computations, FS6 showed a different trajectory highlighting the variability for different release times.

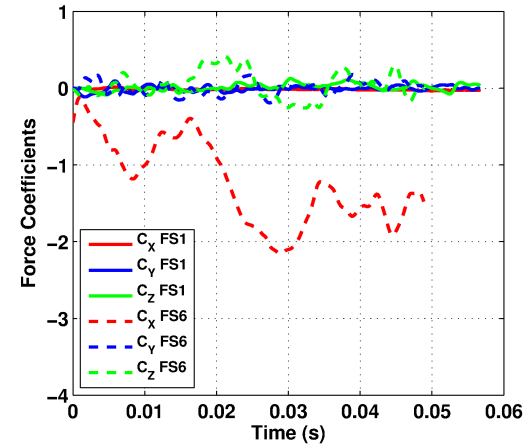

(a) Force Coefficients

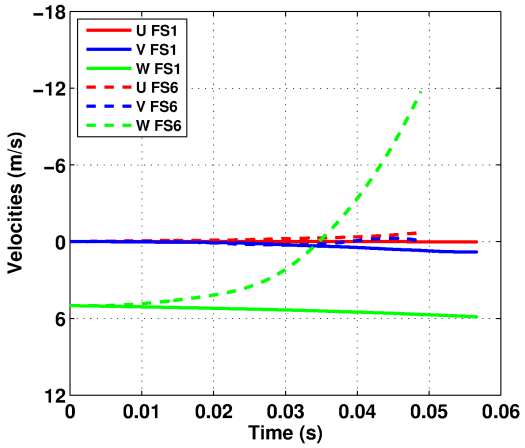

(b) Velocities (m/s)

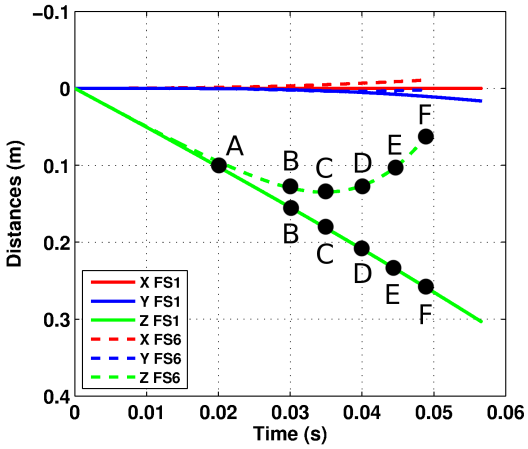

(c) CG Displacements (m)

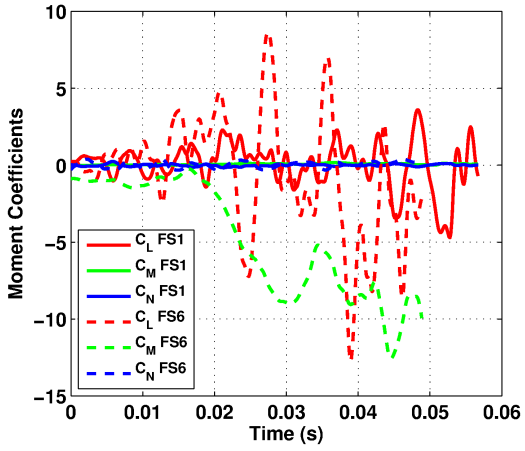

(d) Moment Coefficients

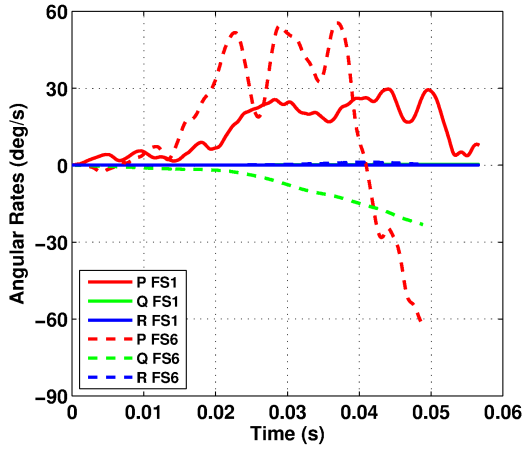

(e) Angular Rates (deg/s)

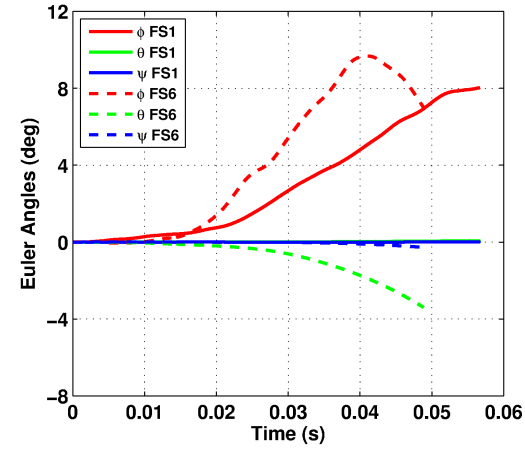

(f) Euler Angles (deg)

Figure 8.25: Comparison of trajectories for computations FS1 and FS6. FS: Full Stroke.

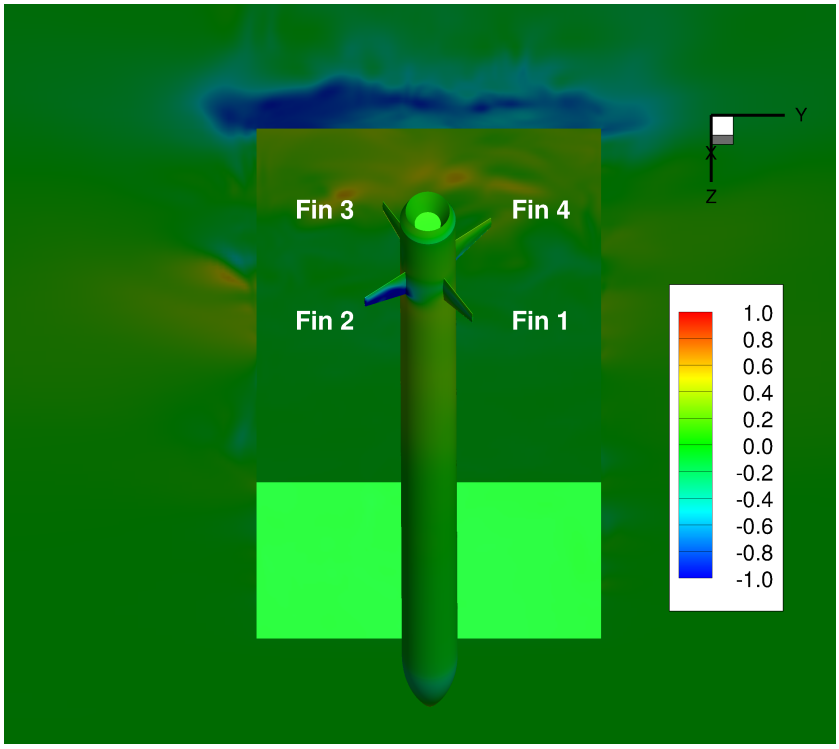

(a) Surface C_P

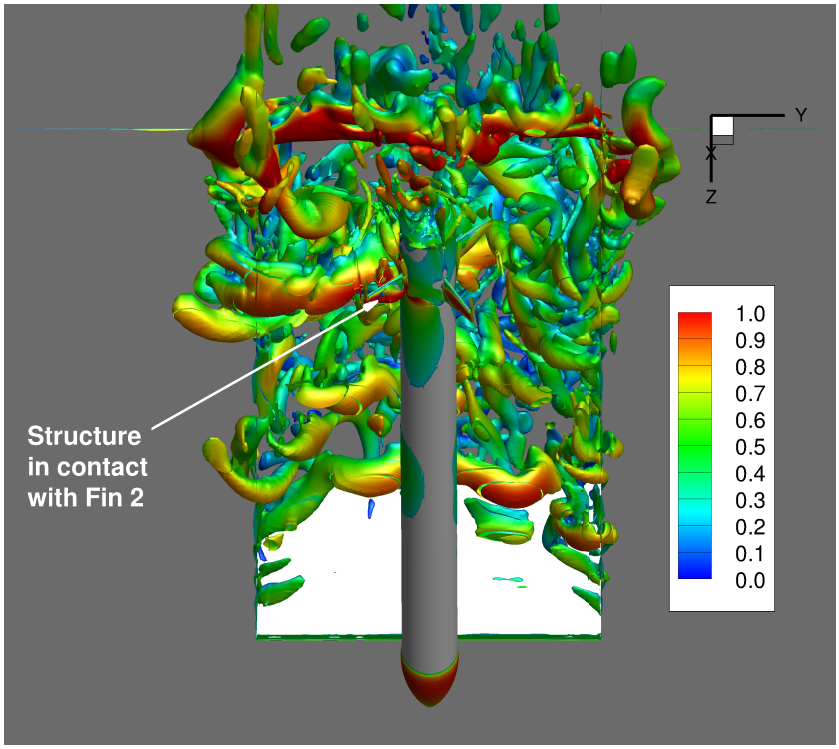

(b) Q-Criteria (Q=2000)

Figure 8.26: Instantaneous contours of surface pressure (a) and structures shown using Q-Criteria coloured with Mach number (b) for case HS1 at an instant in time corresponding to 0.015s after release.

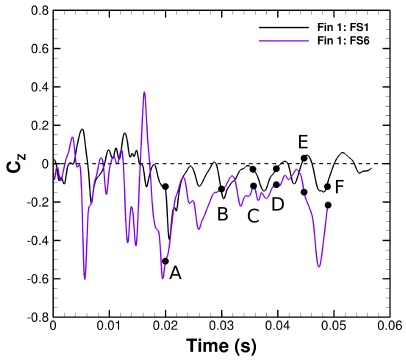

(a) Fin 1: Panel-Normal Force

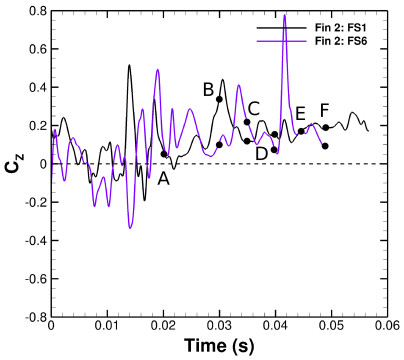

(b) Fin 2: Panel-Normal Force

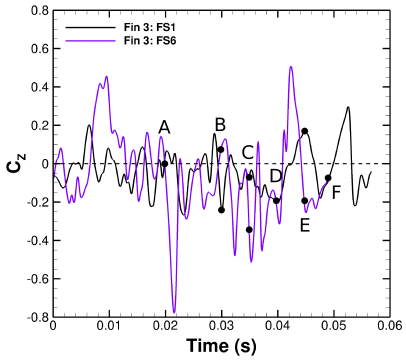

(c) Fin 3: Panel-Normal Force

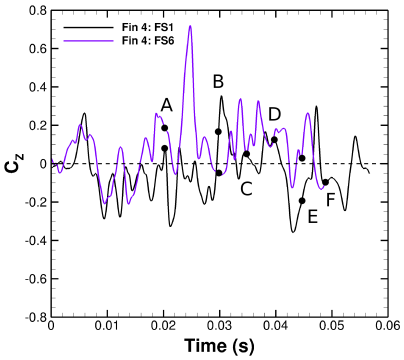

(d) Fin 4: Panel-Normal Force

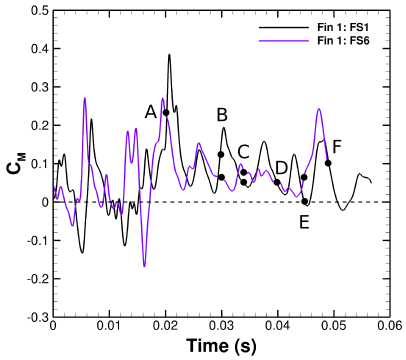

(e) Fin 1: Hinge Moment

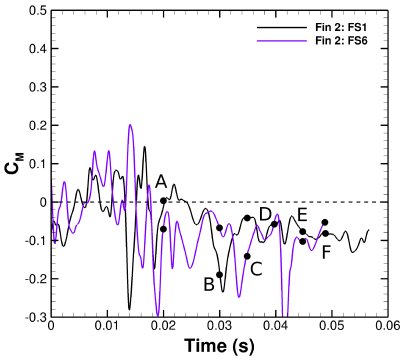

(f) Fin 2: Hinge Moment

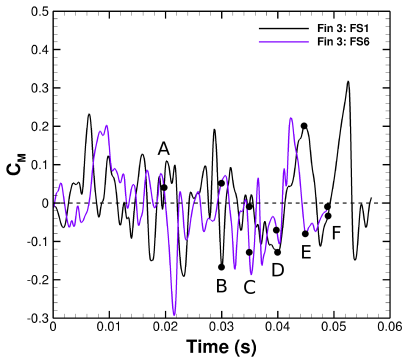

(g) Fin 3: Hinge Moment

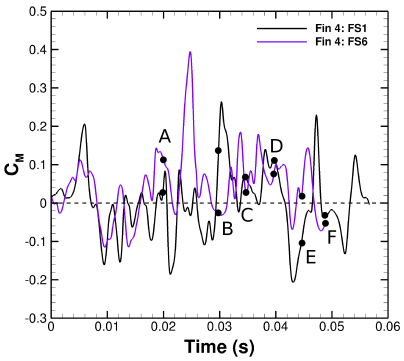

(h) Fin 4: Hinge Moment

Figure 8.27: Time-history of panel-normal-force (a-d) and hinge moment (e-h) coefficients acting on the fins comparing case FS1 and FS6. FS: Full Stroke.

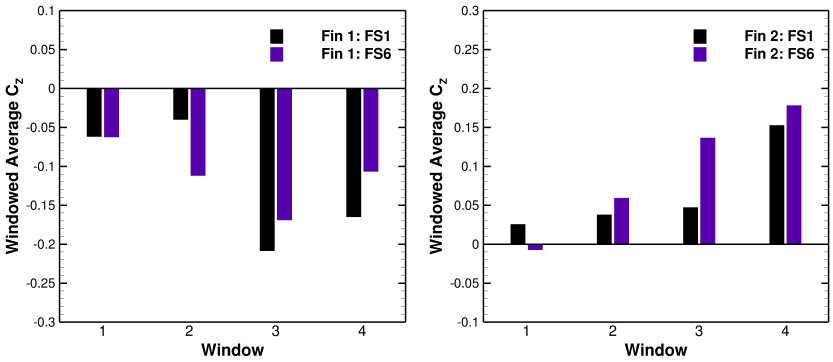

(a) Fin 1: Panel-Normal Force

(b) Fin 2: Panel-Normal Force

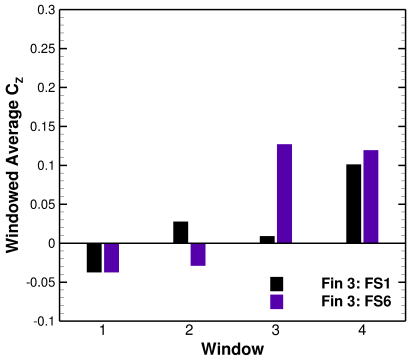

(c) Fin 3: Panel-Normal Force

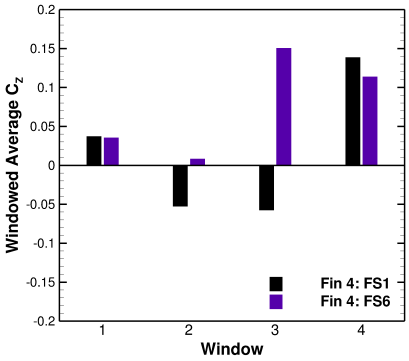

(d) Fin 4: Panel-Normal Force

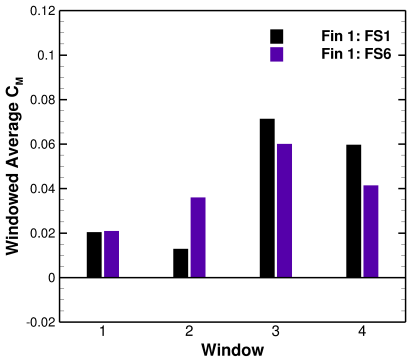

(e) Fin 1: Hinge Moment

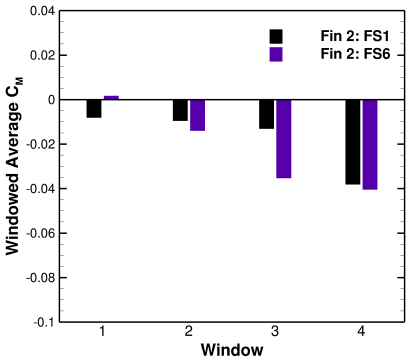

(f) Fin 2: Hinge Moment

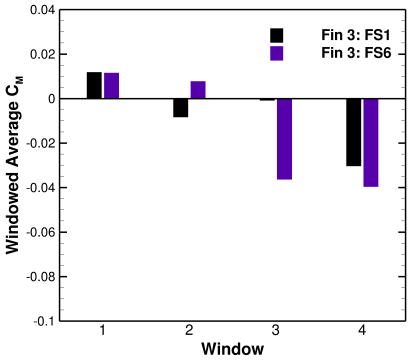

(g) Fin 3: Hinge Moment

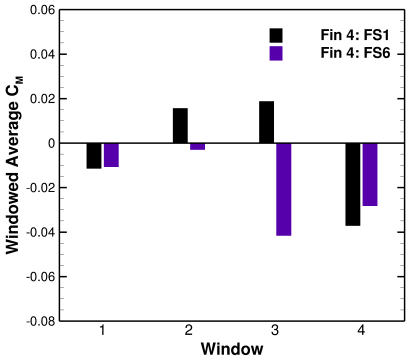

(h) Fin 4: Hinge Moment

Figure 8.28: Time-window-averaged panel-normal-force (a-d) and hinge moment (e-h) coefficients acting on the fins comparing case FS1 and FS6. FS: Full Stroke.

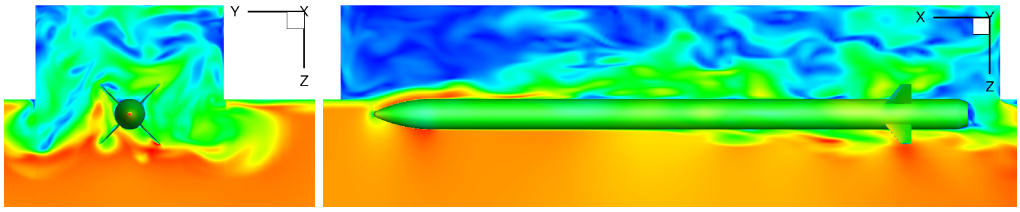

(a) FS1, Time A

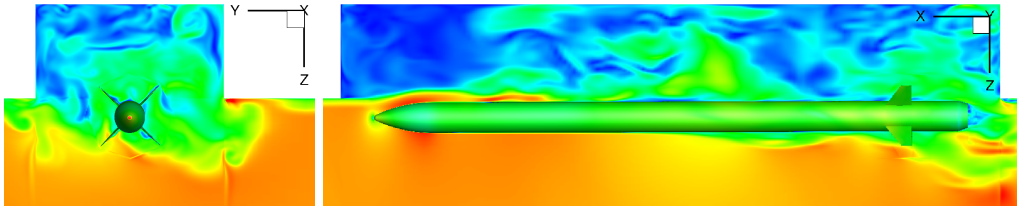

(b) FS6, Time A

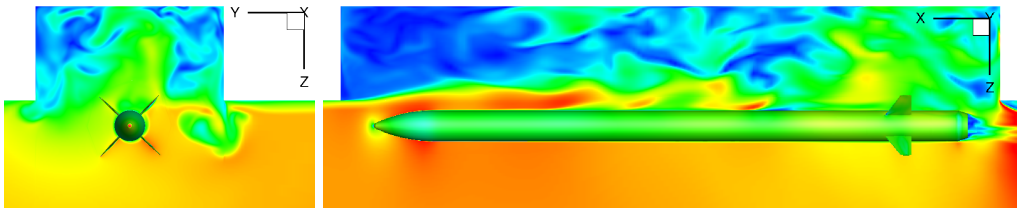

(c) FS1, Time B

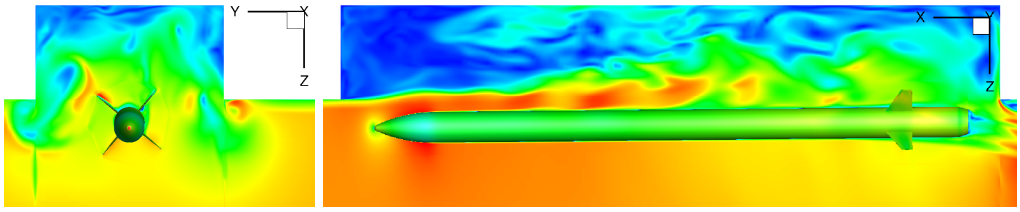

(d) FS6, Time B

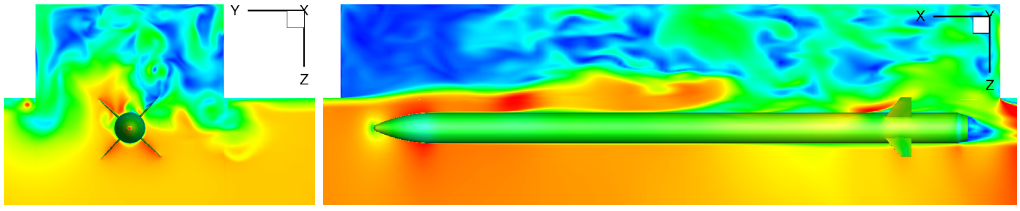

(e) FS1, Time C

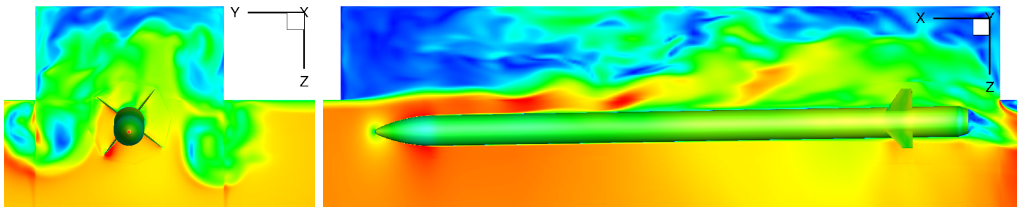

(f) FS6, Time C

Figure 8.29: Instantaneous contours of Mach number for different instances in the release trajectory of case FS1 and FS6. Slices are shown cutting through the fin and along the centreline of the cavity. Contours of Mach number range from 0 (blue) to 1 (red) while contours of surface pressure range from -1 (blue) to 1 (red). (Continued)

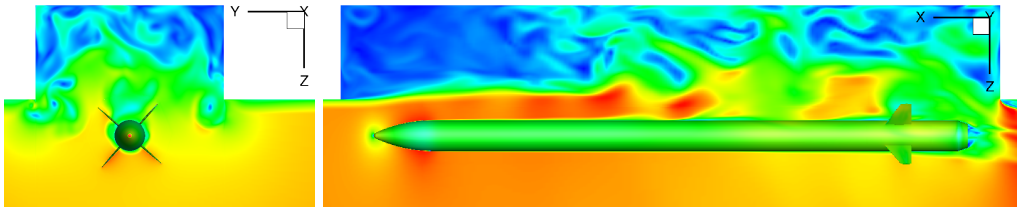

(a) FS1, Time D

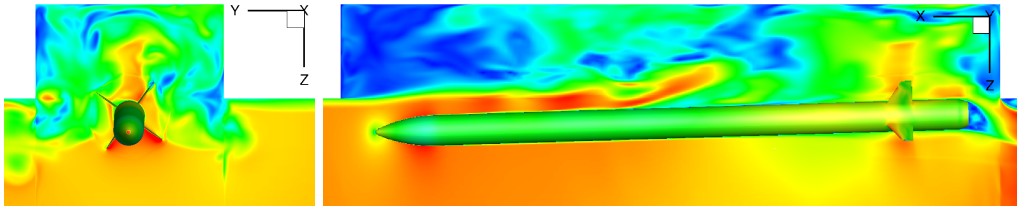

(b) FS6, Time D

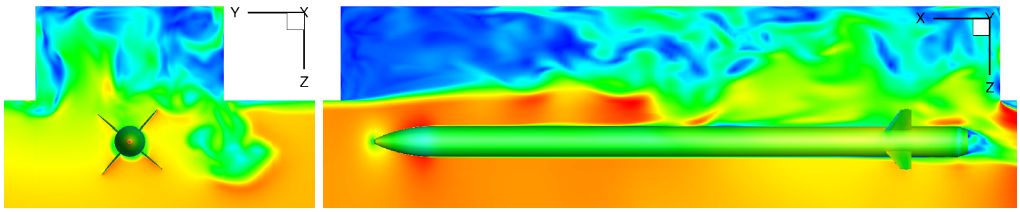

(c) FS1, Time E

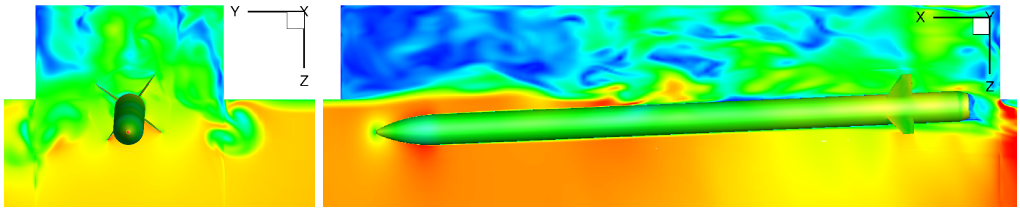

(d) FS6, Time E

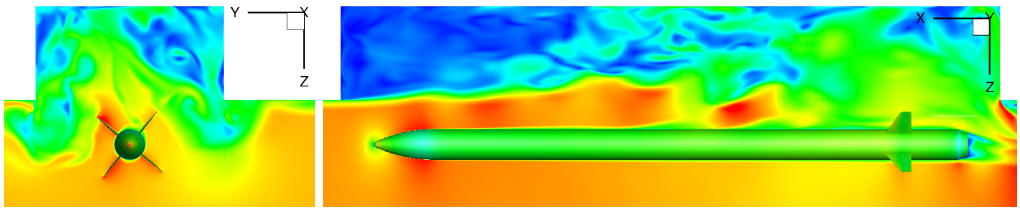

(e) FS1, Time F

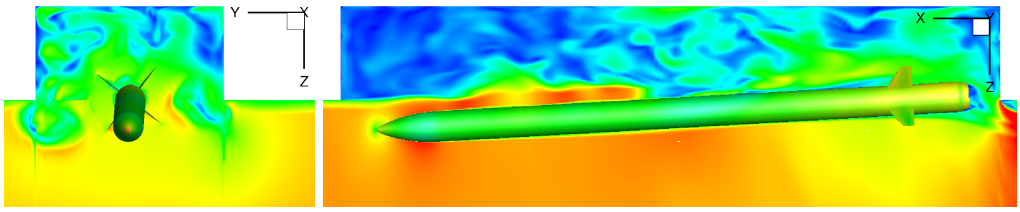

(f) FS6, Time F

Figure 8.29: Instantaneous contours of Mach number for different instances in the release trajectory of case FS1 and FS6. Slices are shown cutting through the fin and along the centreline of the cavity. Contours of Mach number range from 0 (blue) to 1 (red) while contours of surface pressure range from -1 (blue) to 1 (red).

Chapter 9

Conclusions

This thesis presented the use of overset CFD methods to simulate the flow inside clean cavities, investigated the effect of store position on the cavity flow-field and acoustic signature, compared the differences between elastic and rigid store fins and demonstrated the variability of the trajectory of a store released from a cavity due to the unsteady cavity flow-field. The following sections present the conclusions from the study and suggestions for future work.

9.1 Conclusions from Current Work

Detached-Eddy Simulations of clean cavity flow for cavities of L/D=5 and L/D=7, with doors-off and doors-on showed similarities between the two. Both cavities showed the existence of a primary vortex that covered the middle of the cavity with a smaller one in the lower corner. Unsteady pressure data along the floor for the doors-off case were dominated by multiple peaks from the first, second and third Rossiter modes. However, the doors-on case was dominated by the second mode only. Sound pressure levels along the floor also showed that the cavities had similar acoustic signatures reaching close to 170dB. Although relatively coarse grids and short time signals were used for the study, the results are expected to improve with mesh refinement.

The use of POD to reduce the information stored demonstrated that approximately 85% of the flow energy needed to be retained for an accurate flowfield reconstruction. For this flow case, it equated to retaining 151 POD modes and so meant that a reduction of about 30% in disk storage would be achieved over storing all computed flowfield files.

Computations using DES for a store located at carriage position, at the cavity shear layer and half-cavity depth outside a cavity revealed that a store at carriage position had the most pacifying effect on the cavity flow-field, but the overall effect was small. At the carriage position, fin tip displacements were seen to be small with fins exhibiting a buzzing characteristic. When positioned at the shear layer, fins were seen to undergo relatively larger displacements than when they were in carriage. Some of the fin structural modes were seen to lie close to the cavity Rossiter modes. Little to no influence of the cavity was seen on a store outside the cavity, at half-cavity depth. Overall the differences in the loads acting on the rigid and elastic fins, for a store at fixed positions relative to a cavity, were seen to be small and insignificant.

Scale-Adaptive Simulations of clean cavity flow for cavities of L/D=5 and L/D=7, with doors-off and doors-on, were found to be similar to Detached-Eddy Simulation results and could be run at a larger time-step. An order of magnitude larger time-step was used with SAS that gave good comparison with experimental data for the M219 cavity and DES results for the clean cavity with L/D=7, and encouraged its use for store release computations.

A six degrees of freedom method coupled with the HMB2 solver was validated against wind tunnel data for the release of a generic store from a wing. Several computations using SAS were carried out for the release of a store from a cavity with doors-off to investigate trajectory variability due to the unsteadiness of the cavity flow-field. Simulations were performed by releasing a store at different times and by applying full and half stroke lengths for the store ejectors. Small variations were found in the displacement of the centre-of-gravity of the store, while larger variations were found in the roll attitude. The results highlighted the need for a stochastic evaluation of store release trajectories from transonic cavities.

9.2 Future Work

In light of the conclusions from the study, the work could be extended in several directions.

The first could be to modify the aeroelastic method to allow the body of the store to deform in addition to the fins. Body and fin aeroelastics, coupled with the store release from a cavity, including the effect of the ejectors on the deformation of the body, would provide a more realistic simulation of the store trajectory for variability studies.

Investigations into the effect of passive control devices and sloping walls on the trajectory of the store could also be carried out. The chimera method would allow for simple addition of a rod, saw-tooth or flat-top spoiler to the cavity. In addition to this, the effect of the doors-on configuration could also be integrated into the investigation, as this would account for a more realistic simulation. This can be further extended to simulate the entire process of opening of the bay doors, the ejection of a store and the closing of the doors.

Finally, further research is needed to study cavities with more than one store, including the loads and the trajectory of one store released after another. Faster computational times could be achieved through the use of a hybrid structured-unstructured domain where fine meshes can be used around the stores and cavity and coarse meshes that extend to the far-field.

Appendix A

Signal Processing for Transonic Cavity Flows

Transonic cavity flows are characterised by highly unsteady and turbulent stochastic nature as well as strong acoustic emissions. The detailed study of such flows requires signals that are rich in frequency content but also processing methods to identify the dominating cavity frequencies. This technical note utilises experimental and numerical pressure signals to determine the effect of the signal length on the post-processed results. A comparison of different signal processing methods is also presented and summarised.

A.1 Effect of Signal Length

A.1.1 Clean Cavity L/D=5, No Doors

This section presents OASPL and PSD plots using the experimental and numerical signals for the clean cavity with an L/D of 5 with no doors attached. For this case, an experimental signal length of 3s was available while the length of the numerical signal was 0.13s. The 3s long experimental signal was shortened to three different lengths (0.1s, 0.5s and 1s) and the processed results were compared against each other. Each shortened signal overlapped the consecutive signal by 20%. For example, the 0.5s signal overlapped with 20% of the 0.1s signal, the 1s signal overlapped with 20% of the 0.5s signal as shown in Figure A.1. By overlapping the signals in this way, short spectral events can be seen (even if reduced in amplitude) over sets of spectra that are adjacent to each other.

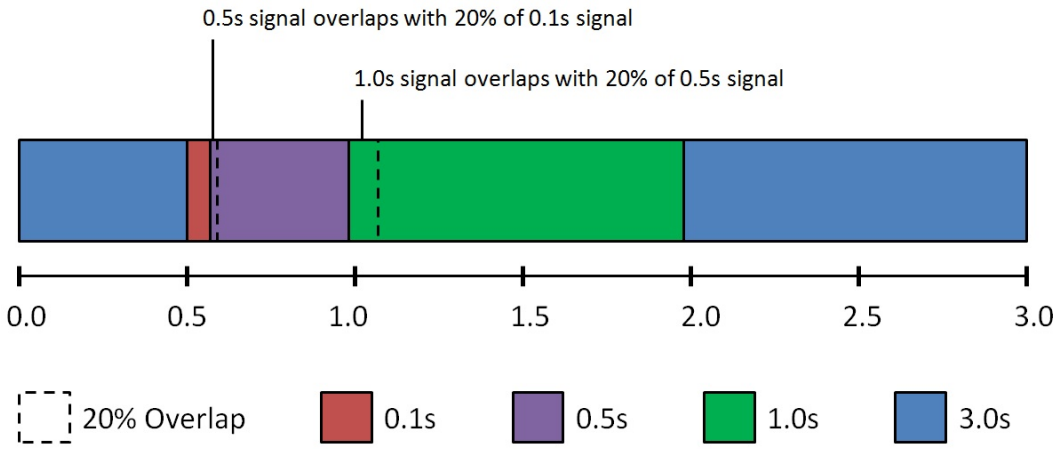

Figure A.1: Overlapping of shortened signals used for post-processing.

The three shortest signals (0.1s, 0.5s and 1s) were compared with the 3s signal, comparing the PSD (Figure A.2, FigureA.3 and Figure A.4) at $x/L = 0.05$, $x/L = 0.50$ and $x/L = 0.95$ and OASPL (Figure A.5) along the cavity length.

PSD plots for the front (Figure A.2), middle (Figure A.3) and rear (Figure A.4) of the cavity showed that the dominant second and third modes were captured for the three signal lengths. Figure A.2(a) shows how the 0.1s signal compared to the 3s signal at the leading edge where the dominant modes were captured along with the low amplitude mode one. Mode four, however, that was a low amplitude mode was not captured with this short signal length.

Similarly at the middle of the cavity, the dominant second mode was captured, however, the lower amplitude mode four was not, and at the rear end of the cavity, the dominant modes two and three were captured, however, the lower amplitude mode one was not. By extending the signal length to 0.5s and further to 1s, good comparisons were obtained across the length of the cavity.

The lower amplitude modes did not make a huge contribution to the overall shape of the curves obtained for the OASPL. This was evident in the shapes of the curves for the different signal lengths seen in Figure A.5, where the shortest signal length was close to the overall shape and the differences lay within 1dB.

The OASPL seen in Figure A.5 showed the differences between the signal lengths that were in the range of 1dB along the length of the cavity. The shortest signal length (0.1s), showed very little variation from the experimental data up until $x/L = 0.55$ where a difference of 1dB was seen up to $x/L = 0.85$.

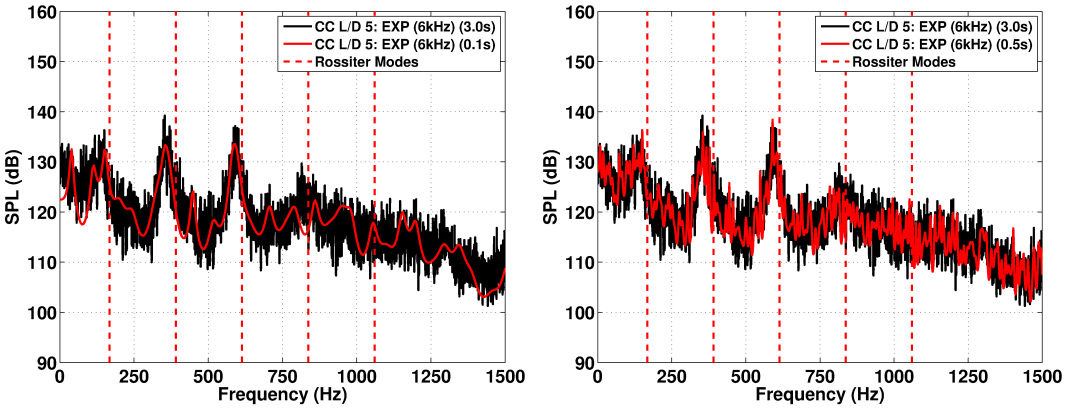

(a) Signal length: 0.1s

(b) Signal length: 0.5s

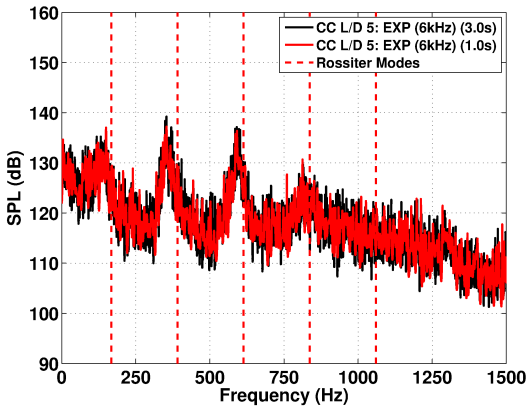

(c) Signal length: 1s

Figure A.2: PSD plots for the clean cavity, L/D=5, without doors comparing results for increasing experimental signal lengths at $x/L = 0.05$ where the probe is near the front of the cavity.

The second set of plots compared the 3s experimental signal to shortened experimental and numerical signals. Here the numerical signals were obtained from DES computations employing the Spalart-Allmaras turbulence model[46]. A signal length of 0.1s was used as the shortened experimental signal length for comparison against the full experimental signal length and the shorter numerical signal. As before, PSD plots are shown for the front (Figure A.6), middle (Figure A.7) and rear (Figure A.8) of the cavity for increasing numerical signal lengths.

The numerical signal had a total length of 0.13s and was shortened into three signals (0.01s, 0.05s and 0.1s) for comparison. Figure A.6(a) showed the shortest numerical signal compared with the 3s and 0.1s experimental signals. None of the dominant modes were captured due to the short length of the signal.

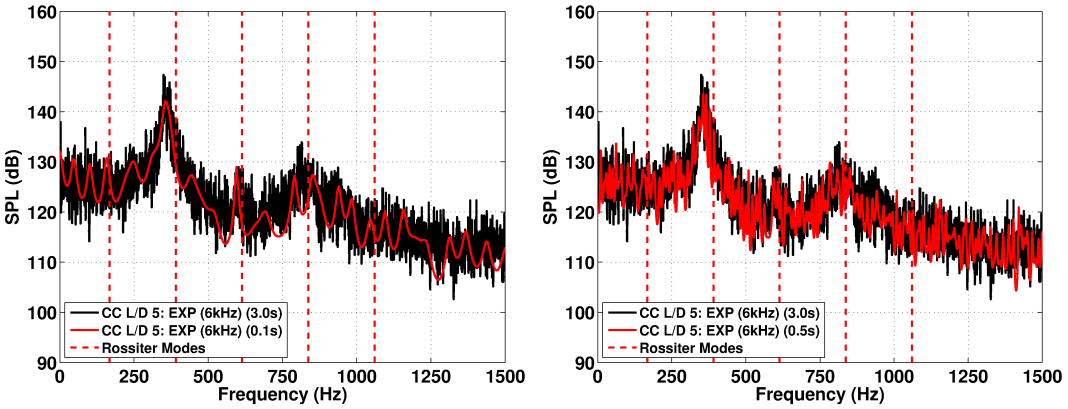

(a) Signal length: 0.1s

(b) Signal length: 0.5s

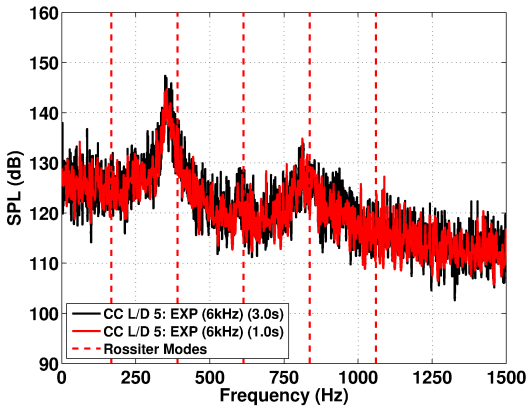

(c) Signal length: 1s

Figure A.3: PSD plots for the clean cavity, L/D=5, without doors comparing results for increasing experimental signal lengths at $x/L = 0.50$ where the probe is near the middle of the cavity.

Increasing the numerical signal to 0.05s (Figure A.6(b)) showed how the dominant modes were captured as well as the the low amplitude modes. Further extensions of the signal length to 0.1s (Figure A.6(c)) and then to 0.13s (Figure A.6(d)), lead to better comparison with the experimental data.

In the middle of the cavity (Figure A.7), the shortest signal was seen to predict two modes in the cavity though not as strong as the experiment. The dominant modes appeared in Figure A.7(b) and showed better comparison against the experimental data. The rear of the cavity (Figure A.8) was seen to have similarities to the front where the shortest signal did not pick up the dominant modes that then improve as the length of the signal was extended.

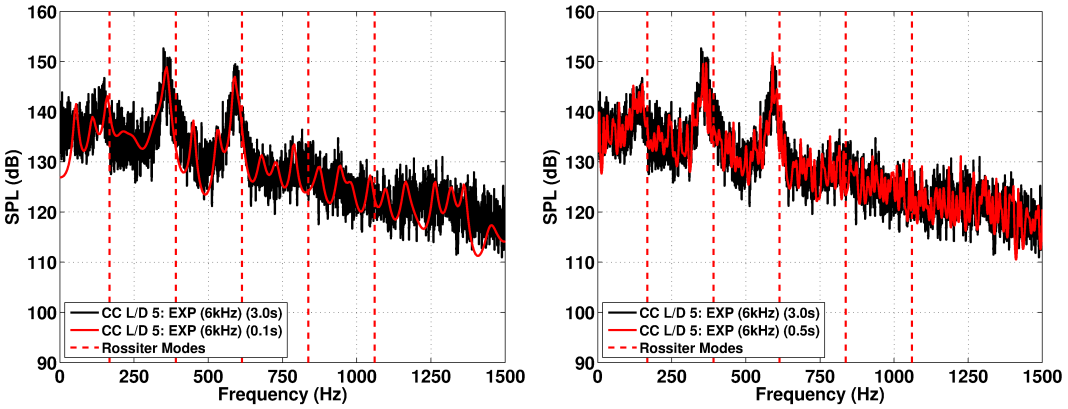

(a) Signal length: 0.1s

(b) Signal length: 0.5s

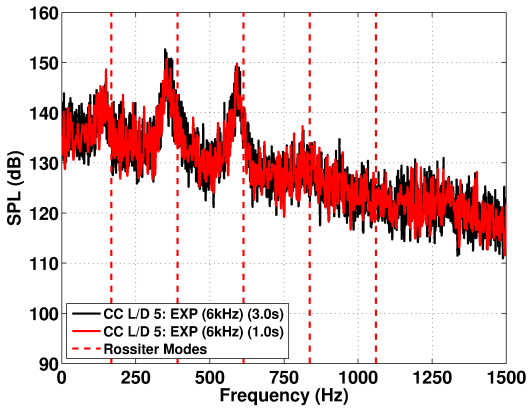

(c) Signal length: 1s

Figure A.4: PSD plots for the clean cavity, L/D=5, without doors comparing results for increasing experimental signal lengths at $x/L = 0.95$ where the probe is near the rear of the cavity.

The OASPL in Figure A.9 showed the comparison of the 3s experimental signal length to the shortened numerical signals for the DES computation. Here, apart from the shortest numerical signal (0.01s), all other signals captured the overall shape of the experimental curve and had an almost constant overprediction of 4dB. This could be reduced by mesh refinement and was not relative to the selected time step and signal length. The shortest signal was seen to have a similar shape and magnitude to the experimental curve, but was seen from the PSD plots before, this curve was lacking the spectral content of the other curves and as a result compensated for the 4dB overprediction that the other shortened signals had.

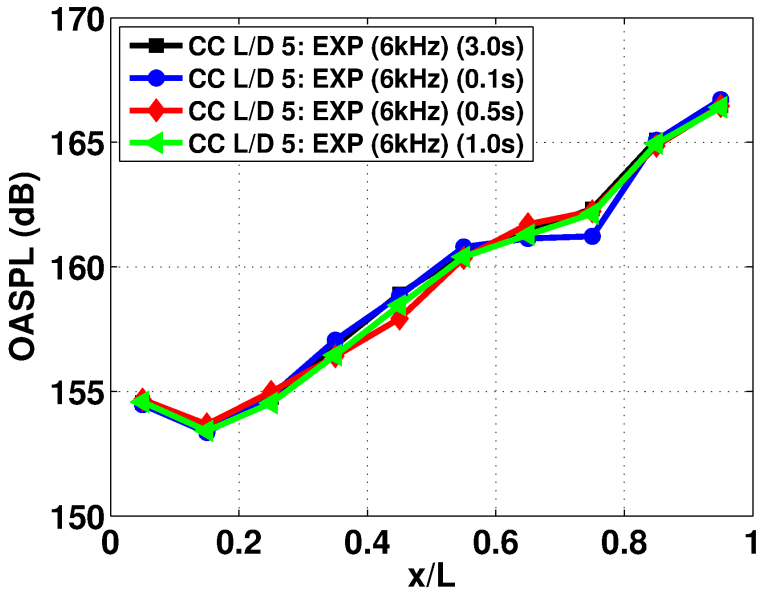

(a) $x/L = 0.00$ to 1.00

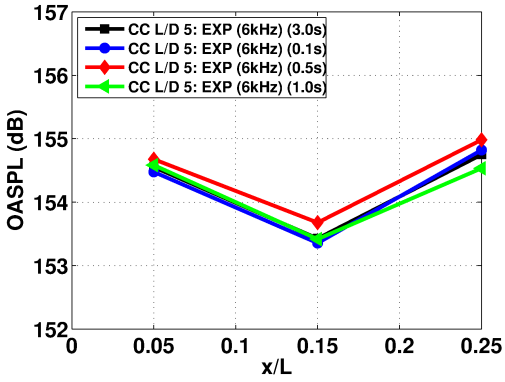

(b) $x/L = 0.00$ to 0.25

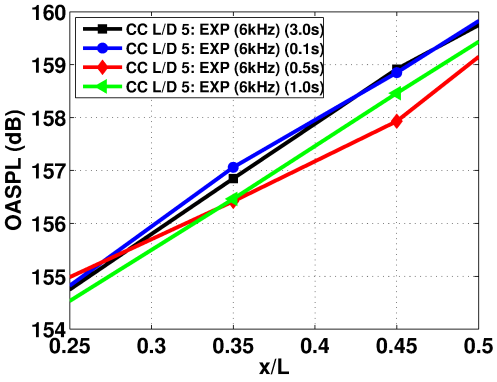

(c) $x/L = 0.25$ to 0.50

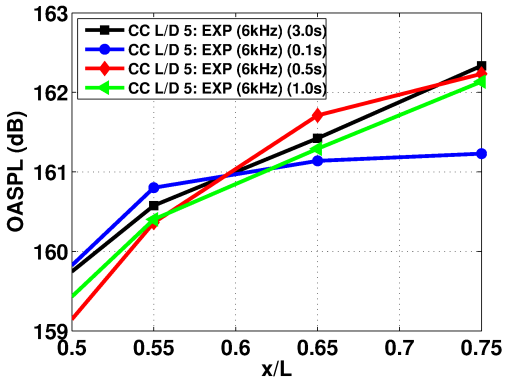

(d) $x/L = 0.50$ to 0.75

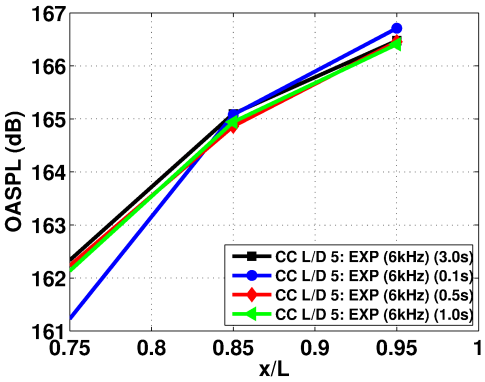

(e) $x/L = 0.75$ to 1.00

Figure A.5: OASPL along the cavity floor for the clean cavity, L/D=5, without doors using experimental data from Nightingale *et al.* [16].

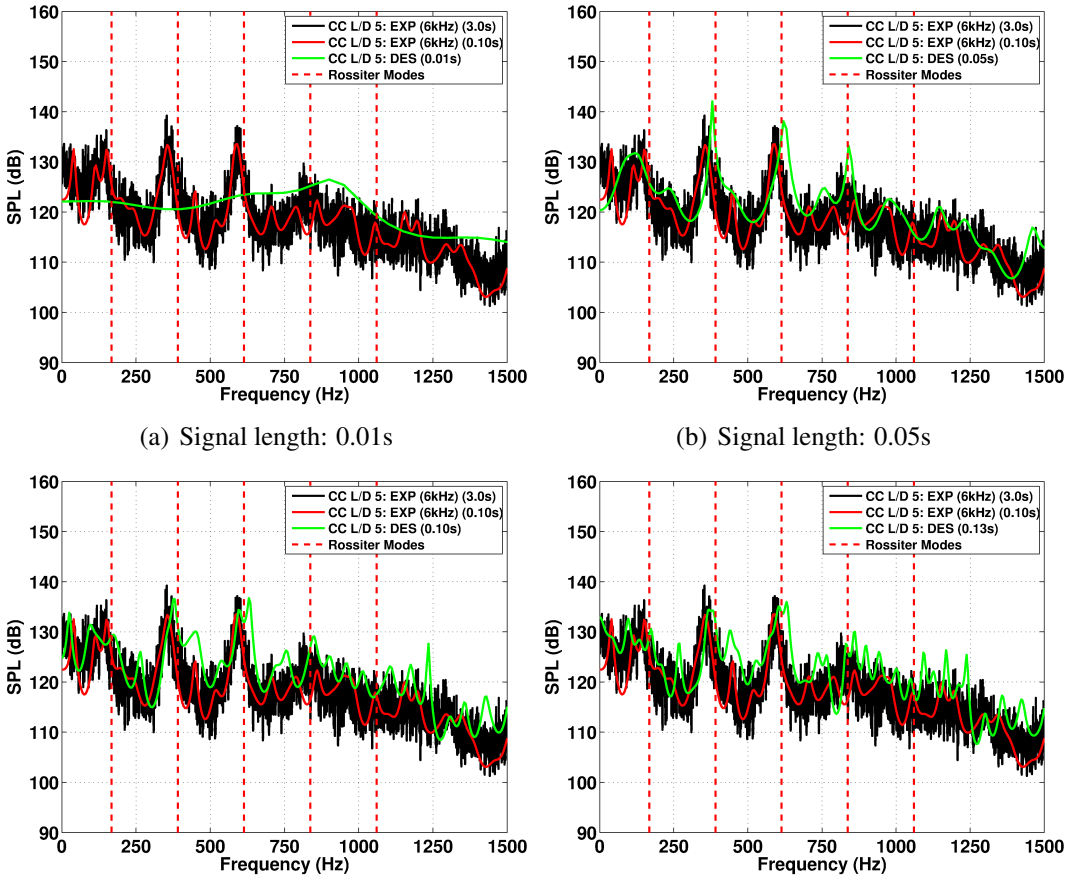

(a) Signal length: 0.01s

(b) Signal length: 0.05s

(c) Signal length: 0.1s

(d) Signal length: 0.13s

Figure A.6: PSD plots for the clean cavity, L/D=5, without doors comparing results for increasing numerical signal lengths at $x/L = 0.05$ where the probe is near the front of the cavity.

A.2 Clean Cavity L/D=5, Doors

This section presents OASPL and PSD plots using the experimental and numerical signals for the clean cavity with an L/D of 5 with doors attached. For this case, an experimental signal length of 3s was available while the length of the numerical signal was 0.08s. The 3s long experimental signal was shortened to three different lengths (0.1s, 0.5s and 1s) and the processed results were compared against each other. Each shortened signal overlapped the consecutive signal by 20%. For example, the 0.5s signal overlapped with 20% of the 0.1s signal, the 1s signal overlapped with 20% of the 0.5s signal and so on.

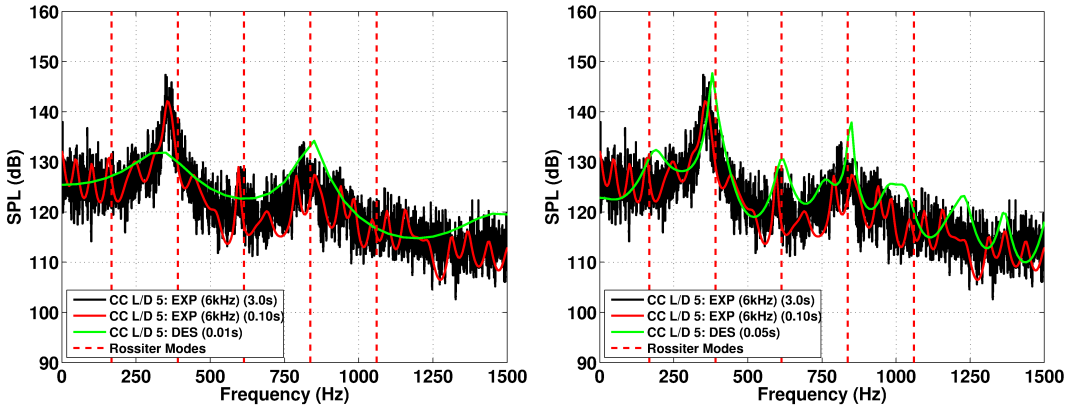

(a) Signal length: 0.01s

(b) Signal length: 0.05s

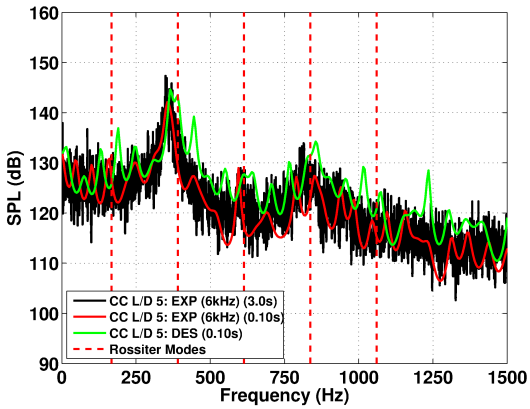

(c) Signal length: 0.1s

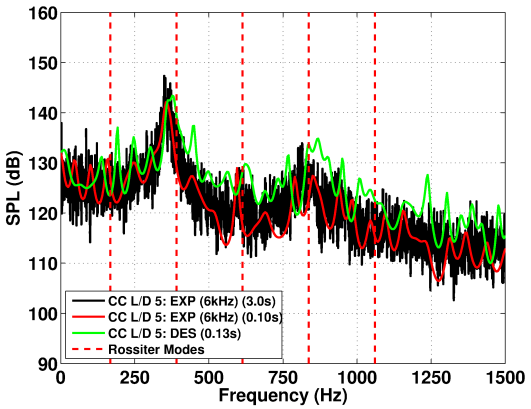

(d) Signal length: 0.13s

Figure A.7: PSD plots for the clean cavity, L/D=5, without doors comparing results for increasing numerical signal lengths at $x/L = 0.50$ where the probe is near the middle of the cavity.

The three shortest signals (0.1s, 0.5s and 1s) were compared with the 3s signal, comparing the PSD (Figure A.10, Figure A.11 and FigureA.12) for locations of $x/L = 0.05$, $x/L = 0.50$ and $x/L = 0.95$ and OASPL (Figure A.13) along the cavity length.

PSD plots for the front (Figure A.10), middle (Figure A.11) and rear (Figure A.12) of the cavity showed that the dominant second mode is captured for the three signal lengths. Figure A.10(a) shows how the 0.1s signal compared to the 3s signal at the leading edge where the dominant mode was captured along with the low amplitude modes one and three.

Similarly at the middle of the cavity (Figure A.11), the dominant mode two was captured by all three signal lengths and so was the low amplitude mode four. By extending the signal length to 0.5 and further to 1s, good comparisons were obtained across the length of the cavity.

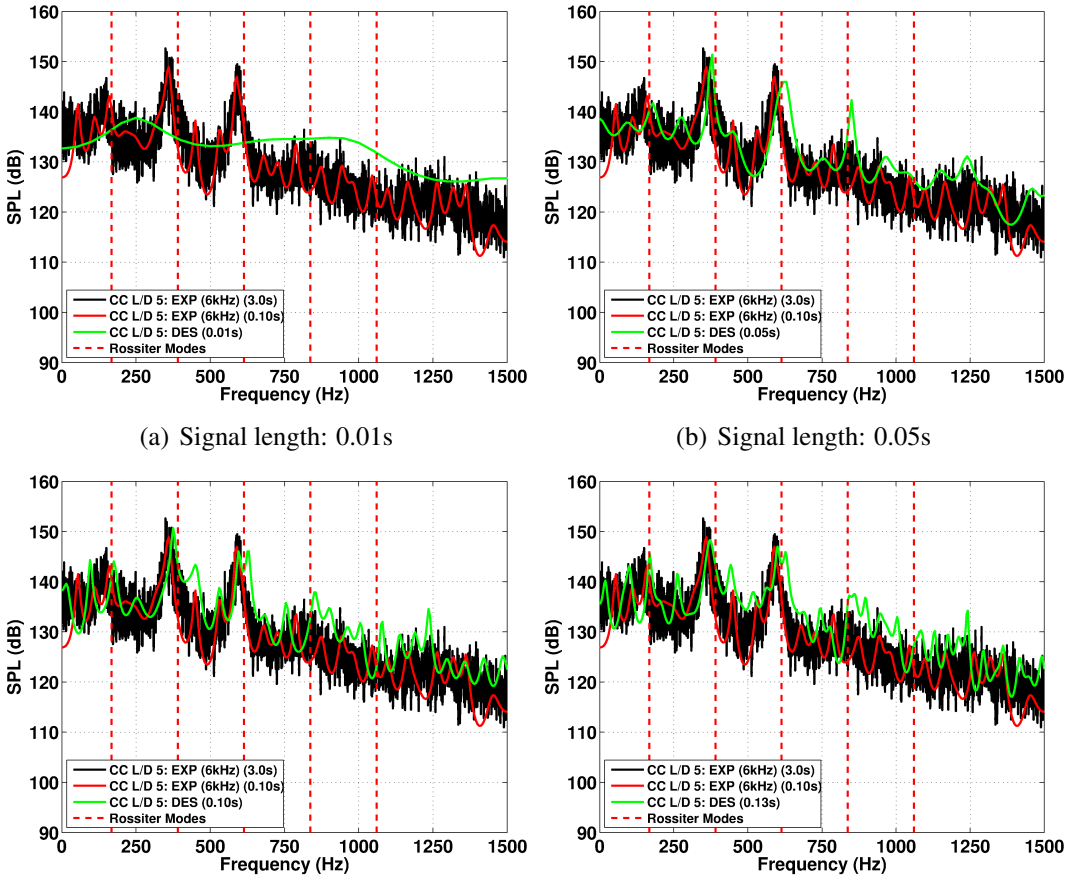

(a) Signal length: 0.01s

(b) Signal length: 0.05s

(c) Signal length: 0.1s

(d) Signal length: 0.13s

Figure A.8: PSD plots for the clean cavity, L/D=5, without doors comparing results for increasing numerical signal lengths at $x/L = 0.95$ where the probe is near the rear of the cavity.

At the rear, mode two was still dominant and captured by all signal lengths. Here, the low amplitude modes one and three, similar to the front of the cavity, were also predicted.

The OASPL along the floor of the cavity is shown in Figure A.13 comparing the full experimental signal to the shortened overlapping experimental signals. The difference in the overall shape and magnitude was similar to the case without doors where the differences were in the range of 1dB.

The second set of plots compare the 3s experimental signal, the shortened 0.1s experimental signal and shortened numerical signals. Here the numerical signals were obtained from DES computations employing the Spalart-Allmaras turbulence model[49]. As before, PSD plots are shown for the front (Figure A.14), middle (Figure A.15) and rear (Figure A.16) of the cavity for increasing numerical signal lengths.

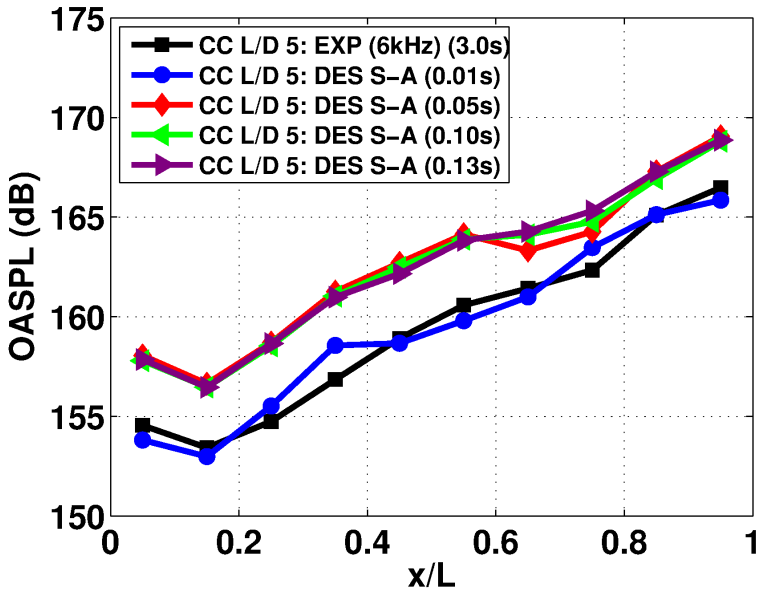

(a) $x/L = 0.00$ to 1.00

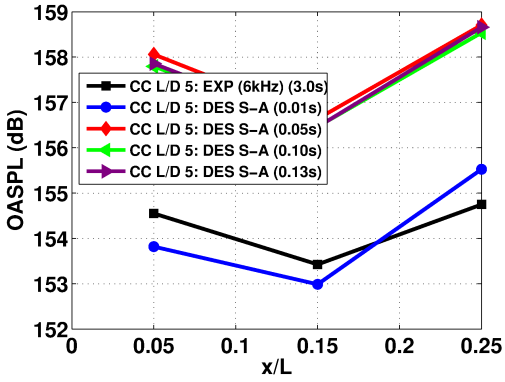

(b) $x/L = 0.00$ to 0.25

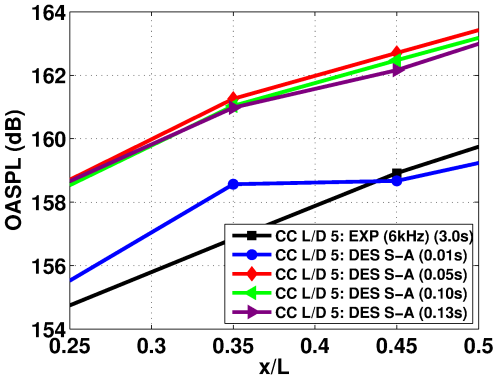

(c) $x/L = 0.25$ to 0.50

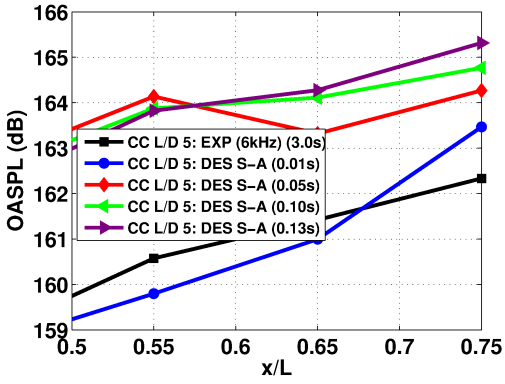

(d) $x/L = 0.50$ to 0.75

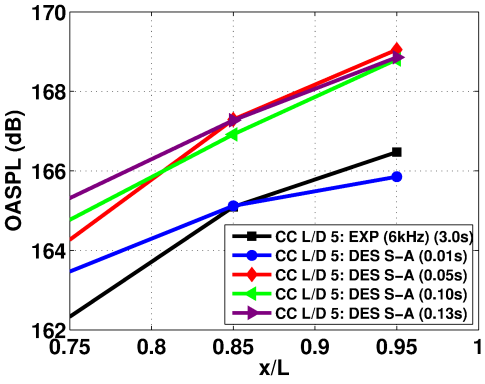

(e) $x/L = 0.75$ to 1.00

Figure A.9: OASPL along the cavity floor for the clean cavity, L/D=5, without doors using experimental data from Nightingale et al[16].

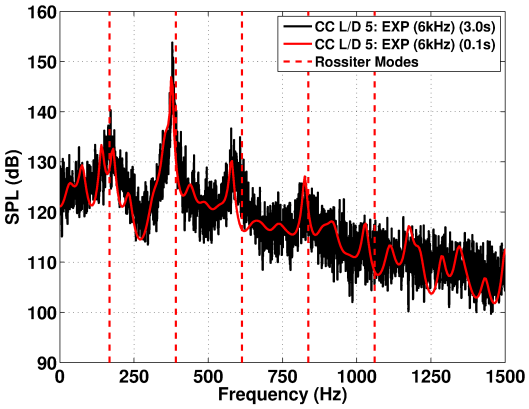

(a) Signal length: 0.1s

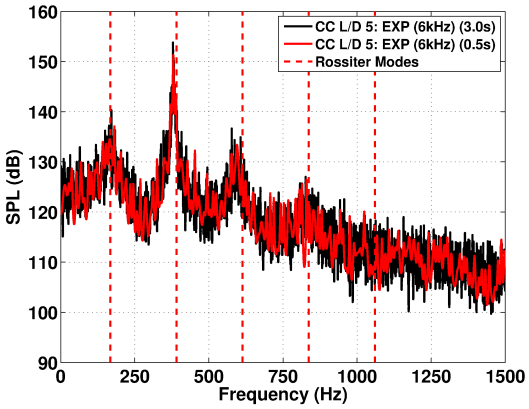

(b) Signal length: 0.5s

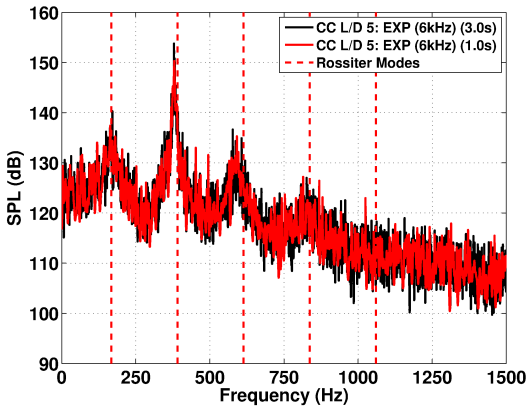

(c) Signal length: 1s

Figure A.10: PSD plots for the clean cavity, L/D=5, with doors comparing results for increasing signal lengths at $x/L = 0.05$ where the probe is near the front of the cavity.

The numerical signal had a total length of 0.08s and was shortened into three signals (0.01s, 0.03s and 0.05s) for comparison. Figure A.14(a) shows the shortest numerical signal compared with the 3s and 0.1s experimental signals, at the front of the cavity. Here none of the dominant modes were captured due to the short length of the signal. Extending the numerical signal to 0.03s (Figure A.14(b)) showed how the dominant mode was better predicted as well as the the low amplitude modes. Further extending the length of the signal to 0.05s (Figure A.14(c)) and then to 0.08s (Figure A.14(d)) showed better comparison against the experimental data.

In the middle of the cavity (Figure A.15), the shortest signal (Figure A.15(a)) was seen to predict the two modes captured in the experiment. As before, extending the signal length made the peaks stronger and improved the comparison with experiments. The rear of the cavity (Figure A.16) was seen to have similarities to the front where the shortest signal picked up the dominant mode but missed the lower amplitude modes.

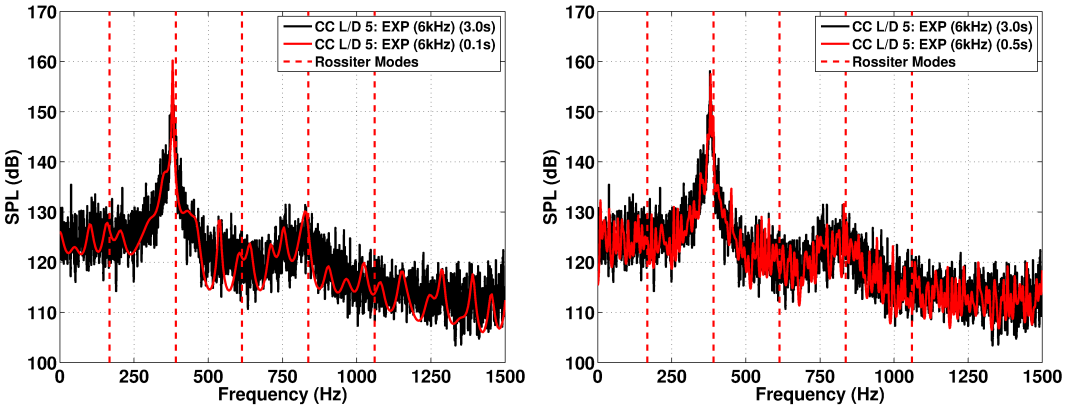

(a) Signal length: 0.1s

(b) Signal length: 0.5s

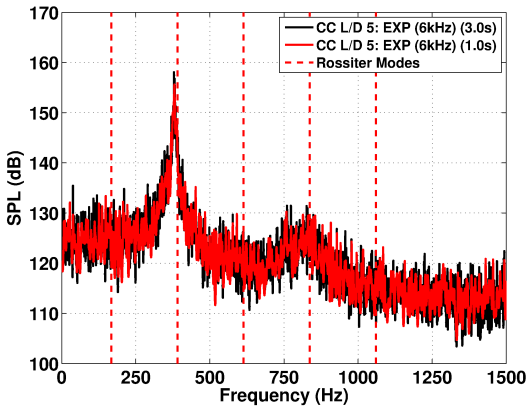

(c) Signal length: 1s

Figure A.11: PSD plots for the clean cavity, L/D=5, with doors comparing results for increasing signal lengths at $x/L = 0.50$ where the probe is near the middle of the cavity.

Much like the cavity without doors, the OASPL seen in Figure A.17 showed how the shortest signal was the closest to the experiment as it did not capture the entire spectrum making it appear quieter. All signal lengths from 0.03s and above showed differences in the region of 1dB and captured the shape of the experimental curve with a maximum overprediction of 4dB.

A.3 Clean Cavity L/D=7, No Doors

Similar to the L/D=5 cavity, this section presents results for shortened signals (0.1s, 0.2s, 0.4s and 0.6s) for a clean cavity with L/D=7. Due to lack of experimental results, only numerical signals were used for the comparison. All numerical signals were obtained from DES computations using the Spalart-Allmaras turbulence model[49].

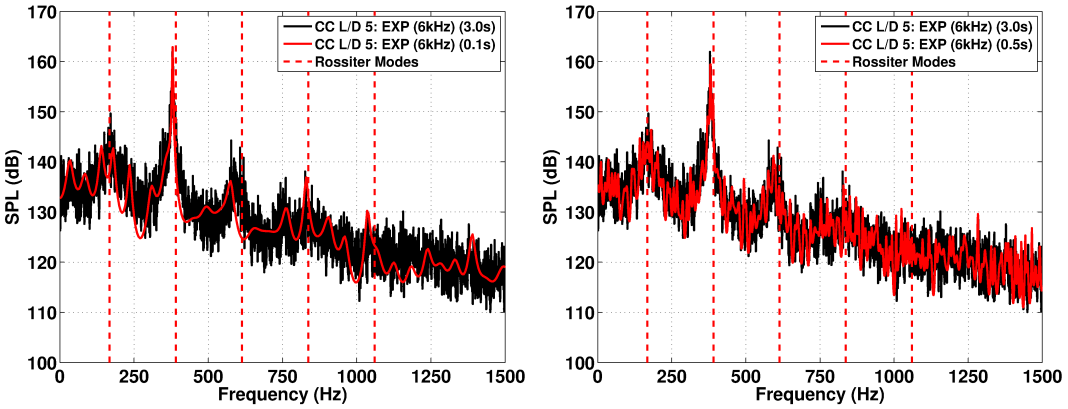

(a) Signal length: 0.1s

(b) Signal length: 0.5s

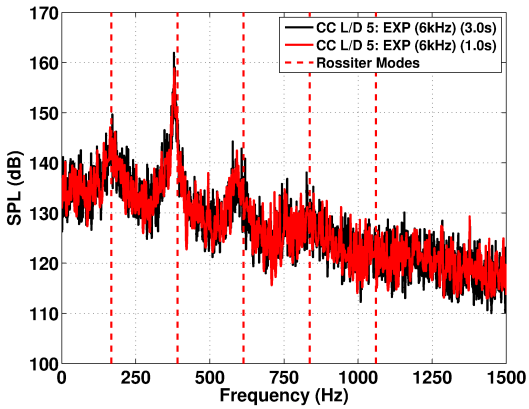

(c) Signal length: 1s

Figure A.12: PSD plots for the clean cavity, L/D=5, with doors comparing results for increasing signal lengths at $x/L = 0.95$ where the probe is near the rear of the cavity.

PSD plots for the front (Figure A.18), middle (Figure A.19) and rear (Figure A.20) of the cavity show that the dominant first and second modes are captured for the four shortened signal lengths. At the front of the cavity (Figure A.18), the shortest signal length of 0.1s was seen to miss out one of the five modes captured by the longer 1s signal. Increasing the signal length to 0.2s created a small peak that was missing before. This peak got sharper, the longer the signal became. In the middle of the cavity (Figure A.19), the three modes predicted by the longer 1s signal was seen to be captured by the shortest signal (Figure A.19(a)), the peaks at these modes got sharper with the length of the signal. At the rear of the cavity, where the flow had completely broken down, several peaks that correspond to Rossiter modes, in the long 1s signal, were missing in the shortened signal. Even at 0.6s (Figure A.20(d)), the peaks at mode three and four were not present.

While the PSD plots showed the effect of the signal length on the prediction of modes, the OASPL showed very little difference between the different signal lengths. Figure A.21, shows that even for the shortest signal length (0.1s) the difference between the longest signal was within 1dB. All shortened signals were seen to be similar in shape and magnitude to the full signal length of 1s.

A.4 Effect of Methods

This section presents a comparison of the effects of three different processing methods applied to experimental signals. The three processing methods are referred to as follows: Method 1: MEM method (Burg's estimator), Method 2: FFT method based on the Welch's method and Method 3: FFT method supplied by MBDA. A 3s long experimental signal was used that was split into 36 sections, each of length 0.1s, where each signal overlaps the next by 20%. PSD plots compared the differences between the three methods for the following cases: clean M219 cavity, with doors-off, sampled at 6kHz, clean M219 cavity, with doors-on, sampled at 6kHz and clean M219 cavity, with doors-on, sampled at 31.2kHz.

A.4.1 Clean M219 Cavity, L/D=5, Doors-Off (6kHz)

Figures A.22 to A.25 compare OASPL for different sections of the full 3s long signal, for the clean M219 cavity with doors-off, sampled at 6kHz. Although each section is 0.1s long, most of them are able to capture the overall shape of the curve obtained from the full 3s signal and lie within a 2dB range.

PSD plots along the floor of the cavity are shown in Figures A.26 to A.28 for the three methods. All 36 sections are shown in each of the plots for each method forming a thick band of lines. The thick red lines denote the maximum, mean and minimum of the banded region while the dashed red lines show the first five Rossiter modes. Plots are shown for the front, middle and rear end of the cavity. All three methods showed peaks near the dominant Rossiter modes; modes one, two and three for the front and rear ends and mode two in the middle of the cavity. In comparison, method 1 and 3 showed oscillations while method 2 appears to be a lot smoother in terms of the maximum, minimum and mean.

The maximum, minimum and mean values obtained from the superimposition of all 36 sections comparing the three methods are shown in Figures A.29 to A.31. Method 1 and method 3 were very similar for the maximum value, while method 2 was lower in comparison. The minimum value however showed more differences between the three methods. Method 1 and 2 had similar magnitude but method 2 produced a smoother curve. Method 3 had the lowest magnitude and with large fluctuations. The mean value in Figure A.31 showed similar magnitude between method 2 and 3 with method 1 having the highest mean at the dominant modes.

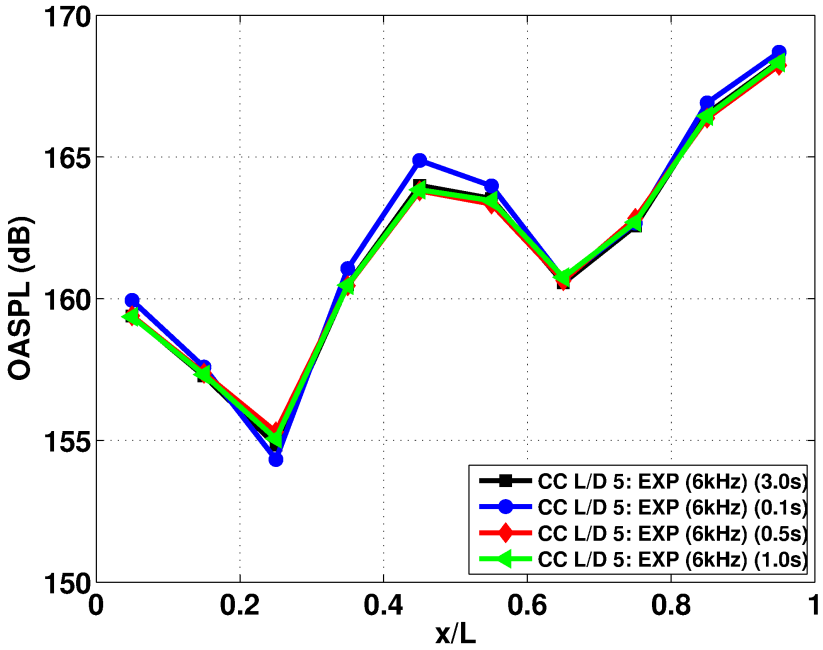

(a) $x/L = 0.00$ to 1.00

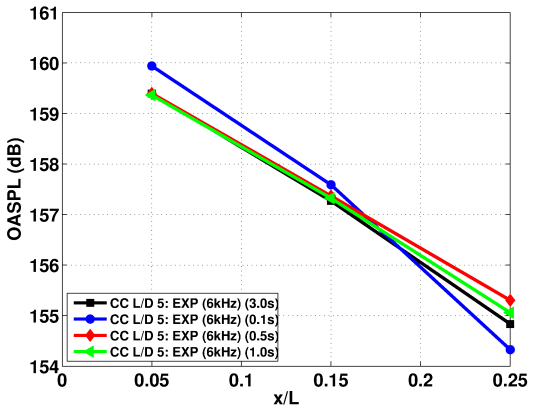

(b) $x/L = 0.00$ to 0.25

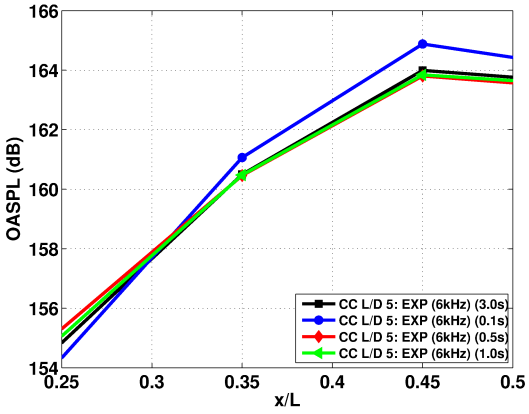

(c) $x/L = 0.25$ to 0.50

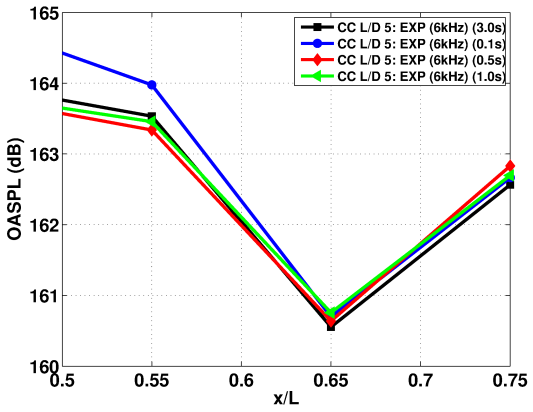

(d) $x/L = 0.50$ to 0.75

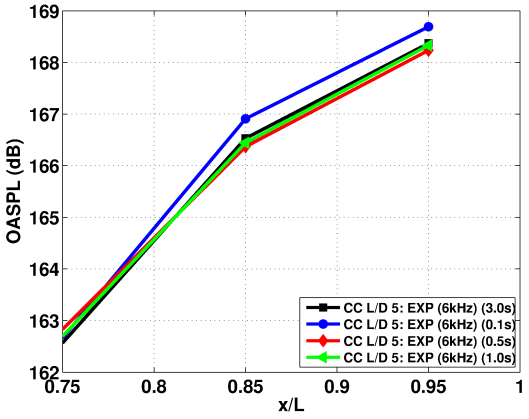

(e) $x/L = 0.75$ to 1.00

Figure A.13: OASPL along the clean cavity, L/D=5, with doors using experimental data from Nightingale et al[16].

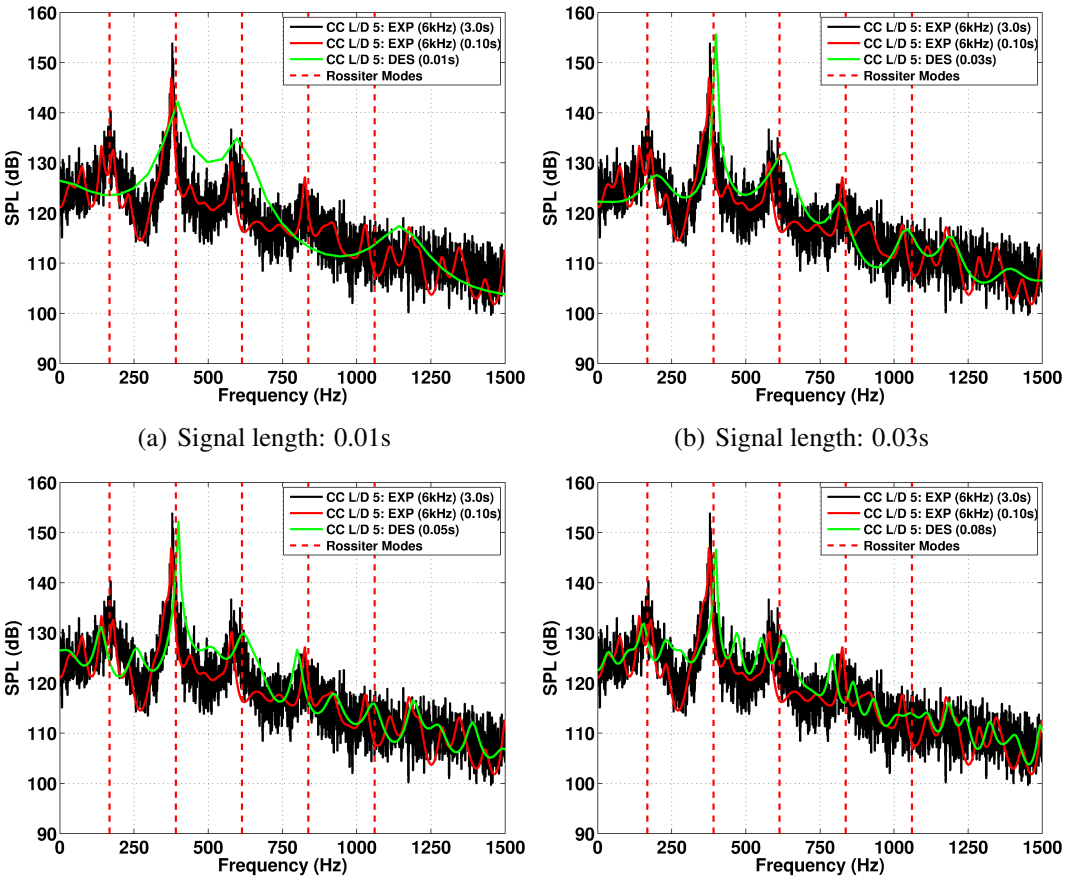

(a) Signal length: 0.01s

(b) Signal length: 0.03s

(c) Signal length: 0.05s

(d) Signal length: 0.08s

Figure A.14: PSD plots for the clean cavity, L/D=5, with doors comparing results for increasing numerical signal lengths at $x/L = 0.05$ where the probe is near the front of the cavity.

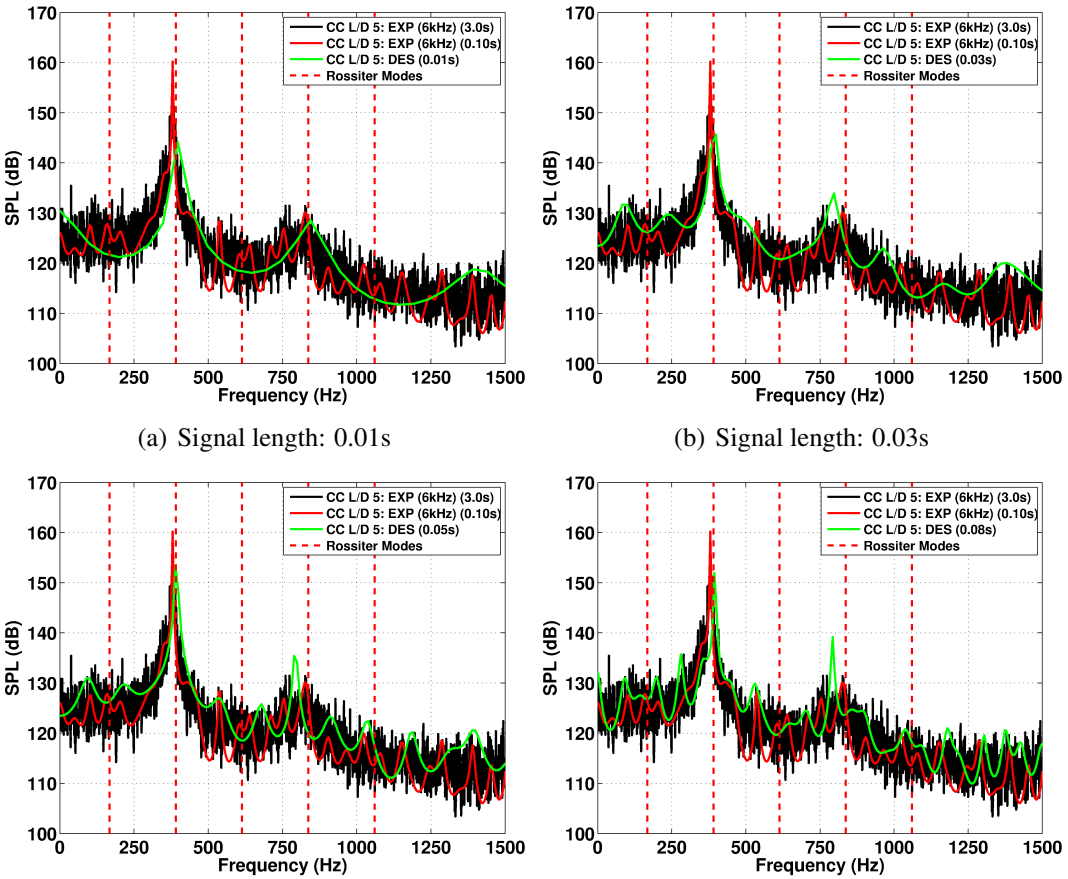

(a) Signal length: 0.01s

(b) Signal length: 0.03s

(c) Signal length: 0.05s

(d) Signal length: 0.08s

Figure A.15: PSD plots for the clean cavity, L/D=5, with doors comparing results for increasing numerical signal lengths at $x/L = 0.50$ where the probe is near the middle of the cavity.

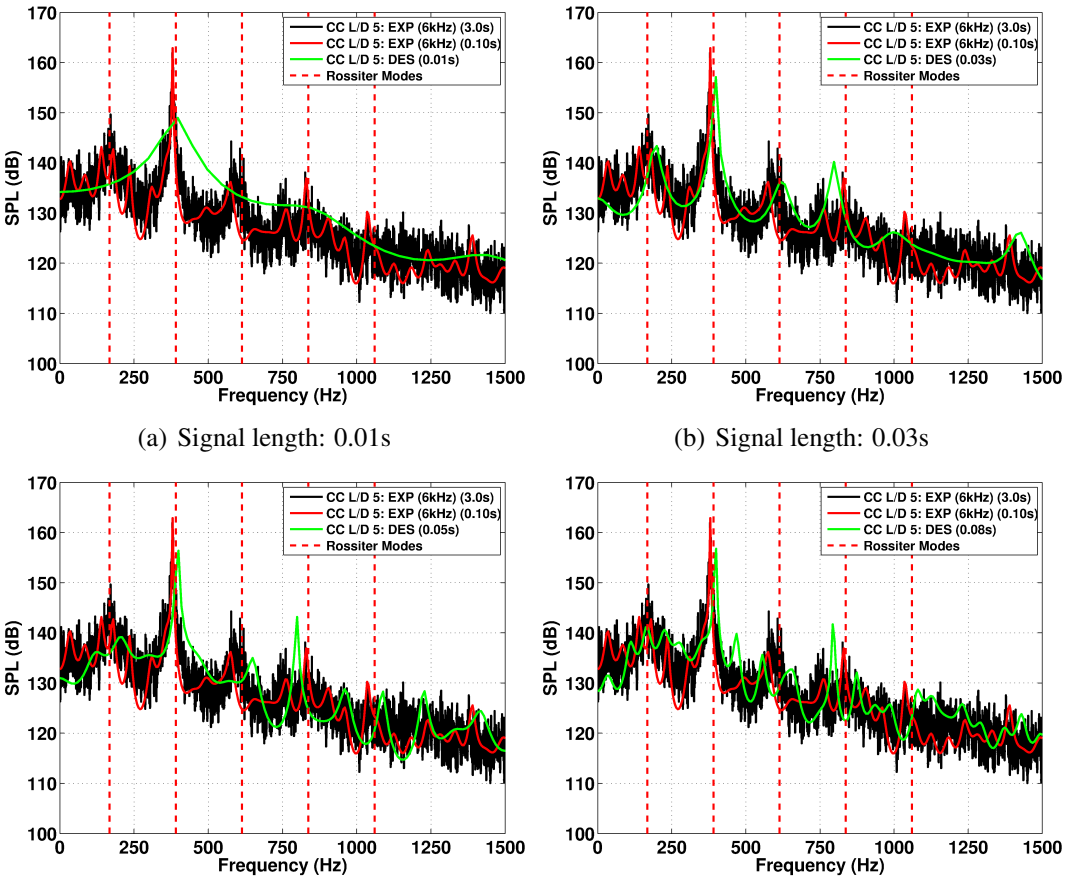

(a) Signal length: 0.01s

(b) Signal length: 0.03s

(c) Signal length: 0.05s

(d) Signal length: 0.08s

Figure A.16: PSD plots for the clean cavity, L/D=5, with doors comparing results for increasing numerical signal lengths at $x/L = 0.95$ where the probe is near the rear of the cavity.

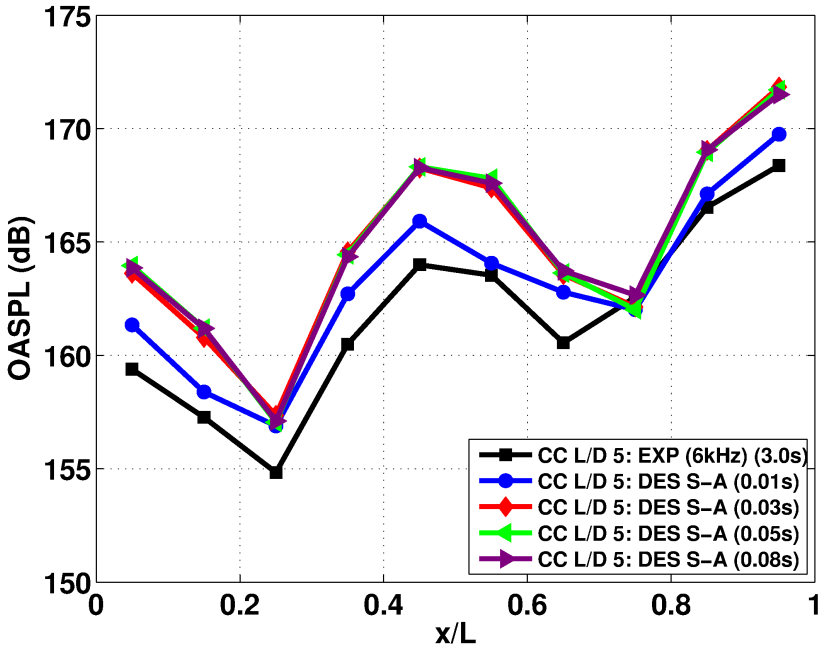

(a) $x/L = 0.00$ to 1.00

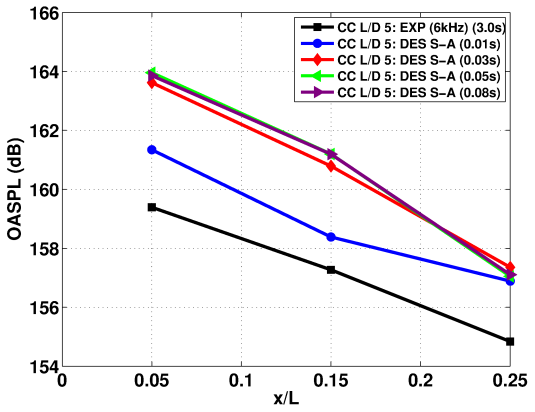

(b) $x/L = 0.00$ to 0.25

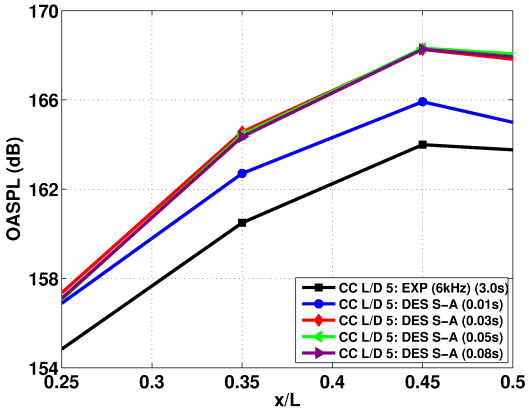

(c) $x/L = 0.25$ to 0.50

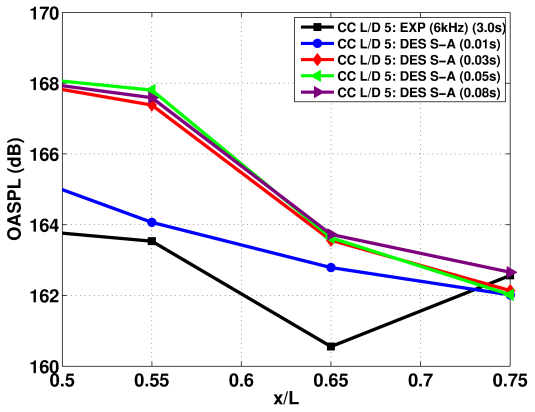

(d) $x/L = 0.50$ to 0.75

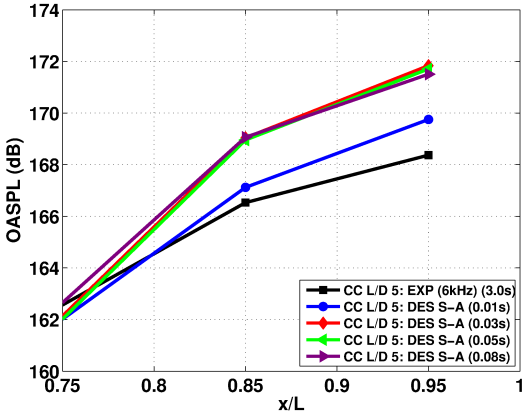

(e) $x/L = 0.75$ to 1.00

Figure A.17: OASPL along the cavity floor for the clean cavity, L/D=5, with doors using experimental data from Nightingale et al[16].

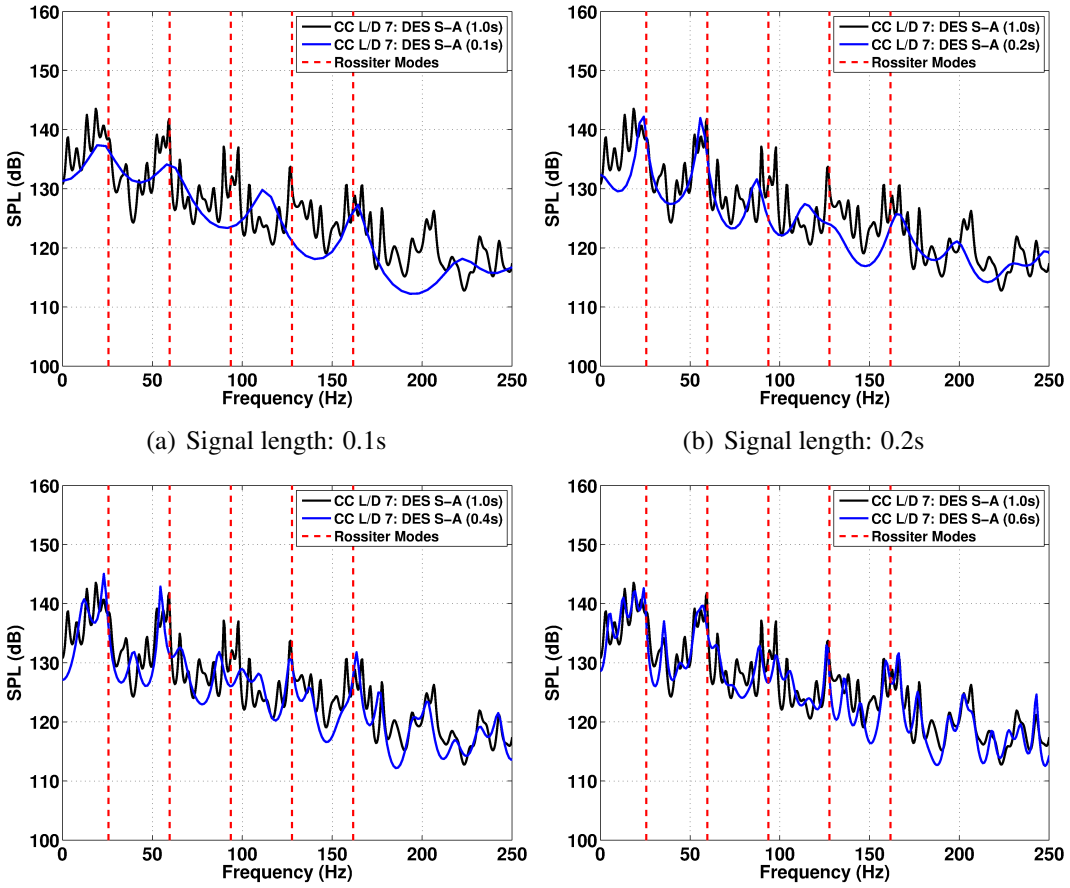

(a) Signal length: 0.1s

(b) Signal length: 0.2s

(c) Signal length: 0.4s

(d) Signal length: 0.6s

Figure A.18: PSD plots for the L/D=7 cavity comparing results for increasing signal lengths at $x/L = 0.05$ where the probe is near the front of the cavity.

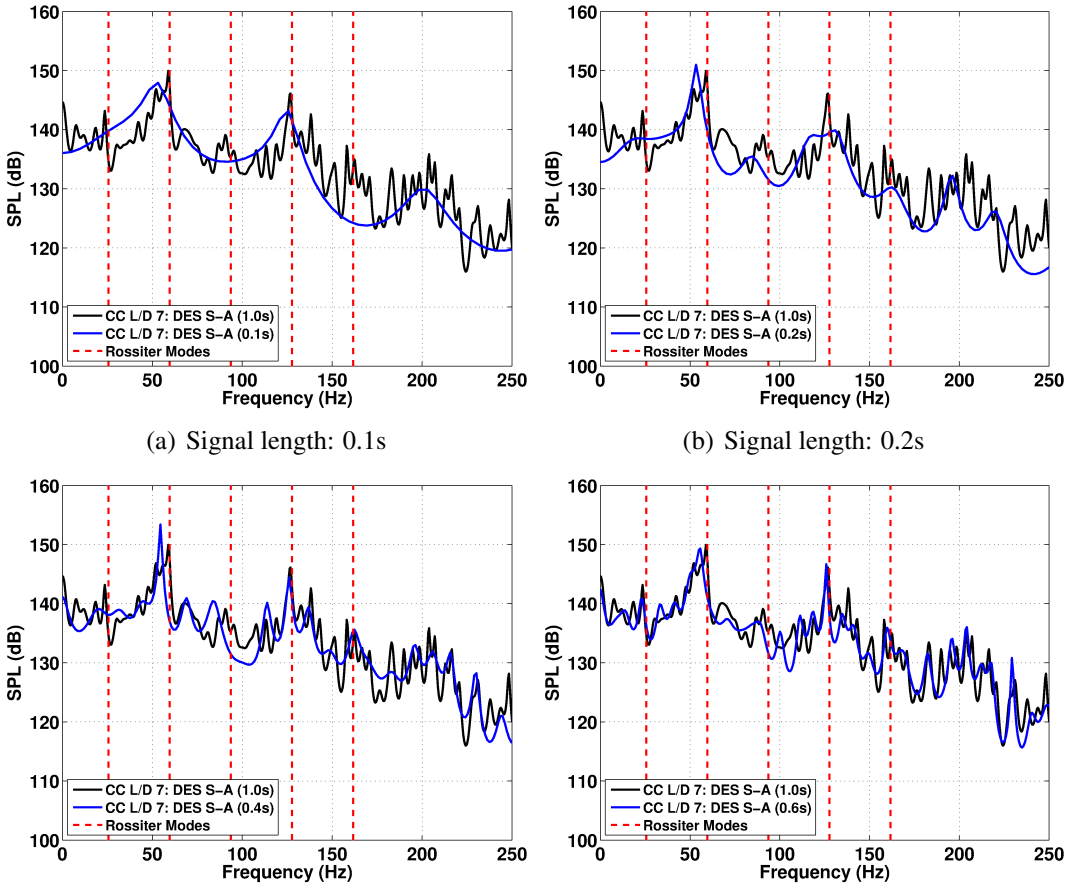

(a) Signal length: 0.1s

(b) Signal length: 0.2s

(c) Signal length: 0.4s

(d) Signal length: 0.6s

Figure A.19: PSD plots for the L/D=7 cavity comparing results for increasing signal lengths at $x/L = 0.50$ where the probe is near the middle of the cavity.

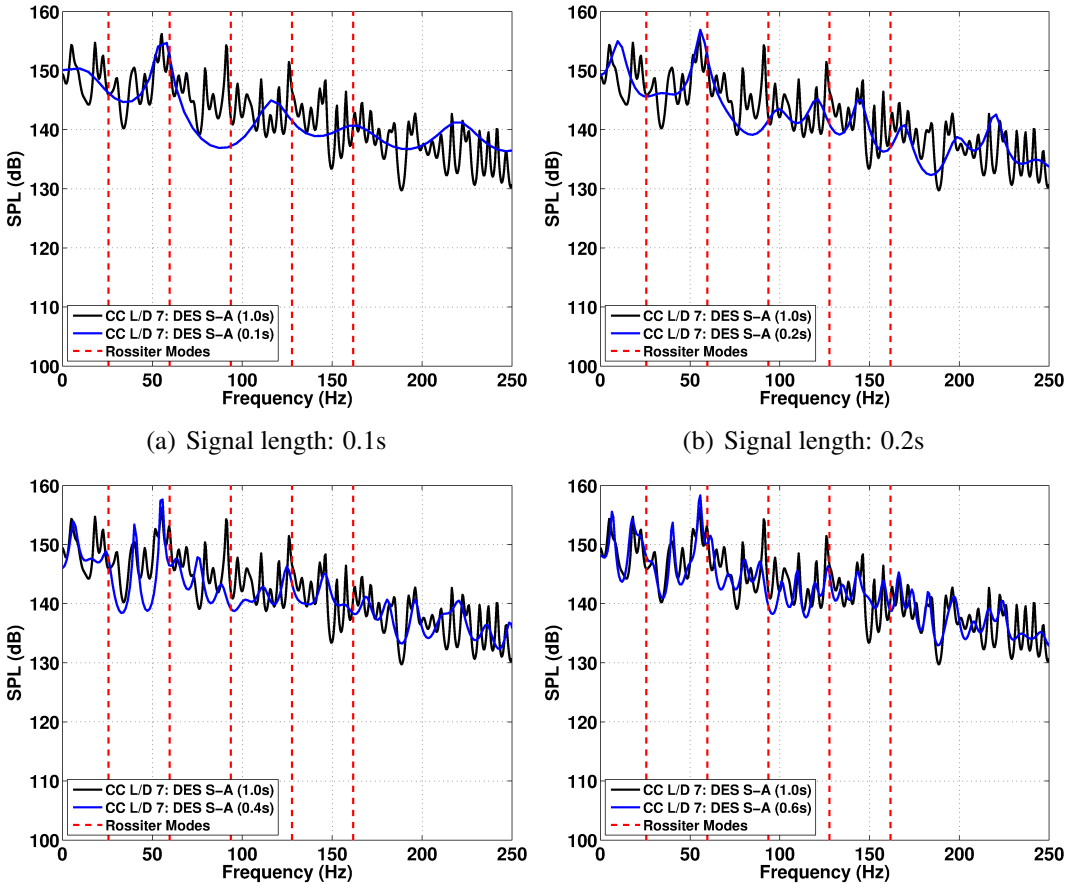

(a) Signal length: 0.1s

(b) Signal length: 0.2s

(c) Signal length: 0.4s

(d) Signal length: 0.6s

Figure A.20: PSD plots for the L/D=7 cavity comparing results for increasing signal lengths at $x/L = 0.95$ where the probe is near the rear of the cavity.

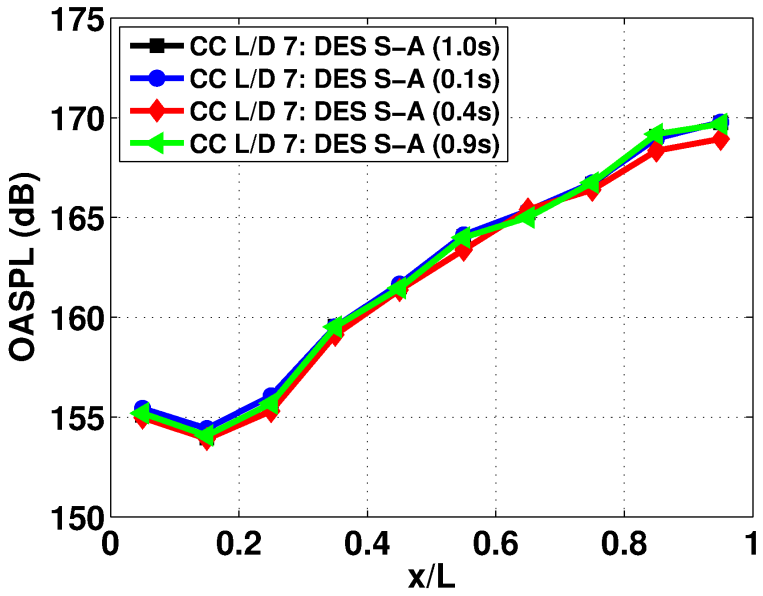

(a) $x/L = 0.00$ to 1.00

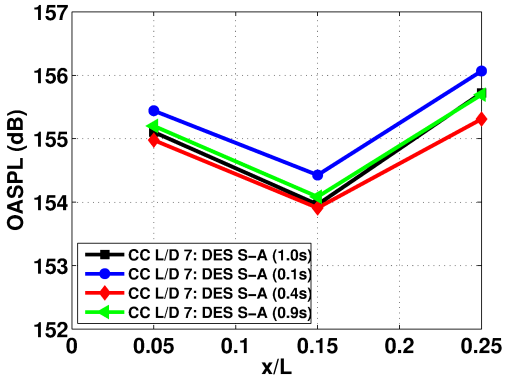

(b) $x/L = 0.00$ to 0.25

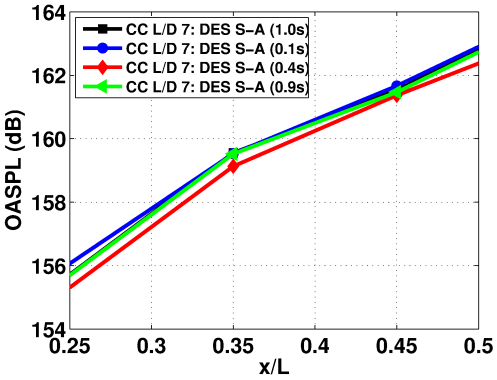

(c) $x/L = 0.25$ to 0.50

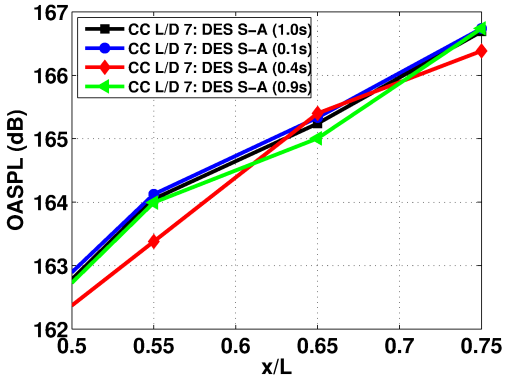

(d) $x/L = 0.50$ to 0.75

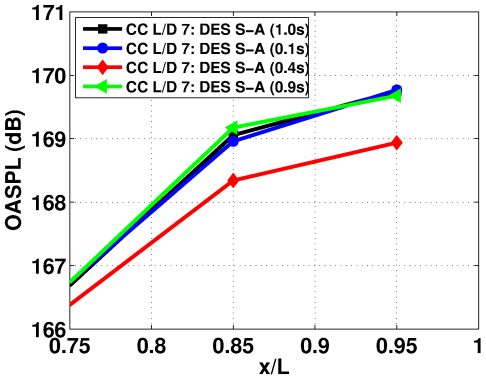

(e) $x/L = 0.75$ to 1.00

Figure A.21: OASPL along the cavity floor for the clean cavity, L/D=7, without doors.

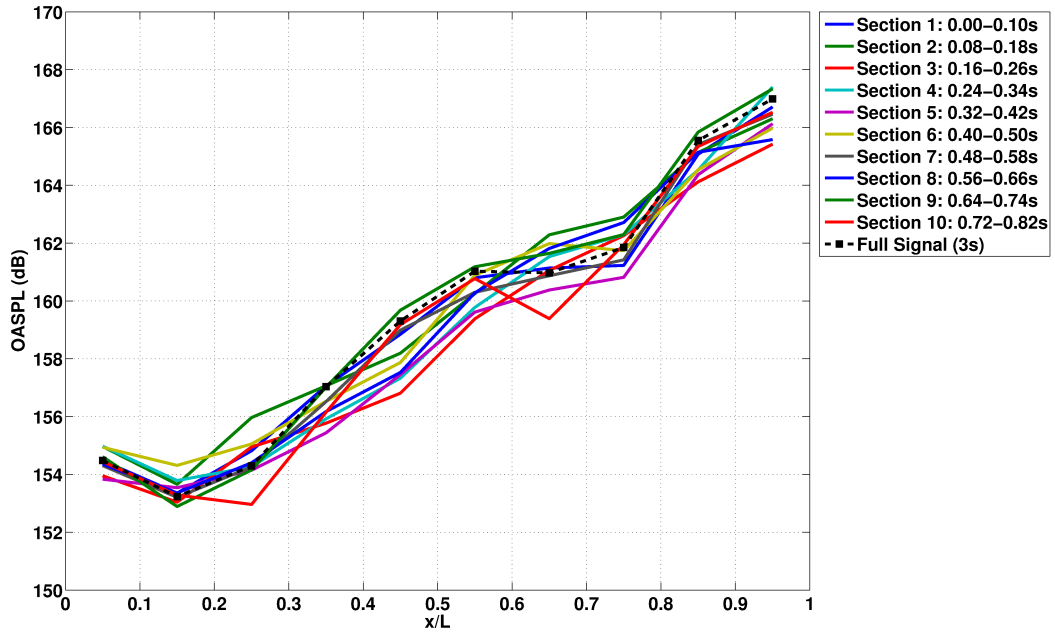

Figure A.22: OASPL along the cavity floor for the clean M219 cavity, L/D=5, with doors-off using experimental data from Nightingale et al[16]. Plot compares sections 1 to 10 to the full 3s signal of the experiment.

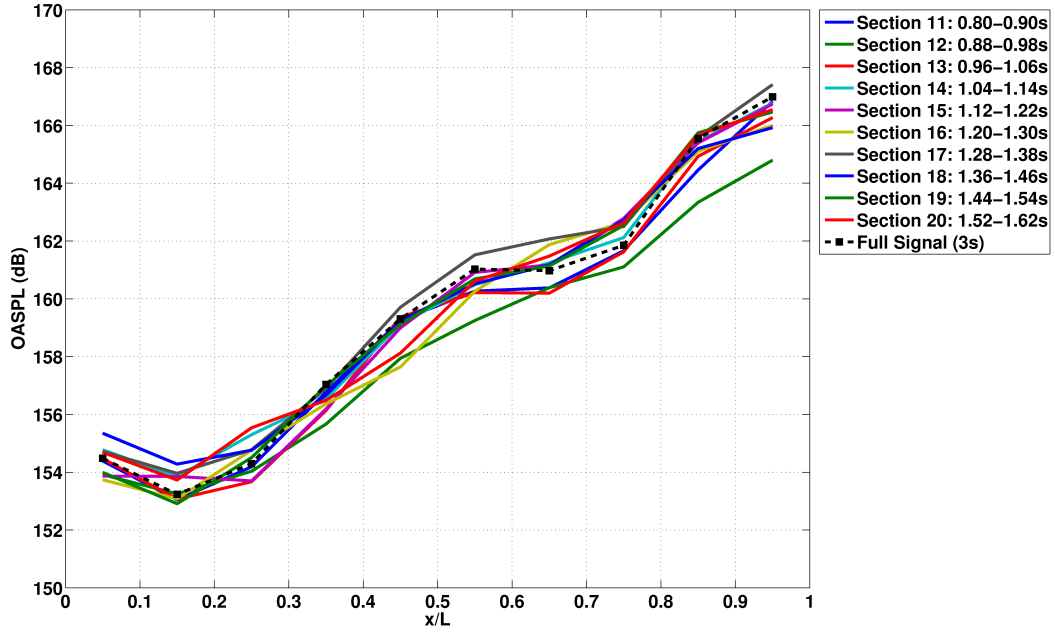

Figure A.23: OASPL along the cavity floor for the clean M219 cavity, L/D=5, with doors-off using experimental data from Nightingale et al[16]. Plot compares sections 11 to 20 to the full 3s signal of the experiment.

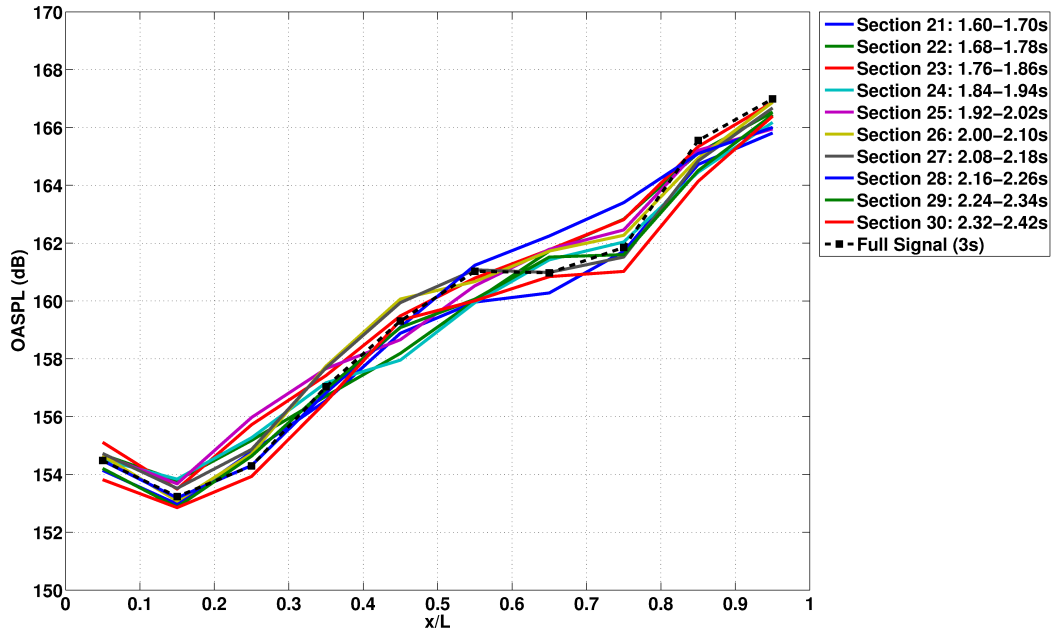

Figure A.24: OASPL along the cavity floor for the clean M219 cavity, L/D=5, with doors-off using experimental data from Nightingale et al[16]. Plot compares sections 21 to 30 to the full 3s signal of the experiment.

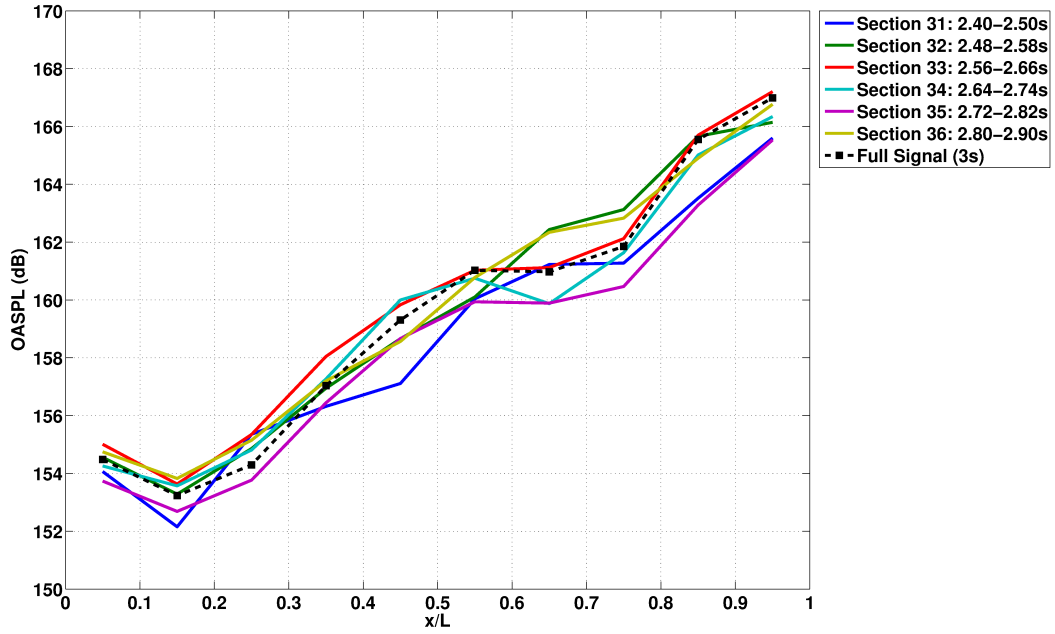

Figure A.25: OASPL along the cavity floor for the clean M219 cavity, L/D=5, with doors-off using experimental data from Nightingale et al[16]. Plot compares sections 31 to 36 to the full 3s signal of the experiment.

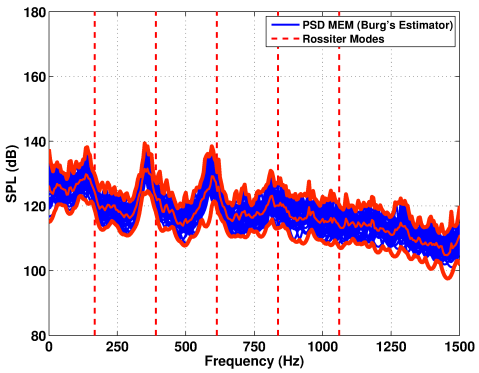

(a) $x/L = 0.05$

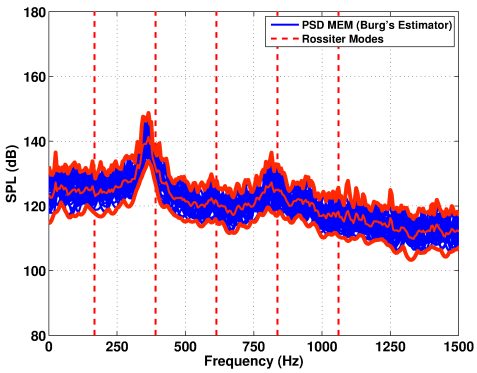

(b) $x/L = 0.50$

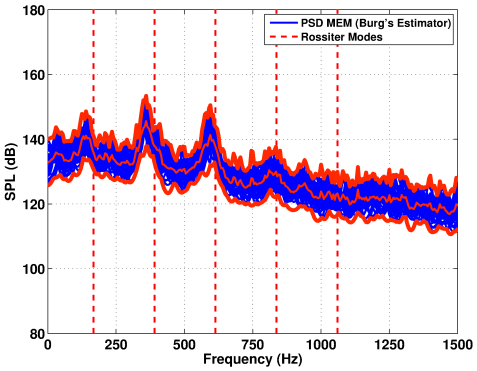

(c) $x/L = 0.95$

Figure A.26: PSD plots along the cavity floor for the clean M219 cavity, L/D=5, with doors-off comparing all 36 sections and showing the maximum, mean and minimum for method 1. Plots are shown for the front, middle and rear of the cavity.

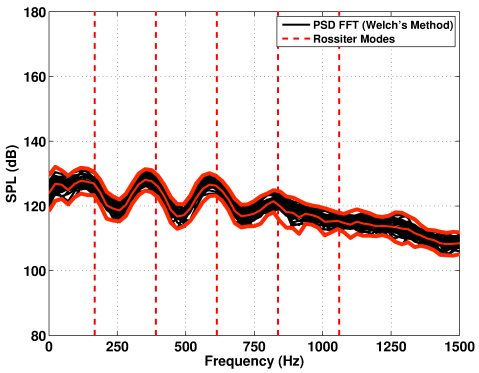

(a) $x/L = 0.05$

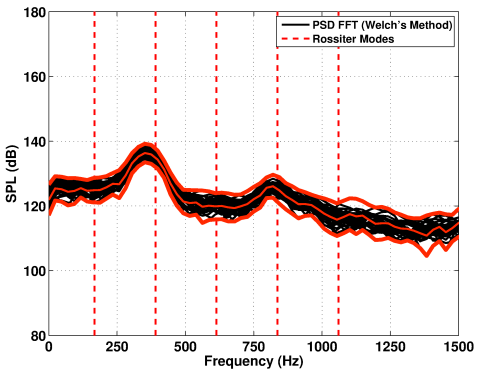

(b) $x/L = 0.50$

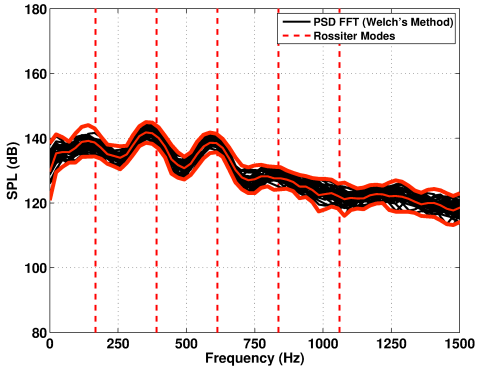

(c) $x/L = 0.95$

Figure A.27: PSD plots along the cavity floor for the clean M219 cavity, L/D=5, with doors-off comparing all 36 sections and showing the maximum, mean and minimum for method 2. Plots are shown for the front, middle and rear of the cavity.

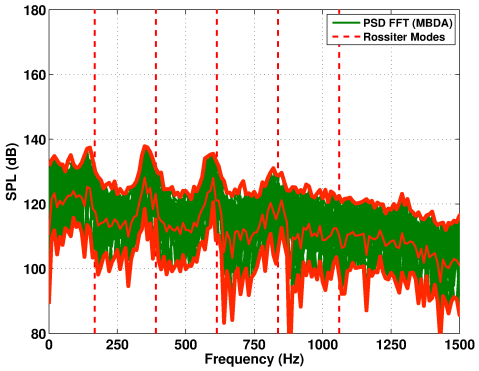

(a) $x/L = 0.05$

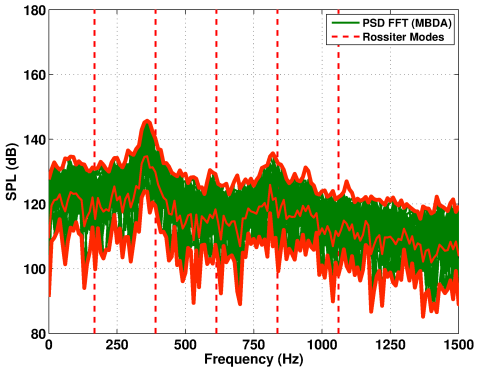

(b) $x/L = 0.50$

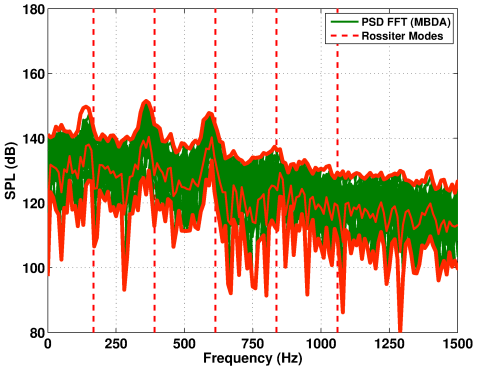

(c) $x/L = 0.95$

Figure A.28: PSD plots along the cavity floor for the clean M219 cavity, L/D=5, with doors-off comparing all 36 sections and showing the maximum, mean and minimum for method 3. Plots are shown for the front, middle and rear of the cavity.

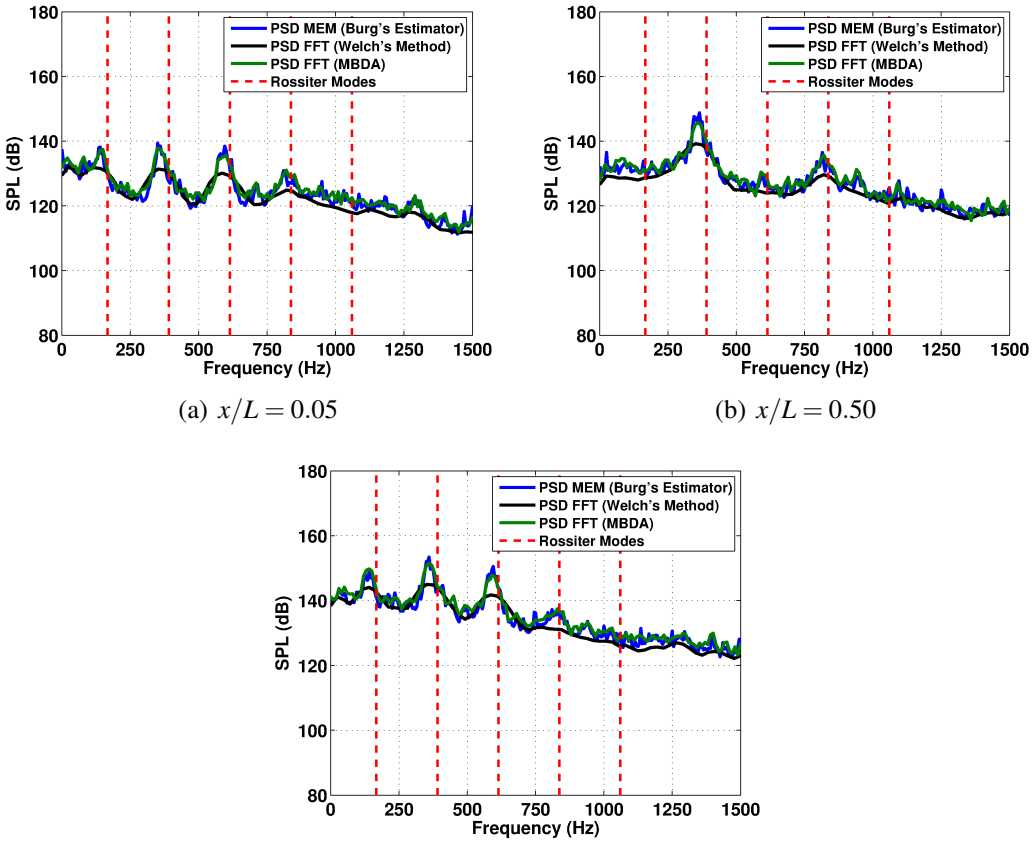

(a) $x/L = 0.05$

(b) $x/L = 0.50$

(c) $x/L = 0.95$

Figure A.29: PSD plots along the cavity floor for the clean M219 cavity, L/D=5, with doors-off comparing the maximum values obtained from the three methods. Plots are shown for the front, middle and rear of the cavity.

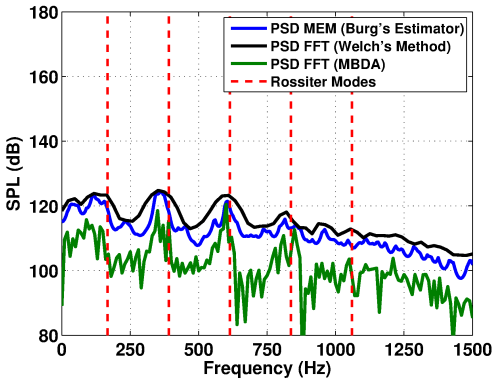

(a) $x/L = 0.05$

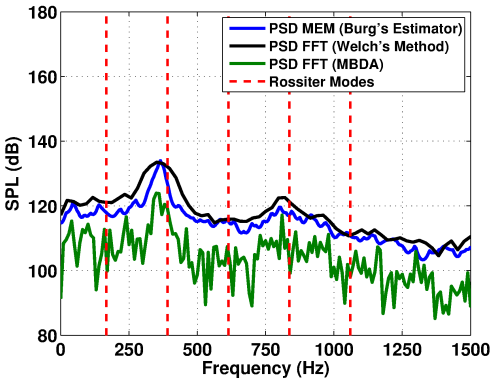

(b) $x/L = 0.50$

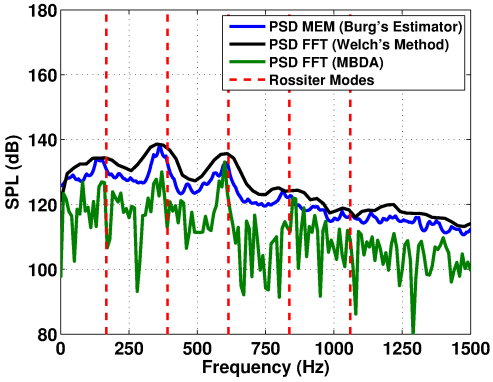

(c) $x/L = 0.95$

Figure A.30: PSD plots along the cavity floor for the clean M219 cavity, L/D=5, with doors-off comparing the minimum values obtained from the three methods. Plots are shown for the front, middle and rear of the cavity.

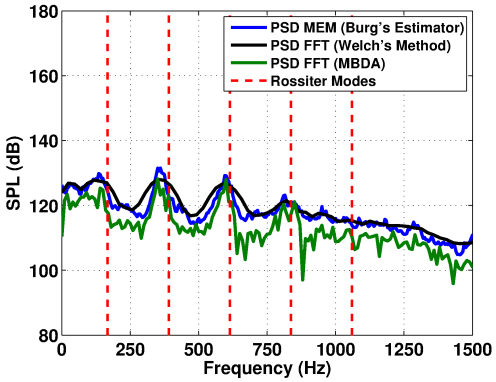

(a) $x/L = 0.05$

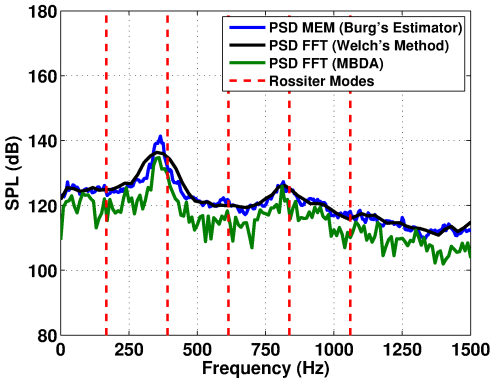

(b) $x/L = 0.50$

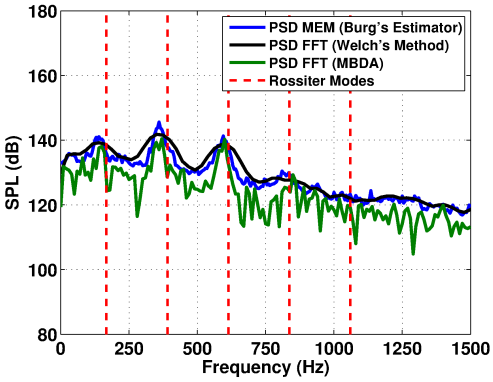

(c) $x/L = 0.95$

Figure A.31: PSD plots along the cavity floor for the clean M219 cavity, L/D=5, with doors-off comparing the mean values obtained from the three methods. Plots are shown for the front, middle and rear of the cavity.

A.4.2 Clean M219 Cavity, L/D=5, Doors-On (6kHz and 31.25kHz)

Figures A.32 to A.39 compare OASPL for different sections of the full 3s long signal for the clean M219 cavity with doors-on, sampled at 6kHz and 31.25kHz. Similar to the case with doors-off, most sections were able to capture the overall shape of the curve obtained from the full 3s signal and lay within a 2dB range.

A similar behaviour was seen between the three methods for the PSD plots along the floor of the cavity. The banded region was thickest for method 3 and thinnest for method 2 for both sampling frequencies. As before, the maximum values at the dominant modes were found in method 1, the minimum value was in method 2 and method 1 and method 3 gave similar mean values that were about 4dB larger than method 2.

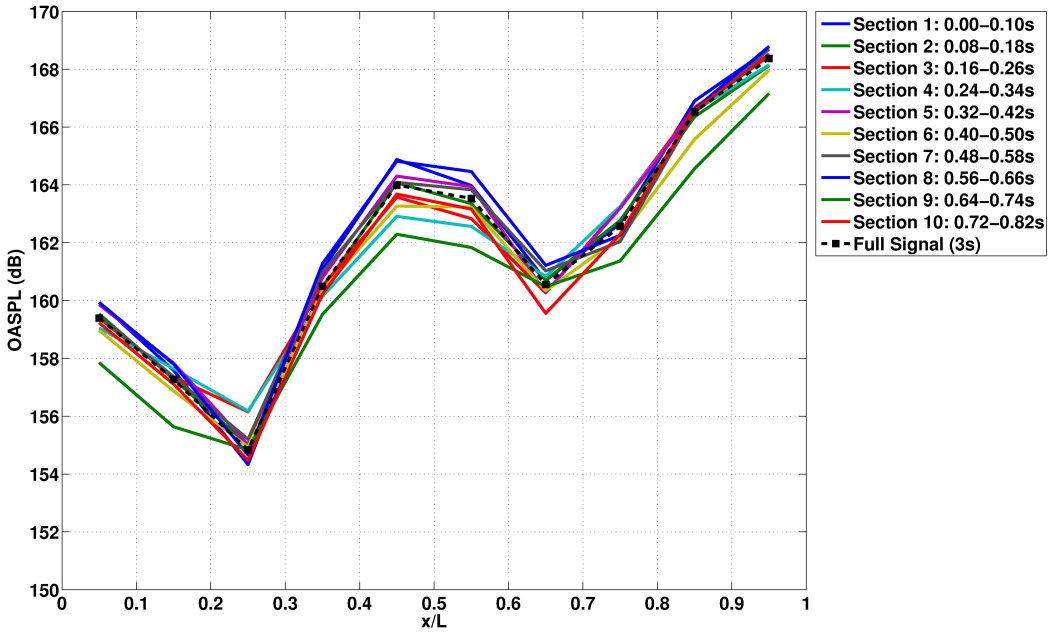

Figure A.32: OASPL along the cavity floor for the clean M219 cavity, L/D=5, with doors-on, sampled at 6kHz using experimental data from Nightingale et al[16]. Plot compares sections 1 to 10 to the full 3s signal of the experiment.

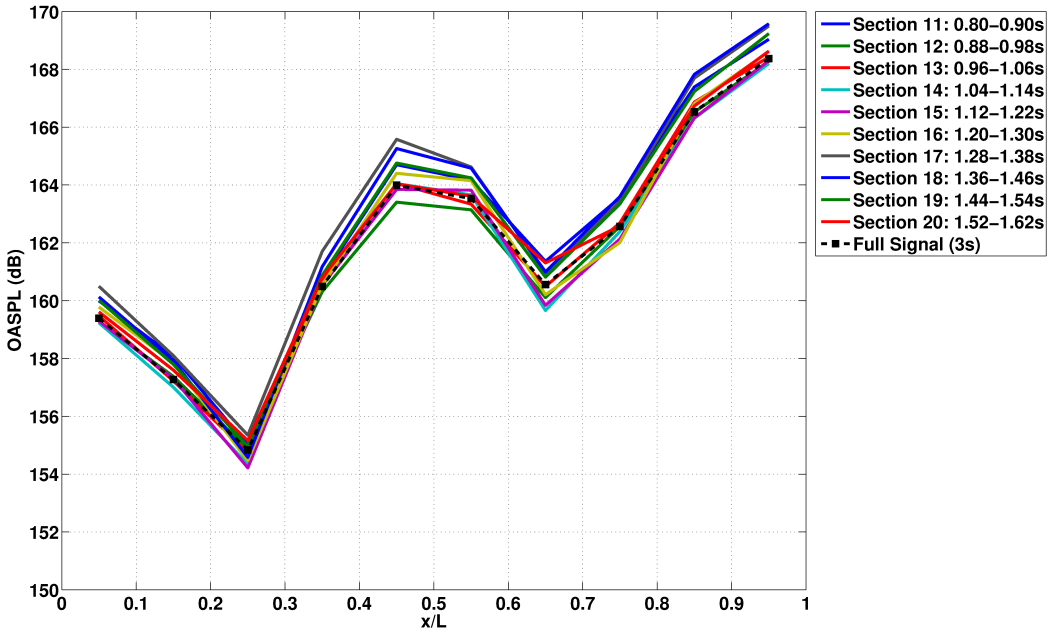

Figure A.33: OASPL along the cavity floor for the clean M219 cavity, L/D=5, with doors-on, sampled at 6kHz using experimental data from Nightingale et al[16]. Plot compares sections 11 to 20 to the full 3s signal of the experiment.

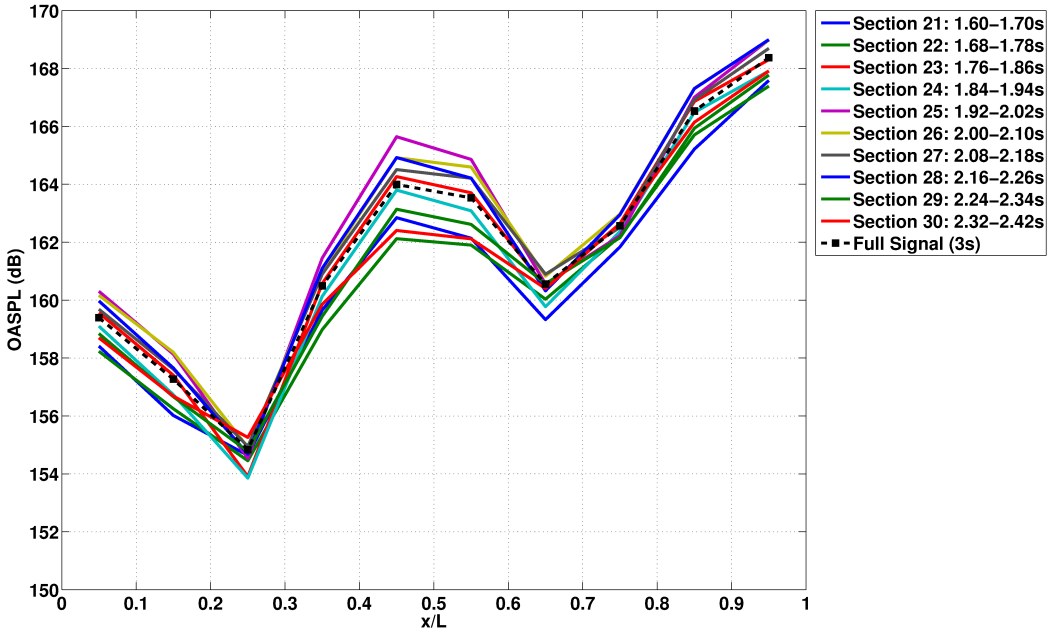

Figure A.34: OASPL along the cavity floor for the clean M219 cavity, L/D=5, with doors-on, sampled at 6kHz using experimental data from Nightingale et al[16]. Plot compares sections 21 to 30 to the full 3s signal of the experiment.

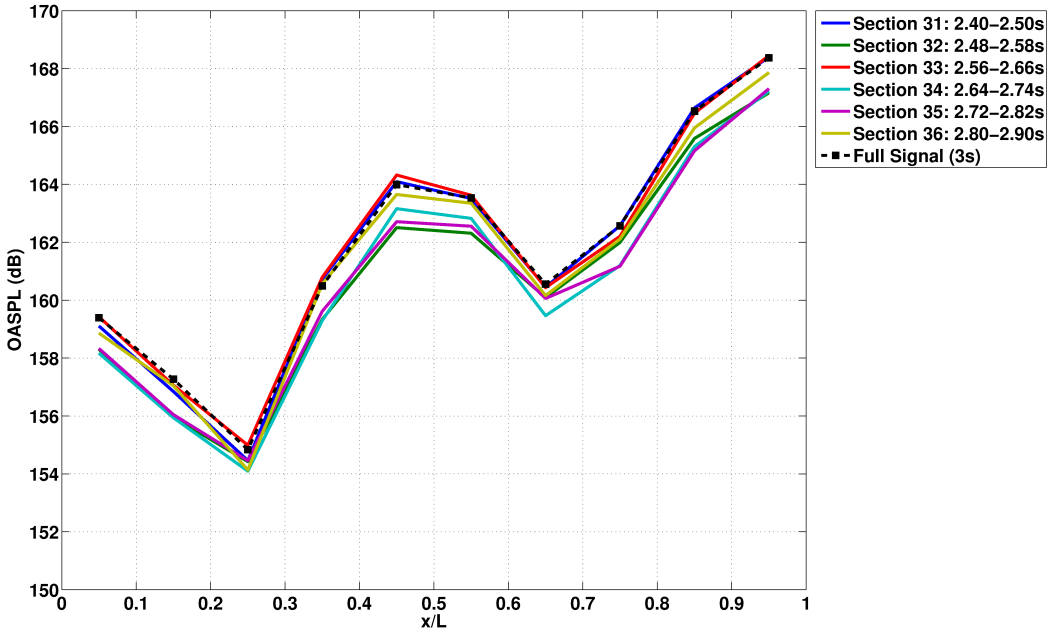

Figure A.35: OASPL along the cavity floor for the clean M219 cavity, L/D=5, with doors-on, sampled at 6kHz using experimental data from Nightingale et al[16]. Plot compares sections 31 to 36 to the full 3s signal of the experiment.

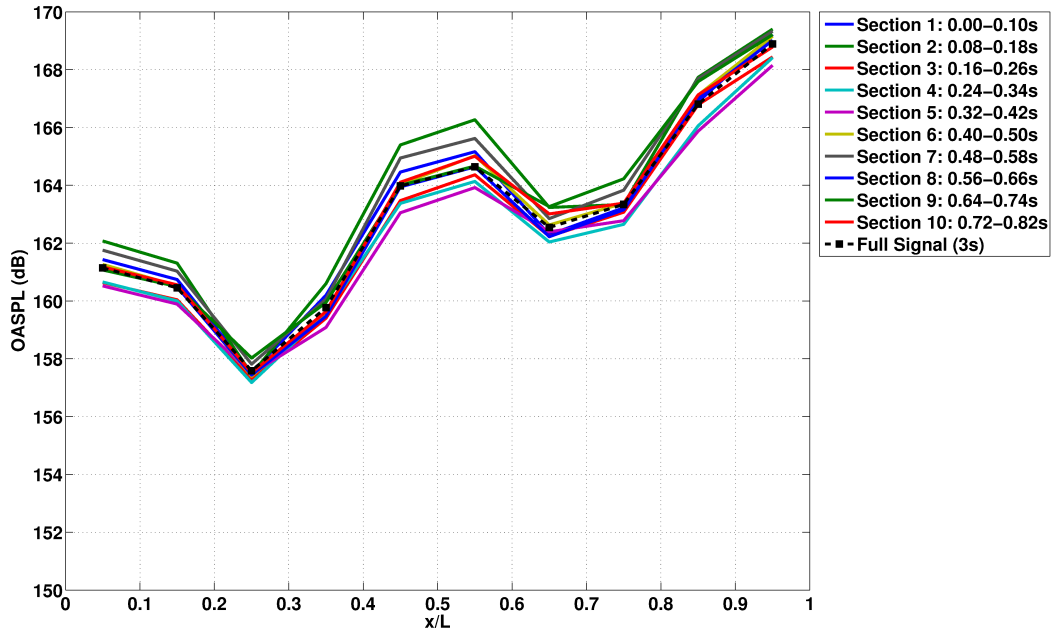

Figure A.36: OASPL along the cavity floor for the clean M219 cavity, L/D=5, with doors-on, sampled at 31.25kHz using experimental data from Nightingale et al[16]. Plot compares sections 1 to 10 to the full 3s signal of the experiment.

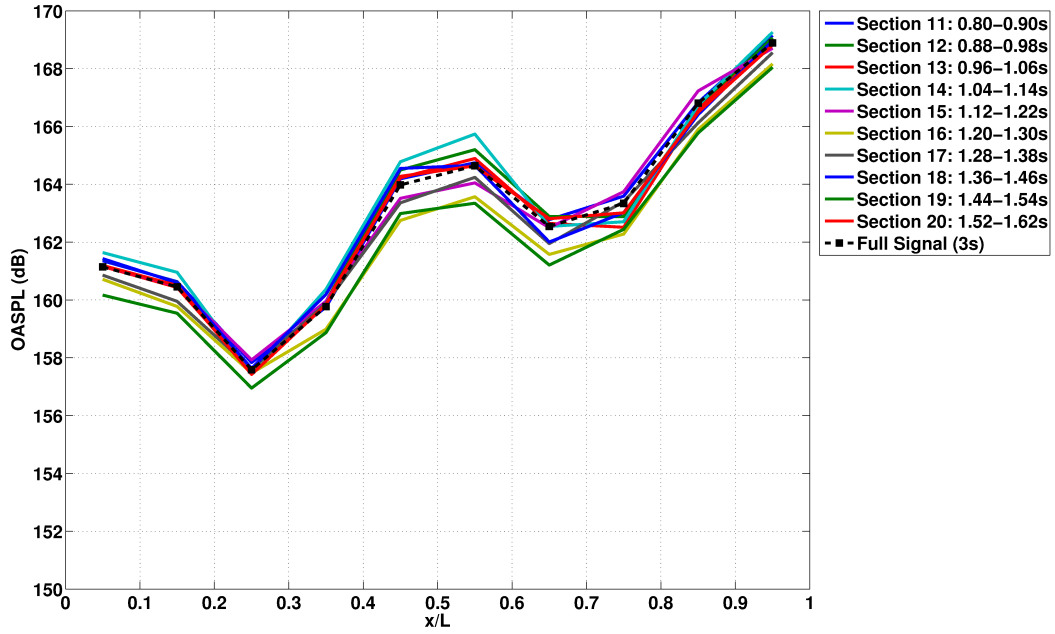

Figure A.37: OASPL along the cavity floor for the clean M219 cavity, L/D=5, with doors-on, sampled at 31.25kHz using experimental data from Nightingale et al[16]. Plot compares sections 11 to 20 to the full 3s signal of the experiment.

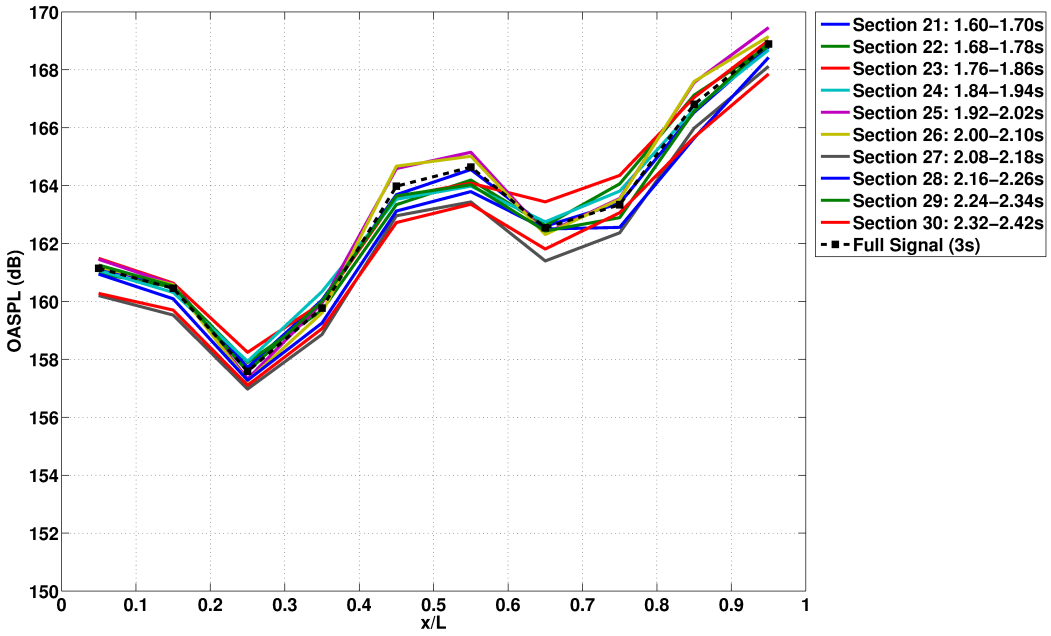

Figure A.38: OASPL along the cavity floor for the clean M219 cavity, L/D=5, with doors-on, sampled at 31.25kHz using experimental data from Nightingale et al[16]. Plot compares sections 21 to 30 to the full 3s signal of the experiment.

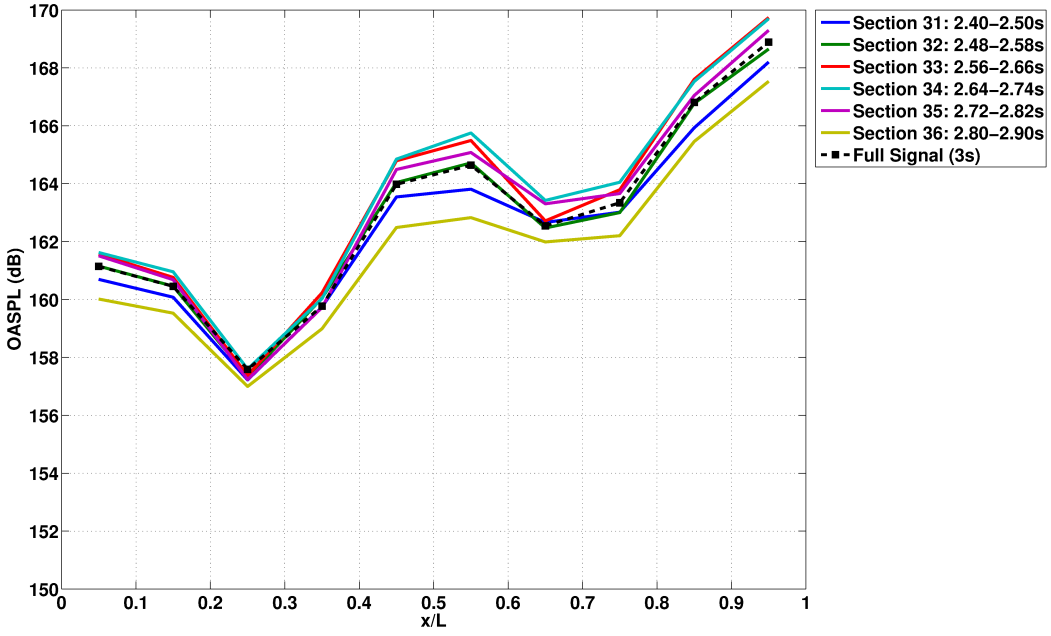

Figure A.39: OASPL along the cavity floor for the clean M219 cavity, L/D=5, with doors-on, sampled at 31.25kHz using experimental data from Nightingale et al[16]. Plot compares sections 31 to 36 to the full 3s signal of the experiment.

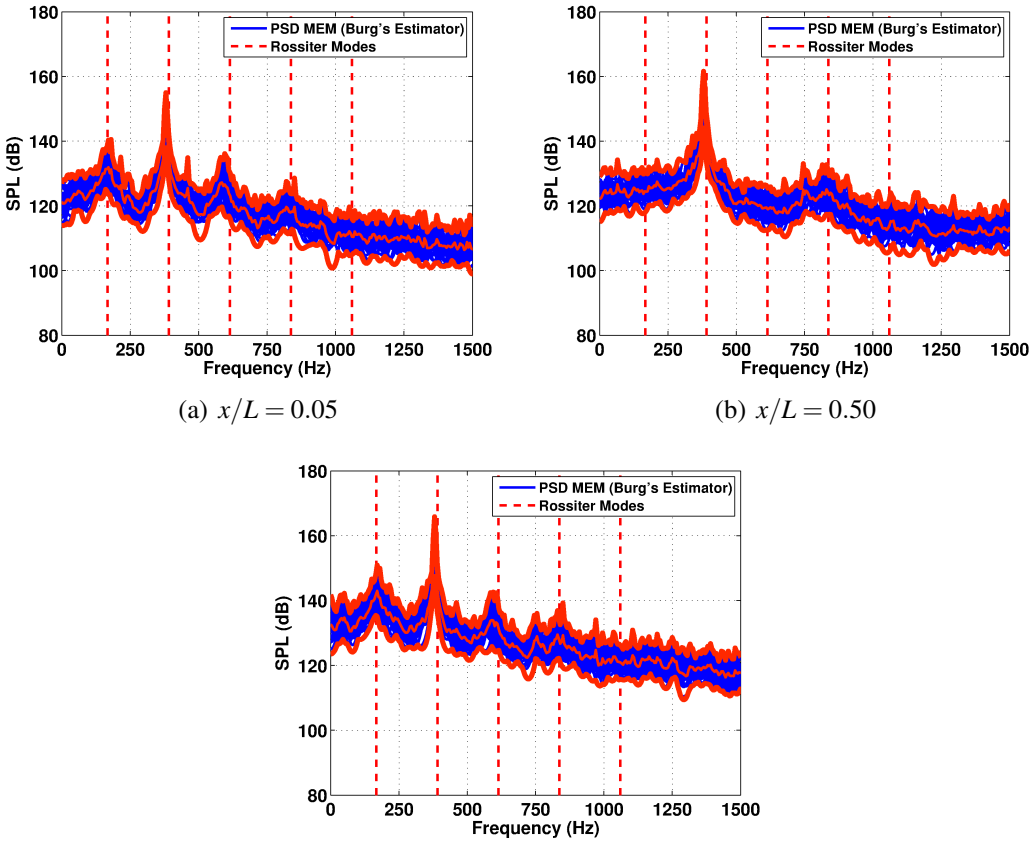

(a) $x/L = 0.05$

(b) $x/L = 0.50$

(c) $x/L = 0.95$

Figure A.40: PSD plots along the cavity floor for the clean M219 cavity, L/D=5, with doors-on, sampled at 6kHz comparing all 36 sections and showing the maximum, mean and minimum for method 1. Plots are shown for the front, middle and rear of the cavity.

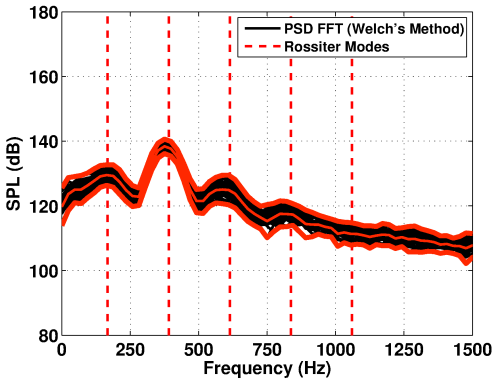

(a) $x/L = 0.05$

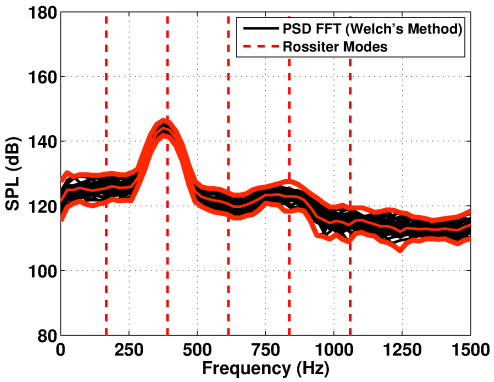

(b) $x/L = 0.50$

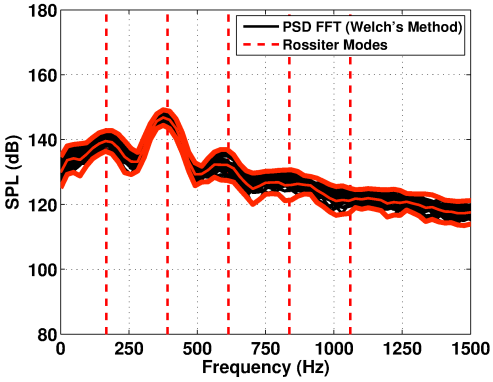

(c) $x/L = 0.95$

Figure A.41: PSD plots along the cavity floor for the clean M219 cavity, L/D=5, with doors-on, sampled at 6kHz comparing all 36 sections and showing the maximum, mean and minimum for method 2. Plots are shown for the front, middle and rear of the cavity.

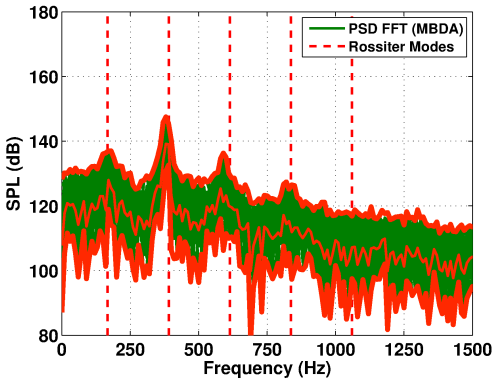

(a) $x/L = 0.05$

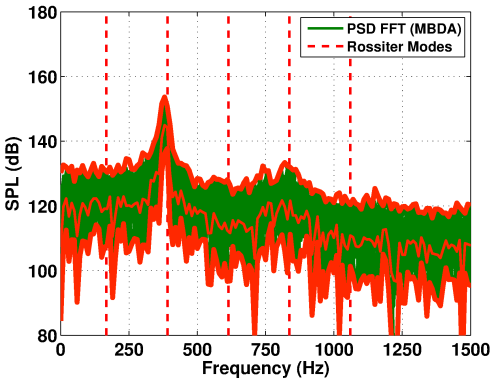

(b) $x/L = 0.50$

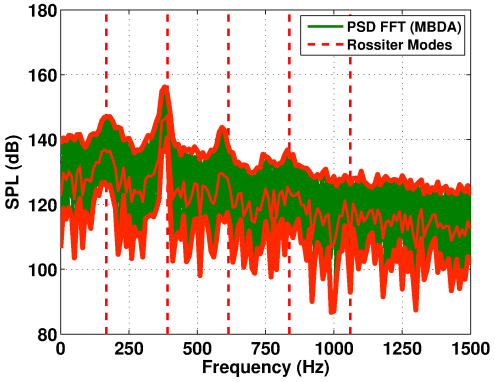

(c) $x/L = 0.95$

Figure A.42: PSD plots along the cavity floor for the clean M219 cavity, L/D=5, with doors-on, sampled at 6kHz comparing all 36 sections and showing the maximum, mean and minimum for method 3. Plots are shown for the front, middle and rear of the cavity.

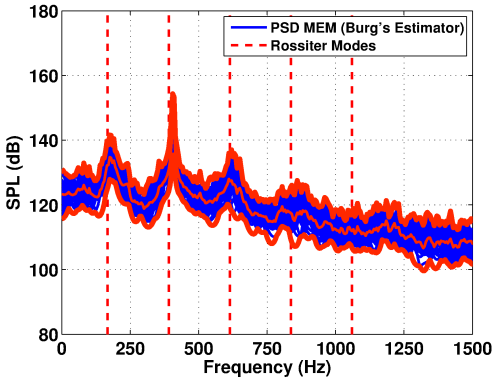

(a) $x/L = 0.05$

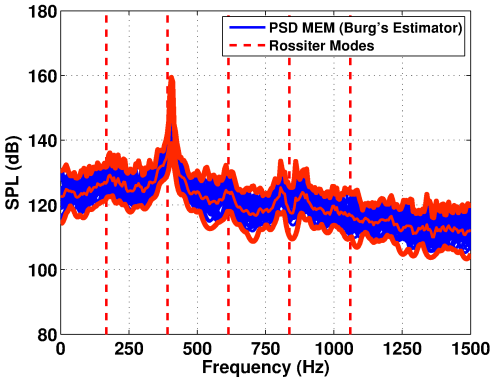

(b) $x/L = 0.50$

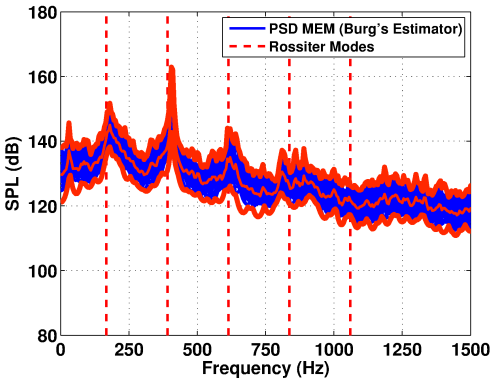

(c) $x/L = 0.95$

Figure A.43: PSD plots along the cavity floor for the clean M219 cavity, L/D=5, with doors-on, sampled at 31.25kHz comparing all 36 sections and showing the maximum, mean and minimum for method 1. Plots are shown for the front, middle and rear of the cavity.

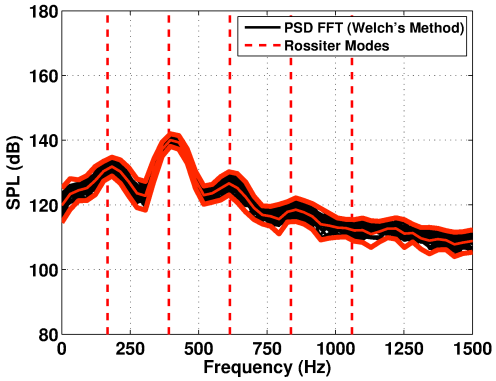

(a) $x/L = 0.05$

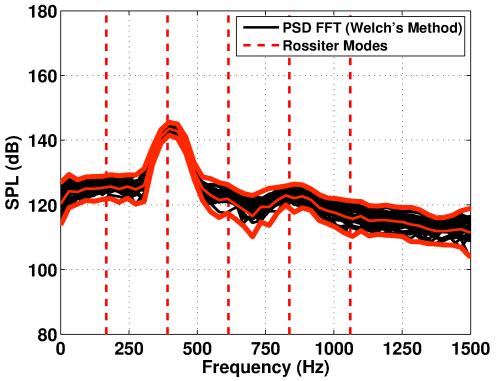

(b) $x/L = 0.50$

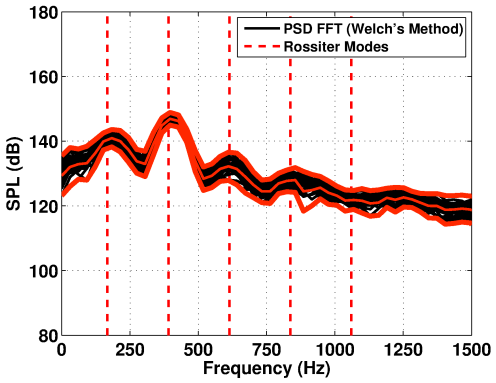

(c) $x/L = 0.95$

Figure A.44: PSD plots along the cavity floor for the clean M219 cavity, L/D=5, with doors-on, sampled at 31.25kHz comparing all 36 sections and showing the maximum, mean and minimum for method 2. Plots are shown for the front, middle and rear of the cavity.

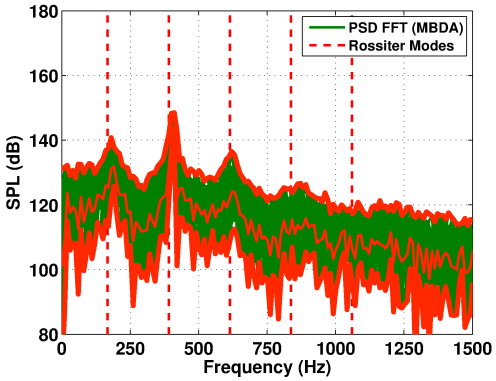

(a) $x/L = 0.05$

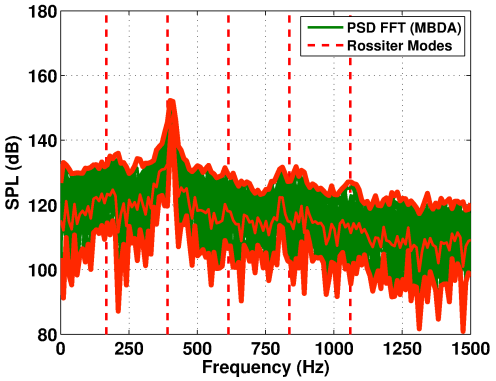

(b) $x/L = 0.50$

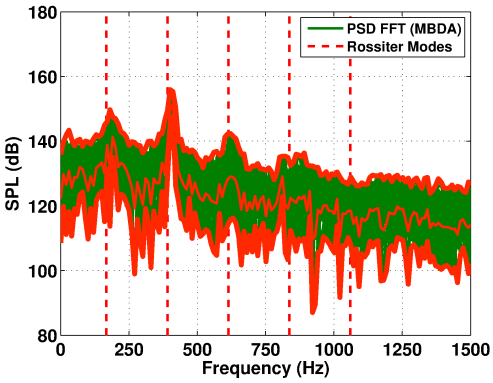

(c) $x/L = 0.95$

Figure A.45: PSD plots along the cavity floor for the clean M219 cavity, L/D=5, with doors-on, sampled at 31.25kHz comparing all 36 sections and showing the maximum, mean and minimum for method 3. Plots are shown for the front, middle and rear of the cavity.

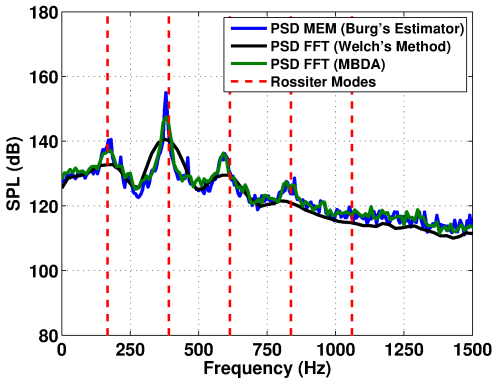

(a) $x/L = 0.05$

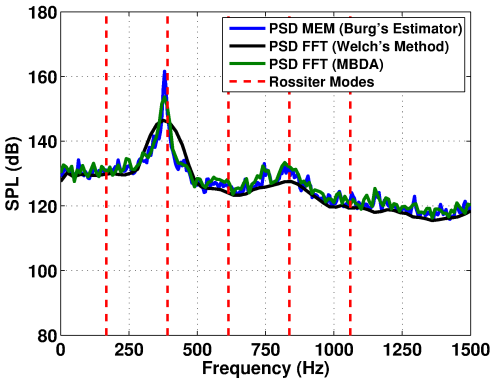

(b) $x/L = 0.50$

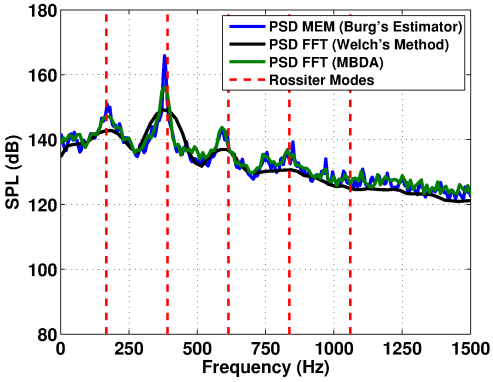

(c) $x/L = 0.95$

Figure A.46: PSD plots along the cavity floor for the clean M219 cavity, L/D=5, with doors-on, sampled at 6kHz comparing the maximum values obtained from the three methods. Plots are shown for the front, middle and rear of the cavity.

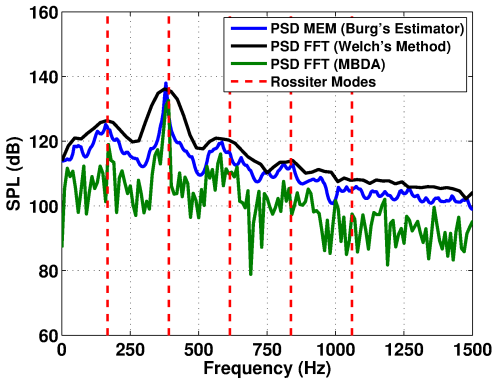

(a) $x/L = 0.05$

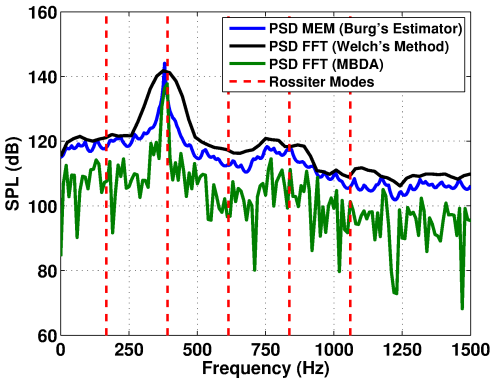

(b) $x/L = 0.50$

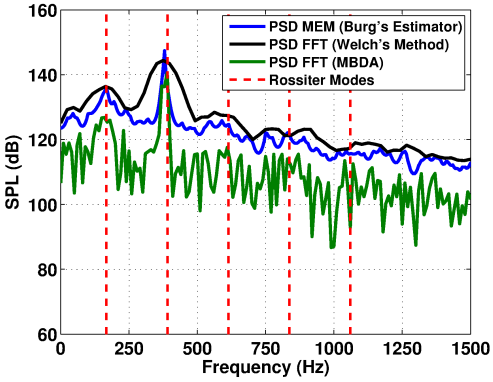

(c) $x/L = 0.95$

Figure A.47: PSD plots along the cavity floor for the clean M219 cavity, L/D=5, with doors-on, sampled at 6kHz comparing the minimum values obtained from the three methods. Plots are shown for the front, middle and rear of the cavity.

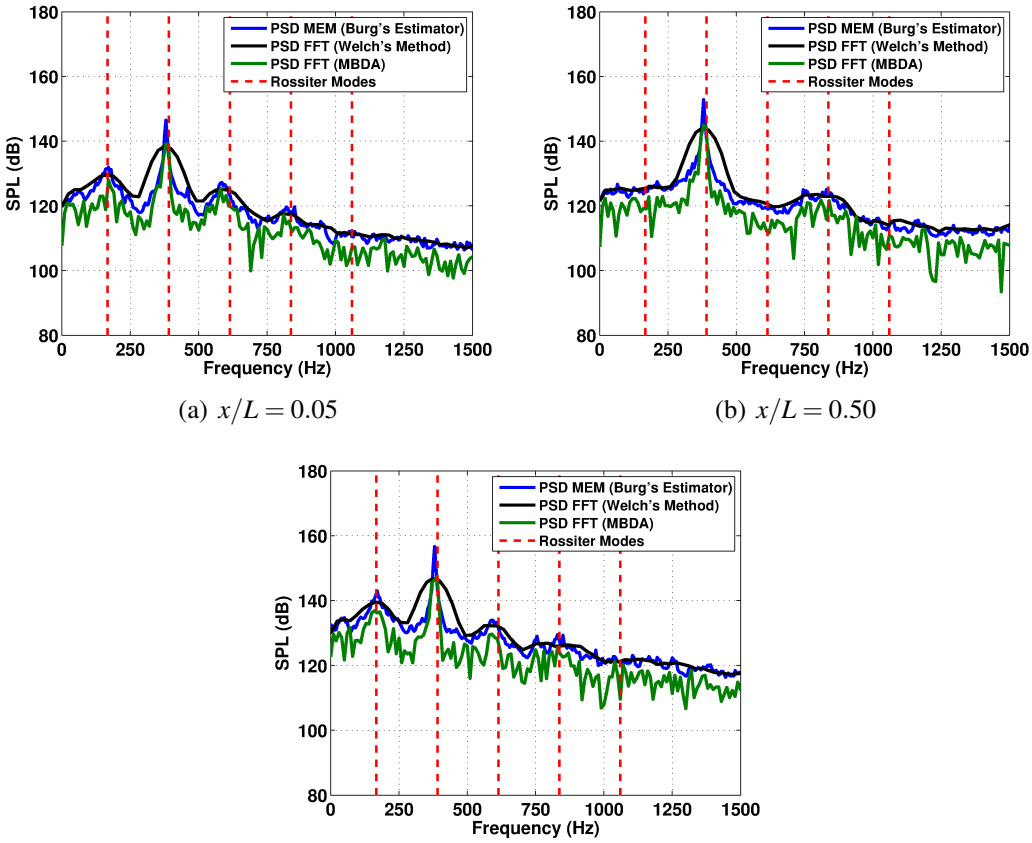

(a) $x/L = 0.05$

(b) $x/L = 0.50$

(c) $x/L = 0.95$

Figure A.48: PSD plots along the cavity floor for the clean M219 cavity, L/D=5, with doors-on, sampled at 6kHz comparing the mean values obtained from the three methods. Plots are shown for the front, middle and rear of the cavity.

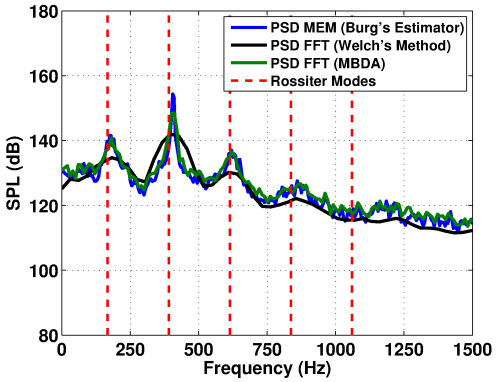

(a) $x/L = 0.05$

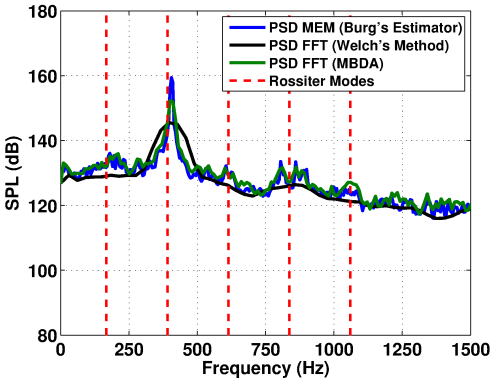

(b) $x/L = 0.50$

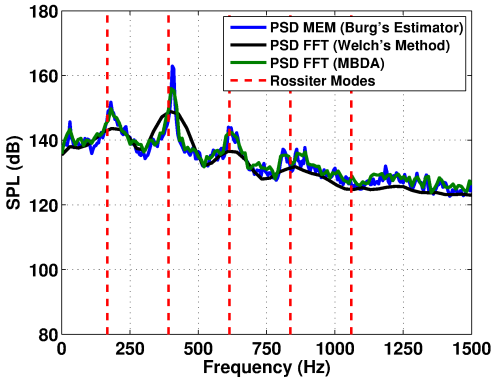

(c) $x/L = 0.95$

Figure A.49: PSD plots along the cavity floor for the clean M219 cavity, L/D=5, with doors-on, sampled at 31.25kHz comparing the maximum values obtained from the three methods. Plots are shown for the front, middle and rear of the cavity.

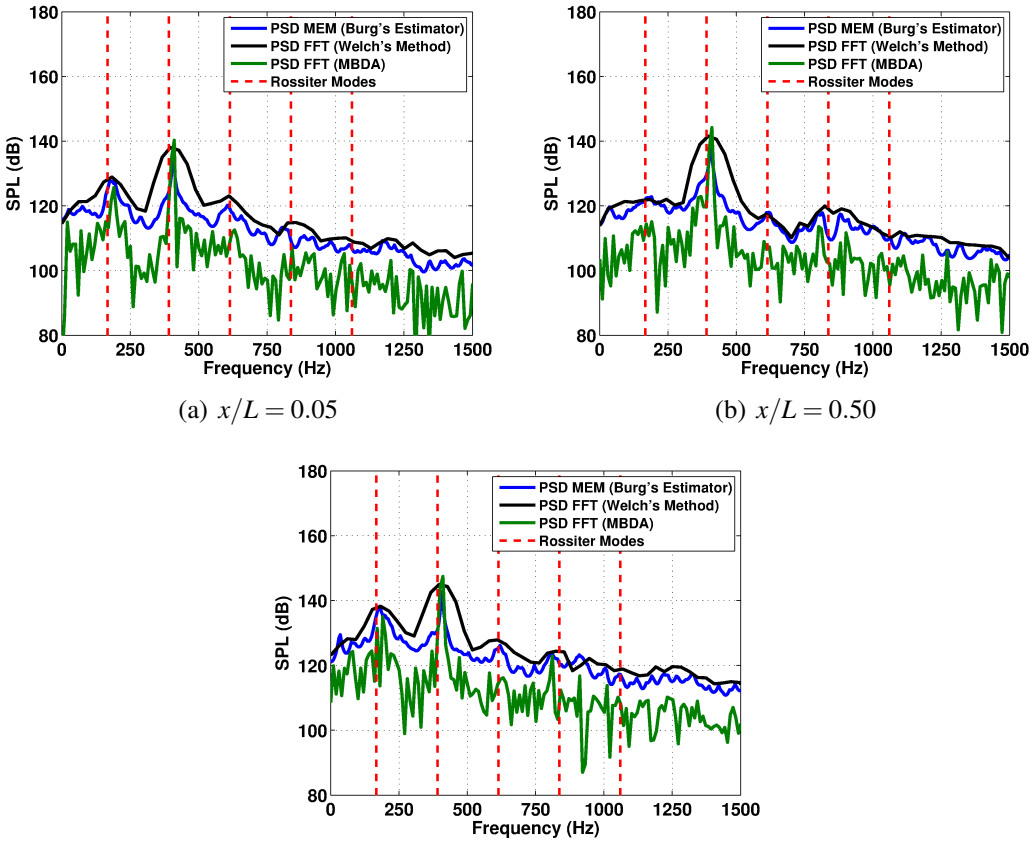

(a) $x/L = 0.05$

(b) $x/L = 0.50$

(c) $x/L = 0.95$

Figure A.50: PSD plots along the cavity floor for the clean M219 cavity, L/D=5, with doors-on, sampled at 31.25kHz comparing the minimum values obtained from the three methods. Plots are shown for the front, middle and rear of the cavity.

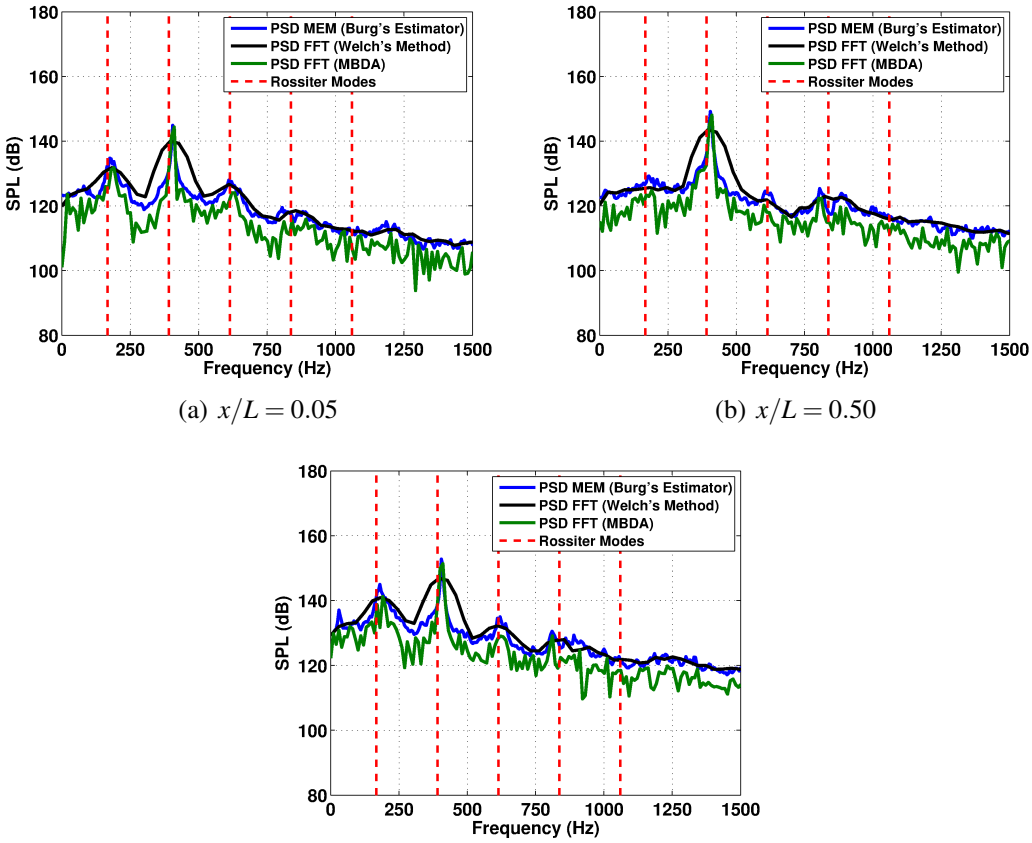

(a) $x/L = 0.05$ (b) $x/L = 0.50$

(c) $x/L = 0.95$

Figure A.51: PSD plots along the cavity floor for the clean M219 cavity, L/D=5, with doors-on, sampled at 31.25kHz comparing the mean values obtained from the three methods. Plots are shown for the front, middle and rear of the cavity.

A.5 Conclusions

Shortened and overlapping experimental and numerical pressure signals for a clean cavity, L/D=5, with and without doors were compared with the full signal to better understand the effect of the signal lengths in capturing the dominant tones in the cavity as well as the OASPL. Similar comparisons were made for a relatively long numerical pressure signal for a clean cavity, L/D=7, without doors. Due to the lack of experimental data, no comparisons could be made other than with the numerical signals themselves.

For the clean cavity, L/D=5, without doors, the experimental signal was shortened to lengths of 0.1s, 0.5s and 1.0s and compared with the full 3s signal. The 0.1s long signal was able to capture all the dominant tones in the cavity as well as the shape and magnitude of the OASPL curve. The maximum differences with the full experimental signal was 1dB and was found that by extending the length of the signal, more of the broadband noise was captured. The numerical signal, computed using DES with the S-A turbulence model, had a total length of 0.13s and was shortened to 0.01s, 0.05s and 0.1s with a 20% overlap. The 0.01s long signal did not capture most of the dominant cavity tones resulting in lower OASPL compared to the longer signals, even if it deceptively agreed better with the experiment. A signal length of 0.05s was adequate to capture the dominant tones in the cavity and expanding the signal length was seen to give better agreement with experiments in the broadband region.

Similarly, for the clean cavity, L/D=5, with doors, the experimental signal was shortened to lengths of 0.1s, 0.5s and 1.0s and compared with the full 3s signal. Again, the 0.1s long signal was able to capture all the dominant tones in the cavity with good prediction for OASPL with differences in the range of 1dB. The main effect of extending the length of the signal was seen in the broadband region giving better comparisons with the experiment. The numerical signal had a length of 0.08s and showed similar comparisons as with the case without doors. The shortest signal did not capture the dominating tones well and showed quieter OASPL than the longer signals. Here, the 0.05s long signal was able to capture the dominant as well as the lower amplitude tones.

The clean cavity, L/D=7, without doors had a numerical signal length of 1s and was shortened to 0.1s, 0.2s, 0.4s and 0.6s. The 0.1s long signal did not compare well with the full signal and missed out one mode entirely. At 0.2s of signal length, the dominant modes were stronger and the lower amplitude modes were reasonably captured. Extending the length further, showed better agreement with the full signal length. Overall the numerical and experimental signal processing show very similar trends for shortened, overlapping signals.

Three methods, an MEM method, an FFT method based on Welch's method and an FFT method provided by MBDA, were used to compare the differences in processing shortened signals. Experimental signals for the clean M219 cavity with doors-on and doors-off were 3s long, and were shortened to 36 sections each of 0.1s overlapped by 20%. The PSD computed using the three methods showed small differences in the maximum but large differences in the minimum and mean values over the 36 sections. Method 1 and 3 had similar fluctuations for each curve while method 2 produced smoother curves. Method 2 also had lower maximum and mean values. Overall method 3 showed the lowest minimum value and method 1 showed the highest maximum value compared to the three methods.

The conclusions from this study are as follows:

1. The minimum CFD signal length required to predict the dominant modes in the cavity is 0.05s.

2. The MEM and MBDA FFT method both predict the dominant modes well, however, since the former method also gives the highest predictions of SPL, it can be used to produce the maximum boundary for a given signal.

3. Based on the above, a CFD signal length of at least 0.05s and post-processing using the MEM method is recommended.

Appendix B

Reconstructing Velocity Variables using POD and MATLAB

B.1 Introduction

The original POD code, developed by Lawson[14,84], was used in Chapter 3 to demonstrate the use of data decomposition for storing large amounts of data, generally associated with cavity flow computations. While the original POD routines are capable of reducing dataset sizes by about 30%[14,84], they require a considerable amount of time and space to store the reduced dataset (of the order of **GB**). Routine engineering analysis in industry requires tools that are fast and work on relatively small datasets (of the order of **MB**), and do not generally require all the flow-field variables outputted from CFD computations.

With the above in mind, modifications were made to the original POD code so that the output produced could be used in MATLAB to reconstruct velocity variables at user specified points in a region of interest. In this way, CFD computations, along with the use of POD can aid quick data extraction and flow-field analysis that are highly repetitive and useful to industry. Modifications made to the original POD code and an example test case for clean cavity flow is presented.

B.2 Modified POD Process

Process flow diagrams showing the original process of flow-field reconstruction and variable reconstructions using MATLAB are presented in Figure B.1. The decomposition part is similar for both, where flow-field outputs, from the HMB2 flow solver, are obtained at regular intervals in the flow, usually over a time period equal to 10 periods of the first Rossiter mode. Routines in C, *pod_calc* and *pod_construct* are used to extract flow variables and temporal information from individual flow-field output files that are then used to construct the POD modes, one mode for each flow-field file and one with the energy contained in the mean flow-field.

In the original process, POD is performed on five primitive variables: density, u, v and w velocities and pressure, and flow-field reconstructions, for a specific instance in time, were obtained by using the *pod_reconstruct* routine. This reconstructs all the flow-field variables at all points in the mesh resulting in a file with the same size as the original flow-field file (approx. 200MB for a 5 million point grid). Note that this is for one instance in time and the reconstruction procedure has to be repeated, producing another file, if other instances in time are required.

For industrial use, velocity information inside and immediately outside the cavity is useful for grid data analysis, where the aerodynamic loads on a store placed at a location relative to a cavity can be determined from the local velocity components. The modified process uses a modified routine, *pod_construct_mod*, that uses an input file, *coords*, generally containing a relatively coarse distribution of points in and around a cavity, at which the mesh, mode and temporal information are stored. This results in files, $flowfield.dat$ and $temporal\_data.dat$, that have a combined size in the range of 5MB. These files are used by a script in MATLAB to reconstruct velocities using an inverse distance interpolation of the POD modes, for a duration of time, within the signal used to construct the POD modes.

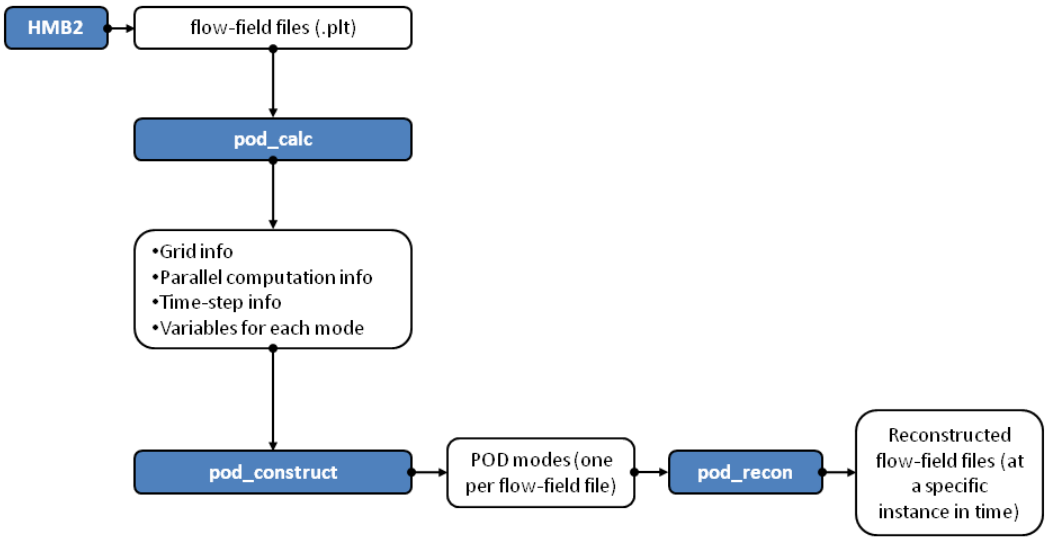

(a) Original POD process

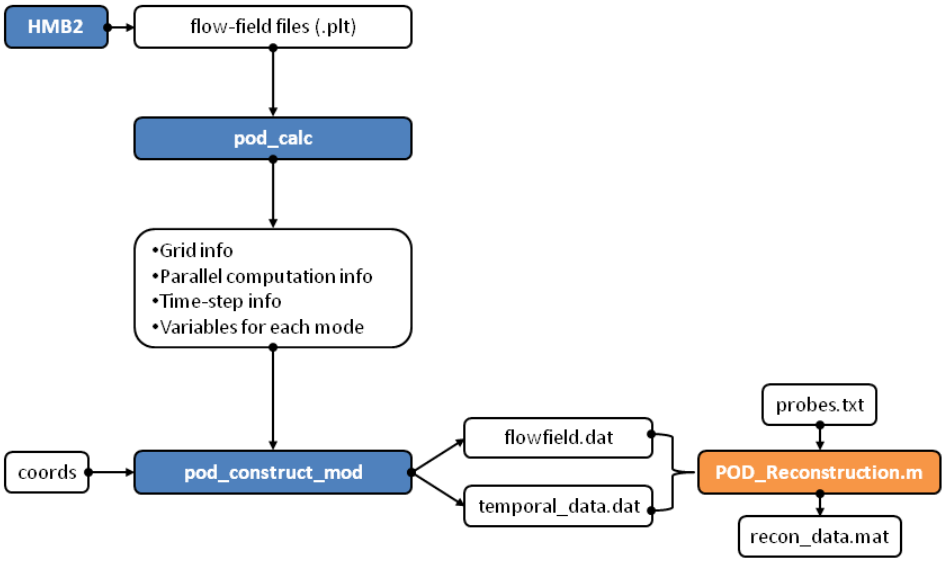

(b) Modified process for reconstructions using MATLAB

Figure B.1: Process flow diagram showing the use of C and MATLAB routines to reconstruct flow-field variables. Blue boxes show C routines while orange boxes show MATLAB routines.

B.3 Example Case: Clean Cavity, L/D=7

The example test case used was the flow inside a clean L/D=7 cavity without doors. The idealised cavity had a non-dimensional length of 1L, depth of 0.1428L and width of 0.2857L.

A coarse distribution of points, at which mode information will be saved and used for reconstructions, was first defined in the cavity region and immediately outside as shown in Figure B.2. The grey shaded region represented the cavity domain and had sets of 8 points along the length, 4 points along the width and height such that there were 128 points in the cavity region. To define the region immediately outside the cavity, a total of 608 points were used such that there were 12 points along the length, 10 points along the width and 8 points along the height. This did not include points where the flow was not calculated in regions just away from the walls of the cavity as shown in Figure B.2. For a case with doors-on, the points outside on either side of the cavity could be reduced as the doors restrict the flow from spilling over the sides of the cavity.

The coordinates of these points were used as input to the *pod_construct_mod* routine that retained temporal mode information at these points. A finer distribution of points that included the cavity and shear layer regions were used as input to the MATLAB script to reconstruct velocity variables at those points as shown in Figure B.3(a) where the points are colours with non-dimensional U velocity. Reconstructions were made at a specific instance in time for which a flow-file file was available. Comparisons made in Figure B.3 show slices along the width and length of the cavity and a set of points at which velocity variables were reconstructed. Non-dimensional U velocity was compared where reconstructed values showed fair agreement with the original flow-field data obtained from HMB2, considering the relative coarseness of the points at which mode information was stored.

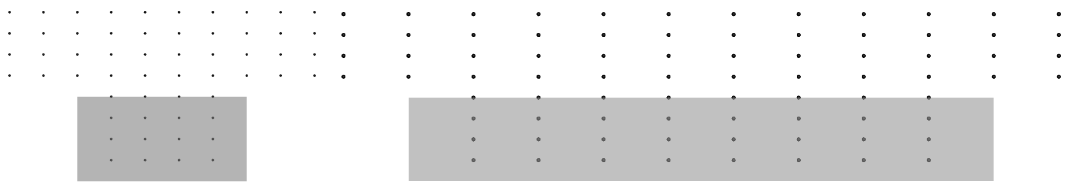

(a) $x/L = 0.5$ (b) $z/L = 0.0$

Figure B.2: Coarse distribution of points in and around the cavity region at which mode information is to be retained.

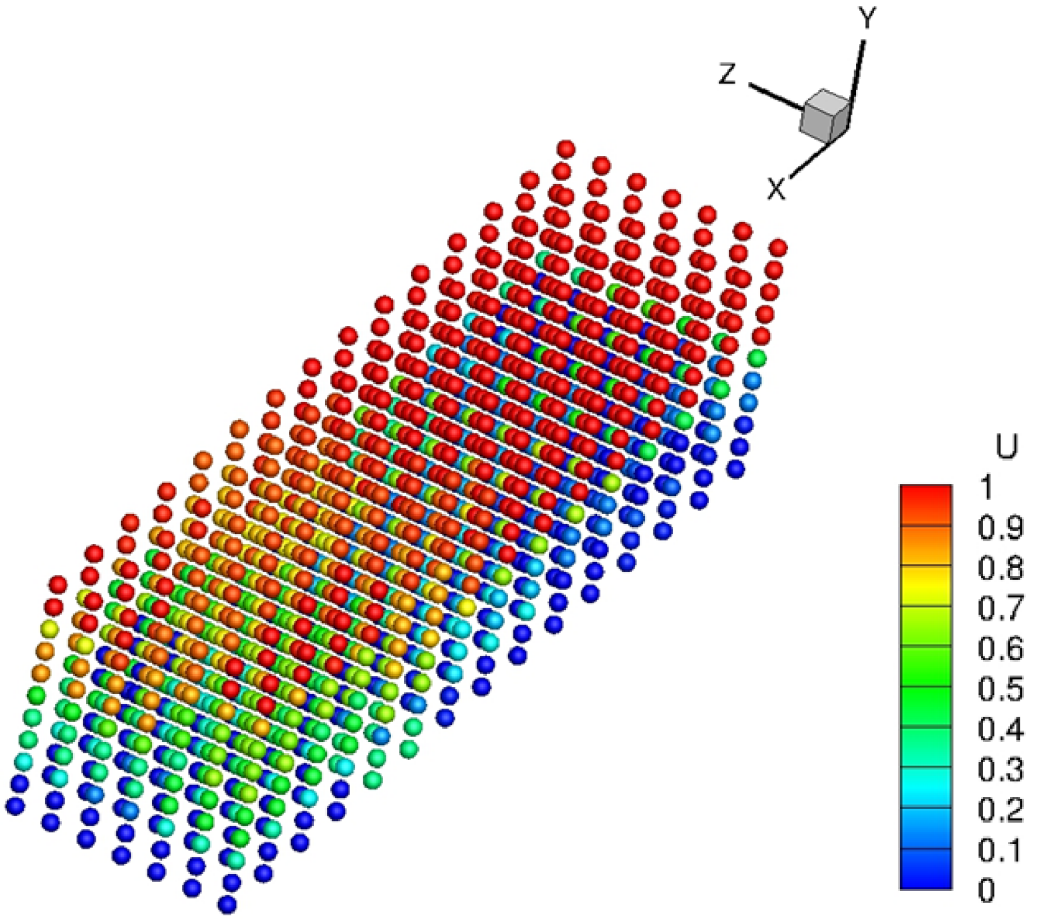

(a) Reconstruction of cavity flow-field using a set of points

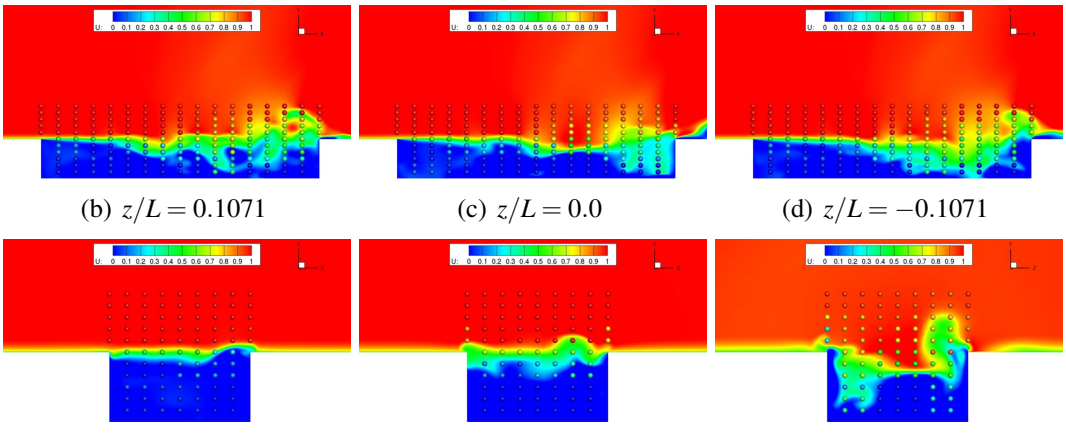

(b) $z/L = 0.1071$ (c) $z/L = 0.0$ (d) $z/L = -0.1071$

(e) $x/L = 0.25$ (f) $x/L = 0.5$ (g) $x/L = 0.85$

Figure B.3: Reconstruction using a set of points (a) and reconstructed points at an instance in time compared with original flow-field at the same time instance. Planes are located at the cavity centreline ($z/L = 0.0$) and to port and starboard of the centreline, and at the front ($x/L = 0.25$), middle ($x/L = 0.5$) and rear end ($x/L = 0.85$) of the cavity.

References

[1] Image of the F-22a Raptor. `www.wikimedia.org/F22.jpg`. Last accessed 11^{th} August 2010.

[2] Image of the F-35 Lightning II. `www.jsf.mil/gallery/galphoto.htm`. Last accessed 11^{th} August 2010.

[3] J. A. Ross and J. Odedra. Time-Averaged and Unsteady Loads on a Missile at Launch From an Internal Weapons Bay. *RTO AVT Symposium on Missile Aerodynamics*, RTO-MP-5, 1998.

[4] N.E. Murray, B.J. Jansen, L. Gui, J.M. Seiner, and R. Birkbeck. Measurements of Store Separation Dynamics. In *Proceedings of the 47^{th} AIAA Aerospace Sciences Meeting including the New Horizons Forum and Aerospace Exposition*, Orlando, Florida, USA, 5-8 January 2009.

[5] B. Khanal, K. Knowles, and A.J. Saddington. Computational Study of Flowfield Characteristics In Cavities With Stores. *The Aeronautical Journal*, 115(1172):669–681, 2011.

[6] M. Smith and S. Schwimley. X-45A/Small Smart Bomb Separation Analysis. In *Proceedings of the 44^{th} AIAA Aerospace Sciences Meeting and Exhibit*, Reno, Nevada, USA, 9-12 January 2006.

[7] C.J. Coley. *An Investigation of Cavity Resonance and its Relationship to Store Force and Moment Loading*. PhD thesis, Air Force Institute of Technology. Wright-Patterson AFB. Department of Aeronautics And Astronautics, March 2011.

[8] L.P. Finney. *Investigation of Cavity Flow Effects on Store Separation Trajectories. Trident Scholar Project Report No. 388*. PhD thesis, U.S. Naval Academy, May 2010.

[9] R. Spinetti and B. Jolly. Time-Accurate Numerical Simulation of GBU-38s Separating from the B-1B Aircraft with Various Ejector Forces, Store Properties, and Load-Out Configurations - IHAAA Store Separation Cavity (SSC) Project. In *Proceedings of the 46^{th} AIAA Aerospace Sciences Meeting and Exhibit*, Reno, NV, United States, 7–10 January 2008.

[10] R. Johnson and A. Cary. F-111 Store Trajectory Analysis. Williamsburg, VA, USA, 7–9 June 2004. RTO AVT Symposium on Functional and Mechanical Integration of Weapons and Land and Air Vehicles, Published in RTO-MP-AVT-108.

[11] S. Arunajatesan, M. Bharadwaj, W. C. Riley, and M. Ross. One-Way Coupled Fluid Structure Simulations of Stores in Weapons Bays. In *Proceedings of the 51st AIAA Aerospace Sciences Meeting including the New Horizons Forum and Aerospace Exposition*, Grapevine, Texas, USA, 7-10 January 2013.

[12] Z. Liu. Line Integral Convolution and Flow Visualisation Techniques. `www.zhanpingliu.org/Research/FlowVis/LIC/LIC.htm`, 2007. Last accessed: 10^{th} April 2014.

[13] S.J. Lawson. *High Performance Computing for HighFidelity MultiDisciplinary Analysis of Weapons Bays*. PhD thesis, University of Liverpool, October 2009.

[14] S.J. Lawson, G.N. Barakos, and A. Simpson. Understanding Cavity Flows using Proper Orthogonal Decomposition and Signal Processing. *Journal of Algorithms and Computational Technology*, 4(1):4769, March 2010.

[15] G.M. Siouris. *Missile Guidance and Control Systems*. Springer-Verlag New York Inc., 1st edition, 2008.

[16] D.A. Nightingale, J.A. Ross, and G.W. Foster. Cavity Unsteady pressure measurements - Examples from Wind-Tunnel Tests. Technical Report Version 3, Aerodynamics & Aeromechanics Systems Group, QinetiQ, November 2005.

[17] J.H. Fox. Generic Wing Pylon, and Moving Finned Store. TN. 37389-6001. Arnold Engineering Development Center (AEDC), Arnold AFB, USA, 2000.

[18] Scopus. `www.scopus.com`.

[19] Web of Knowledge. `www.isiknowledge.com`.

[20] DTIC Defense Technical Information Center. `www.dtic.mil/dtic/stresources/journals/index.html`.

[21] American Institute of Aeronautics and AIAA Astronautics. `http://arc.aiaa.org/search`.

[22] NASA Technical Report Server. `http://ntrs.nasa.gov/search.jsp`.

[23] R.F. Tomaro, F.C. Witzeman, and W.Z. Strang. Simulation of Store Separation for the F/A-18C Using Cobalt60. *Journal of Aircraft*, 37(3):361–367, 2000.

[24] J. Sahu. Time-accurate numerical prediction of free flight aerodynamics of projectiles. *Journal of Spacecraft and Rockets*, 45(5):946–954, June 2008.

[25] A. Cenko, E. N. Tinoco, R. D. Dyer, and J. DeJongh. PAN AIR Applications to Weapons Carriage and Separation. *Journal of Aircraft*, 18(2):128–134, 2014/02/11 1981.

[26] Samir Bennani, Jan-Willem Van Staveren, Bert Beuker, and Joshua J. Meijer. Flutter analysis of an f-16a/b in heavy store configuration. *Journal of Aircraft*, 42(6):1565–1574, 2014/02/05 2005.

[27] W.E. Triplett, H.P.F. Kappus, and R.J. Landy. Active flutter control-an adaptable application to wing/store flutter. *Journal of Aircraft*, 10(11):669–678, 1973.

[28] S.J. Lawson and G.N. Barakos. Review of Numerical Simulations For High-Speed, Turbulent Cavity Flows. *Progress in Aerospace Sciences*, 47(3):186 – 216, 2011.

[29] R.L. Stallings. Store Separation from Cavities at Supersonic Flight Speeds. *Journal of Spacecraft and Rockets*, 20(2):129–132, 1983.

[30] V.I. Shalaev, A.V. Fedorov, and N.D. Malmuth. Dynamics of Slender Bodies Separating from Rectangular Cavities. *AIAA Journal*, 40(3):517–525, March 2002.

[31] D. Sahoo, A. Annaswamy, and F. Alvi. Active Store Trajectory Control in Supersonic Cavities Using Microjets and Low-Order Modeling. *AIAA Journal*, 45(3):516–531, 2007.

[32] N. Kraft and A. Lofthouse. Non-Repeatability of Store Separation Trajectories from Internal Weapon Bays Due to Unsteady Cavity Flow Effects - Lessons Learned from a 2D Investigation. In *Proceedings of the 49th AIAA Aerospace Sciences Meeting including the New Horizons Forum and Aerospace Exposition*, Orlando, Florida, USA, 4-7 January 2011.

[33] R.H. Nichols and P.G. Buning. *User Manual for OVERFLOW 2.1, Version 2.1*. Birmingham, AL, August 2008.

[34] R. Johnson, M.B. Davis, and D. Finley. Relaxed Fidelity CFD Methods Applied to Store Separation Problems. Williamsburg, VA, USA, 7–9 June 2004. RTO AVT Symposium on Functional and Mechanical Integration of Weapons and Land and Air Vehicles, Published in RTO-MP-AVT-108.

[35] J. Lee, A. Piranian, J. Martel, D. Crowe, and M. Rizk. Store Separations in Jet Flow Environments. In *Proceedings of the 48th AIAA Aerospace Sciences Meeting Including the New Horizons Forum and Aerospace Exposition*, Orlando, Florida, USA, 4-7 January 2010.

[36] N.C. Prewitt, D.M. Belk, and R.C. Maple. Multiple-Body Trajectory Calculations Using the Beggar Code. *Journal of Aircraft*, 36(5):802–808, 1999.

[37] T. Berglind, S.H. Peng, and L. Tysell. FoT25: Studies of Embedded Weapons Bays Summary Report. Technical Report: FOI-R-2775-SE, FOI, Swedish Defence Research Agency, June 2009.

[38] A. Cenko, R. Deslandes, M. Dillenius, and M. Stanek. Unsteady Weapon Bay Aerodynamics - Urban Legend or Flight Clearance Nightmare. In *Proceedings of the 46th AIAA Aerospace Sciences Meeting and Exhibit*, Reno, Nevada, USA, 7-10 January 2008.

[39] A. Cenko and A. Piranian. Advances in Modeling and Simulation Capabilities for Predicting Store Trajectories Past Success and Future Challenges. *RTO Air Vehicle Technology Meeting 108*, 24, 2004.

[40] J. Lee and A. Cenko. Evaluation of the GBU-38 Store Separation from B-1 Aft Bay. In *Proceedings of the 46th AIAA Aerospace Sciences Meeting and Exhibit*, Reno, Nevada, USA, 7-10 January 2008.

[41] J.A. Freeman. Applied Computational Fluid Dynamics in Support of Aircraft/Store Compatibility and Weapons Integration. In *Proceedings of the 31st Annual International Symposium on Computer Architecture*, pages 132 – 137. IEEE, 7–11 June 2004.

[42] J.L. Wagner, S.J. Beresh, K.M. Casper, J. Henfling, R. Spillers, P. Hunter, and R. Mayes. Experimental Investigation of Fluid-Structure Interactions in Compressible Cavity Flows. In *Proceedings of the 43rd Fluid Dynamics Conference*, San Diego, California, USA, 24-27 June 2013.

[43] W. Sutherland. The Viscosity of Gases and Molecular Force. *Philosophical Magazine*, 5(36):507–531, 1893.

[44] J. Boussinesq. Essai Sur La Thorie Des Eaux Courantes. *Mmoires Prsents par Divers Savants L'Acadmie Des Sciences*, 23(1):1–680, 1872.

[45] S.J. Lawson and G.N. Barakos. Evaluation of DES for Weapons Bays in UCAVs. *Aerospace Science and Technology*, 14(6):397 – 414, 2010.

[46] P.R. Spalart and S.R. Allmaras. A One-Equation Turbulence Model for Aerodynamic Flows. *La Recherche Aerospatiale*, 1:5–21, 1994.

[47] D.C. Wilcox. Multiscale Model for Turbulent Flows. *AIAA Journal*, 26(11):1311–1320, 1988.

[48] F.R. Menter. Two–Equation Eddy–Viscosity Turbulence Models for Engineering Applications. *AIAA Journal*, 32(8):1598–1605, August 1994. Also paper AIAA-1993-2906.

[49] P.R. Spalart, W-H. Jou, M. Strelets, and S.R. Allmaras. Comments on the Feasibility of LES for Wings, and on a Hybrid RANS/LES Approach. In *Proceedings of the 1st AFOSR International Conference On DNS/LES, Columbus, OH, August 4-8*, 1997.

[50] J. Smagorinsky. General Circulation Experiments with the Primitive Equations. *Monthly Weather Review*, 91(3):99–164, March 1963.

[51] F.R. Menter, M. Kuntz, and R. Bender. A Scale-Adaptive Simulation Model for Turbulent Flow Predictions. In *Proceedings of the 41st Aerospace Sciences Meeting and Exhibit*, Reno, Nevada, USA, 6-9 January 2003.

[52] F.R. Menter and Y. Egorov. Revisiting The Turbulent Length Scale Equation. In *IUTAM Symposium: One Hundred Years of Boundary Layer Research*, Gottingen, 2004.

[53] F.R. Menter and Y. Egorov. A Scale Adaptive Simulation Model using Two-Equation Models. In *Proceedings of the 43rd AIAA Aerospace Sciences Meeting and Exhibit*, San Diego, California, USA, 24-27 June 2005.

[54] F.R. Menter and Y. Egorov. The Scale-Adaptive Simulation Method for Unsteady Turbulent Flow Predictions. Part 1: Theory and Model Description. *Flow, Turbulence and Combustion*, 85(1):113–138, 2010.

[55] Y. Egorov, F.R. Menter, R. Lechner, and D. Cokljat. The Scale-Adaptive Simulation Method for Unsteady Turbulent Flow Predictions. Part 2: Application to Complex Flows. *Flow, Turbulence and Combustion*, 85(1):139–165, 2010.

[56] S. Osher and S. Chakravarthy. Upwind Schemes and Boundary Conditions with Applications to Euler Equations in General Geometries. *Journal of Computational Physics*, 50:447–481, 1983.

[57] B. Van Leer. Towards the Ultimate Conservative Conservative Difference Scheme II: Monotonicity and Conservation Combined in a Second Order Scheme. *Journal of Computational Physics*, 14:361–374, 1974.

[58] G.D. van Albada, B. van Leer, and W.W. Roberts. A Comparative Study of Computational Methods in Cosmic Gas Dynamics. *Astronomy and Astrophysics*, 108:76–84, April 1982.

[59] A. Jameson. Time Dependent Calculations Using Multigrid, with Applications to Unsteady Flows Past Airfoils and Wings. In *Proceedings of the 10th AIAA Computational Fluid Dynamics Conference, Honolulu, Hawaii, USA, 24-26 June*, 1991. AIAA-1991-1596.

[60] J. E. Rossiter. A Preliminary Investigation into Armament Bay Buffet at Subsonic and Transonic Speeds. Technical Report AERO.679, Royal Aircraft Establishment, August 1960.

[61] J. E. Rossiter. A Note on Periodic Pressure Fluctuations in the Flow Over Open Cavities. Technical Report AERO.743, Royal Aircraft Establishment, November 1961.

[62] J. E. Rossiter. The Effects of Cavities on the Buffetting of Aircraft. Technical Report AERO.754, Royal Aircraft Establishment, April 1962.

[63] J.E. Rossiter and A.G. Kurn. Wind Tunnel Measurements of the Unsteady Pressures In and Behind a Bomb Bay (Canberra). Technical Report AERO.2845, Royal Aircraft Establishment, October 1962.

[64] J.E. Rossiter and A.G. Kurn. Wind Tunnel Measurements of the Unsteady Pressures In and Behind a Bomb Bay (T.S.R.2). (AERO.2677), August 1963.

[65] J. E. Rossiter. Wind Tunnel Experiments on the Flow Over Rectangular Cavities at Subsonic and Transonic Speeds. Technical Report 64037, Royal Aircraft Establishment, October 1964.

[66] H.H. Heller, D.G. Holmes, and E.E. Covert. Flow-Induced Pressure Oscillations In Shallow Cavities. *Journal of Sound and Vibration*, 18(4):545 – 553, 1971.

[67] D.G. Childers (ed.). *Modern Spectrum Analysis*. Chapter 2, pp. 23-148. IEEE Press, New York, 1978.

[68] L. Larcheveque, P. Sagaut, and P. Comte. Large-Eddy Simulation of a Compressible Flow in a Three-Dimensional Open Cavity at High Reynolds Number. *Journal of Fluid Mechanics*, 516:265–301, 2004.

[69] A.D. Pierce. *Acoustics: An Introduction to its Physical Principles and Applications*. Woodbury, New York: Acoustical Society of America, 1989.

[70] S. Qian and D. Chen. Joint Time-Frequency Analysis. *Signal Processing Magazine, IEEE*, 16(2):52–67, March 1999.

[71] M.A. Kegerise, E.F. Spina, S. Garg, and L.N. Cattafesta. Mode-Switching and Nonlinear Effects In Compressible Flow Over a Cavity. *Physics of Fluids (1994-present)*, 16(3):678–687, 2004.

[72] J.C.R Hunt, A.A. Wray, and P. Moin. Eddies, Streams and Convergence Zones in Turbulent Flows. In *Proceedings of the Summer Program, Center for Turbulence Research*, pages 193–207, 1988. N89-24555.

[73] J. Jeong and F. Hussain. On the Identification of a Vortex. *Journal of Fluid Mechanics*, 285:69–94, 1995.

[74] M. Wu and M.P. Martin. Direct Numerical Simulation of Supersonic Turbulent Boundary Layer over a Compression Ramp. *AIAA Journal*, 45:879–889, April 2007.

[75] B. Cabral and L.C. Leedom. Imaging Vector Fields using Line Integral Convolution. In *SIGGRAPH*, pages 263–270. ACM, 1993.

[76] R.D. Knowles, M.V. Finnis, A.J. Saddington, and K. Knowles. Planar visualization of vortical flows. *Proceedings of the Institution of Mechanical Engineers, Part G: Journal of Aerospace Engineering*, 220(6):619–627, 2006.

[77] B. Khanal, K. Knowles, and A.J. Saddington. Computational Investigation of Cavity Flow Control Using a Passive Device. *The Aeronautical Journal*, 116(1176):153–174, 2012.

[78] G. Berkooz, P. Holmes, and J.L. Lumley. The Proper Orthogonal Decomposition in the Analysis of Turbulent Flows. *Annual Review of Fluid Mechanics*, 25:539–575, 1993.

[79] J.L. Lumley. *Stochastic Tools in Turbulence, Volume 12*. Applied Mathematics and Mechanics, An International Series of Monographs. Academic Press, 1970.

[80] L. Sirovich. Turbulence and the Dynamics of Coherent Structures. *Quarterly of Applied Mathematics*, 45(3):561–571, October 1987.

[81] C.W. Rowley, T. Colonius, and R.M. Murray. Model Reduction for Compressible Flows Using POD and Galerkin Projection. *Physica D*, 189:115–129, 2004. http://dx.doi.org/10.1016/j.physd.2003.03.001.

[82] N. Sinha, S. Arunajatesan, and L.S. Ukeiley. High Fidelity Simulation of Weapon Bay Aeroacoustics and Active Flow Control. In *Proceedings of the 6^{th} AIAA/CEAS Aeroacoustics Conference, Lahaina, Hawaii, June 12–14*, 2000. AIAA-2000-1968.

[83] B. Podvin, Y. Fraigneau, F. Lusseyran, and P. Gougat. A Reconstruction Method for the Flow Past an Open Cavity. *Journal of Fluids Engineering*, 128:531–540, May 2006.

[84] S.J. Lawson. Parallel Performance of Library Algorithms for Computational Engineering. Master's thesis, University of Edinburgh, October 2007.

[85] X. Gloerfelt. Compressible Proper Orthogonal Decomposition/Galerkin Reduced–Order Model of Self–Sustained Oscillations in a Cavity. *Physics of Fluids*, 20(115105), November 2008.

[86] L. S. Blackford, J. Choi, A. Cleary, E. D'Azevedo, J. Demmel, I. Dhillon, J. Dongarra, S. Hammarling, G. Henry, A. Petitet, K. Stanley, D. Walker, and R. C. Whaley. *ScaLAPACK Users' Guide*. Society for Industrial and Applied Mathematics, Philadelphia, PA, 1997.

[87] M. Jarkowski, M.A. Woodgate, G.N. Barakos, and J. Rokicki. Towards Consistent Hybrid Overset Mesh Methods for Rotorcraft CFD. *International Journal for Numerical Methods in Fluids*, 74(8):543–576, 2014.

[88] N. Taylor. Initial Aero and Structural Datapack (for use in accordance with GS31072009). Technical Report AERO/IRAD/11/M-034, MBDA, 2011.

[89] MSC Software Corporation. MSC Nastran 2005 Release Guide. 2005.

[90] F. Dehaeze and G.N. Barakos. Mesh Deformation Method for Rotor Flows. *Journal of Aircraft*, 49(1):8292, January 2012.

[91] G.N. Barakos, S.J. Lawson, R. Steijl, and P. Nayyar. Numerical Simulations of High–Speed Turbulent Cavity Flows. *Flow, Turbulence and Combustion*, 83(4):569–585, December 2009. doi:10.1007/s10494-009-9207-1.

[92] S.J. Lawson and G.N. Barakos. Assessment of Passive Flow Control Devices for Transonic Cavity Flows Using DetachedEddy Simulation. *Journal of Aircraft*, 46(3):10091029, MayJune 2009.

[93] ANSYS. Documentation for ANSYS ICEM CFD v13 - User Manual. `www.academia.edu/3196257/ANSYS_ICEM_CFD_13_User_Manual`. Accessed on 28th March 2014.

[94] P. Nayyar. *CFD Analysis of Transonic Turbulent Cavity Flows*. PhD thesis, University of Glasgow, August 2005.

[95] T. Berglind and L. Tysell. Time-Accurate CFD Approach to Numerical Simulation of Store Separation Trajectory Prediction. In *Proceedings of the 29th AIAA Applied Aerodynamics Conference*, Honolulu, Hawaii, USA, 27-30 June 2011.

[96] H. Yang, R. Kannan, and A. Przekwas. A Nonlinear Reduced Order Method with Overset Adaptive Cartesian/Unstructured Grid for Moving Body Simulation. In *Proceedings of the 50st AIAA Aerospace Sciences Meeting*, Nashville, Tennessee, USA, 6-9 January 2012.

[97] H.O. Demir and N. Alemdaroglu. Trajectory calculation of a store released from a fighter aircraft. In *Proceedings of the 43rd AIAA Aerospace Sciences Meeting and Exhibit*, San Diego, California, USA, 24-27 June 2005.

[98] E. Oktay, O. Merttopcuoglu, and H.U. Akay. An Approach for Parallel CFD Solutions of Store Separation Problems. In *Parallel Computational Fluid Dynamics 2007*, volume 67 of *Lecture Notes in Computational Science and Engineering*, pages 393–400. Springer Berlin Heidelberg, 2009.

[99] E.E. Panagiotopoulos and S.D. Kyparissis. CFD Transonic Store Separation Trajectory Predictions with Comparison to Wind Tunnel Investigations. *International Journal of Engineering*, 3, January 2010.

[100] D. Snyder, E. Koutsavdis, and J. Anttonen. Transonic Store Separation Using Unstructured CFD with Dynamic Meshing. In *Proceedings of the 33rd AIAA Fluid Dynamics Conference and Exhibit*, Orlando, Florida, USA, 23-26 June 2003.

[101] L. Tang, J. Yang, and J. Lee. Hybrid Cartesian Grid/Gridless Algorithm for Store Separation Prediction. In *Proceedings of the 48th AIAA Aerospace Sciences Meeting Including the New Horizons Forum and Aerospace Exposition*, Orlando, Florida, USA, 4-7 January 2010.

[102] T.K. Ching. Grid Survey Approach to Store Separation Trajectory Prediction. *Journal of Aircraft*, 37(4):736–738, 2000.

[103] S. Lee, M. Park, K.W. Cho, and J.H. Kwon. New Fully Automated Procedure for the Prediction of Store Trajectory. *Journal of Aircraft*, 37(6):1038–1049, 2000.

[104] L.E. Lijewski and N.E. Suhs. Time-Accurate Computational Fluid Dynamics Approach to Transonic Store Separation Trajectory Prediction. *Journal of Aircraft*, 31(4):886–891, 1994.

[105] M.H. Pandya, N.T. Frink, and R.W. Noack. Progress Toward Overset-Grid Moving Body Capability for USM3D Unstructured Flow Solver. *AIAA Journal*, June 2005.

[106] G. Power, J. Calahan, and D. Hensley. A System for Moving Body CFD Simulations on Overset Structured and Unstructured Grids. In *Proceedings of the 42nd AIAA Aerospace Sciences Meeting and Exhibit*, Reno, Nevada, USA, 5-8 January 2004.

[107] Z.J. Wang and R. Kannan. An Overset Adaptive Cartesian/Prism Grid Method for Moving Boundary Flow Problems. In *Proceedings of the 43rd AIAA Aerospace Sciences Meeting and Exhibit*, San Diego, California, USA, 24-27 June 2005.

[108] Peter Cavallo, Neeraj Sinha, and Gregory Feldman. Parallel Unstructured Mesh Adaptation for Transient Moving Body and Aeropropulsive Applications. In *Proceedings of the 42nd AIAA Aerospace Sciences Meeting and Exhibit*, Reno, Nevada, USA, 5-8 January 2004.

[109] M. Davis and T. Welterlen. Minimized Domain CFD for Store Separation. In *Proceedings of the 41st Aerospace Sciences Meeting and Exhibit*, Reno, Nevada, USA, 6-9 January 2003.

[110] J.R. Hooker and J.A. Gudenkauf. Application of the Unstructured Chimera Method for Rapid Weapons Trajectory Simulations. In *Proceedings of the 45th AIAA Aerospace Sciences Meeting and Exhibit*, Reno, Nevada, USA, 8-11 January 2007.

[111] R. Noack and D. Boger. Improvements to SUGGAR and DiRTlib for Overset Store Separation Simulations. In *Proceedings of the 47th AIAA Aerospace Sciences Meeting including The New Horizons Forum and Aerospace Exposition*, Orlando, Florida, USA, 5-8 January 2009.

[112] J. Gong, Z. Zhou, and B. Liu. Using the Unstructured Dynamic Mesh to Simulate Multi-Store Separating from Aircraft. *Procedia Engineering*, 16:572–580, 2011. International Workshop on Automobile, Power and Energy Engineering.